Control of laminar streaks and Görtler vortices in pre-transitional boundary layers

Ludovico Fossà

A thesis submitted in partial fulfilment of the requirements for the degree of

Doctor of Philosophy

University of Sheffield

Faculty of Engineering

School of Mechanical, Aerospace & Civil Engineering

Submission Date

18 October 2024

Devo tutto alla mia famiglia per la fiducia, per il supporto e per aver sempre incoraggiato la curiosità verso le cose del mondo.
Un grazie particolare a mia sorella Daria, per l'affetto che mi ha sempre dimostrato e perché mi costringe a fare i conti con me stesso di tanto in tanto.

Acknowledgements

The author acknowledges the financial support of the U.S. Air Force through AFOSR grant FA8655-21-1-7008 (International Program Office - Dr Douglas Smith). The views and conclusions contained herein are those of the author and should not be interpreted as necessarily representing the official policies or endorsements, either expressed or implied, of the funding agencies or the U.S. Government.

The author is indebted to Prof Pierre Ricco for his guidance. Pierre is a caring supervisor and a passionate scientist, and the author feels fortunate to have been one of his students. The author also extends his thanks to Prof Lian Duan and his research group, who hosted him at Ohio State University in November 2022, and to the examiners Dr Ashley Willis (University of Sheffield) and Prof Xuesong Wu (Imperial College London), whose comments enhanced the quality of this thesis.

The colleagues in the Farm have provided the perfect environment. The author thanks them for the good times together, the trips to the Peaks, the bouldering sessions, and even for some (rare) thought-provoking discussions. A special mention goes to Dr Dongdong Xu and Ms Kaixin Zhu for sharing their expertise in asymptotics with a 盲人摸象.

Finally, the author expresses sincere and heartfelt gratitude to the wonderful people he met in Sheffield, whose warmth and kindness made him feel at home from the moment he arrived.

Abstract

Maintaining persistent laminar flow over high-speed vehicles and in supersonic wind-tunnel nozzles is essential: for vehicles, it minimizes friction drag and thermal load, while for wind tunnels, it ensures the development of facilities with low background turbulence. This thesis investigates the effects of active and passive control techniques on the receptivity and growth of laminar streaks and Görtler vortices in pre-transitional compressible boundary layers using asymptotic and numerical methods.

In chapter 2, the effect of uniform suction on pre-transitional compressible Görtler vortices is studied. Uniform suction reduces the amplitude of steady and unsteady Görtler vortices and is more effective when the Blasius boundary layer rapidly adjusts to the asymptotic-suction boundary layer. Its effect weakens as the free-stream Mach number increases. A thinner boundary layer prevents the exponential growth of the vortices because the wall-normal momentum equation becomes uninfluential at leading order and therefore the curvature effects responsible for the inviscid pressure-centrifugal imbalance are negligible. Uniform suction leads to a broadening of the the stability regions and favors the presence of weak Tollmien-Schlichting waves at the expense of more energetic Görtler vortices for relatively high disturbance frequencies and Mach numbers.

In chapter 3, supersonic pre-transitional boundary layers flowing over porous surfaces are studied. The porous wall is composed of thin equally-spaced cylindrical microcavities. When the spanwise wavelength is much larger than the boundary-layer thickness, these disturbances are effectively attenuated by the porous surface. The unsteady laminar streaks evolve into oblique Tollmien-Schlichting waves through a leading-edge-adjustment receptivity mechanism. The wavenumber of these waves is only slightly modified over the porous surface, while the growth rate increases, thus confirming previous experimental results. An asymptotic

analysis based on the triple-deck theory confirms these numerical findings. When the wall is concave, the amplitude of the laminar streaks is enhanced by the wall curvature and is attenuated by the wall porosity during the initial development.

In chapter 4, a compressible laminar boundary layer developing over an isotropic porous substrate is studied. The substrate is modeled as an array of cubes. The momentum and enthalpy balance equations are derived by volume averaging. The self-similar solution proposed by Tsiberkin (*Transp. Porous Media* 121(1):109–120, 125(2):259–269, 2018) for streamwise-growing permeability is extended to include compressibility, heat conduction and a nonlinear drag. The velocity profile shows an inflection point at the free fluid-porous interfacial layer, below which it decreases to zero. In the upstream (i.e. boundary-layer) limit of the disturbance flow, the velocity and temperature streaks are enhanced by wall porosity.

Contents

List of Figures

List of Tables

Journal articles and conferences

This thesis includes research that has been presented in the following publications and conferences.

Journal articles

- P. Ricco and L. Fossà [July 2023b]. "Receptivity of compressible boundary layers over porous surfaces". In: *Phys. Rev. Fluids* 8 [7], p. 073903. DOI: 10.1103/PhysRevFluids.8.073903
- L. Fossà and P. Ricco [2024a]. "Attenuation of compressible Görtler vortices by uniform suction". In: *J. Fluid Mech.* Submitted (second revision).
- L. Fossà and P. Ricco [2024b]. "Compressible laminar boundary layers over isotropic porous substrates". In: *Transp. Porous Media.* Submitted.

Conferences

- L. Fossà and P. Ricco [Nov. 2023a]. "Compressible Boundary Layers over Isotropic Porous Substrates". In: *76th Ann. Meet. Div. Fluid Dyn.* Bull. Am. Phys. Soc. Washington, DC, USA
- L. Fossà and P. Ricco [Oct. 2023b]. "Compressible Boundary Layers over Isotropic Porous Substrates". In: *UK Fluids Conf.* UKFC. Glasgow, United Kingdom
- L. Fossà and P. Ricco [Aug. 2023d]. "Supersonic Pre-Transitional Disturbances in Boundary Layers on Porous Surfaces". In: *10th Int. Congr. Ind. Appl. Math.* ICIAM. Tokyo, Japan
- P. Ricco and L. Fossà [July 2023a]. "Receptivity and Passive Control of Compressible Boundary Layers". In: *2023 AFOSR/ONR/HVSI Ann. High-Speed Aerodyn. Portf. Rev.* AFOSR/ONR/HVSI. College Park, MD, USA

- L. Fossà and P. Ricco [June 2023c]. "Receptivity of compressible boundary layers on flat and concave porous surfaces". In: *22nd Int. Couette-Taylor Workshop*. ICTW. Barcelona, Spain

- L. Fossà and P. Ricco [Nov. 2022a]. "Supersonic Pre-Transitional Disturbances in Boundary Layers on Porous Surfaces". In: *75th Ann. Meet. Div. Fluid Dyn.* Bull. Am. Phys. Soc. Indianapolis, IN, USA

- L. Fossà and P. Ricco [Sept. 2022b]. "Supersonic Pre-Transitional Streaks over Porous Surfaces". In: *Joint ERCOFTAC/EU-CTFF Eur. Drag Reduct. Flow Control Meet. EDRFCM*. Paris, France

Chapter 1

Introduction

Active and passive control methods for delaying the laminar-to-turbulent transition in high-speed boundary layers have been extensively studied using numerical, experimental and theoretical approaches. Developing effective control strategies is crucial for aerospace applications, such as heat-transfer management in reentry vehicles and supersonic transport systems [Martin et al., 2012; Schmisseur, 2015], as well as for the design of hypersonic quiet tunnels, where minimizing noise contamination is critical [F.-J. Chen et al., 1989; F.-J. Chen et al., 1992; Schneider, 2008a]. These strategies primarily aim to modify boundary-layer properties near the wall, suppressing disturbance growth and extending the laminar regime.

This thesis investigates the effects of uniform wall suction and passive porous walls on the excitation and evolution of unsteady, three-dimensional disturbances using asymptotic and numerical methods. Section 1.1 discusses the mechanisms of disturbance excitation and transient growth. The influence of wall suction is reviewed in §1.2, while §1.3 introduces porous media flows and examines the role of passive porous coatings. Finally, the thesis is outlined in §1.4.

1.1 Receptivity and disturbance growth in laminar boundary layers

Laminar boundary layers are susceptible to free-stream disturbances that excite the growth of persistent velocity and temperature perturbations in the early stage of transition. In the words of Morkovin [1969], the term receptivity refers to the internalization of external agents and their subsequent evolution within the boundary layer. Disturbances of the vortical, acoustic and entropic type were first distinguished by Kovasznay [1953]: vortical disturbances consist in transversal velocity waves and

exist at all speeds, while the acoustic and entropy ones are only present in compressible flows. The disturbance amplitude is sometimes characterized by the turbulence intensity, $Tu = u^*_{rms}/U^*_\infty$, where u^*_{rms} is the root mean square of the fluctuations about the free-stream velocity U^*_∞.

When Tu is very low ($< 0.1\%$), the early stage of transition is dominated by the exponential growth of the unstable eigenmodes such as the Tollmien-Schlichting (TS) waves described by linear stability theory [Criminale et al., 2003]. Goldstein and Hultgren [1989] pointed out that the pioneering experiment of Schubauer and Skramstad [1947] was indeed a study on the receptivity of a laminar boundary layer to low-amplitude harmonic disturbances and the excitation and linear growth of TS waves. In incompressible flat-plate boundary layers, TS waves are excited by free-stream velocity fluctuations via a leading-edge adjustment mechanism [Goldstein, 1983].

When Tu is relatively high ($0.1\% \leq Tu < 1\%$), the early stage of transition in flat-plate boundary layers is dominated by the algebraic growth of externally forced perturbations rather than the exponential amplification of unstable eigenmodes. Albeit still present, modal growth ceases to be predominant and transient-growth [Reshotko, 2001] and bypass mechanisms [Dryden, 1937; Morkovin, 1985] take over. The high-amplitude, low-frequency streamwise velocity fluctuations that result define streamwise-elongated, spanwise-adjacent regions of accelerating and decelerating flow, the spanwise (transverse) direction being perpendicular to the streamwise and wall-normal ones.

Receptivity, transient growth and bypass transition are more complex and multifaceted in high-speed compressible flows. TS waves are also excited by the scattering of acoustic waves with roughness elements [Goldstein, 1985] or by the interaction of acoustic and free-stream vortical disturbances [X. Wu, 1999] and the first and second Mack modes arise in the supersonic regime [Mack, 1984]. Early measurements on supersonic and hypersonic boundary layers reported higher critical Reynolds numbers compared to the incompressible case [Demetriades, 1960] and highlighted the significance of vortical and acoustic disturbances near the leading edge [Laufer and Vrebalovich, 1960]. These findings suggested a complex picture of the early stage of transition at moderate supersonic Mach numbers. Although the inviscid second Mack mode is often considered the predominant source of instability in supersonic boundary layers [Mack, 1984; Schneider, 2001], the presence of first-mode disturbances and laminar streaks excited by free-stream vorticity has been reported in

supersonic and hypersonic wind tunnels [Schneider, 2008a; Schneider, 2008b]. Vortical fluctuations cannot be ruled out in the low-frequency band below 8 kHz, as the hot-wire signal distills the velocity fluctuations of the vortical and acoustic disturbances together [Morkovin, 1959; Duan et al., 2019], and disturbances of all types are present downstream of a shock wave [McKenzie and Westphal, 1968] and have been reported in supersonic and hypersonic wind tunnels [Schneider, 2008a]. Graziosi and G. L. Brown [2002] reported low-frequency disturbances in a pre-transitional Mach-3 boundary layer exposed to vortical and acoustic free-stream fluctuations. In the experiments of Hofferth et al. [2013] and Borg et al. [2015], the energy content measured at low frequencies was comparable with that at the significantly higher frequency associated with the second Mack mode for all the unit Reynolds numbers considered. In spite of these findings, recent experiments have either focused exclusively on the characterization of acoustic pressure fluctuations [Duan et al., 2019] or postulated the rapid decay of free-stream vorticity across the throat section of the tunnel [Thasu and Duvvuri, 2024]. Nevertheless, the evolution of the laminar streaks is of interest in the investigation and implementation of control techniques in high-speed wind tunnels where levels of Tu are relatively high and the streaks can turn into Görtler vortices over smooth concave walls [F.-J. Chen et al., 1992; Schneider, 2008a].

1.1.1 Disturbances on flat plates: laminar streaks

In his pioneering account of bypass transition, Dryden [1937] reported the onset of spanwise-adjacent, streamwise-elongated laminar structures in a Blasius boundary layer perturbed by free-stream turbulence. Klebanoff and Tidstrom [1959] and Klebanoff, Tidstrom, and Sargent [1962] used the vibrating-ribbon technique of Schubauer and Skramstad [1947] to generate controlled disturbances in an incompressible wind tunnel. They observed a spanwise-periodic thickening and thinning of the boundary layer which was later described empirically [Bradshaw, 1965] and via asymptotic methods [Crow, 1966]. Mounting evidence [Tani, 1969] pointed to the key role played by free-stream turbulence on the excitation and disturbance growth in laminar boundary layers. Motivated by this findings, Klebanoff investigated the effect of disturbances of moderate amplitude ($Tu \leq 0.3\%$) on transition. His results, which were presented at a conference meeting [Klebanoff, 1971] and yet never published on a journal [Kendall, 1985; Kendall, 1990; Kendall, 1998; Goldstein and Wundrow, 1998], showed the presence of streamwise-elongated (*streaky*) fluctuations of very low frequency ($\leq$ 12Hz) and a cyclic spanwise thinning and thickening of the boundary layer. These laminar streaks have been referred to as *breathing modes* or

Klebanoff modes within the transition community, although their growth is strictly non-modal. Incompressible laminar streaks were studied by Westin et al. [1994], who compared the autocorrelation function and the power spectral density of the free-stream and the boundary-layer regions and attributed the observed low-frequency peak to streamwise-elongated structures with a constant spanwise wavelength. Their findings were supported by the hot-wire measurements of Matsubara and Alfredsson [2001], who observed that the disturbance energy increases with the Reynolds number based on the streamwise coordinate and provided clear visualizations of the breakdown of laminar streaks. The energy growth was initially observed for low wavenumbers (figure 13 therein), and the measured spanwise spectra showed a higher energy content at low frequency and a lower energy content at high frequency compared to the free stream. These results suggested the role of the boundary layer as a low-pass filter [Ricco, Walsh, et al., 2016].

Measurements in compressible wind tunnels have focused on the role of high-frequency ($\geq$ 10kHz) perturbations [F.-J. Chen et al., 1989; Maslov, Shiplyuk, et al., 2001; Graziosi and G. L. Brown, 2002], while the excitation of low-frequency laminar streaks by free-stream turbulence has drawn far less attention. Kendall [1975] argued that, even in the presence of relatively high-amplitude acoustic disturbances, the second Mack mode may play a minor role in transition compared to the nonlinear low-frequency perturbations. In fact, velocity spectra sampled at Mach 8.5 showed a marked peak at frequencies below the first Mack mode, a hallmark of periodic laminar structures. Recently Muñoz et al. [2014] observed streaky structures in the cross flow over a cone in a Ludwieg tube at Mach 6.

The effect of free-stream turbulence on bypass transition has been investigated also via direct numerical simulations of incompressible flat-plate boundary layers [Rai and Moin, 1993; Nagarajan et al., 2007; Ovchinnikov et al., 2008; Brinkerhoff and Yaras, 2015]. In these studies, the isotropic grid turbulence at the inlet was seeded sufficiently far upstream of the leading edge to capture the excitation and the evolution of the streaks. Ohno et al. [2023] performed direct numerical simulations of bypass transition in a compressible boundary layer. Instead of imposing an isotropic turbulent field upstream of the leading edge, they seeded the inflow using a continuous spectrum of Orr-Sommerfeld modes [Jacobs and Durbin, 2001]. The practice of imposing free-stream disturbances described by the linear stability analysis of a parallel wall flow was questioned by X. Wu and Dong [2016], who pointed out that neglecting non-parallel effects leads to a spurious entanglement of Fourier modes and an unrealistically high magnitude of the streamwise disturbance velocity component in the free

stream [Ricco, Walsh, et al., 2016]. Direct numerical simulations of boundary layers perturbed by grid turbulence in the fashion of Ovchinnikov et al. [2008] remain an expensive task and have not been performed in the compressible regime.

1.1.2 Disturbances on concave plates: Görtler vortices

A convective instability affects laminar boundary layers developing over streamwise-concave surfaces. An inviscid mechanism similar to the one responsible of Couette-Taylor instability [Saric, 1994] leads to the formation of Görtler vortices, streamwise-oriented and spanwise-adjacent counterrotating structures which ensue when the wall-normal pressure gradient cannot balance the centrifugal force. This behavior was reportedly first illustrated by von Kármán [1934] with an argument based on Kelvin's circulation theorem [Charru and Forcrand-Millard, 2011]. The perturbations evolve as laminar streaks near the leading edge and engage in a quasi-exponential growth downstream. The rapid amplification of the velocity disturbances causes the breakdown to turbulence via secondary-instability mechanisms [Swearingen and Blackwelder, 1987]. In compressible boundary layers, temperature fluctuations also play an important role in the transition process [Q. Wang et al., 2018]. Amongst different external perturbations, free-stream vortical disturbances have been recognized as powerful external initiators of convective instability at low speeds [Swearingen and Blackwelder, 1987; Tandiono et al., 2008; Borodulin et al., 2018] and results from direct numerical simulations indicate free-stream vorticity as a critical cause of Görtler vortices in the supersonic and hypersonic regime [Zhong and Whang, 2002; Whang and Zhong, 2003]. Nevertheless, many wind tunnel measurements in the incompressible regime [Tani, 1962; Finnis and A. Brown, 1997] and the compressible regime [de Luca et al., 1993; Ciolkosz, 2006; Q. Wang et al., 2018] have focused on the streamwise evolution of the vortices without addressing receptivity. A comprehensive review of wind-tunnel experiments and numerical simulations on compressible Görtler vortices is given by Xu, Ricco, et al. [2024].

1.1.3 Receptivity: an asymptotic framework

The accurate computation of the generation and evolution of laminar streaks and Görtler vortices is crucial for predicting transition, yet it presents significant theoretical challenges. Experimental evidence of non-modal growth in laminar boundary layers motivated research into the algebraic amplification of streaks in the 1970s. Originally formulated for inviscid parallel flows [Ellingsen and Palm, 1975; Landahl, 1980],

transient-growth theory describes disturbance growth due to the non-orthogonality of the linearized Navier-Stokes operators, primarily through the lift-up effect and vortex tilting of wall-normal vorticity [Butler and Farrell, 1992; Trefethen et al., 1993]. This input-output framework has since been extended to account for non-parallel effects and to study optimal disturbances in developing boundary layers [Andersson et al., 1999; Luchini, 2000]. As pointed out by Wundrow and Goldstein [2001], while transient-growth computations predict normalized streamwise velocity perturbation profiles in good agreement with experiments, they fail to capture the correct streamwise evolution of the disturbance amplitude when the upstream and outer boundary conditions are not rigorously specified and receptivity is neglected. This limitation also applies to boundary layers on concave surfaces: as first noted by Hall [1983], the convective nature of the centrifugal instability results in a critical dependence of the disturbance growth and neutral curves on the upstream flow conditions. The asymptotic analysis by Hall [1983] revealed that the eigenvalue approach [e.g. El-Hady and Verma, 1981] is not tenable in general and that the rigorous computation of the vortices requires the solution of an initial-boundary-value problem where the boundary-layer disturbances match the external perturbation flow [X. Wu, D. Zhao, et al., 2011; Xu, Ricco, et al., 2024].

A rigorous description of the incompressible laminar streaks was developed by Goldstein and co-workers [Leib et al., 1999, hereafter referred to as LWG99] and later extended by X. Wu, D. Zhao, et al. [2011] (hereafter WZL11) to Görtler vortices on concave walls. Through an asymptotic approach, they unraveled the physical interaction between the disturbances in the free stream and the laminar boundary layer. Their formulation hinges on the assumption of streamwise-elongated structures of small streamwise wavenumber $k_x \ll 1$ (i.e. negligible streamwise diffusion and streamwise pressure gradient), high Reynolds number $Re = U_\infty^* \lambda_z^* / \nu_\infty^* \gg 1$ (where λ_z^* is the spanwise wavelength and ν_∞^* the dynamic viscosity) and small amplitude $\epsilon \ll 1$. The laminar streaks and the Görtler vortices appear where the boundary-layer thickness is comparable to λ_z^*, and their evolution is governed by the unsteady boundary-region equations, which are streamwise-parabolic and crossflow-elliptic. The difference in magnitude between the spanwise and streamwise scales results in $O(\epsilon)$ free-stream fluctuations generating $O(\epsilon Re) = O(\epsilon / k_x)$ streamwise velocity disturbances in the boundary layer [Gulyaev et al., 1989; Choudhari, 1996].

The initial-value problem that arises is of parabolic nature, and thus suitable to a downstream-marching treatment. The computational cost is considerably lower than that required by the numerical solution of the complete Navier-Stokes equations.

LWG99's theory is based on the precise specification of the initial and boundary conditions and accounts the continuous outer forcing of the external vortical flow. The disturbances are linearized about the laminar Blasius boundary layer under the assumption that $\epsilon Re, \epsilon/k_x \ll 1$, resulting in a one-way coupling between the base flow and the superposed disturbances. The linear theory describes rather well the initial excitation and growth of the laminar streaks, their amplitude still being small and the intermodal coupling being negligible. The contribution of each monochromatic mode can be studied separately in this case. The linear incompressible theories of LWG99 and WZL11 were extended to the compressible case by Ricco and X. Wu [2007] and Viaro and Ricco [2019a], respectively.

The nonlinear theory instead applies when the amplitude of the the disturbances is comparable with that of the base flow ϵRe, $\epsilon/k_x = O(1)$. Nonlinearity results in a two-way coupling between the boundary-layer and external disturbance flow Ricco, Luo, et al. [2011]. Nonlinear Görtler vortices were investigated by Xu, Y. Zhang, et al. [2017], Marensi and Ricco [2017] and Xu, J. Liu, et al. [2020] in the asymptotic framework of LWG99. Their accurate specification of the initial and outer boundary conditions resulted in good agreement with the wind-tunnel data of Swearingen and Blackwelder [1987] and Tandiono et al. [2008]. For a review of LWG99's framework, a validation with wind-tunnel measurements and a comparison with optimal-growth, Taylor-Stewartson and Orr-Sommerfeld theories, the reader is referred to Ricco, Walsh, et al. [2016].

Compressible Görtler vortices engendered by free-stream vortical disturbances were studied by Viaro and Ricco [2019a], while the growth of nonlinear compressible streaks was addressed by Marensi, Ricco, and X. Wu [2017]. The combined effect of a continuous free-stream spectrum of vortical disturbances and nonlinearity was considered by Y. Zhang et al. [2011], while X. Wu and Dong [2016] included the contribution of short-wavelength free-stream disturbances in incompressible and compressible boundary layers.

1.2 Laminar flow control with wall suction

The persistence of laminar streaks and Görtler vortices in boundary layers and their role in bypass transition calls for control techniques aimed at their attenuation. Uniform wall suction is achieved by imposing a uniformly distributed wall-normal velocity across a permeable surface, thereby modifying the two-dimensional steady base flow.

Suction has been employed to prolong laminar flow in boundary layers, and significant effort has been dedicated to designing and testing suction actuators for aircraft wings, where TS waves [Reed et al., 1996] and crossflow instability are often regarded as primary transition mechanisms [Krishnan et al., 2017]. However, the influence of uniform suction on the excitation and growth of compressible laminar streaks and Görtler vortices remains unexplored and it is the object of chapter 2 of this thesis. This section focuses on the use of suction to attenuate laminar streaks and Görtler vortices in laminar boundary layers. Experimental studies, direct numerical simulations, and theoretical works are reviewed in §1.2.1, §1.2.2, and §1.2.3, respectively.

1.2.1 Experimental studies

The use of transpiration devices on wind-tunnel walls dates back to the 1960s [Schneider, 2008a]. Efforts to delay transition in supersonic wind tunnels were undertaken using longitudinal slots [Beckwith and Bertram, 1972; Beckwith, Harvey, et al., 1973] and perforated plates [Leontiev and Pavlyuchenko, 2008]. An issue with transpiration surfaces is related to their non-uniformities and defects. These imperfections are known to generate an isolated or distributed roughness effect to which the thinner suction boundary layer may be susceptible [Saric, 1985; Messing and Kloker, 2010]. The impact of distributed roughness on high-speed transition is however still poorly understood [Schneider, 2008b; Running et al., 2023]. While relatively large roughness (50µm to 500µm) dramatically triggers the breakdown to turbulence in absence of suction [Bountin et al., 2016; Gui, C. Zhang, et al., 2023], Ludwieg-tube measurements at subsonic speeds [Dimond, Costantini, Risius, et al., 2020; Dimond, Costantini, and Klein, 2022] and experiments in incompressible wind tunnels [Methel et al., 2021] suggest that suction effectively delays transition even in the presence of suction holes as large as 100 µm.

Fransson and Alfredsson [2003] applied uniform suction through a sintered-plastic plate with small pores ($\cong$ 10 µm) and reported an attenuation of TS waves and laminar streaks at low speeds and high free-stream turbulence levels Tu. Their results show a gradual evolution from the Blasius boundary layer to the asymptotic-suction boundary layer (ASBL) over the porous plate. Despite a twofold reduction in the boundary-layer thickness, the spanwise wavelength of the streaks λ_z^* was not affected. Yoshioka et al. [2004] measured λ_z^* in a series of experiments with suction, concluding that its value was primarily determined by the shape of the leading edge and the oncoming free-stream perturbation flow. Kurian and Fransson [2011] investigated the evolution of disturbances induced in an ASBL by an array of roughness elements.

Their findings showed good agreement with optimal growth predictions when the optimization time was chosen to fit the experimental data.

The experimental studies on the influence of suction on Görtler vortices are very limited. Mangalam et al. [1987] placed spanwise-aligned rods on the concave section of a wing profile and reported an attenuation of the velocity fluctuations associated with Görtler vortices. A selective transpiration technique was employed by Myose and Blackwelder [1995] on a concave boundary layer. They applied suction at periodic spanwise locations where the low-speed streaks were known to develop and reported a delay in the breakdown of the Görtler vortices.

To the best of the author's knowledge, there are no experimental investigations on compressible Görtler vortices evolving in suction boundary layers. Li et al. [2018] examined the use of uniform suction to mitigate Görtler instability on flared cones at zero angle of attack in a hypersonic wind tunnel. To that end, they manufactured a model comprising an aft cone and a rear flared cone with a truncated permeable volume installed on the aft section, although no measurements of the perturbed flow in the boundary layer were conducted. Furthermore, wall suction has never been used to attenuate Görtler vortices in boundary layers along the nozzles of supersonic wind tunnels, nor over the wetted surfaces of aircraft fuselages or engine intakes. Suction actuators have successfully delayed transition in boundary layers on aircraft wings, yet with no evidence that the perturbations involved were Görtler vortices [Krishnan et al., 2017].

1.2.2 Studies based on direct numerical simulations

Sescu et al. [2018] and Sescu et al. [2019] investigated the effect of localised blowing and suction by performing direct numerical simulations of a supersonic concave boundary layer. They implemented a feedback control algorithm to attenuate the nonlinear growth of the vortices. Direct numerical simulations were also employed to study how wall transpiration modifies perturbed Mach-6 boundary layers over flared cones, by Hader and Fasel [2021] for the case of alternate blowing and suction and by Hollender et al. [2019] for the case of distributed suction with the objective to reproduce the flow configuration studied experimentally by Li et al. [2018].

1.2.3 Theoretical studies

The effect of uniform wall transpiration on the linear stability of Görtler vortices has been studied for self-similar and asymptotic suction [Kobayashi, 1972; Kobayashi,

1974; El-Hady and Verma, 1981; El-Hady and Verma, 1984; Floryan and Saric, 1983]. Self-similar suction, which features an unbounded wall-normal velocity as the leading edge is approached, has never been implemented in laboratory. Self-similar solutions offer the advantage of being more tractable theoretically and often provide valuable insights into stability and transition, especially when solving a system of partial differential equations is not feasible [Stewartson, 1964; Anderson, 2019; Al-Malki et al., 2021]. Ricco and Dilib [2010] and Ricco, Shah, et al. [2013] imposed self-similar suction on incompressible and compressible laminar base flows to study the receptivity and growth of streaks and oblique TS waves within the asymptotic framework of Ricco and X. Wu [2007] and LWG99. Marensi and Ricco [2017] solved the nonlinear boundary-region equations in the asymptotic framework of LWG99 and reported a marked attenuation of the Görtler vortices in the presence of spanwise-dependent wall suction. Es-Sahli et al. [2023] applied an optimal-control technique to the nonlinear boundary-region equations and reported a marked attenuation of the energy growth. Within these theoretical frameworks, uniform wall suction has never been utilised to attenuate the growth of Görtler vortices at any Mach number.

The laminar flow modified by uniform suction is initially streamwise-dependent, with the asymptotic-suction solution being valid only sufficiently downstream of the onset of suction. The ASBL solution was first derived by Griffith and Meredith [1936] and later extended to the compressible regime by Young [1948]. Morduchow [1963] showed that it remains valid even in the presence of streamwise pressure gradients. An exact compressible solution was derived by Lew and Fanucci [1955] for the case where the wall suction was uniform at any streamwise location, while Görtler [1957] treated the case of arbitrary distributions of the suction velocity in the incompressible regime. Boundary layer receptivity plays a critical role at the leading edge, where the suction velocity is either zero or finite in practical applications [Fransson and Alfredsson, 2003]. In such cases, the self-similar suction model and the ASBL model may not accurately capture the effect of control on disturbance growth.

1.3 Laminar flow control with porous walls

The implementation of uniform wall suction requires the installation of actuators that are often heavy, voluminous and energy-consuming [Krishnan et al., 2017]. Albeit less flexible, passive control mechanisms such as porous walls effectively delay transition in high-speed boundary layers perturbed by acoustic waves at high frequency [Fedorov,

2011]. The impact of passive porous walls on receptivity to free-stream turbulence is the focus of chapters §3 and §4 of this thesis.

This section contains a general introduction to porous media flows in §1.3.1. Literature reviews on laminar flow control with passive (i.e. without suction) porous coatings and highly permeable porous coatings are presented in §1.3.2 and §1.3.3, respectively.

1.3.1 A preliminary introduction to porous media flows

A porous medium is a heterogeneous mixture of a solid material and a fluid phase. Consolidated porous media consist in a continuous solid matrix saturated by a liquid, a gas, or both [Attenborough, 1982]. The motion of the fluid phase is restricted by the geometry of the solid matrix. Most porous media feature a large separation of scales and are described either from a microscopic or from a macroscopic perspective. The microscopic approach focuses on the small-scale geometry of the pores and on the local interaction between the saturating fluid and the solid matrix [Bear, 2018]. The macroscopic approach considers the porous medium in its entirety and focuses on its bulk properties [Bear and Bachmat, 1990; Whitaker, 1998]. Adopting the macroscopic approach inevitably sacrifices some detail on local microscopic processes but reduces complexity. The pioneering work of Darcy [1856] followed this idea in deriving a linear relation between the efflux (seepage) velocity and the pressure gradient across the medium

$$\langle u_i \rangle_f^* = -\frac{K^*}{\mu^*} \frac{\partial \langle p \rangle_f^*}{\partial x_i^*}, \tag{1.1}$$

where $\langle u_i \rangle_f^*$ and $\langle p \rangle_f^*$ are the bulk velocity and pressure, μ^* the dynamic viscosity and K^* [m^2] the permeability, a macroscopic parameter measured in m^2 which accounts for the global effect of the microscopic geometry on the macroscopic motion. The non-dimensional form of (1.1) is

$$\langle u_i \rangle_f = -ReDa \frac{\partial \langle p \rangle_f}{\partial x_i}, \tag{1.2}$$

where $Re = \rho^* \langle u^* \rangle_f L^*/\mu^*$ is a Reynolds number, $Da = K^*/L^{*2}$ is Darcy number, L^* is a length of macroscopic heterogeneity (i.e., a spatial scale over which the macroscopic properties vary considerably). $Da \ll 1$ in a wide range of practical applications [Nield, 2000]. The linearity of (1.1) limits its validity to relatively small Reynolds numbers based on the pore diameter d_p^* or the grain diameter d_g^*, as the onset of nonlinearity is observed for $Re_d = O(1)$ or larger. The definition of Re_d is anything

but unique, as different lengths (e.g. $\sqrt{K^*}$, d_g^*) are often used [Goharzadeh et al., 2005]. Beavers and Sparrow [1969] performed experiments on metallic fiber lattices of different shape and size, and found that for all cases the pressure gradient was accurately represented by a second-degree polynomial of $\langle u_i \rangle_f^*$. Forchheimer [1901] had proposed an extension to 1.1

$$\frac{\partial \langle p \rangle_f}{\partial x_i} = -a \langle u_i \rangle_f - b \left| \langle u_i \rangle_f \right| \langle u_i \rangle_f , \tag{1.3}$$

which is known as the Darcy-Forchheimer equation [Joseph et al., 1982]. The coefficients a and b in (1.3) are not sensitive to the presence of solid boundaries [Beavers, Sparrow, and Rodenz, 1973] and the onset of nonlinearity does not imply that the microscopic flow is transitioning to turbulence [Wood et al., 2020]. The physical variables that appear in Darcy's law (1.2) and its extension (1.3) are empirical, and efforts have been made to express them in terms of macroscopic quantities.

Brinkman [1949] tried to reconcile Darcy's law (1.1) with the Navier-Stokes equations. He argued that, in the absence of inertial and unsteady terms, a small transition region exists at the interface of a porous medium and a free fluid region where K^* is unbounded. He added a term to the right-hand side of Darcy's law (often referred to as *Brinkman correction*)

$$\frac{\partial \langle p \rangle_f^*}{\partial x_i^*} = -\frac{\mu^*}{K^*} \langle u_i \rangle_f^* + \underbrace{\breve{\mu}^* \frac{\partial^2 \langle u_i \rangle_f^*}{\partial x_j^{*2}}}_{\substack{\text{Brinkman} \\ \text{correction}}} . \tag{1.4}$$

Here, $\breve{\mu}^*$ is a modified viscosity coefficient (*effective viscosity*) which is assumed equal to the dynamic viscosity μ^* in most practical cases [Nield and Bejan, 1999]. The Darcy and Forchheimer terms have been often introduced directly into the momentum balance together with the Brinkman correction [Joseph et al., 1982; Nield, 1991; Nield, 1994].

Further efforts [Whitaker, 1969; Hassanizadeh and Gray, 1979; Bachmat and Bear, 1986; Whitaker, 1966; Whitaker, 1967; Gray, 1975] aimed to reconcile (1.1) with the Navier-Stokes equations through a macroscopic approach. Their studies focused on the transport of extensive quantities – such as mass, momentum, and energy – within a saturated porous medium. The microscopic motion of the fluid phase is described by a set of macroscopic variables obtained by averaging the microscopic quantities over a representative elementary volume (REV), henceforth denoted with Ω_0^* [Bear

and Bachmat, 1967; Howes and Whitaker, 1985]. An important macroscopic property that arises is the volume porosity of the fluid phase

$$\theta_f = \frac{\Omega_f^*}{\Omega_0^*}, \tag{1.5}$$

which indicates the volume fraction of the porous medium saturated by the fluid phase Ω_f^*. The solid and fluid continua are distilled in a porous continuum governed by volume-averaged transport equations. The volume-averaging technique is similar to the Reynolds-averaging used for turbulent flows in that the extensive quantities q are decomposed in their volume-averaged $\langle q \rangle_f$ and fluctuating $\tilde{q}$ parts [Gray, 1975; Howes and Whitaker, 1985]

$$q = \langle q \rangle_f + \tilde{q}, \tag{1.6}$$

and the surface integral of the fluctuating shear stresses and the fluctuating pressure gradient needs to be expressed by means of a Darcy-Forchheimer closure model (1.3) [Whitaker, 1986; Whitaker, 1996]. Conversely, the volume averages of the nonlinear products of the velocity fluctuations $\langle u_i u_j \rangle_f$ account for what is known as *mechanical dispersion* [Bear and Bachmat, 1990; Bear, 2018], and are asymptotically smaller than the linear Darcy term and the nonlinear advection terms [refer to appendix A in Breugem, Boersma, and Uittenbogaard, 2006]. Whitaker [1996] derived the Forchheimer term by solving the Darcy-Forchheimer closure problem for the velocity and pressure fluctuations. He suggested that the inertial term should be neglected when the Forchheimer correction is present, as suggested by Nield [1991].

1.3.1.1 Flows at the interface of an isotropic porous medium

Fluid flows over saturated porous media are common in industrial and engineering contexts [Nield and Bejan, 2017; Vafai and Kim, 1990; Nield and Kuznetsov, 2003; Breugem, Boersma, and Uittenbogaard, 2005; Tsiberkin, 2016]. The effect of a porous boundary on a pressure driven channel-flow was first investigated by Beavers and Joseph [1967]. They considered a channel bounded by an impermeable wall at the top and a semi-infinite porous medium at the bottom and assumed a Darcy flow (1.2) in the porous region. They did not assume continuity in the velocity at the boundary, and defined the jump condition at the porous-channel interface located at $y = 0^+$

$$\left.\frac{\mathrm{d}u^*}{\mathrm{d}y^*}\right|_{0^+} = \frac{\beta_{int}}{\sqrt{K^*}} \left(u^*|_{0^+} - u_D^* \right) \tag{1.7}$$

where $u^*(0^+)$ is the slip velocity at the interface, u_D^* is the seepage velocity computed from Darcy's law (1.1) and β_{int} is a constant which distills the properties of

the interface. The square root of the permeability $\sqrt{K^*}$ represents the interfacial thickness. Taylor [1971] and Richardson [1971] found that β_{int} was not independent on the channel flow dynamics. The first experimental evidence of the destabilizing effect of a porous medium was given by Beavers, Sparrow, and Magnuson [1970]. Sparrow, Beavers, et al. [1973] imposed the boundary condition (1.7) in solving the Orr-Sommerfeld equations on a channel flow. The permeable cases featured lower critical Reynolds numbers as compared to the impermeable ones. Theoretical grounds to the empirical model of Beavers and Joseph [1967] were provided by Saffman [1971], who employed the volume averaging technique and asymptotic analysis. Neale and Nader [1974] used the Brinkman correction (1.4) to model the porous-free fluid interface, which matched Darcy's law within the porous layer. Their solution adjusted across a interfacial layer of thickness $\delta_{int} = O(Da^{1/2})$.

Ochoa-Tapia and Whitaker [1995a] argued that the inertial terms are not negligible in the interfacial layer, where the fluid motion is still affected by the geometry of the solid matrix. They derived a continuity condition for the velocity and a jump condition for the shear stresses across the interface from the continuity and momentum balance, respectively. Their shear-stress jump relation is

$$\frac{1}{\theta_f}\left.\frac{\partial \langle u\rangle_f^*}{\partial y^*}\right|_{0^-} - \left.\frac{\partial \langle u\rangle_f^*}{\partial y^*}\right|_{0^+} = \frac{\bar{\beta}_{int}}{\sqrt{K^*}}\left.\langle u\rangle_f^*\right|_{0^-} \tag{1.8}$$

where $\bar{\beta}_{int} = O(1)$ is a non-dimensional empirical coefficient. The results obtained with these boundary conditions were in good agreement with those of Beavers and Joseph [1967] [Ochoa-Tapia and Whitaker, 1995b] and values of $\bar{\beta}_{int}$ ranging between -1 and 1.5. Jump conditions for the static temperature equations were derived by Ochoa-Tapia and Whitaker [1997] who assumed thermal equilibrium between the fluid and solid phases. Angot et al. [2017] extended the jump conditions to two and three-dimensional flows.

Experimental evidence [Sahraoui and Kaviany, 1992; Ochoa-Tapia and Whitaker, 1995b; Goyeau et al., 2003; Z. Wu and Mirbod, 2018; Härter et al., 2023] supports the hypothesis that the depth of the interfacial layer is at least on the order of the grain diameter d_g^*. Goharzadeh et al. [2005] performed a series of PIV measurements on a channel flow lying on a packed bed of spheres at low Re_d and found that the thickness of the interfacial layer increases with K^*. Similar results were obtained by Morad and Khalili [2008]. Chandesris and Jamet [2006] assumed an analytical functional shape for K^* and θ_f across the interface, and found an expression for the jump condition consistent with both (1.7) and (1.8). An alternative interfacial

treatment was employed by Breugem and Boersma [2005] and Breugem, Boersma, and Uittenbogaard [2006], who validated the solution of the volume-averaged Navier-Stokes equations in the turbulent channel over a set of equally spaced cubes with direct numerical simulations. They used the parameterization of the Darcy-Forchheimer integral derived by Whitaker [1996] and assumed a smooth variation of the porosity and the permeability across the interface. The problem of the interfacial conditions has recently been addressed using multi-scale homogenization [Bottaro, 2019; Naqvi and Bottaro, 2021] and numerical simulations at the pore scale [Kang and M. Wang, 2024].

1.3.1.2 Incompressible parallel flows on porous walls: effect on linear stability

The impact of a porous walls on the linear stability of channel flows was studied by Tilton and Cortelezzi [2006] and Tilton and Cortelezzi [2008] using the volume-averaged equations with the momentum jump conditions of Ochoa-Tapia and Whitaker [1998]. Their analysis neglected the nonlinear effects at the interface. Higher permeability was shown to destabilize the TS waves, whereas increasing the value of $\bar{\beta}_{int}$ at a constant permeability resulted in a higher critical Reynolds number compared to that observed for impermeable walls. Similar results were obtained for the incompressible asymptotic suction boundary layer over a permeble porous plate [Tilton and Cortelezzi, 2015]. The TS waves propagated in both the boundary layer and the porous layer underneath, and formed a set of counterrotating vortices. The slip velocity at the wall destabilised the viscous modes and hindered the beneficial effects of suction. Conversely, self-similar suction over a porous, heated wall has a stabilizing effect when the disturbances do not propagate within the medium and a no-slip condition is imposed at the interface [Al-Malki et al., 2021]. The destabilizing effect of wall porosity on a steady channel flow was also studied by Ghosh et al. [2019], who employed the interfacial treatment of Breugem and Boersma [2005]. They attributed the destabilization to viscous (TS) instability at low θ_f, and inviscid (Rayleigh) instability at high θ_f.

1.3.1.3 Compressible flows in porous media

Theoretical and numerical analyses of compressible flows within porous media have drawn far less attention. Emanuel and Jones [1968] proposed a Fanno flow-like [Anderson, 2020] model for the one-dimensional flow through an adiabatic, isotropic porous plate. The experiments of Shreeve [1968] confirmed the validity of his approach.

Emanuel and Jones [1968] noted that, for small pressure ratios, the incompressible and compressible models yield almost identical results, and argued that Darcy's law (1.1) can accurately describe the behavior of a compressible flow at low Mach numbers. Their idea was considered again by Beavers and Sparrow [1971], who included a Forchheimer term in the form of Beavers and Sparrow [1969]. The Darcy-Forchheimer equation (1.3) has been extensively used to characterise the blowing and suction rates through porous surfaces in compressible flows [Schmidt, 2014; Schmidt et al., 2016; Traub et al., 2024].

In deriving the balance equations for both the saturating fluid and the solid matrix, Bear and Bachmat [1986] and Bear and Bachmat [1990] assumed microscopic incompressibility, while Ruth and Ma [1992] started from compressible microscopic balances. Nield [1994] argued that the omission of the advection terms [Nield, 1991; Tilton and Cortelezzi, 2006; Tilton and Cortelezzi, 2015] was not suitable for compressible flows and obtained a solution of the momentum balance equation by applying the volume average operators of Bear and Bachmat [1990] to the compressible momentum balance.

Continuum models must incorporate slip-gas effects when dealing with low-permeability porous media and Knudsen numbers $Kn = \ell^*_{mfp}/d^*_p$ (where ℓ^*_{mfp} is the mean-free-path length) in the range $0.001 \leq Kn < 0.1$ [Chapman and Cowling, 1990; Shepherd and Begeal, 1988]. Appropriate slip-velocity and temperature-jump conditions of the Maxwell type [Chapman and Cowling, 1990, eq. 6.21-3] are imposed at the boundary of the solid matrix. When volume averaging is used and the closure of the Darcy problem is performed, the intrinsic permeability of the medium is enhanced by a factor proportional to Kn. This enhancement is known as the Klinkenberg effect [Lasseux and Valdés-Parada, 2017; Yang and Weigand, 2018]. To the author's knowledge, no correction has ever been proposed for the Forchheimer term and most studies have considered inertial and rarified-gas effects separately [e.g. L. Chen et al., 2015], while Innocentini and Pandolfelli [2001] argued that the two are closely related and should be described by a single quadratic term in the momentum equation. An exception is the recent work of Zolotukhin and Gayubov [2022], who proposed a new Darcy-Forchheimer relation accounting for rarified-gas effects in porous media of very-low permeability.

Passive porous substrates have been used to delay boundary-layer transition to turbulence in supersonic wind-tunnels [Running et al., 2023]. Most studies have focused on the attenuation of small-amplitude acoustic disturbances in flat-plate bound-

ary layers rather than the modification of the velocity profiles of the laminar base flows [Mironov et al., 2015; Maslov, Mironov, et al., 2019].

1.3.2 Passive porous coatings without slip and suction

Passive porous coatings have the advantage of interacting with small-amplitude disturbances without affecting the laminar base flow, as only the wall-normal component of the disturbance velocity interacts with the pores. Fedorov and colleagues were the first to attenuate second-mode growth in a supersonic boundary layer using a perforated plate, though this came at the cost of a slight enhancement of the first Mack mode [Malmuth et al., 1998; Fedorov, Malmuth, et al., 2001; Rasheed et al., 2002; Fomin et al., 2002; Maslov, 2003].

These early analyses paved the way to further studies on ultrasonically absorptive coatings [Fedorov, Kozlov, et al., 2006; Wartemann, Lüdeke, et al., 2012; Wartemann, Wagner, et al., 2014] and have been extended to include non-regular geometries, acoustic scattering effects, and coupling mechanisms between adjacent pores [R. Zhao, T. Liu, et al., 2018; R. Zhao, X. X. Zhang, et al., 2020; Gui, W. Wang, et al., 2022]. Other researchers have studied surfaces with two-dimensional, equally-spaced grooves of constant width [Brès et al., 2013] and porous surfaces with non-regular microstructures [Sousa et al., 2019]. Egorov et al. [2008] investigated the effect of a porous layer on the receptivity of a boundary layer to acoustic disturbances. The combined effect of wall cooling and a porous layer was recently investigated by Oz and Kara [2024] on a wedge in a supersonic flow. In his review paper, Fedorov [2011] advocated further study on porous coatings for the control of boundary-layer receptivity and transient growth.

1.3.3 Permeable isotropic substrates with slip and suction

Several theoretical, numerical, and experimental studies have focused on wall-bounded flows through a semi-infinite porous medium [Kaviany, 1987; Nakayama et al., 1990; Papalexandris, 2023]. Much less attention has been devoted to the coupling between an unbounded free fluid and a porous medium. Vafai and Kim [1990] studied the effects of a porous substrate on the heat transfer and the drag exerted by an overflowing fluid subject to a streamwise pressure gradient. They solved the steady, two-dimensional Navier-Stokes equations with a Darcy term and a Forchheimer term. The boundary-layer approximation was not imposed and the governing equations were elliptic, yet their results featured a marked parabolic character. Nield and

Kuznetsov [2003] modeled the influence of a uniform porous substrate on an incompressible Blasius boundary layer by expanding the streamfunction in a power series of $(K^*/x^*)^{1/2}$, where x^* is the streamwise coordinate and K^* is a sufficiently small permeability. They implicitly assumed continuity in the velocity and shear stresses across the fluid-porous interface [Neale and Nader, 1974]. Using a similar approach, Breugem, Boersma, and Uittenbogaard [2005] proposed a theoretical model for an incompressible laminar boundary layer over a porous flat plate and adopted the interfacial conditions of Ochoa-Tapia and Whitaker [1995a]. The pores were assumed to be small enough for the nonlinear terms to be negligible below the interface.

The modelling and computation of boundary-layer flows over (and within) porous surfaces of constant thickness and uniform permeability pose significant challenges. Firstly, the geometry of the problem cannot generally be represented in parabolic coordinates [van Dyke, 1975]. The thickness of the boundary layer grows downstream, while that of the porous substrate is usually constant. The use of a double-domain setting with two different wall-normal coordinates is thus necessary. This issue can be partially circumvented by considering a porous substrate of infinite thickness [Tsiberkin, 2018a] or an asymptotic-suction boundary layer [Tilton and Cortelezzi, 2015]. Secondly, self-similar solutions can not be derived when uniform porous substrates are considered [Vafai and Kim, 1990; Papalexandris, 2023]. Hence, even when the reduction to a system of parabolic equations is possible, its computation by a streamwise-marching procedure relies on the existence a self-similar solution upstream [Sparrow, Quack, et al., 1970; Cebeci, 2002], which is not available in general. Finally, the velocity profiles feature an inflection point near the porous-free fluid interface that can be the cause of an instability of the Kelvin-Helmholtz type. The solution may or may not break down eventually [Vafai and Kim, 1990; Antoniadis and Papalexandris, 2015; Antoniadis and Papalexandris, 2016]. If it does, the computation of the parabolized equations becomes unreliable in the vicinity of the separation point [Cebeci, 2002].

A similarity solution was found by Tsiberkin [2016], Tsiberkin [2018a], and Tsiberkin [2018b] for the case of an incompressible boundary layer on a porous substrate of infinite thickness and streamwise-increasing permeability. His analysis did not take the nonlinear Forchheimer term into account. He concluded that neither the Brinkman nor the advection term can be neglected without losing important features of the momentum transfer and interfacial stability. Albeit stemming from an idealized setting, self-similar solutions permit to overcome all these issues and to unravel

physical mechanisms that are relevant to more realistic scenarios, particularly when the effects of compressibility are important [Stewartson, 1964; Anderson, 2019].

1.4 Thesis outlook

In chapter 2, the asymptotic framework of LWG99 is extended to non-similar compressible base flows to study the effect of uniform wall suction on the receptivity and growth of compressible steady and unsteady Görtler vortices. The realistic scenario of a concave plate with an impermeable-entry region near the leading edge is considered. The laminar base flow under the effect of suction is validated against low-speed wind tunnel experiments and direct numerical simulations in the hypersonic regime. The evolution of the vortices with and without suction is analysed at subsonic and supersonic speeds, and the neutral maps of Görtler instability with uniform wall suction are computed for the first time.

In chapter 3, the effect of a porous wall on the receptivity and growth of laminar streaks and oblique TS waves is investigated in the hypersonic regime. The porous wall features a regular microstructure composed of uniformly spaced cylindrical pores. The unsteady flow within a pore is studied asymptotically, and the wall's response to free-stream vortical disturbances of different frequencies and spanwise wavelengths is discussed. The effect of wall porosity on the onset of oblique TS waves and laminar streaks with mild wall curvature is investigated.

Chapter 4 explores the effect of high wall porosity and permeability on pre-transitional laminar boundary layers. The self-similar solution proposed by Tsiberkin [2018a] for porous substrates of streamwise-growing permeability is extended to take into account the effect of compressibility and a Forchheimer drag. The governing equations are derived by volume averaging using a single-domain approach in which the properties of the medium vary smoothly across the porous-free fluid interface. The base-flow solutions are computed for different volume porosities, grain diameters and free-stream Mach numbers. The compressible boundary-region equations for the flow over and within the porous layer are derived, and the upstream boundary-layer solutions are presented.

Conclusions are drawn in chapter 5.

Appendix A contains a detailed derivation of the compressible Navier-Stokes equations in the curvilinear coordinate system of a streamwise-concave plate.

Appendix B contains the detailed derivation of the non-similar laminar boundary layer solution used in chapter 2.

Appendix C contains details on the asymptotic framework of LWG99. The outer inviscid flow upstream is discussed and a thorough derivation of the initial and outer boundary conditions of the boundary-region equations is provided.

Chapter 2

Attenuation of linear compressible Görtler vortices by uniform suction

This chapter focuses on the excitation and growth of compressible Görtler vortices developing on a concave wall with steady, uniform suction applied downstream of an impermeable region. The receptivity of the base flow to external perturbations is a central ingredient of the present framework, i.e. the Görtler vortices are generated by and continuously exposed to free-stream vortical disturbances. The theoretical framework of LWG99 and WZL11 is thus formulated and solved for non-similar compressible boundary layers over concave walls for the first time.

The velocity and temperature distributions of the laminar base flow do not obey self-similarity because uniform suction is applied downstream of an impermeable region. The evolution of the laminar flow must therefore be described by the non-similar boundary-layer equations [e.g. Cebeci, 2002], as shown by Fransson and Alfredsson [2003]. Furthermore, the receptivity of the base flow to free-stream vorticity plays a critical role in the vicinity of the leading edge where the suction velocity is zero or finite. This effect is another compelling reason why neither the self-similar suction model nor the ASBL model can provide an accurate description of the base flow of interest in the present case.

The asymptotic framework, the governing equations of the base flow and the disturbance flow, and the boundary conditions are discussed in §2.1. The validation of the non-similar laminar base flow, the effect of suction on the growth of the compressible Görtler vortices and the behaviour of the neutral stability curves are discussed in §2.2.

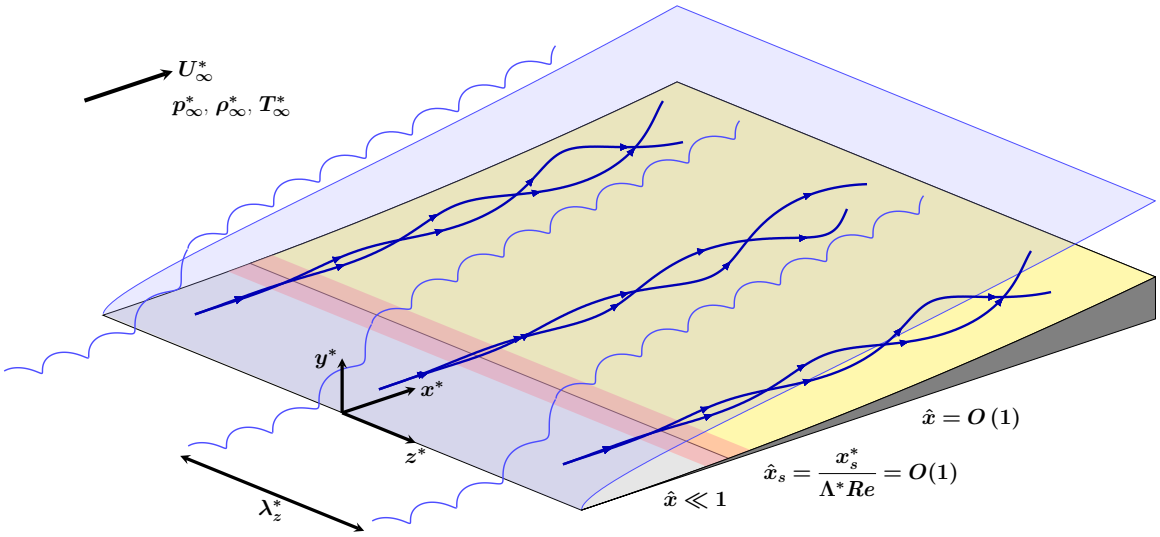

Figure 2.1: Schematic of the flow system. Görtler vortices grow over a concave plate under the continuous forcing of free-stream vorticity. The plate is infinitely thin at the leading edge and uniform suction is applied in the yellow region $\hat{x} > \hat{x}_s$.

2.1 Mathematical formulation

As shown in figure 2.1, a uniform flow of velocity U^*_∞ and temperature T^*_∞ past a thin concave plate with radius of curvature r^*_c is considered. This flow generates a thin boundary layer of thickness $\delta^* \ll r^*_c$ over the plate. Wall suction is applied by imposing a streamwise-dependent wall-normal velocity V_w at the wall. Downstream of an impermeable region (gray area in figure 2.1) followed by a short adjustment region centred at x^*_s (red area in figure 2.1), the wall suction velocity is uniform (yellow area in figure 2.1). The flow is described in a curvilinear, orthogonal system of coordinates $\{x^*, y^*, z^*\}$ centred at the leading edge. The streamwise coordinate x^* follows the curvature of the plate, and y^* and z^* denote the wall-normal and spanwise coordinates, respectively. All dimensional quantities are denoted by the superscript $*$. The governing equations are recovered by introducing the Lamé coefficients $\{1 - y^*/r^*_c, 1, 1\}$ in the Navier-Stokes equations [e.g. El-Hady and Verma, 1984; Viaro and Ricco, 2019a] and their derivation is outlined in appendix A. The spatial coordinates are normalised with $\Lambda^* = \lambda^*_z/2\pi$, where λ^*_z is the spanwise wavelength of the disturbances. The velocity components $\{u^*, v^*, w^*\}$, the density ρ^* and the temperature T^* scale with their reference free-stream values, U^*_∞, ρ^*_∞ and T^*_∞. The pressure is normalised by $\rho^*_\infty U^{*2}_\infty$ and the time is scaled by Λ^*/U^*_∞. The Reynolds number is $Re = \rho^*_\infty U^*_\infty \Lambda^*/\mu^*_\infty \gg 1$, while the Mach number $Ma = U^*_\infty/\left(\gamma \mathcal{R}^* T^*_\infty\right)^{1/2} = O(1)$, where μ^* is the dynamic viscosity, $\gamma = 1.4$ is the heat capacity ratio and $\mathcal{R}^* = 287.05\,\mathrm{J\,kg^{-1}\,K^{-1}}$ the perfect

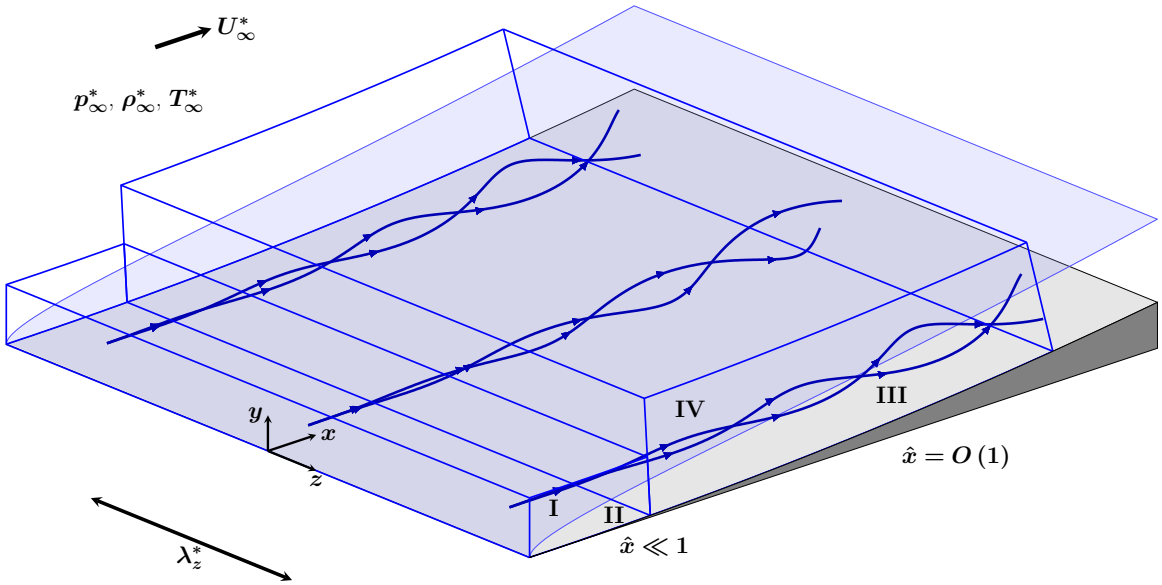

Figure 2.2: Flow configuration for a concave wall. The four asymptotic regions are indicated in roman numbers. Their width is not to scale. Regions I and II are located near the leading edge, where $1 \ll x \ll Re$ ($\hat{x} \ll 1$), while regions III and IV are situated further downstream at $x = O(Re)$ ($\hat{x} = O(1)$). The disturbance flow in regions II and III is governed by the unsteady boundary-layer equations and the unsteady boundary-region equations, respectively.

gas constant of air. The Prandtl number is $Pr = \gamma\,(\gamma-1)^{-1}\,\mu^*_\infty \mathcal{R}^*/k^*_\infty = 0.71$, where k^* is the thermal conductivity. Scaled quantities are not indicated by any symbol.

We follow the receptivity framework first introduced in LWG99. The framework relies on the assumption of large-Re flows and streamwise-elongated, spanwise-periodic structures with a small streamwise wavenumber $k_x \ll 1$. It is convenient to introduce the scaled coordinates $\hat{x} = x/Re$ and $\hat{t} = t/Re$. A distinguished scaling emerges and the domain splits in the four asymptotic regions that are depicted in figure 2.2. Regions I and II are near the leading edge, at $1 \ll x \ll Re$ ($\hat{x} \ll 1$), where the boundary-layer thickness is smaller than the spanwise wavelength of the disturbance, i.e. $\delta \ll 1$. The viscous effects are confined in this thin boundary layer in region II, where the disturbance flow is governed by the unsteady boundary-layer equations. Small-amplitude, non-interacting vortical disturbances are passively advected by the inviscid flow in region I, where $y = O(1)$. They take the form of monochromatic perturbations of the gust type (see §C.1 in the appendix),

$$\boldsymbol{u} - \boldsymbol{i} = \epsilon \hat{\boldsymbol{u}}^\infty \mathrm{e}^{\mathrm{i}\left(\boldsymbol{k}\cdot\boldsymbol{x} - \mathcal{F}\hat{t}\right)} + \text{c.c.}. \tag{2.1}$$

Regions III and IV are located further downstream at $\hat{x} = O(1)$. Here, low-frequency, streamwise-elongated gusts induce three-dimensional disturbances within

the boundary layer $\delta = O(1)$ and the spanwise and wall-normal viscous diffusion are comparable. Viscous effects are confined within the thicker boundary layer in region III, where $y = O(1)$ and the laminar streaks and the Görtler vortices ensue. The evolution of these structures is governed by the unsteady boundary-region equations, which represent the rigorous asymptotic limit of the Navier-Stokes equations for $k_x \ll 1$ and $Re \gg 1$. The large disparity between spanwise and streamwise scales results in $O(\epsilon)$ free-stream fluctuations generating $O(\epsilon Re)$ streamwise velocity disturbances in region III. The inviscid outer flow is influenced by the boundary-layer displacement in region IV, where $y = O(Re)$ and the gusts (2.1) decay as they are advected downstream.

For asymptotically small disturbance amplitude $r_t = \epsilon Re \ll 1$, the unsteady, three-dimensional disturbance flow $\grave{\boldsymbol{q}}$ is linearised about the steady, two-dimensional laminar base flow $\boldsymbol{Q}$, i.e. $\boldsymbol{q}\left(\hat{x}, y, z, \hat{t}\right) = \boldsymbol{Q}\left(\hat{x}, y\right) + \epsilon \grave{\boldsymbol{q}}\left(\hat{x}, y, z, \hat{t}\right)$:

$$\begin{aligned}\{u, v, w, \tau, p\}\left(\hat{x}, y, z, \hat{t}\right) = \\ = \left\{U, V, 0, T, \frac{1}{\gamma Ma^2}\right\}\left(\hat{x}, y\right) + \epsilon\left\{\grave{u}, \grave{v}, \grave{w}, \grave{\tau}, \grave{p}\right\}\left(\hat{x}, y, z, \hat{t}\right). \quad (2.2)\end{aligned}$$

In the case of uniform suction downstream of an impermeable region, the base flow $\boldsymbol{Q}$ is not self-similar. It is governed by a system of parabolic partial differential equations, the compressible Blasius solution being valid only along the impermeable region $\hat{x} < \hat{x}_s$.

2.1.1 The non-similar laminar base flow

This section introduces the non-similar, compressible boundary-layer equations with emphasis on the derivation of the wall-normal velocity component V. A streamfunction $\psi\left(\hat{x}, y\right)$ that satisfies the continuity equation $\rho U = \partial\psi/\partial y$ and $\rho V = -Re^{-1}\partial\psi/\partial\hat{x}$ is defined. The governing equations (B.3) are derived in terms of the normalised streamfunction $F\left(\hat{x}, \eta\right) = \psi\left(\hat{x}, y\right)\left(2\hat{x}\right)^{-1/2}$ and the similarity variable $\eta(\hat{x}, y) = \bar{Y}(\hat{x}, y)\left(2\hat{x}\right)^{-1/2}$ where

$$\bar{Y}\left(\hat{x}, y\right) \equiv \int_0^y \left[T\left(\hat{x}, \breve{y}\right)\right]^{-1} \mathrm{d}\breve{y} \quad (2.3)$$

is the Dorodnitsyn-Howarth variable [Stewartson, 1964]. Inverting (2.3) yields

$$y\left(\hat{x}, \eta\right) = \left(2\hat{x}\right)^{1/2} \int_0^\eta T\left(\hat{x}, \breve{\eta}\right) \mathrm{d}\breve{\eta}. \quad (2.4)$$

The use of η is convenient because the boundary layer is self-similar along the impermeable region and because the initial and outer boundary conditions are more

readily specified in terms of η [Xu, J. Liu, et al., 2020]. The streamwise momentum and static-enthalpy balance equations that govern the base flow $\boldsymbol{Q}$ are [e.g. Cebeci, 2002]

$$\left(\frac{\mu}{T}F''\right)' + FF'' = 2\hat{x}\left(F'\left.\frac{\partial F'}{\partial \hat{x}}\right|_{\eta} - F''\left.\frac{\partial F}{\partial \hat{x}}\right|_{\eta}\right), \tag{2.5a}$$

$$FT' + (\gamma-1)\,Ma^2\frac{\mu}{T}\left(F''\right)^2 + \frac{1}{Pr}\left(\frac{\mu}{T}T'\right)' = 2\hat{x}\left(F'\left.\frac{\partial T}{\partial \hat{x}}\right|_{\eta} - T'\left.\frac{\partial F}{\partial \hat{x}}\right|_{\eta}\right), \tag{2.5b}$$

where the prime denotes differentiation in η. The viscosity μ is modelled with Sutherland's law. The complete derivation of (2.5) is found in appendix B. The wall-normal velocity component is recovered by applying the chain rule to $\partial\psi/\partial\hat{x}$ and introducing the perfect gas equation $\rho T = 1$

$$V(\hat{x},\eta) = -\frac{T}{Re}\frac{\partial\psi}{\partial\hat{x}} = -\frac{1}{Re\,(2\hat{x})^{1/2}}\left(TF + 2\hat{x}T\left.\frac{\partial F}{\partial\hat{x}}\right|_{\eta} + 2\hat{x}T\left.\frac{\partial\eta}{\partial\hat{x}}\right|_{y}F'\right). \tag{2.6}$$

The unknown term $\partial\eta/\partial\hat{x}|_y$ is found by recalling that $\hat{x}$ and y are orthogonal, and thus the total derivative of (2.4) with respect to $\hat{x}$ is null. Using the chain rule yields

$$\frac{\partial y(\hat{x},\eta)}{\partial\hat{x}} = \left.\frac{\partial y(\hat{x},\eta)}{\partial\hat{x}}\right|_{\eta} + \left.\frac{\partial\eta(\hat{x},y)}{\partial\hat{x}}\right|_{y}\left.\frac{\partial y(\hat{x},\eta)}{\partial\eta}\right|_{\hat{x}} = 0, \tag{2.7}$$

where

$$\left.\frac{\partial y(\hat{x},\eta)}{\partial\hat{x}}\right|_{\eta} = \frac{1}{(2\hat{x})^{1/2}}\int_0^{\eta} T(\hat{x},\breve{\eta})\,\mathrm{d}\breve{\eta} + (2\hat{x})^{1/2}\int_0^{\eta}\left.\frac{\partial T}{\partial\hat{x}}\right|_{\eta}\mathrm{d}\breve{\eta}, \tag{2.8a}$$

$$\left.\frac{\partial y(\hat{x},\eta)}{\partial\eta}\right|_{\hat{x}} = (2\hat{x})^{1/2}\,T(\hat{x},\eta). \tag{2.8b}$$

The derivative (2.8a) represents the rate of change in y due to a change in $\hat{x}$ while moving along a path at fixed η. The derivative (2.8b) is the rate of change in y due to a variation in η while $\hat{x}$ is fixed. The sought derivative $\partial\eta/\partial\hat{x}|_y = -\,\partial y/\partial\hat{x}|_\eta\,(\partial y/\partial\eta|_{\hat{x}})^{-1}$ is

$$\left.\frac{\partial\eta(\hat{x},y)}{\partial\hat{x}}\right|_{y} = -\frac{1}{2\hat{x}T(\hat{x},\eta)}\int_0^{\eta} T(\hat{x},\breve{\eta})\,\mathrm{d}\breve{\eta} - \frac{1}{T(\hat{x},\eta)}\int_0^{\eta}\left.\frac{\partial T}{\partial\hat{x}}\right|_{\breve{\eta}}\mathrm{d}\breve{\eta} \equiv -\frac{\eta_c}{2\hat{x}}, \tag{2.9}$$

where the compressible similarity variable $\eta_c(\hat{x},\eta)$

$$\eta_c(\hat{x},\eta) \equiv \frac{1}{T(\hat{x},\eta)}\int_0^{\eta}\left[T(\hat{x},\breve{\eta}) + 2\hat{x}\left.\frac{\partial T}{\partial\hat{x}}\right|_{\breve{\eta}}\right]\mathrm{d}\breve{\eta}, \tag{2.10}$$

is defined. Equation (2.10) reduces to $\eta_c(\eta) = T^{-1}\int_0^\eta T\mathrm{d}\breve{\eta}$ in the self-similar case [Viaro and Ricco, 2019a]. The self-similar form of (2.10) can also be derived by expanding the integral in (3.1.5) in Stewartson [1964, p. 36].

The base-flow velocity components are

$$U(\hat{x},\eta) = F', \tag{2.11a}$$

$$V(\hat{x},\eta) = \frac{T}{Re\,(2\hat{x})^{1/2}}\left(\eta_c F' - F - 2\hat{x}\,\frac{\partial F}{\partial \hat{x}}\bigg|_\eta\right), \tag{2.11b}$$

and reduce to (2.7a,b) in Viaro and Ricco [2019a] in the self-similar case. The wall is adiabatic, $T'(\hat{x},0) = 0$. A no-slip condition is imposed on the streamwise velocity component, $F'(\hat{x},0) = 0$, while the effect of the transpiration velocity $V_w = V(\hat{x},0)$ is described by the equation

$$\left[F + 2\hat{x}\,\frac{\partial F}{\partial \hat{x}}\bigg|_\eta + \frac{\gamma_w\,(2\hat{x})^{1/2}}{T}\right](\hat{x},0) = 0, \tag{2.12}$$

where $\gamma_w(\hat{x}) = V_w Re = O(1)$ is the suction parameter. The incompressible definition of γ_w [Floryan and Saric, 1983] is adopted instead of the compressible one [El-Hady and Verma, 1984] because $T(\hat{x},0)$ is not constant. The non-dimensional suction velocity $V_w \ll 1$ is also known as the suction coefficient in the experimental literature [e.g. Myose and Blackwelder, 1995; Fransson and Alfredsson, 2003; Leontiev and Pavlyuchenko, 2008] and is typically in the range $10^{-5} \leq V_w < 10^{-3}$. The velocity and the temperature are uniform in the external region $\eta \gg 1$, $F' = T = 1$.

In the limit of large streamwise distance, the boundary-layer equations (B.3) tend to the compressible asymptotic-suction (ASBL) system of ordinary differential equations [Young, 1948; Morduchow, 1963; Ricco, Shah, et al., 2013],

$$\frac{\mathrm{d}}{\mathrm{d}N}\left(\frac{\mu}{T}\frac{\mathrm{d}U}{\mathrm{d}N} + U\right) = 0, \tag{2.13a}$$

$$\frac{1}{Pr}\frac{\mathrm{d}}{\mathrm{d}N}\left(\frac{k}{T}\frac{\mathrm{d}T}{\mathrm{d}N} + T\right) + (\gamma-1)\,Ma^2\frac{\mu}{T}\left(\frac{\mathrm{d}U}{\mathrm{d}N}\right)^2 = 0, \tag{2.13b}$$

where $N = -\gamma_w \bar{Y}/T_w$, T_w is the wall temperature and $\bar{Y}$ is defined in (2.3).

2.1.2 The unsteady, three-dimensional disturbance flow

The disturbance flow $\grave{\boldsymbol{q}}$ in region III is governed by the compressible linearised unsteady boundary-region equations (CLUBR). By substituting the expansion (2.2) with

the disturbances

$$\grave{\boldsymbol{q}} = \mathrm{i}k_z\check{w}Re\left\{\bar{u},\frac{(2\hat{x})^{1/2}}{Re}\bar{v},\frac{\bar{w}}{\mathrm{i}k_zRe},\bar{\tau},\frac{\bar{p}}{Re^2}\right\}\mathrm{e}^{\mathrm{i}\left(k_zz-\mathcal{F}\hat{t}\right)} \tag{2.14}$$

where

$$\check{w} = \hat{w}^{\infty} + \mathrm{i}k_z\hat{v}^{\infty}/\left(k_x^2+k_z^2\right)^{1/2} = O(1) \tag{2.15}$$

into the Navier-Stokes equations, and by assuming $r_c = r_c^*/\Lambda^* = O(Re^2)$, the CLUBR continuity $\mathcal{C}$, streamwise momentum $\mathcal{X}$, wall-normal momentum $\mathcal{Y}$, spanwise momentum $\mathcal{Z}$, and enthalpy $\mathcal{E}$ balances are recovered

$$\begin{aligned}\mathcal{C}|\ &\left(\frac{\eta_cT'}{2\hat{x}T}-\frac{1}{T}\left.\frac{\partial T}{\partial\hat{x}}\right|_\eta\right)\bar{u}+\left.\frac{\partial\bar{u}}{\partial\hat{x}}\right|_\eta-\frac{\eta_c}{2\hat{x}}\frac{\partial\bar{u}}{\partial\eta}-\frac{T'}{T^2}\bar{v}+\frac{1}{T}\frac{\partial\bar{v}}{\partial\eta}+\bar{w}+\\&+\left(\frac{\mathrm{i}\mathcal{F}}{T}+\frac{F'}{T^2}\left.\frac{\partial T}{\partial\hat{x}}\right|_\eta-\frac{T'}{T^2}\left.\frac{\partial F}{\partial\hat{x}}\right|_\eta-\frac{FT'}{2\hat{x}T^2}\right)\bar{\tau}-\frac{F'}{T}\left.\frac{\partial\bar{\tau}}{\partial\hat{x}}\right|_\eta+\\&+\left(\frac{F}{2\hat{x}T}+\frac{1}{T}\left.\frac{\partial F}{\partial\hat{x}}\right|_\eta\right)\frac{\partial\bar{\tau}}{\partial\eta}=0,\end{aligned} \tag{2.16a}$$

$$\begin{aligned}\mathcal{X}|\ &\left(k_z^2\mu T-\mathrm{i}\mathcal{F}-\frac{\eta_cF''}{2\hat{x}}+\left.\frac{\partial F'}{\partial\hat{x}}\right|_\eta\right)\bar{u}+F'\left.\frac{\partial\bar{u}}{\partial\hat{x}}\right|_\eta-\left(\frac{F}{2\hat{x}}+\left.\frac{\partial F}{\partial\hat{x}}\right|_\eta\right)\frac{\partial\bar{u}}{\partial\eta}+\\&+\frac{1}{2\hat{x}}\left(\frac{\mu}{T}\frac{\partial\bar{u}}{\partial\eta}\right)'+\frac{F''}{T}\bar{v}+\left(\frac{FF''}{2\hat{x}T}-\frac{F'}{T}\left.\frac{\partial F'}{\partial\hat{x}}\right|_\eta+\frac{F''}{T}\left.\frac{\partial F}{\partial\hat{x}}\right|_\eta\right)\bar{\tau}+\\&-\left(\frac{\mu'F''}{2\hat{x}T}\bar{\tau}\right)'=0,\end{aligned} \tag{2.16b}$$

$$\begin{aligned}\mathcal{Y}|\ &\left(\frac{TF-\eta_cTF'+\eta_cT'F-\eta_c^2TF''}{4\hat{x}^2}-\left.\frac{\partial T}{\partial\hat{x}}\right|_\eta\left.\frac{\partial F}{\partial\hat{x}}\right|_\eta-T\left.\frac{\partial^2F}{\partial\hat{x}^2}\right|_\eta-\frac{F}{2\hat{x}}\left.\frac{\partial T}{\partial\hat{x}}\right|_\eta+\right.\\&\left.+\frac{\eta_cT'-2T}{2\hat{x}}\left.\frac{\partial F}{\partial\hat{x}}\right|_\eta+\frac{TF'}{2\hat{x}}\left.\frac{\partial\eta_c}{\partial\hat{x}}\right|_\eta+\frac{\eta_cT}{\hat{x}}\left.\frac{\partial F'}{\partial\hat{x}}\right|_\eta+\frac{2GF'}{(2\hat{x})^{1/2}}\right)\bar{u}+\frac{\mu'T'}{3\hat{x}}\left.\frac{\partial\bar{u}}{\partial\hat{x}}\right|_\eta+\\&+\left[\frac{(\eta_c\mu)'}{12\hat{x}^2}-\frac{\mu'}{2\hat{x}}\left.\frac{\partial T}{\partial\hat{x}}\right|_\eta\right]\frac{\partial\bar{u}}{\partial\eta}-\frac{\mu}{6\hat{x}}\frac{\partial}{\partial\hat{x}}\left(\frac{\partial\bar{u}}{\partial\eta}\right)_\eta+\frac{\eta_c\mu}{12\hat{x}^2}\frac{\partial^2\bar{u}}{\partial\eta^2}+\left(k_z^2\mu T-\mathrm{i}\mathcal{F}+\frac{F'}{2\hat{x}}-\frac{FT'}{2\hat{x}T}+\right.\\&\left.-\frac{T'}{T}\left.\frac{\partial F}{\partial\hat{x}}\right|_\eta-\left.\frac{\partial F'}{\partial\hat{x}}\right|_\eta+\frac{F'}{T}\left.\frac{\partial T}{\partial\hat{x}}\right|_\eta+\frac{\eta_cF''}{2\hat{x}}\right)\bar{v}+F'\left.\frac{\partial\bar{v}}{\partial\hat{x}}\right|_\eta-\left(\frac{F}{2\hat{x}}+\left.\frac{\partial F}{\partial\hat{x}}\right|_\eta\right)\frac{\partial\bar{v}}{\partial\eta}+\\&-\left(\frac{2\mu}{3\hat{x}T}\frac{\partial\bar{v}}{\partial\eta}\right)'+\frac{\mu'T'}{3\hat{x}}\bar{w}-\frac{\mu}{6\hat{x}}\frac{\partial\bar{w}}{\partial\eta}+\left\{\frac{\eta_c\left(FF'\right)'}{4\hat{x}^2}-\frac{FF'}{4\hat{x}^2}-\frac{F^2T'}{4\hat{x}^2T}-\frac{G}{(2\hat{x})^{1/2}}\frac{\left(F'\right)^2}{T}+\right.\end{aligned}$$

$$+\left(\frac{\mu' T' F}{3\hat{x}^2 T}\right)' - \frac{(\eta_c \mu' F'')'}{4\hat{x}^2} + \left[\frac{F'T - FT'}{2\hat{x}T} + \frac{\eta_c F''}{2\hat{x}} + \left(\frac{2\mu' T'}{3\hat{x}T}\right)'\right] \left.\frac{\partial F}{\partial \hat{x}}\right|_\eta + \left(\frac{2\mu' T'}{3\hat{x}T} + \right.$$
$$\left. + \frac{\mu'' T'}{\hat{x}} - \frac{F}{2\hat{x}} - \frac{\eta_c F'}{2\hat{x}}\right) \left.\frac{\partial F'}{\partial \hat{x}}\right|_\eta + \left.\frac{\mu'}{2\hat{x}} \frac{\partial F''}{\partial \hat{x}}\right|_\eta + \left[\frac{FF'}{\hat{x}T} - \frac{\eta_c (F')^2}{2\hat{x}T} - \left(\frac{2\mu' F'}{3\hat{x}T}\right)' + \right.$$
$$\left. - \frac{\mu'' F''}{2\hat{x}}\right] \left.\frac{\partial T}{\partial \hat{x}}\right|_\eta + \left.\frac{2F'}{T} \frac{\partial F}{\partial \hat{x}}\right|_\eta \left.\frac{\partial T}{\partial \hat{x}}\right|_\eta + F' \left.\frac{\partial^2 F}{\partial \hat{x}^2}\right|_\eta - \left.\frac{(F')^2}{2\hat{x}} \frac{\partial \eta_c}{\partial \hat{x}}\right|_\eta - \frac{T'}{T}\left(\left.\frac{\partial F}{\partial \hat{x}}\right|_\eta\right)^2 +$$
$$\left. - \left.\frac{\partial F}{\partial \hat{x}}\right|_\eta \left.\frac{\partial F'}{\partial \hat{x}}\right|_\eta - \left.\frac{2\mu' F'}{3\hat{x}T} \frac{\partial T'}{\partial \hat{x}}\right|_\eta\right\} \bar{\tau} - \left.\frac{\mu' F''}{2\hat{x}} \frac{\partial \bar{\tau}}{\partial \hat{x}}\right|_\eta + \left(\frac{\mu' T' F}{3\hat{x}^2 T} - \frac{\eta_c \mu' F''}{4\hat{x}^2} + \right.$$
$$\left. + \left.\frac{2\mu' T'}{3\hat{x}} \frac{\partial F}{\partial \hat{x}}\right|_\eta + \left.\frac{\mu'}{\hat{x}} \frac{\partial F'}{\partial \hat{x}}\right|_\eta - \left.\frac{2\mu' F'}{3\hat{x}T} \frac{\partial T}{\partial \hat{x}}\right|_\eta\right) \frac{\partial \bar{\tau}}{\partial \eta} + \frac{1}{2\hat{x}} \frac{\partial \bar{p}}{\partial \eta} = 0, \quad (2.16c)$$

$$\mathcal{Z}| \left(k_z^2 T \mu' \left.\frac{\partial T}{\partial \hat{x}}\right|_\eta - k_z^2 \frac{\eta_c \mu' T T'}{2\hat{x}}\right) \bar{u} + \left.\frac{k_z^2 \mu T}{3} \frac{\partial \bar{u}}{\partial \hat{x}}\right|_\eta - k_z^2 \frac{\eta_c \mu T}{6\hat{x}} \frac{\partial \bar{u}}{\partial \eta} + k_z^2 \mu' T' \bar{v} +$$
$$+ \frac{k_z^2 \mu}{3} \frac{\partial \bar{v}}{\partial \eta} - \left(\mathrm{i}\mathcal{F} - \frac{4}{3} k_z^2 \mu T\right) \bar{w} + F' \left.\frac{\partial \bar{w}}{\partial \hat{x}}\right|_\eta - \left(\frac{F}{2\hat{x}} + \left.\frac{\partial F}{\partial \hat{x}}\right|_\eta\right) \frac{\partial \bar{w}}{\partial \eta} - \left(\frac{\mu}{2\hat{x}T} \frac{\partial \bar{w}}{\partial \eta}\right)' +$$
$$+ \left(\frac{k_z^2 \mu' T' F}{3\hat{x}} + \left.\frac{2k_z^2 \mu' T'}{3} \frac{\partial F}{\partial \hat{x}}\right|_\eta - \left.\frac{2k_z^2 \mu' F'}{3} \frac{\partial T}{\partial \hat{x}}\right|_\eta\right) \bar{\tau} - k_z^2 T \bar{p} = 0, \quad (2.16d)$$

$$\mathcal{E}| \left(\left.\frac{\partial T}{\partial \hat{x}}\right|_\eta - \frac{\eta_c T'}{2\hat{x}}\right) \bar{u} - (\gamma - 1)\, Ma^2 \frac{\mu F''}{\hat{x}T} \frac{\partial \bar{u}}{\partial \eta} + \frac{T'}{T} \bar{v} + \left[\frac{FT'}{2\hat{x}T} - \mathrm{i}\mathcal{F} - \frac{F'}{T} \left.\frac{\partial T}{\partial \hat{x}}\right|_\eta + \right.$$
$$\left. + \frac{T'}{T} \left.\frac{\partial F}{\partial \hat{x}}\right|_\eta - (\gamma - 1)\, Ma^2 \frac{\mu' (F'')^2}{2\hat{x}T} + \frac{k_z^2 \mu T}{Pr}\right] \bar{\tau} - \frac{1}{Pr}\left(\frac{\mu' T'}{2\hat{x}T} \bar{\tau}\right)' + F' \left.\frac{\partial \bar{\tau}}{\partial \hat{x}}\right|_\eta +$$
$$- \left(\frac{F}{2\hat{x}} + \left.\frac{\partial F}{\partial \hat{x}}\right|_\eta\right) \frac{\partial \bar{\tau}}{\partial \eta} - \frac{1}{Pr}\left(\frac{\mu}{2\hat{x}T} \frac{\partial \bar{\tau}}{\partial \eta}\right)' = 0, \quad (2.16e)$$

where

$$G = \frac{Re^2}{r_c} = \left(\frac{\rho_\infty^* U_\infty^*}{\mu_\infty^*}\right)^2 \frac{\lambda_z^{*3}}{8\pi^3 r_c^*} = O(1) \quad (2.17)$$

is the global Görtler number [Kobayashi, 1972], [WZL11] and $\mu' \equiv \mathrm{d}\mu/\mathrm{d}T$. Equations (2.16a)–(2.16e) are parabolic in $\hat{x}$ and represent an initial-boundary value problem that needs to be solved subject to appropriate initial and boundary conditions.

2.1.2.1 Wall boundary conditions

The no-slip and no-penetration conditions $\bar{u} = \bar{v} = \bar{w} = 0$ are assumed over an adiabatic wall, $\partial\bar{\tau}/\partial\eta = 0$ [El-Hady and Verma, 1984; Viaro and Ricco, 2019a]. The

use of the no-penetration condition $\bar{v} = 0$ at the wall is justified as follows. In a laboratory, distributed suction is usually applied through a porous substrate where $\bar{v}$ and $\bar{p}$ are coupled via a Darcy law [e.g. Wedin, Cherubini, and Bottaro, 2015]

$$v^* = -\frac{K^*}{\mu^*}\frac{\partial p^*}{\partial y^*}, \tag{2.18}$$

where $K^*\,[\mathrm{m}^2]$ is the permeability. In non-dimensional form, relation (2.18) at the wall becomes

$$\grave{v}|_{y=0} = -\frac{DaRe}{\mu_w}\frac{\partial \grave{p}}{\partial y}\,\Big|_{y=0}, \tag{2.19}$$

where $\mu_w = \mu(T_w) = O(1)$ is the dynamic viscosity at the wall, the Darcy number $Da \equiv K^*/\Lambda^{*2} \ll 1$ is typically $O(Re^{-1})$ or smaller and $DaRe = O(1)$. Equation (2.19) is the extension of (1.2) to account for a variable temperature within the boundary layer. Introducing the asymptotic scaling (2.14) in (2.19) leads to $\bar{v}(\partial\bar{p}/\partial\eta)^{-1} = O(Da)$, i.e. the coupling is inhibited, thus justifying the no-penetration condition at the wall.

Suction non-uniformities are not considered in this study because their length scale is smaller than or comparable to the pore size d_p^* and thus negligible when compared to the length scales of the disturbance flow, i.e. $d_p^* \ll \lambda_z^*$. Wall roughness can also be neglected because the height of the roughness element is assumed to be comparable with the pore size d_p^* and, therefore, to be much smaller than the boundary-layer thickness δ^*. The use of the no-slip conditions, $\bar{u} = \bar{w} = 0$, is thus justified. These assumptions are consistent with the experiments of Fransson and Alfredsson [2003] who used a sintered-plastic porous layer with a permeability of $K^* = 3.7\,\mu\mathrm{m}^2$, an average pore size of $d_p^* = 16\,\mu\mathrm{m}$ and a roughness of $0.38\,\mu\mathrm{m}$. Such a low roughness is typical of polished, non-permeable surfaces used in supersonic quiet tunnels [Schneider, 2008a].

2.1.2.2 Outer boundary conditions

Both $\bar{u}$ and $\bar{\tau}$ vanish in the free stream ($\eta \gg 1$), while $\bar{v}$, $\bar{w}$ and $\bar{p}$ satisfy mixed-type boundary conditions as $\eta \to \infty$,

$$\frac{\partial\bar{v}}{\partial\eta} + |k_z|\,(2\hat{x})^{1/2}\,\bar{v} \to -\mathrm{e}^{\mathrm{i}\mathcal{F}\hat{x}+\mathrm{i}k_y(2\hat{x})^{1/2}[\eta-\beta_c(\hat{x})]-\left(k_y^2+k_z^2\right)\hat{x}}, \tag{2.20a}$$

$$\frac{\partial\bar{w}}{\partial\eta} + |k_z|\,(2\hat{x})^{1/2}\,\bar{w} \to \mathrm{i}k_y\,(2\hat{x})^{1/2}\,\mathrm{e}^{\mathrm{i}\mathcal{F}\hat{x}+\mathrm{i}k_y(2\hat{x})^{1/2}[\eta-\beta_c(\hat{x})]-\left(k_y^2+k_z^2\right)\hat{x}}, \tag{2.20b}$$

$$\frac{\partial\bar{p}}{\partial\eta} + |k_z|\,(2\hat{x})^{1/2}\,\bar{p} \to 0. \tag{2.20c}$$

Equations (2.20) are essentially the same as those presented in LWG99, Ricco and X. Wu [2007] and Viaro and Ricco [2019a] except for the term $\beta_c(\hat{x}) = \eta - F(\hat{x}, \eta)$, which here is streamwise-dependent.

The outer boundary conditions (2.20) are derived by matching the outer limit of region III (i.e. the large-η limit of the CLUBR equations (2.16a)–(2.16e)) with the inner limit of region IV. Following Wundrow and Goldstein [2001], the flow in region IV - where $\hat{x}, \hat{y} = O(1)$ and $\hat{y} = Re^{-1}y$ - is decomposed in its steady, two-dimensional and unsteady, three-dimensional parts at $O(\epsilon)$

$$\boldsymbol{u} = \{1, 0, 0\} + \epsilon \{\acute{u}, \acute{v}, 0\}(\hat{x}, \hat{y}) + \epsilon \{\grave{u}, \grave{v}, \grave{w}\}\left(\hat{x}, y, \hat{y}, z, \hat{t}\right) + \dots \tag{2.21a}$$

$$p = \frac{1}{\gamma Ma^2} + \epsilon \acute{p} \{\acute{u}, \acute{v}, 0\}(\hat{x}, \hat{y}) + \epsilon^2 \grave{p}\left(\hat{x}, y, \hat{y}, z, \hat{t}\right) + \dots \tag{2.21b}$$

The steady, two-dimensional part $\epsilon \{\acute{u}, \acute{v}, 0\}(\hat{x}, \hat{y})$ is induced by the base-flow displacement and is governed by the steady Euler equations and its wall-normal velocity component $\epsilon\acute{v}$ matches the base flow velocity V (2.11b) when $r_t \ll 1$

$$\lim_{\hat{y}\to 0} \epsilon\acute{v} = \lim_{\eta\to\infty} V = \frac{1}{Re}\frac{\mathrm{d}}{\mathrm{d}\hat{x}}\left[(2\hat{x})^{1/2}\beta_c(\hat{x})\right] + \frac{1}{Re}\frac{\gamma_c(\hat{x})}{(2\hat{x})^{1/2}}, \tag{2.22}$$

where $\gamma_c(\hat{x}) = \lim_{\eta\to\infty}(\eta_c - \eta)$. The streamfunction for the first two terms in (2.21a) is $\Psi(\hat{x}, y, \hat{y}) = y + \psi_1(\hat{x}, \hat{y})$, where

$$\epsilon\acute{v} = -\frac{1}{Re}\frac{\partial\psi_1}{\partial\hat{x}} = -\frac{1}{Re}\frac{\partial\Psi}{\partial\hat{x}}. \tag{2.23}$$

Equating (2.22) and (2.23) and integrating yields the asymptote

$$\Psi(\hat{x}, y) = y - (2\hat{x})^{1/2}\beta_c(\hat{x}) - \int^{\hat{x}} \frac{\gamma_c(\hat{x})}{(2\hat{x})^{1/2}}\mathrm{d}\breve{x}, \text{ for } \hat{y} \ll 1,\ y = O(1). \tag{2.24}$$

Note that an analytical expression for $\psi_1(\hat{x}, \hat{y})$ cannot be obtained for all $\hat{y}$ in the non-similar case and when the self-similar flow is supersonic. However, the focus is on the asymptotic behaviour of ψ_1 as $\hat{y} \to 0$ (i.e. $\hat{y} \ll 1$) and $y = O(1)$. The unsteady, three-dimensional part of (2.21) is governed by

$$\mathcal{C}|\ \frac{\partial\grave{v}}{\partial y} + \frac{\partial\grave{w}}{\partial z} = 0, \tag{2.25a}$$

$$\mathcal{Y}|\ \frac{\partial\grave{v}}{\partial\hat{t}} + \frac{\partial\grave{v}}{\partial\hat{x}} + r_t\left[(\acute{v} + \grave{v})\frac{\partial\grave{v}}{\partial y} + \grave{w}\frac{\partial\grave{v}}{\partial z} + \frac{\partial\grave{p}}{\partial y}\right] = \frac{\partial^2\grave{v}}{\partial y^2} + \frac{\partial^2\grave{v}}{\partial z^2}, \tag{2.25b}$$

$$\mathcal{Z}|\ \frac{\partial\grave{w}}{\partial\hat{t}} + \frac{\partial\grave{w}}{\partial\hat{x}} + r_t\left[(\acute{v} + \grave{v})\frac{\partial\grave{w}}{\partial y} + \grave{w}\frac{\partial\grave{w}}{\partial z} + \frac{\partial\grave{p}}{\partial z}\right] = \frac{\partial^2\grave{w}}{\partial y^2} + \frac{\partial^2\grave{w}}{\partial z^2}, \tag{2.25c}$$

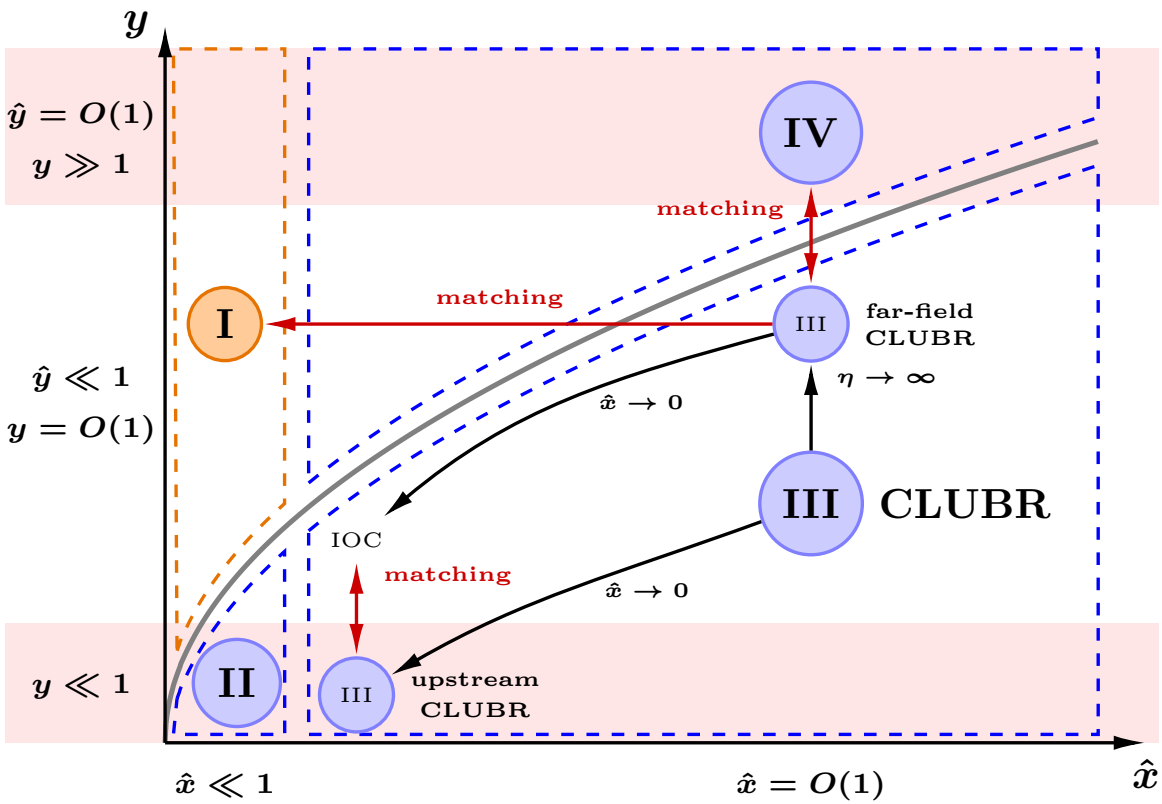

Figure 2.3: Schematic of the four asymptotic regions introduced in LWG99 and their domains (dashed lines). The disturbance flow is inviscid in region I (orange) and viscous in regions II, III, and IV (blue). The boundary layer thickness is shown in gray. Laminar streaks and Görtler vortices develop in region III, where the flow is governed by the CLUBR equations. The solution to the far-field ($\eta \gg 1$) form of the CLUBR equations matches the inviscid flow in region I (2.1) as $\hat{x} \to 0$ and the inner limit ($\hat{y} \to 0$) of region IV for large $y \to \infty$. The initial conditions are obtained by solving the upstream form of the CLUBR equations, subject to the initial outer conditions (IOC), which are derived by taking the small-$\hat{x}$ limit of the upstream CLUBR equations.

$\grave{u} = \grave{\tau} = 0$, and $\grave{\rho} = 0$ because of the perfect gas equation. The system (2.25) is elliptic in the cross-flow (y-z) plane and the two-dimensional and three-dimensional components are coupled because $\acute{v}$ appears in (2.25). These components are decoupled by substituting (2.23) and (2.24) into (2.25), which yields the linearised momentum balances valid for $\hat{y} \ll 1$ [LWG99],

$$\left(\frac{\partial}{\partial \hat{t}} + \frac{\partial}{\partial \hat{x}}\bigg|_{\Psi} - \frac{\partial^2}{\partial \Psi^2} - \frac{\partial^2}{\partial z^2}\right)\{\grave{v}, \grave{w}\} = 0. \tag{2.26}$$

The solution to (2.26) is

$$\{\grave{v}, \grave{w}\}\left(\hat{x}, \Psi, z, \hat{t}\right) = \{\hat{v}, \hat{w}\}\left(\hat{x}\right) \mathrm{e}^{-\mathrm{i}\mathcal{F}\hat{t} + \mathrm{i}k_y \Psi + \mathrm{i}k_z z} + \text{c.c.}, \tag{2.27}$$

where the amplitude is found by matching with (2.1) for $\Psi \sim y = O(1)$ and $\hat{x} \ll 1$,

$$\{\hat{v}, \hat{w}\}\left(\hat{x}\right) = \{\hat{v}^{\infty}, \hat{w}^{\infty}\} \mathrm{e}^{\mathrm{i}\mathcal{F}\hat{x} - \left(k_y^2 + k_z^2\right)\hat{x}}. \tag{2.28}$$

As $T \sim 1$ and $\bar{Y} = O(y)$ for $y, \eta \gg 1$, the far-field variable for region III, $y^{(0)}$, is defined consistently with the asymptote (2.24) [Viaro and Ricco, 2019a]

$$y^{(0)} \equiv \left(2\hat{x}\mathcal{F}\right)^{1/2}\left[\eta - \beta_c\left(\hat{x}\right)\right] - \mathcal{F}^{1/2}\int^{\hat{x}} \frac{\gamma_c\left(\hat{x}\right)}{\left(2\hat{x}\right)^{1/2}} \mathrm{d}\breve{x}. \tag{2.29}$$

By applying the transformation $(\hat{x}, \eta) \rightarrow (\hat{x}, y^{(0)})$ to the large-η form of (2.16a)–(2.16e), the far-field balances are recovered,

$$\mathcal{C}|\left(2\hat{x}\mathcal{F}\right)^{1/2} \frac{\partial \bar{v}}{\partial y^{(0)}} + \bar{w} = 0, \tag{2.30a}$$

$$\mathcal{Y}|\left(\frac{1}{2\hat{x}} + k_z^2 - \mathrm{i}\mathcal{F}\right)\bar{v} + \frac{\partial \bar{v}}{\partial \hat{x}}\bigg|_{y^{0)}} - \frac{\mathcal{F}^{1/2}\gamma_c(\hat{x})}{\left(2\hat{x}\right)^{1/2}}\frac{\partial \bar{v}}{\partial y^{(0)}} + \\ - \mathcal{F}\frac{\partial^2 \bar{v}}{\partial y^{(0)2}} + \frac{\mathcal{F}^{1/2}}{\left(2\hat{x}\right)^{1/2}}\frac{\partial \bar{p}}{\partial y^{(0)}} = 0, \tag{2.30b}$$

$$\mathcal{Z}|\left(k_z^2 - \mathrm{i}\mathcal{F}\right)\bar{w} + \frac{\partial \bar{w}}{\partial \hat{x}}\bigg|_{y^{(0)}} - \frac{\mathcal{F}^{1/2}\gamma_c(\hat{x})}{\left(2\hat{x}\right)^{1/2}}\frac{\partial \bar{w}}{\partial y^{(0)}} - \mathcal{F}\frac{\partial^2 \bar{w}}{\partial y^{(0)2}} - k_z^2 \bar{p} = 0. \tag{2.30c}$$

The solution (2.20) that matches with (2.1) for $\hat{x} \ll 1$, $y^{(0)} = O(1)$ and (2.27) for $\hat{x} = O(1)$, $y^{(0)} \gg 1$ is first derived for $\bar{p}$ by combining the wall-normal derivative of (2.30b) with (2.30c) and using (2.30a).

The spanwise component $\bar{w}$ is obtained by solving the inhomogeneous heat equation

$$\frac{\partial \bar{w}^0}{\partial \hat{x}}\bigg|_{\hat{y}^{(0)}} - \mathcal{F}\frac{\partial^2 \bar{w}^0}{\partial \hat{y}^{(0)2}} = k_z^2 \bar{p} \mathrm{e}^{\left(k_z^2 - \mathrm{i}\mathcal{F}\right)\hat{x}}, \tag{2.31}$$

found by using the change of variable $\bar{w} = \bar{w}^0 \mathrm{e}^{\left(\mathrm{i}\mathcal{F} - k_z^2\right)\hat{x}}$ and

$$\grave{y}^{(0)} = (2\hat{x}\mathcal{F})^{1/2} \left[\eta - \beta_c\left(\hat{x}\right)\right] \tag{2.32}$$

to simplify (2.30c) [Polyanin and Nazaikinskii, 2015, §3.8.7.4]. Equation (2.31) is solved subject to initial and outer boundary conditions as shown in figure 2.3: the initial conditions are recovered by matching with region I (2.1), while the outer conditions are found by matching with the small-$\hat{y}$ limit of region IV (2.27). The wall-normal component $\bar{v}$ is obtained by integrating (2.30a). The detailed derivation of (2.30), (2.31) and (2.20) is found in §C.2 in the appendix.

2.1.2.3 Initial conditions

The initial conditions are imposed in the impermeable region at $\hat{x} \ll 1$ and are therefore those of Viaro and Ricco [2019a, appendix B]. Upstream, the dependent variables expand as a power series of $\hat{x}$ whose coefficients are governed by a set of ordinary differential equations in η (upstream CLUBR in figure 2.3). These equations are solved subject to the initial outer boundary conditions (IOC in the schematic 2.3), which are the small-$\hat{x}$ limit of the solution of the far-field equations (C.11). For more details, the reader is referred to §C.3 in the appendix. The evolution from the impermeable to the suction region occurs gradually across an adjustment strip of finite width $\Delta\hat{x}_s$ (red area in figure 2.1) and centred at a prescribed $\hat{x}_s$. In this region, the suction velocity varies as $V_w S(\hat{x})$, where

$$S(\hat{x}) = \begin{cases} 0, & \text{for } \hat{x} - \hat{x}_s \leq -\Delta\hat{x}_s/2, \\ \left[1 + \exp\left(\dfrac{1}{\tilde{x}-1} + \dfrac{1}{\tilde{x}}\right)\right]^{-1}, & \text{for } |\hat{x} - \hat{x}_s| \leq \Delta\hat{x}_s/2, \\ 1, & \text{for } \hat{x} - \hat{x}_s > \Delta\hat{x}_s/2, \end{cases} \tag{2.33}$$

and $\tilde{x} = \left(\hat{x} - \hat{x}_s + \Delta\hat{x}_s/2\right)/\Delta\hat{x}_s$ [Negi et al., 2015]. The author has verified that varying the length of the adjustment strip in the range $0.01 \leq \Delta\hat{x}_s < 0.1$ has a negligible effect on the results. A $\Delta\hat{x}_s = 0.05$ is taken for all the computations. In the results section, γ_w indicates the constant suction value attained at the end of the adjustment strip.

A few comments about the initial conditions are in order. The plate is assumed to be infinitely thin and therefore the free-stream base flow is not distorted at leading order as the fluid encounters the flat plate. The only distortion of the base-flow streamlines is produced by the thickening of the boundary layer. As the free-stream disturbances are transported by the base flow, they are neither stretched nor tilted

by the leading edge. The leading-edge bluntness effects can play a central role on the free-stream distortion and therefore on the boundary-layer response. This problem is however out of the scope of the present study because these effects only occur when the characteristic dimension of the rounded leading edge is comparable with the spanwise length scale [Goldstein, Leib, and Cowley, 1992; Goldstein and Leib, 1993; Goldstein and Wundrow, 1998; Goldstein, 2014]. Furthermore, the disturbance flow in the very proximity of the leading edge is not considered because the inviscid flow outside of the boundary layer is solved for $x \gg 1$, i.e. at a distance much larger than the spanwise wavelength. As discussed in LWG99, streamwise-decaying disturbances emerging from the interaction between the free-stream vorticity disturbances and the leading edge, obtained by Choudhari [1996] by using the Wiener-Hopf technique, decay to a very small amplitude when $x \gg 1$ and, therefore, they play a negligible role in the boundary-layer response. As the initial conditions are obtained by taking the limit $\bar{x} \ll 1$ of the CLUBR equations, they constitute the asymptotically rigorous upstream behaviour of the CLUBR solution at locations $1 \ll x \ll Re$.

2.1.3 Numerical solution of the compressible boundary-region equations on non-uniform grids

The base flow and the CLUBR equations are solved by marching downstream as they are parabolic in $\hat{x}$. At each $\hat{x}$ location, the CLUBR equations reduce to a system of ordinary differential equations in η and the solution is obtained by a block-elimination algorithm [Cebeci, 2002], also used to solve (B.22) and (2.13). When suction is applied, the boundary layer becomes thinner in η and thus a non-uniform grid is used to resolve the near-wall region.

A schematic of the streamwise and wall-normal grid is shown in figure 2.4 (left). The base-flow equations (2.5) are discretized on the Keller-box grid (red rectangle) centered on the red point $(\hat{x}_{n-1/2}, \eta_{j-1/2})$ and uses the variables defined at the vertices of the red rectangle $(\hat{x}_n, \eta_j)$, $(\hat{x}_n, \eta_{j-1})$, $(\hat{x}_{n-1}, \eta_{j-1})$ and $(\hat{x}_{n-1}, \eta_j)$. For further details, the reader is referred to Keller and Cebeci [1970] and Keller and Cebeci [1972].

Once F and T are known, a finite difference scheme is employed to compute the velocity components, $\bar{u}$, $\bar{v}$, $\bar{w}$, the temperature $\bar{\tau}$ and the pressure $\bar{p}$. The terms that multiply $\bar{u}$, $\bar{v}$, $\bar{w}$, $\bar{\tau}$, and $\bar{p}$ are defined at the point $(\hat{x}_n, \eta_j)$ denoted by the olive square. A uniform marching step is used in $\hat{x}$, the streamwise derivatives are estimated by backward differencing and the variables at $(\hat{x}_{n-1}, \eta_j)$ and $(\hat{x}_{n-2}, \eta_j)$ are stored from upstream computations. The wall-normal derivatives are approximated with finite

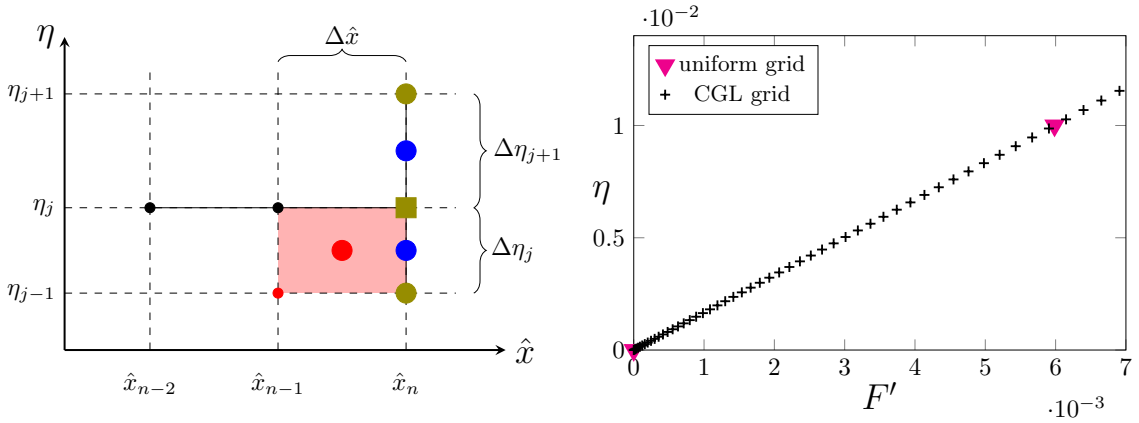

Figure 2.4: Left: schematic of the non-uniform spatial discretization used in the computation of the boundary-region equations. Right: base-flow streamwise velocity profile $U = F'$ in the near wall region. A uniform (magenta triangles) and a CGL grid (black crosses) were used to collocate the same number of points $N_p = 3000$ on a width $\eta_{max} = 30$.

differences centred in $(\hat{x}_n, \eta_j)$

$$\left(\frac{\partial \bar{u}}{\partial \eta}\right)_j = \frac{\mathcal{C}_j \bar{u}_{j+1} + (1 - \mathcal{C}_j)\,\bar{u}_j - \bar{u}_{j-1}}{\mathcal{C}_j \Delta\eta_{j+1} + \Delta\eta_j}, \tag{2.34a}$$

$$\left(\frac{\partial^2 \bar{u}}{\partial \eta^2}\right)_j = 2\frac{\mathcal{P}_j \bar{u}_{j+1} - (1 + \mathcal{P}_j)\,\bar{u}_j + \bar{u}_{j-1}}{\mathcal{P}_j \Delta\eta_{j+1}^2 + \Delta\eta_j^2}, \tag{2.34b}$$

where the weights are $\mathcal{C}_j = (\Delta\eta_j/\Delta\eta_{j+1})^2$ and $\mathcal{P}_j = \Delta\eta_j/\Delta\eta_{j+1}$. Upward finite differences are used to enforce the adiabatic condition at the wall $j = 1$

$$\left(\frac{\partial \bar{\tau}}{\partial \eta}\right)_1 = \frac{\mathcal{C}_{up,1}\bar{\tau}_3 - \bar{\tau}_2 + (1 - \mathcal{C}_{up,1})\,\bar{\tau}_1}{\mathcal{C}_{up,1}\,(\Delta\eta_3 + \Delta\eta_2) - \Delta\eta_2} = 0, \tag{2.35}$$

and $\mathcal{C}_{up,1} = \Delta\eta_2^2/\left(\Delta\eta_3 + \Delta\eta_2\right)^2$. Downward finite differences are used to enforce the boundary conditions of the mixed type (2.20) at the outer boundary $j = N_p$ - where N_p is the number of points in the wall-normal direction -

$$\left(\frac{\partial \bar{v}}{\partial \eta}\right)_{N_p} = \frac{\mathcal{C}_{down,N_p}\bar{v}_{N_p-2} - \bar{v}_{N_p-1} - (\mathcal{C}_{down,N_p} - 1)\bar{v}_{N_p}}{\Delta\eta_{N_p} - \mathcal{C}_{down,N_p}(\Delta\eta_{N_p} + \Delta\eta_{N_p-1})}, \tag{2.36}$$

where $\mathcal{C}_{down,N_p} = \Delta\eta_{N_p}^2/(\Delta\eta_{N_p} + \Delta\eta_{N_p-1})^2$. The asymptotic outer boundary conditions are imposed by introducing

$$\bar{v}_{N_p} = \frac{\mathcal{C}_{back,N_p}\bar{v}_{N_p-2} - \bar{v}_{N_p-1} - \mathcal{A}_{N_p} \mathrm{e}^{\mathrm{i}\mathcal{F}\hat{x} + \mathrm{i}k_y(2\hat{x})^{1/2}[\eta - \beta_c(\hat{x})] - \left(k_y^2 + k_z^2\right)\hat{x}}}{\mathcal{C}_{back,N_p} - 1 + \mathcal{A}_{N_p}\,|k_z|\,(2\hat{x})^{1/2}}, \tag{2.37a}$$

$$\bar{w}_{N_p} = \frac{\mathcal{C}_{back,N_p}\bar{w}_{N_p-2} - \bar{w}_{N_p-1}}{\mathcal{C}_{back,N_p} - 1 + \mathcal{A}_{N_p}\left|k_z\right|\left(2\hat{x}\right)^{1/2}} + \\ + \frac{\mathcal{A}_{N_p}\mathrm{i}k_y\left(2\hat{x}\right)^{1/2}\mathrm{e}^{\mathrm{i}\mathcal{F}\hat{x}+\mathrm{i}k_y(2\hat{x})^{1/2}[\eta-\beta_c(\hat{x})]-\left(k_y^2+k_z^2\right)\hat{x}}}{\mathcal{C}_{back,N_p} - 1 + \mathcal{A}_{N_p}\left|k_z\right|\left(2\hat{x}\right)^{1/2}}, \quad (2.37b)$$

$$\bar{p}_{N_p} = \frac{\mathcal{C}_{back,N_p}\bar{p}_{N_p-2} - \bar{p}_{N_p-1}}{\mathcal{C}_{back,N_p} - 1 + \mathcal{A}_{N_p}\left|k_z\right|\left(2\hat{x}\right)^{1/2}}, \quad (2.37c)$$

- where $\mathcal{A}_{N_p} = \mathcal{C}_{back,N_p}(\Delta\eta_{N_p} + \Delta\eta_{N_p-1}) - \Delta\eta_{N_p}$ - in the discretization at η_{N_p-1}. The pressure is computed on the staggered grid (blue circles in figure 2.4) to avoid the odd-even decoupling

$$\bar{p}_{j+1/2} = \frac{\bar{p}_{j+1} + \bar{p}_j}{2}, \quad (2.38)$$

and the wall-normal pressure gradient is

$$\frac{\partial\bar{p}}{\partial\eta} = \frac{\bar{p}_{j+1} - \bar{p}_j}{\Delta\eta_{j+1}}. \quad (2.39)$$

A Chebyshev-Gauss-Lobatto (CGL) grid is used to distribute the grid points (olive points in figure 2.4) in the wall-normal direction [Aref and Balachandar, 2018]. The location of each point is given by

$$\eta_j = \eta_{max}\left[1 - \cos\left(\frac{\pi j}{2N_p}\right)\right] \text{ for } 0 \leq j \leq N_p, \quad (2.40)$$

in the range $\eta \in [0, \eta_{max}]$. The base-flow results obtained on uniform and CGL grids with $N_p = 3000$ and $\eta_{max} = 30$ are compared in figure 2.4 (right plot). The CGL grid (black crosses) is substantially more refined than the uniform grid (magenta triangles) in the near-wall region.

Following WZL11, in order to validate the algorithm and the use of the CGL grid, the present solution to (2.16a)–(2.16e) - which reduce to the form of Viaro and Ricco [2019a] in absence of suction - is validated against the incompressible wind tunnel data of Tani [1962, T62] and Finnis and A. Brown [1997, FB97]. Since the amplitude of the free-stream gusts ϵ was not provided in their works, the numerical results were rescaled with respect to the experimental data point located furthest upstream [Xu, Y. Zhang, et al., 2017]. The agreement is good for all the cases (refer to figure 2.5). Unfortunately, a direct comparison with the supersonic wind tunnel data of Q. Wang et al. [2018] is not possible and an experimental validation cannot be performed in the compressible regime. The code reproduces the computations of Viaro and Ricco [2019a] for the compressible case (refer to figure 9a therein and to the right plot in figure 2.5).

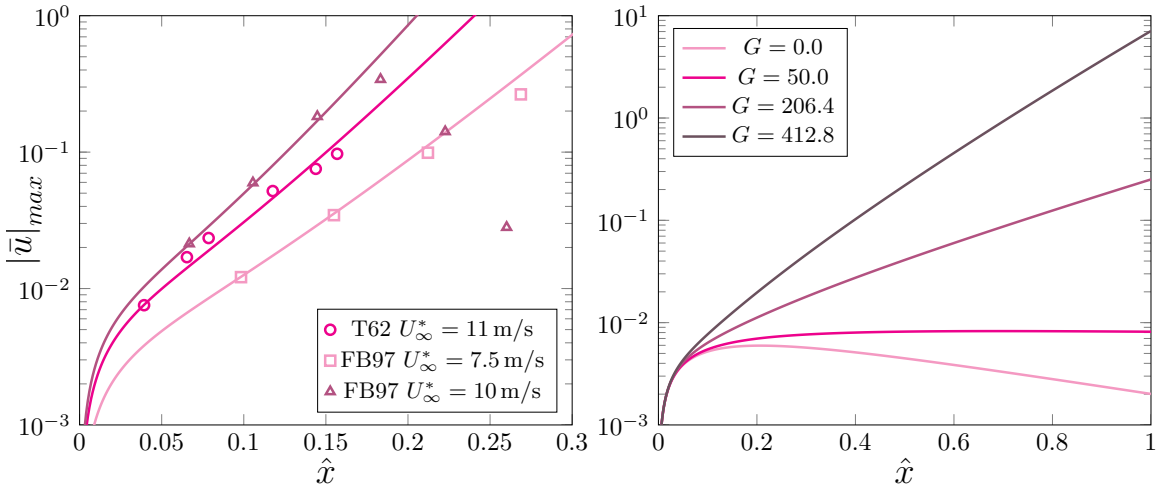

Figure 2.5: Validation of the disturbance flow without suction computed on the CGL grid. Left: the growth of the steady, incompressible Görtler vortices compared against the experimental data of Tani [1962, T62] and Finnis and A. Brown [1997, FB97] as in WZL11. Right: the growth of compressible steady Görtler vortices compares well with the results of Viaro and Ricco [2019a, fig. 9a] for $Ma = 4.0$ and $k_y = 1$.

Finally, the discrete points of the neutral stability curves in §2.2.3 were computed by solving the CLUBR equations for increasing G and storing the streamwise location of the neutral point. In most cases, the neutral curves are functions $G_\varsigma(\hat{x})$, where G_ς is the Görtler number corrisponding to a neutral point, and a Quicksort algorithm [Hoare, 1962] was used to sort the detected points for ascending $\hat{x}$.

2.2 Results

The base-flow solution (2.5) is validated in §2.2.1.1 against wind-tunnel measurements and direct numerical simulations of boundary layers with uniform suction. The free-stream conditions outlined in table 2.1 are used in the rest of §2.2. The characteristics of the porous wall and the base-flow properties are discussed in §2.2.1.2 and §2.2.1.3, respectively. The effect of uniform suction on the receptivity (excitation) and growth of Görtler vortices is studied in §2.2.2, and the neutral curves are examined in §2.2.3.

2.2.1 Laminar base flow

2.2.1.1 Comparison with experiments and direct numerical simulations

The non-similar laminar base flow (2.5) with wall suction is validated against the low-speed wind tunnel data of Fransson and Alfredsson [2003] (figure 2.6, left). The free-

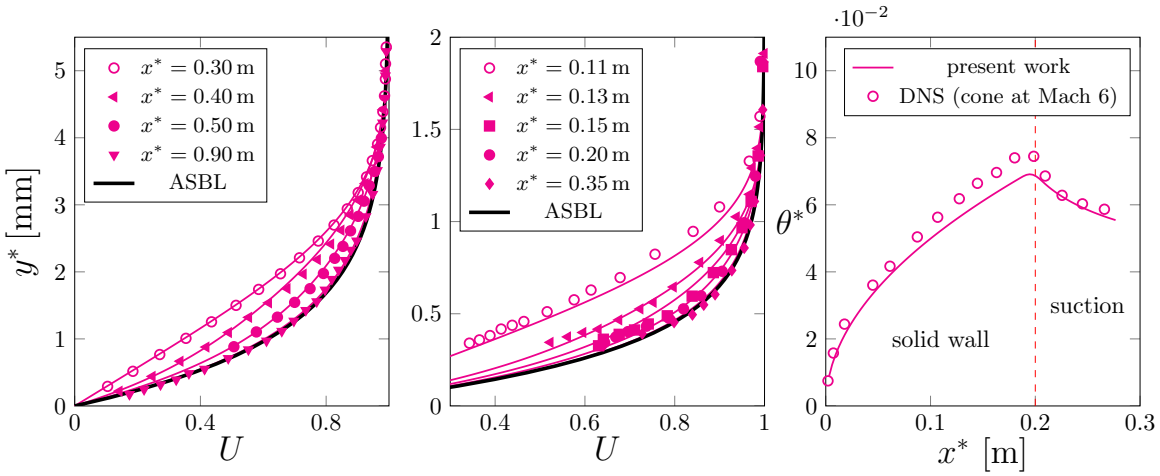

Figure 2.6: Left and centre: laminar velocity profiles in the suction region (solid curves) compared with the incompressible data (marks) of Fransson and Alfredsson [2003] (left plot, $x_s^* = 0.34\,\mathrm{m}$) and Kay [1953] (central plot, $x_s^* = 0.11\,\mathrm{m}$). Asymptotic-suction profiles are plotted in bold black. Right: momentum thickness along the surface of a cone at Mach 6 and the numerical data of Hollender et al. [2019] (right plot, $x_s^* = 0.2\,\mathrm{m}$).

stream velocity is $U_\infty^* = 5\,\mathrm{m\,s^{-1}}$ and a region of uniform suction velocity $V^*(\hat{x}, 0) = -1.44\,\mathrm{cm\,s^{-1}}$ begins at $x_s^* = 0.36\,\mathrm{m}$. A spanwise wavelength $\lambda_z^* = \delta_{99}^*(x_s^*) = 5.2\,\mathrm{mm}$ is assumed, which yields $Re = 275$ and $\gamma_w = -0.79$. The results of (2.5) (figure 2.6, left) show excellent agreement with the wind tunnel data. The boundary layer reaches the asymptotic-suction state (black bold curve) at $x^* = 0.9\,\mathrm{m}$. The incompressible asymptotic-suction profile is $U = 1 - \exp(\gamma_w y)$. Fransson and Alfredsson [2003] had previously validated their results by solving a non-similar, incompressible boundary-layer equation with $\Delta\hat{x}_s = 0$. Their mathematical formulation differs in that it features the streamwise variable $\xi = \gamma_w \hat{x}^{1/2}$, and the scalings $F(\xi, \eta) = \psi(\hat{x}, y)\gamma_w \xi^{-1}$ and $\eta = y\gamma_w \xi^{-1}$, all dependent on the suction rate γ_w.

A good agreement is also found with the wind-tunnel data of Kay [1953] (figure 2.6, centre). They studied an incompressible boundary layer with $U_\infty^* = 17.37\,\mathrm{m\,s^{-1}}$ and developing over a porous surface. The boundary-layer thickness was $\delta_{99}^* = 1.5\mathrm{mm}$ at the beginning of the suction region, located at $x_s^* = 0.11\mathrm{m}$, the kinematic viscosity was $\nu^* = 1.43 \cdot 10^{-5}\,\mathrm{m^2/s}$ and the Reynolds number based on δ_{99}^* was 290. A uniform suction velocity $V(\hat{x}, 0) = -5.1\,\mathrm{cm\,s^{-1}}$ was applied and the laminar asymptotic suction profile was attained at $x^* = 0.35\,\mathrm{m}$.

The velocity and temperature profiles of compressible laminar boundary layers over porous plates with suction are not readily available in the experimental and nu-

merical literature. The wall-normal profiles reported in Leontiev and Pavlyuchenko [2008] at $Ma = 2.5$ cannot be used for comparison because they were measured in a high-intermittency region downstream of a perforated suction plate, where the flow was already transitional. Hollender et al. [2019] performed direct numerical simulations on the cone-flared cone geometry studied by Li et al. [2018]. Unfortunately, it is not possible to validate the present computations against the velocity profile they sampled in the suction region as neither the corresponding boundary-layer thickness nor the exact location of the suction region on the cone was specified. Nevertheless, they reported the distribution of the momentum thickness upstream of and over the suction region. They imposed a constant mass flow rate $\dot{m}_w^* = -0.5\,\mathrm{g\,s^{-1}}$ on the surface of a truncated section of a cone with a half-angle $\alpha_{cone} = 7°$. The fore section of the model was conical and had a slant height of 0.3 m. The suction region was located between $\ell_1^* = 0.20\,\mathrm{m}$ and $\ell_2^* = 0.28\,\mathrm{m}$ from the tip and covered an estimated area

$$A_{suc}^* = \pi\,(\ell_1^* + \ell_2^*)\sin(\alpha_{cone})\,(\ell_2^* - \ell_1^*) = 0.0147\,\mathrm{m}^2. \tag{2.41}$$

The free-stream density and temperature were $\rho_\infty^* = 0.035\,\mathrm{kg/m^3}$ and $T_\infty^* = 52.6\,\mathrm{K}$. The boundary layer on the cone at zero angle of attack develops downstream of an axisymmetric conical shock wave, with no fluid motion occurring along the meridian planes. The inviscid flow properties at the cone surface are described by the Taylor-Maccoll theory and the boundary layer is governed by the compressible Blasius solution [Stewartson, 1964, §5.2]. For $Ma = 6$ and $\alpha_{cone} = 7.5°$, the tables in Sims [1964] report the following thermodynamic properties at the cone surface

$$\frac{p_{sur}^*}{p_\infty^*} = 2.08, \quad \frac{\rho_{sur}^*}{\rho_\infty^*} = 1.68, \quad \frac{T_{sur}^*}{T_\infty^*} = 1.24, \quad Ma_{sur} = 5.3.$$

The inviscid surface velocity is $U_{sur}^* = Ma_{sur}\sqrt{\gamma \mathcal{R}^* T_\infty^*} = 857.53\,\mathrm{m\,s^{-1}}$. Assuming $\lambda_z^* = \delta_{99}^* = 1\,\mathrm{mm}$ [Li et al., 2018], the Reynolds number is $Re_{sur} = \rho_{sur}^* U_{sur}^* \lambda_z^* / (2\pi\mu_{sur}^*)$, where the viscosity at the surface is estimated using Sutherland's law

$$\frac{\mu^*}{\mu_{ref}^*} = \left(\frac{T^*}{T_{ref}}\right)^{3/2} \frac{\chi^* + T_{ref}^*}{\chi^* + T^*}, \tag{2.42}$$

with $\mu_{ref}^* = 1.85 \cdot 10^{-5}\,\mathrm{Pa\,s}$, $T_{ref}^* = 300\,\mathrm{K}$, $\chi^* = 129\,\mathrm{K}$. The adiabatic recovery temperature is [Anderson, 2016]

$$T_w^* = T_{sur}^* \left(1 + \frac{\gamma - 1}{2} Pr^{1/2} Ma_{sur}^2\right) = 374\,\mathrm{K}. \tag{2.43}$$

The wall-normal velocity is found from the mass flow rate $\dot{m}_w^*$

$$V_w^* = \frac{\dot{m}_w^*}{\rho_w^* A_{suc}^*} = \frac{\dot{m}_w^*}{A_{suc}^*} \frac{T_w^*}{\rho_{sur}^* T_{sur}^*}. \tag{2.44}$$

The surface temperature of the cone is $T_w^* = 300\,\mathrm{K}$ and the suction parameter is

$$\gamma_w = \frac{\dot{m}_w^*}{A_{suc}^*} \frac{T_w^*}{T_{sur}^*} \frac{\lambda_z^*}{2\pi\mu_{sur}^*} = -6.01. \tag{2.45}$$

The boundary-layer momentum thickness is computed from the present base-flow solution (2.5)

$$\theta_{BL} = \int_0^\infty \frac{U}{T}\,(1-U)\,\mathrm{d}y, \tag{2.46}$$

and agrees well with the DNS results (figure 2.6, right).

2.2.1.2 Suction rates through the porous wall

The results presented from this point onwards are computed using the free-stream conditions of cases F76 and W18 in table 2.1. Since suction is typically achieved by generating a pressure gradient across a porous membrane, the implementation of a transpiration surface is constrained by the low static pressures in supersonic wind tunnels. Therefore, one might question whether the values of γ_w considered herein are feasible in practice. Although the design of suction actuators is beyond the scope of this work, an estimate of the membrane's thickness is provided in this section. The velocity through the porous layer is assumed to be uniform $V_w = V(\hat{x}, 0)$ and described by the linear Darcy law (2.18) [Schmidt et al., 2016; Traub et al., 2024]. Its use is justified when the pore-scale Reynolds number is sufficiently small

$$Re_d \equiv \frac{\rho_w^* V_w^* d_p^*}{\mu_w^*} = \frac{p_\infty^*}{\mathcal{R}^* T_w^*} \frac{\gamma_w U_\infty^*}{Re} \frac{d_p^*}{\mu_w^*} \ll 1. \tag{2.47}$$

In (2.47), T_w^* is computed using (2.43) with T_∞^* and Ma instead of T_{sur}^* and Ma_{sur}. The effect of choking, which may be important at high suction rates [Li et al., 2018], is not considered [Schmidt et al., 2016]. The pore diameter and permeability of Fransson and Alfredsson [2003], $d_p^* = 16\,\mu\mathrm{m}$ and $K^* = 3.7 \cdot 10^{-12}\,\mathrm{m}^2$, are used. The combination of low pressure and high recovery temperature yields a relatively high mean-free path $\ell_{mfp}^* = (\pi\mathcal{R}^* T_w^*/2)^{1/2} \mu_w^*/p_\infty^*$ and Knudsen number based on the pore diameter $Kn = \ell_{mfp}^*/d_p^*$. The flow within the pores lies in the slip regime ($0.001 < Kn \leq 0.1$), and the permeability is enhanced by a factor $1 + 7.23Kn$ [Yang and Weigand, 2018]. The theoretical maximum pressure difference across a porous layer of thickness Δh^* is the static pressure in the free stream, $\Delta p^* = p_\infty^*$, if one assumes that a steady

Table 2.1: Free-stream conditions reported in wind-tunnel tests over impermeable surfaces. From Flechner et al. [1976, F76], Graziosi and G. L. Brown [2002, GB02], Maslov, Shiplyuk, et al. [2001, p. M01], Running et al. [2023, R23], Tani [1962, T62], Finnis and A. Brown [1997, FB97], Ciolkosz [2006, CS06], Q. Wang et al. [2018, W18], Li et al. [2018, p. L18] and de Luca et al. [1993, p. L93]. The flow conditions used in §2.2.2 and §2.2.3 are highlighted in pink. The subscript o denotes the stagnation quantities.

Ref.	type	Ma	p_o^* [kPa]	T_o^* [K]	p_∞^* [kPa]	T_∞^* [K]	Re_u^* [10^6m^{-1}]
F76	flat plate	0.8	97	322	64	284	10.7
GB02	flat plate	2.98	32	290	0.9	104	2.62
M01	flat plate	5.92	1080	390	0.74	49	19.4
R23	flat plate	6.1	$[490, 3044]$	$[458, 488]$	$[0.28, 1.74]$	$[54.25, 57.81]$	$[6.3, 35.3]$
T62	concave plate	0.03	101325	303.15	101325	303.15	0.687
FB97	concave plate	0.02	101325	293.15	101325	293.15	$[0.5, 0.6]$
CS06	concave plate	$[1.06, 2.87]$	n.a.	n.a.	n.a.	n.a.	$[41.8, 59.6]$
W18	concave plate	2.95	85.2	288	2.5	105	7.15
L18	flared cone	6	1109	426	0.71	52	12.9
L93	concave plate	7	$[4500, 10^4]$	800	$[1.82, 4.05]$	74	$[12.9, 28.6]$

Table 2.2: Properties of the flow within the porous wall from Flechner et al. [1976, F76] and Q. Wang et al. [2018, W18].

Ref.	Ma -	Kn -	γ_w -	Re_d (2.47) -	Δp^* [Pa]	$\partial p^*/\partial y^*$ [kPa/m]	Δh^* (2.48) [mm]
F76	0.8	0.007	-2	0.083	63634	715	89.1
			-5	0.210		182	35.6
W18	2.95	0.090	-2	0.017	2500	1437	1.7
			-5	0.043		3597	0.7
			-10	0.087		7018	0.3

vacuum is generated underneath. Assuming $\partial p^*/\partial y^* \cong \Delta p^*/\Delta h^*$, the Darcy law (2.18) becomes

$$\frac{\Delta h^*}{p_\infty^*} = -\frac{K^*\,(1+7.23Kn)}{\mu_w^*}\frac{Re}{\gamma_w U_\infty^*}, \tag{2.48}$$

where Δh^* represents the maximum theoretical thickness of the porous layer through which a given suction rate γ_w can be realized assuming a vacuum is generated underneath.

The estimated maximum thicknesses pertinent to the considered range of γ_w are shown in the rightmost column in table 2.2 along with the pore-scale Reynolds number and the Knudsen number. In all cases, Kn is within the limits of the slip regime and Re_d is much smaller than unity. The value of Δh^* decreases dramatically in the supersonic case due to the higher γ_w, higher T_w^* and lower p_∞^*. The smallest thickness $\Delta h^* = 348\,\mu\text{m}$ corresponds to the case $Ma = 2.95$ and $\gamma_w = -10$, and is about 21 times d_p^*.

2.2.1.3 Compressible boundary layers

The streamwise evolution of the base flow profiles at $Ma = 0.80$ [F76] and $Ma = 2.95$ [W18] are shown in figures 2.7 and 2.8, respectively. The ASBL profiles (circles) are obtained by solving the system (2.13). All the profiles are markedly affected by suction. As the wall is adiabatic and $\hat{x}_s$ and $\Delta\hat{x}_s$ are fixed, the behaviour of the laminar base flow is determined by γ_w and Ma.

When suction is less intense, such as for $\gamma_w = -2$ at $Ma = 0.80$ (figure 2.7, left) or $\gamma_w = -5$ at $Ma = 2.95$ (figure 2.8, right), the boundary-layer thickens over the suction region before reaching the ASBL state. Moreover, when γ_w is low or moderate and Ma is fixed, the temperature adjusts more gradually than the velocity to the ASBL conditions. The opposite occurs for intense suction, such as for $\gamma_w = -5$

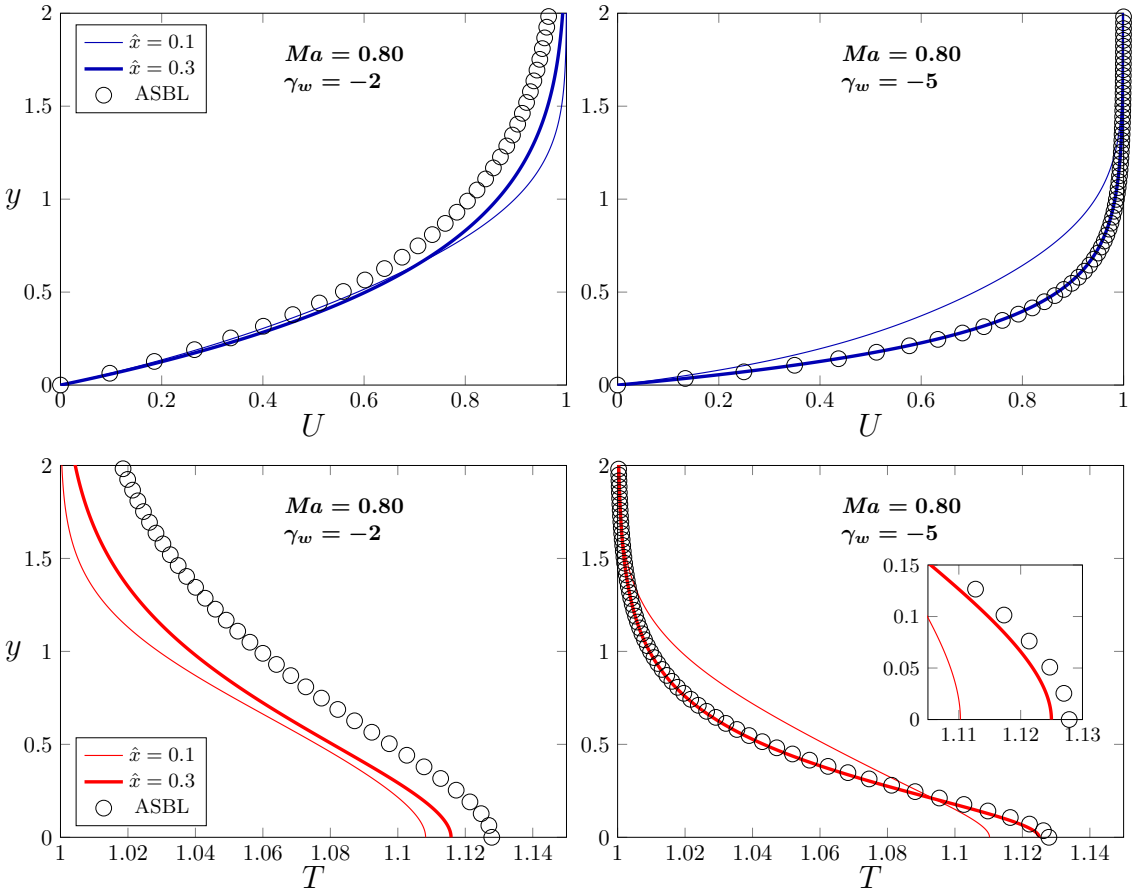

Figure 2.7: Effect of uniform suction on the velocity and temperature base-flow profiles at $Ma = 0.80$ and for different $\hat{x}$. The evolution of the velocity U (top) and temperature T (bottom) profiles is shown for $\gamma_w = -2$ (left) and $\gamma_w = -5$ (right). The asymptotic suction profiles are plotted with the circles.

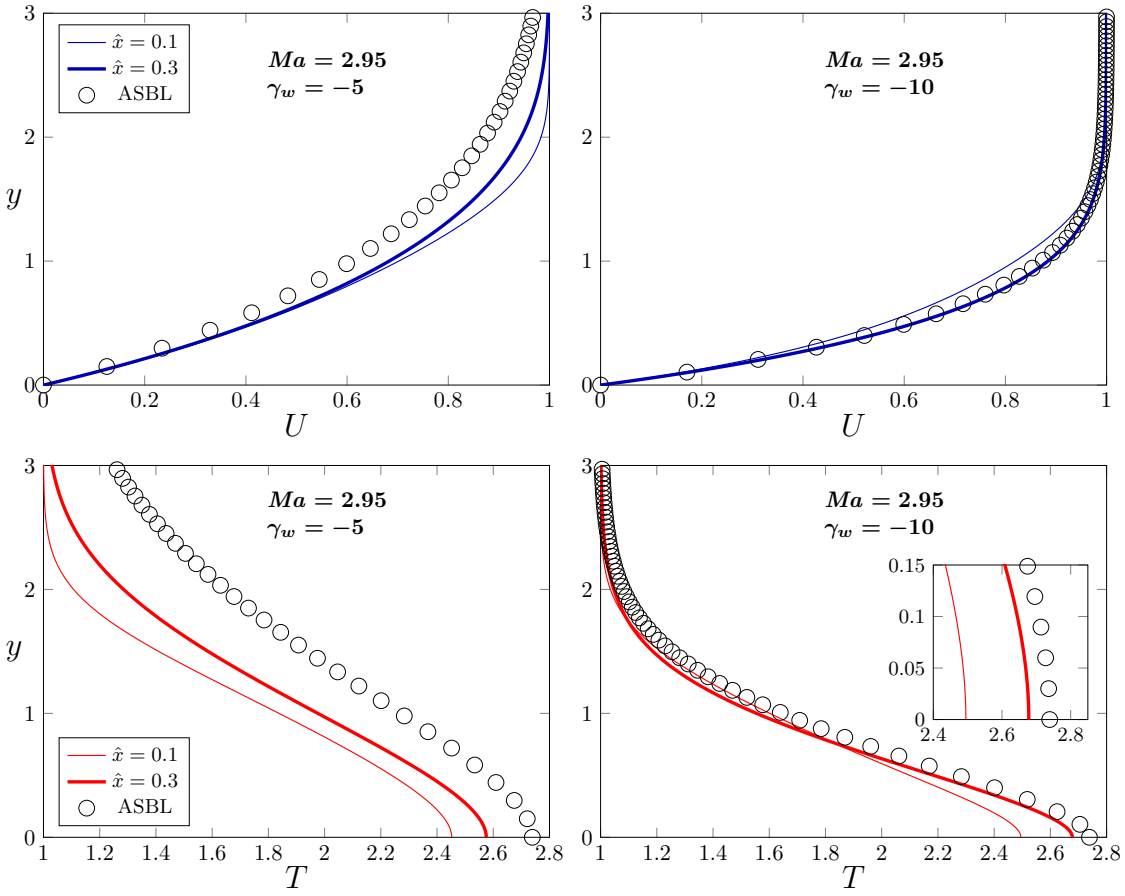

Figure 2.8: Effect of uniform suction on the velocity and temperature base-flow profiles at $Ma = 2.95$ and for different $\hat{x}$. The evolution of the velocity U (top) and temperature T (bottom) profiles is shown for $\gamma_w = -5$ (left) and $\gamma_w = -10$ (right). The asymptotic suction profiles are plotted with the circles.

at $Ma = 0.80$ (figure 2.7, left) or $\gamma_w = -10$ at $Ma = 2.95$ (figure 2.8, right), in which case the boundary-layer thickness decreases downstream of $\hat{x}_s$. A thinning boundary layer is also observed in the direct numerical simulations of Hollender et al. [2019] (figure 2.6, right). The streamwise distance along which the Blasius profile shifts to the asymptotic-suction profile becomes shorter as γ_w increases and Ma is fixed. Even when γ_w is intense, the streamwise-evolving temperature profile and the ASBL temperature profile still differ slightly near the wall, even though the streamwise velocity profiles show excellent collapse (insets in figures 2.7 and 2.8).

For a given γ_w, the effect of suction weakens as the Mach number and the wall temperature increase. For instance, the same suction rate $\gamma_w = -5$ produces a slower adjustment at $Ma = 2.95$ than at $Ma = 0.80$ from the Blasius boundary layer to the ASBL. A higher wall temperature $T_w = T(\hat{x}, 0)$ decreases the amplitude of the forcing term in the boundary condition (2.12), and a given V_w generates a lower mass flow rate through the wall when Ma is higher.

2.2.2 Attenuation of compressible Görtler vortices

The effect of suction on the receptivity to steady free-stream vorticity is examined. In this section, the geometry is fixed. A typical $r_c^* = 5\,\mathrm{m}$ is considered for the subsonic case [Viaro and Ricco, 2019a] and $r_c^* = 1\,\mathrm{m}$, as in the experiments of W18, is assumed for the supersonic case. The free-stream conditions of F76 and W18 are adopted (with fixed $k_y = 1$) and the effect of different γ_w and λ_z^* on the boundary-layer perturbations is studied. For given free-stream conditions and wall curvature, varying γ_w impacts the base flow only, while varying λ_z^* changes Re and G (the latter grows with the third power of λ_z^*, as given in (2.17)).

The evolution of the amplitudes of the streamwise velocity and temperature perturbations is shown in figure 2.9 for $\lambda_z^* = 1\,\mathrm{mm}$ (magenta) and $2\,\mathrm{mm}$ (orange) as a function of x^*/x_s^*. Suction markedly attenuates the growth of the streamwise velocity and temperature fluctuations ($|\bar{u}|$ and $|\bar{\tau}|$ are multiplied by Re in figure 2.9 to study quantities that are proportional to the physical quantities in (2.14) as λ_z^* varies). The attenuation effect of suction intensifies as γ_w increases, although it weakens as the conditions changes from subsonic to supersonic, in qualitative agreement with the results of linear stability theory [El-Hady and Verma, 1984]. In the high-subsonic case (figure 2.9, left), a suction rate of $\gamma_w = -5$ turns exponentially-growing Görtler vortices with $\lambda_z^* = 1\,\mathrm{mm}$ into decaying laminar streaks. In the supersonic case, an intense suction rate of $\gamma_w = -10$ renders the perturbations constant along the streamwise direction. A transient behaviour is observed around x_s^* in the supersonic case

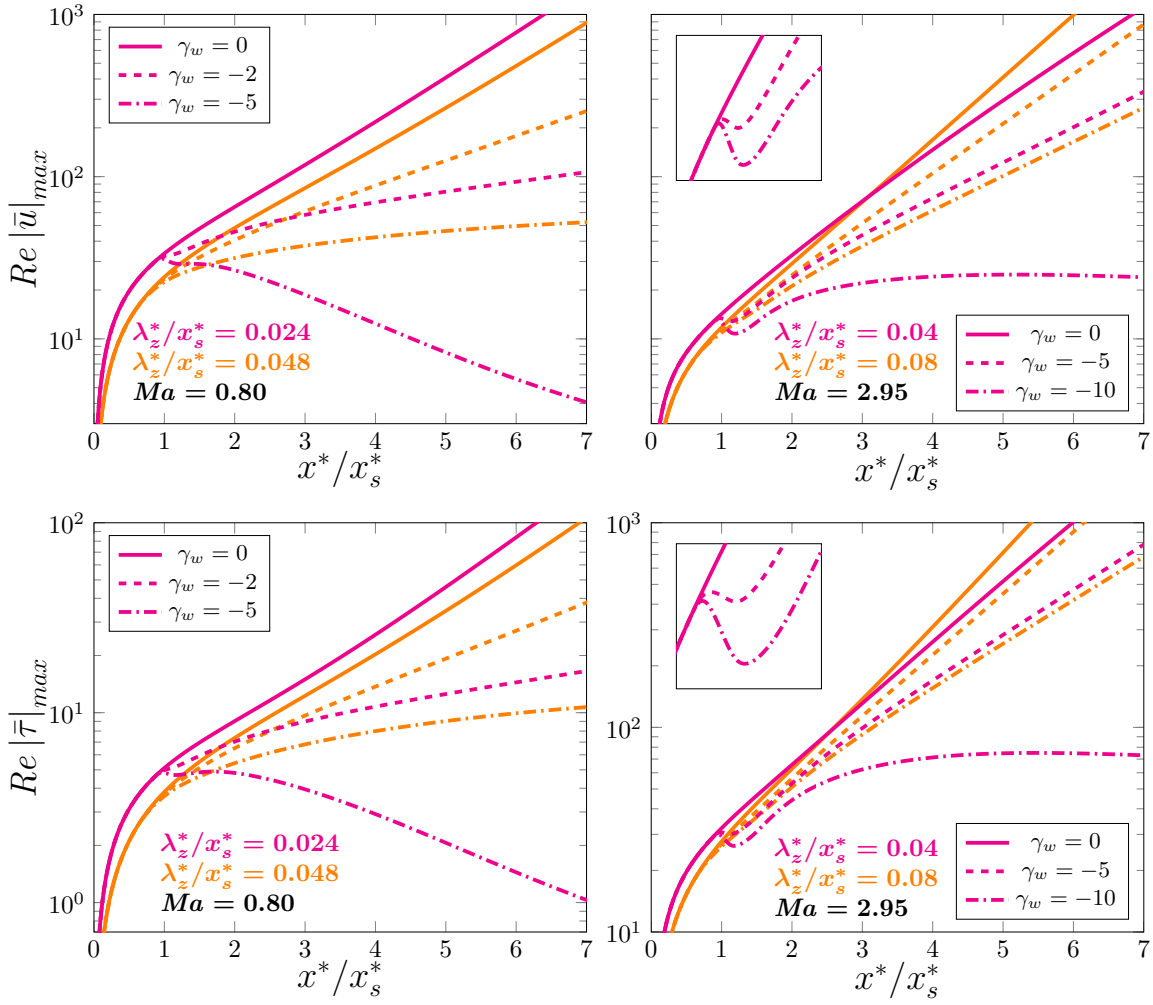

Figure 2.9: Uniform suction: effect of γ_w and λ_z^* on the maximum of the streamwise-velocity disturbances (top) and the temperature disturbances (bottom) in steady conditions at $Ma = 0.8$ (left) and $Ma = 2.95$ (right). The length of the impermeable region is $x_s^* = 4.2\,\mathrm{cm}$ in the subsonic case and $x_s^* = 2.5\,\mathrm{cm}$ in the supersonic case. The magenta and orange curves show the cases $\lambda_z^* = 1\,\mathrm{mm}$ and $2\,\mathrm{mm}$, respectively.

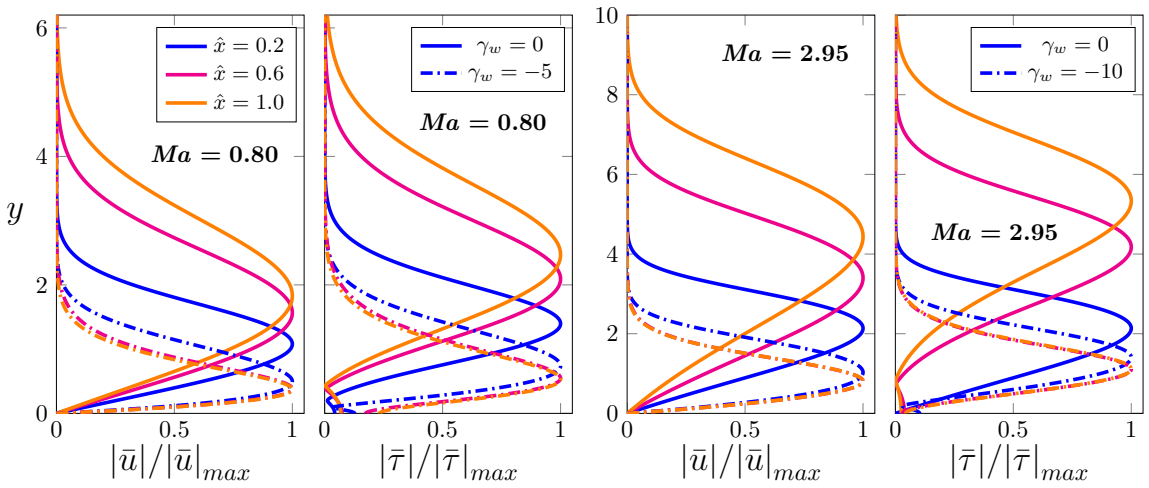

Figure 2.10: Perturbation velocity and temperature with (dash dot) and without solid suction at $Ma = 0.80$ (left) and $Ma = 2.95$ (right).

for $\gamma_w = -10$ (refer to inset in the top right plot of figure 2.9). The disturbance amplitude rapidly decreases, reaches a minimum downstream and then increases again under the forcing exerted by free-stream vorticity.

In the absence of suction, increasing λ_z^* delays the onset of Görtler vortices. The delay occurs because the condition for large centrifugal growth is weakened, i.e. δ^* becomes comparable with λ_z^* further downstream and thus the role of the $\mathcal{Y}$-momentum balance, where the centrifugal effect is active, is postponed. The influence of suction on the growth of Görtler vortices decreases as λ_z^* increases, in both subsonic and supersonic conditions.

The normalised velocity and temperature perturbation profiles at different streamwise locations are plotted in figure 2.10 for $\gamma_w = 0$ (solid curves), $\gamma_w = -5$ (subsonic, left plot) and $\gamma_w = -10$ (supersonic, right plot). The peaks of the fluctuations move to higher y (but lower η) as the boundary layer thickens when suction is absent or mild. When suction is intense enough to induce the decay of the streaks, the latter are confined within the asymptotic suction boundary layer of constant thickness and the shape of the normalised perturbation profiles is unaltered. A marked thinning of the boundary layer prevents the exponential growth of the vortices because the ratio δ^*/λ_z^* is reduced to a constant, thereby inducing a compression of the three-dimensional spanwise-adjacent structures [Fransson and Alfredsson, 2003]. The thinning of the boundary layer inhibits the generation of the spanwise and wall-normal pressure gradients, and the spanwise viscous diffusion of the disturbances that are instrumental in the growth of the Görtler vortices. Since $\hat{x} = x/Re = O(\delta^2)$ and $\delta \to 0$, the flow tends to be described by the boundary-layer equations, which, for solid walls, apply

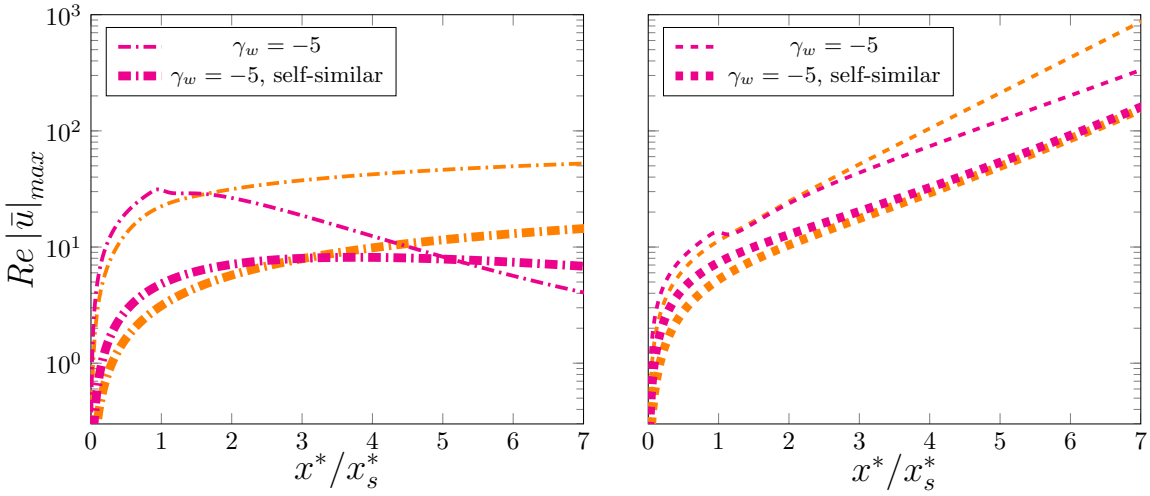

Figure 2.11: Comparison with self-similar suction: effect of γ_w and λ_z^* on the maximum of the streamwise-velocity disturbances in steady conditions at $Ma = 0.8$ (left) and $Ma = 2.95$ (right). The magenta and orange curves show the cases $\lambda_z^* = 1\,\text{mm}$ and $2\,\text{mm}$, respectively. The effect of self-similar suction (thick curves) is reported for comparison.

at locations closer to the leading edge where the pertubations grow at a slower rate [Viaro and Ricco, 2019a]. This slower growth is due to the $\mathcal{Y}$-momentum equation (2.16c) not entering the dynamics at leading order in the the boundary-layer equations, analogous to the laminar base flow. The curvature effects that are responsible for the inviscid pressure-centrifugal imbalance are therefore negligible.

The effect of self-similar suction $V(\hat{x}, 0) = V_0/(2\hat{x})^{1/2}$ where $V_0 Re = -5$, is shown in figure 2.11 (thick curves) and compared with the results of figure 2.9 (thin curves) for $\gamma_w = -5$ in the subsonic (left plot) and supersonic case (right plot). In the case of self-similar suction, the boundary-region equations (2.14) reduce to those of Viaro and Ricco [2019a]. Self-similar suction (thick curves) significantly attenuates the streaks and prevents the onset of the vortices in the subsonic case, thereby damping the disturbance growth right from its inception at the leading edge. The blowing velocity decreases downstream and self-similar suction is outperformed by the uniform suction with $\gamma_w = -5$ and $\lambda_z^* = 1\,\text{mm}$ (magenta curves). An analogous behaviour is reported in the supersonic case (figure 3, right). The curves for the self-similar and non-similar suction cases differ in both shape and amplitude and the results cannot be reconciled by rescaling the plots.

The effect of the free-stream gust frequency on the growth of Görtler vortices under the same conditions of figure 2.9 is shown in the left plot of figure 2.12 ($Ma = 0.80$, $G = 905$, $Re = 3771$ and $x_s^* = 4.2\,\text{cm}$). A frequency of $1260\,\text{Hz}$ is representative

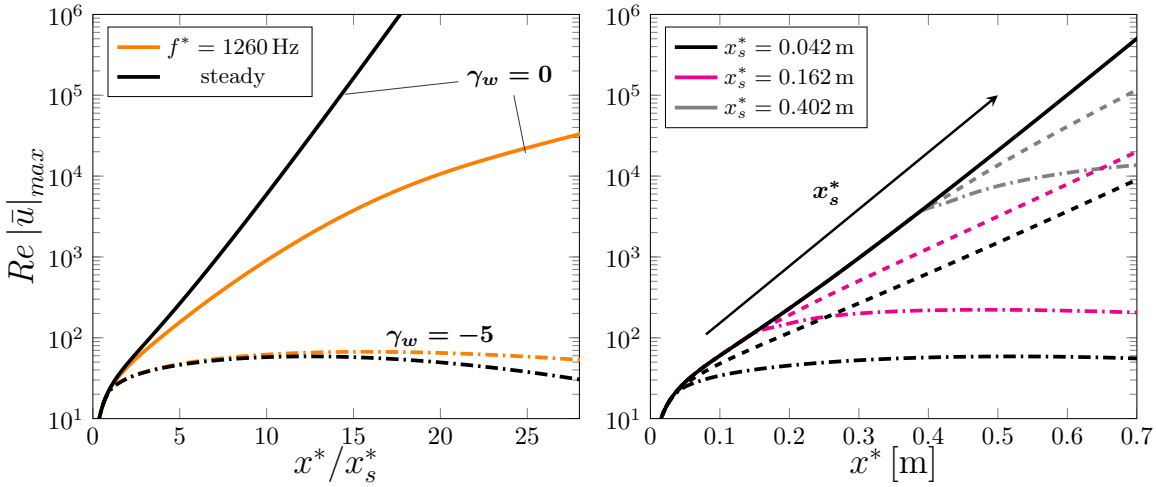

Figure 2.12: Left: effect of γ_w on steady and unsteady Görtler vortices. Right: effect of γ_w and x_s^* on steady Görtler vortices. For both graphs, $Ma = 0.8$, $G = 905$ and $Re = 3771$. The pattern of the curves denotes the suction rate $\gamma_w = 0$ (solid), $\gamma_w = -2$ (dashed) and $\gamma_w = -5$ (dash dot).

of wind-tunnel conditions at moderate Mach numbers [Viaro and Ricco, 2019a; Xu, Ricco, et al., 2024]. Uniform suction attenuates steady and unsteady vortices and, when $\gamma_w = -5$, the effect of frequency is negligible. When the boundary layer becomes thinner due to suction, the dynamics is analogous to that near the leading edge. As $\hat{x} \to 0$, the asymptotic behaviour is described by a regular perturbation of the boundary-region equations, expressed as a series summation [Leib et al., 1999; Viaro and Ricco, 2019a]. The first terms in this series are governed by the steady boundary-layer equations, which explains the negligible influence of unsteadiness.

The influence of x_s^* on the evolution of the steady vortices is shown in the right plot of figure 2.12. The growth rate for $\gamma_w = -2$ does not depend on x_s^*, while the value of maximum streamwise velocity at a given x^* increases with x_s^*. For $\gamma_w = -5$, the disturbance growth is no longer quasi-exponential and settles to an almost constant amplitude for relatively low x_s^*. For the largest tested x_s^*, the boundary layer has grown thicker and the same control is not as effective.

2.2.3 Neutral stability curves

The mathematical formulation presented in §2.1 incorporates the receptivity of the base flow to free-stream vortical disturbances, allowing a rigorous study of the evolution of the vortices and the plotting of neutral curves for the Görtler instability. The shape of the neutral curves, - i.e. curves in the parameter space that distinguish

conditions of growth and decay - is significantly influenced by the initial conditions [Hall, 1983] which can only be determined by matching with the outer flow, i.e. by taking receptivity into account. As suggested by Kobayashi [1972], the neutral curves can be easily interpreted if drawn in terms of G (2.17), which only depends on the free-stream conditions and wall curvature, and not on the boundary-layer thickness. Thus, the curves are represented as the points of the $\hat{x}$–G parameter space that satisfy the condition $\varsigma(\hat{x}) = 0$, where $\varsigma(\hat{x}) = \mathrm{d}E(\hat{x})/\mathrm{d}\hat{x}$ and

$$E(\hat{x}) = \int_0^\infty |\bar{u}(\hat{x}, \eta)|^2 \, \mathrm{d}\eta \tag{2.49}$$

is the scaled perturbation energy divided by $(2\hat{x})^{1/2}$ [Hall, 1983; Viaro and Ricco, 2019b]. The curves in figure 2.13 are drawn for given $\mathcal{F}$, Ma and $\hat{x}_s$. They separate stable ($\varsigma < 0$) and unstable ($\varsigma > 0$) regions, with colours denoting the suction rate γ_w. The curves embody the convective nature of Görtler instability: a perturbation evolving in $\hat{x}$ at a fixed G grows in unstable regions and decays in stable regions. The influence of the curvature radius on the Görtler instability when all the other physical parameters are fixed is obtained by changing G at fixed $\hat{x}$ in the maps of figure 2.13. When r_c is large, G is small, the perturbations evolve as laminar streaks and eventually decay by viscous effects. As r_c decreases, G increases and the laminar streaks become Görtler vortices as they undergo a quasi-exponential growth.

The importance of receptivity is revealed unequivocally in the influence of the wall-normal wavenumber k_y, a quantity that only enters the problem though the free-stream boundary conditions. A larger k_y stabilises the flow, i.e. the curves for $k_y = 2$ (solid) feature a pronounced peak near the leading edge (letter A) that is almost absent for $k_y = 1$ (dashed). The solid and dashed curves merge at large $\hat{x}$ and the disturbance growth is less impacted by receptivity as the perturbations evolve downstream. The reason for this result resides in the decay of the external perturbations by viscous dissipation, as evident in the outer boundary conditions (2.20). The eigenvalue approach becomes tenable because the external forcing is uninfluential sufficiently downstream [Viaro and Ricco, 2019a].

In the subsonic case ($Ma = 0.8$, figure 2.13, left), the stable region ($\varsigma < 0$) expands considerably and the marked peak near the leading edge becomes more pronounced as γ_w increases. The broadening of the stable region and the reduction in the growth rate caused by increasing suction are similar to those obtained by increasing Ma at constant $\hat{x}$ and Re.

The effect of suction is much weaker in the supersonic case ($Ma = 2.95$, right plot in figure 2.13), where the stable region does not broaden as significantly as in the

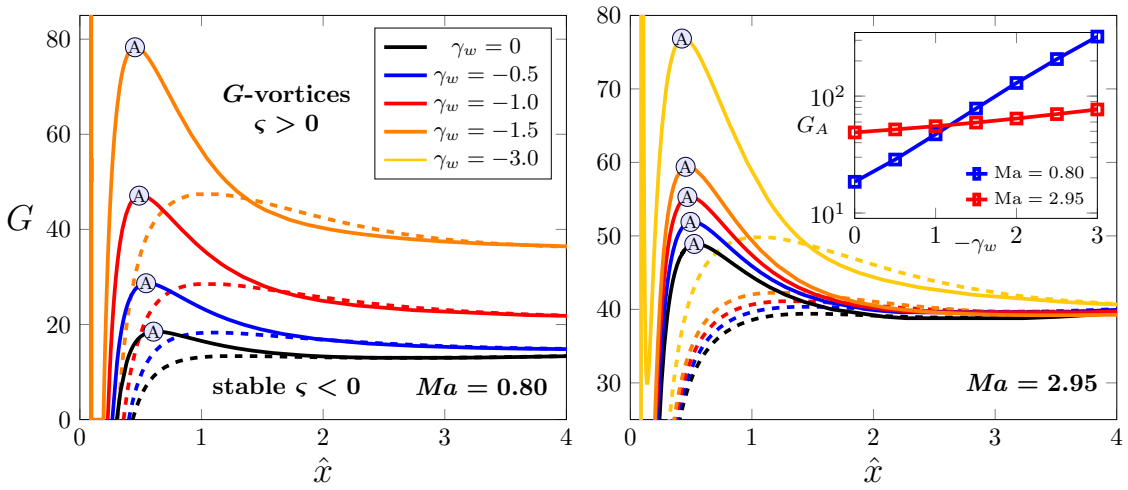

Figure 2.13: Neutral stability maps of steady ($\mathcal{F} = 0$) Görtler vortices with suction for $k_y = 2$ (solid curves) and $k_y = 1$ (dashed curves) at $Ma = 0.8$ (left) and $Ma = 2.95$ (right) for the conditions of table 2.1 and $\hat{x}_s = 0.1$. The maximum stable Görtler number G_A is shown in the inset as a function of γ_w.

subsonic case, especially downstream of its leading-edge peak. The neutral curves in absence of suction are inherently broader for supersonic Mach numbers because of the stabilising effect of compressibility on the centrifugal growth [Viaro and Ricco, 2019a], also caused by the strength of the suction term in the wall boundary condition (2.12) being reduced as T_w increases. The narrow vertical band in figure 2.13 (left) is due to the transient behaviour shown in the inset of figure 2.9, where suction decreases downstream of $\hat{x}_s$, reaches a minimum, and increases again. As γ_w increases, the stability region broadens upstream and eventually merges with this band (refer to yellow neutral curve in figure 2.13, right).

The maximum stable Görtler number G_A – which corresponds to the peak of the curves with $k_y = 2$ – increases quasi-exponentially with $|\gamma_w|$ (inset in figure 2.13). This change of G_A with $|\gamma_w|$ is more pronounced in the subsonic case. For both Mach numbers, wall suction is more stabilising at larger k_y. Higher suction rates shift the location where the boundary-layer perturbations become independent of the initial and outer conditions farther downstream.

The neutral stability curves of figure 2.14 (left) show the effect of suction for relatively high disturbance frequency $\mathcal{F}$ in supersonic flows. The shape of this neutral curve for unsteady conditions is markedly different from the map of figure 2.13 for steady conditions. At $\mathcal{F}$ increases, the peak denoted by the letter A in figure 2.13 becomes more pronounced and, eventually, the stable region splits in two branches

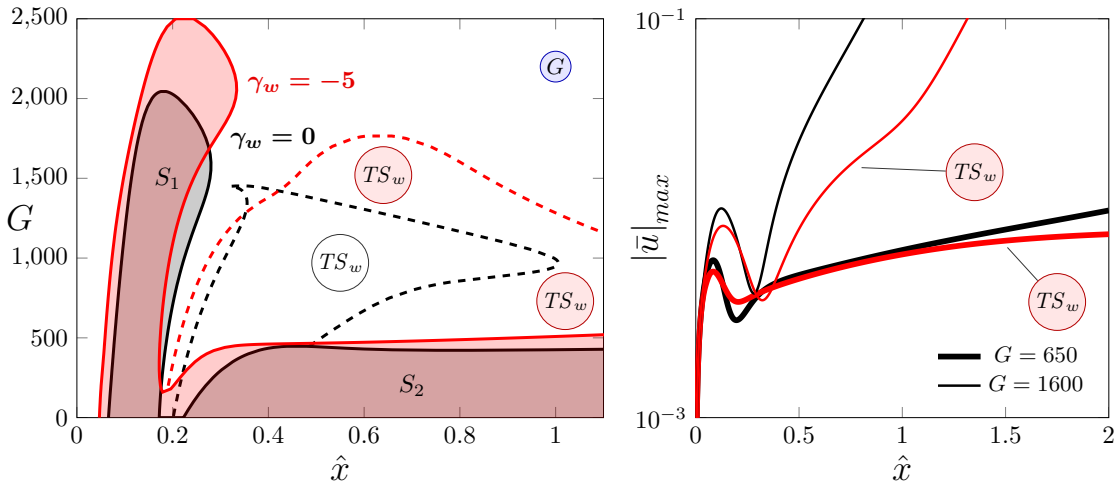

Figure 2.14: Left: neutral maps of Görtler instability (solid curves) at moderate Mach numbers and relatively high disturbance frequency. The stable regions (S_1 and S_2) are enclosed within the solid curves and the regions of weak TS growth (TS_w) within the dashed curves. Right: evolution of $|\bar{u}|_{max}$ for $G = 650$ (thick) and $G = 1600$ (thin). For both graphs, $Ma = 2.95$, $k_y = 1$, $\mathcal{F} = 150.3$, and $\gamma_w = 0$ (black) and $\gamma_w = -5$ (red).

denoted by S_1 and S_2 in figure 2.14 (left) [Viaro and Ricco, 2019b]. The flow experiences three types of instability: laminar streaks, Görtler vortices and oblique TS waves. The latter are generated by a wavelength-shortening mechanism related to the spanwise pressure gradient of the disturbance, as first shown by Ricco and X. Wu [2007]. For moderate G, the disturbance growth in absence of suction is described by the thick black curve for $G = 650$ in figure 2.14 (right). Laminar streaks develop upstream of (and attenuate within) S_1. Downstream of S_1, they either decay in S_2 or amplify again as TS waves, their growth being independent of the curvature [Viaro and Ricco, 2019b]. Here, a strong or weak TS growth occurs depending on whether

$$\beta = \frac{\mathrm{d}^2 |\bar{u}|_{max}}{\mathrm{d}\hat{x}^2} \tag{2.50}$$

is positive or negative, respectively. Regions of $\beta < 0$ are enclosed in the dashed curves in figure 2.14. Immediately downstream of S_1, β is positive and the TS waves undergo an intense growth ($\beta > 0$). The disturbances then enter the region enclosed by the dashed curve and turn into weak TS waves (TS_w). Only for very large G the perturbations turn into quasi exponentially-growing Görtler vortices, as shown by the thin black curve for $G = 1600$ in figure 2.14 (right).

Uniform suction with $\gamma_w = -5$ (red curves in figure 2.14) broadens the stable regions. The branches S_1 and S_2 merge and all disturbances are attenuated for

$G < 150$. Region S_1 broadens almost vertically, while the influence on region S_2 is milder. This finding is consistent with the results for steady conditions at moderate Mach numbers (figure 2.13, right). The region of the weak TS waves spreads and covers a large portion of the $\hat{x}$–G plane that would otherwise host the more powerful exponential growth of the strong TS waves or the Görtler vortices. The thick curves for $G = 650$ in figure 2.14 (right) illustrate the shift from strong to weak ($\beta < 0$) TS growth. When the curvature is more marked (thin curves for $G = 1600$), suction delays the onset of the strong TS waves and the Görtler vortices farther downstream.

Chapter 3

Receptivity over porous walls with a regular microstructure

This chapter investigates the effect of porous surfaces on the receptivity of supersonic boundary layers to free-stream vortical disturbances, focusing on the generation and evolution of compressible laminar streaks and highly-oblique Tollmien-Schlichting (TS) waves over these surfaces. The study is motivated by the findings of Egorov et al. [2008] and Fedorov [2011]. The porous-layer model used in this chapter was first employed by Fedorov, Malmuth, et al. [2001], and is characterized by a regular microstructure of thin, uniformly spaced cylindrical pores. To the best of the author's knowledge, it is the first time that porous surfaces are utilized to control laminar streaks and Görtler vortices over flat and concave porous surfaces.

The mathematical framework, based on Ricco and X. Wu [2007] and discussed in §3.1, is essentially the same as that introduced in chapter 2, the main difference being in that the dimensional lengths are scaled on the spanwise wavelength λ_z^* and the streamwise coordinate x on the streamwise wavenumber $k_x \ll 1$. The laminar streaks are studied in §3.2.1 and the receptivity and exponential growth of the TS waves are investigated in §3.2.2. The combined effect of wall porosity and curvature is the subject of §3.2.3.

3.1 Mathematical formulation

A supersonic uniform air flow with free-stream velocity U_∞^* and static temperature T_∞^* past an infinitely-thin plate is considered. The flow is described in a Cartesian frame of reference, where x^*, y^* and z^* define the streamwise, wall-normal and spanwise coordinates, respectively. The leading edge of the plates is located at $x^* = y^* = 0$. The Mach number is $Ma \equiv U_\infty^*/c_\infty^*$, where $c_\infty^* = \sqrt{\gamma \mathcal{R}^* T_\infty^*}$ is the speed of sound

in the free stream, $\gamma = 1.4$ is the heat capacity ratio, and $\mathcal{R}^* = 287.05\,\mathrm{J\,kg^{-1}\,K^{-1}}$ is the specific gas constant of air. All dimensional quantities are denoted by the superscript *. Schematics of the physical domains are shown in figure 3.1. The top sketch depicts the flat-wall system where laminar streaks turn into TS waves and the bottom sketch represents the concave-wall system where laminar streaks turn into Görtler vortices. The steady compressible laminar boundary layer forming over the plate is referred to as the base flow [Stewartson, 1964]. The free stream is perturbed by small-amplitude, homogeneous disturbances of the convected gust type, i.e. vortical perturbations which are purely advected by the free-stream base flow.

The spatial coordinates and all the boundary-layer lengths and wavenumbers are scaled by the spanwise wavelength of the gust, λ_z^*. The time is scaled by λ_z^*/U_∞^*. The velocity components, the density, the viscosity and the temperature are normalized by their free-stream values and the pressure is scaled by $\rho_\infty^* U_\infty^{*2}$, where ρ_∞^* is the density of the fluid in the free stream.

The small-amplitude, non-interacting perturbations in the free-stream are modeled by a single monochromatic perturbation of the gust type,

$$\boldsymbol{u} - \boldsymbol{\imath} = \epsilon \hat{\boldsymbol{u}}^\infty e^{\mathrm{i}(k_z z - k_x t)} + \text{c.c.}, \tag{3.1}$$

where $\boldsymbol{u}$ is the free-stream velocity vector, $\boldsymbol{\imath}$ is the streamwise unit vector, $\epsilon \ll 1$ indicates the amplitude of the gust, $\hat{\boldsymbol{u}}^\infty = \{\hat{u}^\infty, \hat{v}^\infty, \hat{w}^\infty\} = O(1)$, and c.c. its complex conjugate. The gust is characterized by a large wavelength ratio $\lambda_x^*/\lambda_z^* \gg 1$ and a small frequency $k_x = \omega^* \lambda_z^*/U_\infty^* \ll 1$, where ω^* is the angular frequency. A Reynolds number $\mathrm{R}_\lambda \equiv U_\infty^* \lambda_z^*/\nu_\infty^* \gg 1$ is defined, where ν_∞^* is the kinematic viscosity of the fluid in the free stream. Equation (3.1) differs from (2.1) in that

3.1.1 The self-similar laminar base flow: validation of the compressible Blasius solution

The steady compressible boundary-layer equations are cast into a more compact form by applying the Dorodnitsyn-Howarth coordinate transformation (2.3). In the absence of a streamwise pressure gradient, a similarity solution exists and a wall-normal similarity variable $\eta \equiv \overline{Y}\,[k_x \mathrm{R}_\lambda/(2\bar{x})]^{1/2}$ is defined. The streamwise velocity, the wall-normal velocity and the temperature of the base flow are

$$U = F'(\eta), \quad V = (2x\mathrm{R}_\lambda)^{-1/2}\,(\eta_c T F' - T F)\,, \quad T = T(\eta), \tag{3.2}$$

where the prime denotes differentiation with respect to η and

$$\eta_c \equiv \frac{1}{T}\int_0^\eta T\,(\breve{\eta})\,\mathrm{d}\breve{\eta}. \tag{3.3}$$

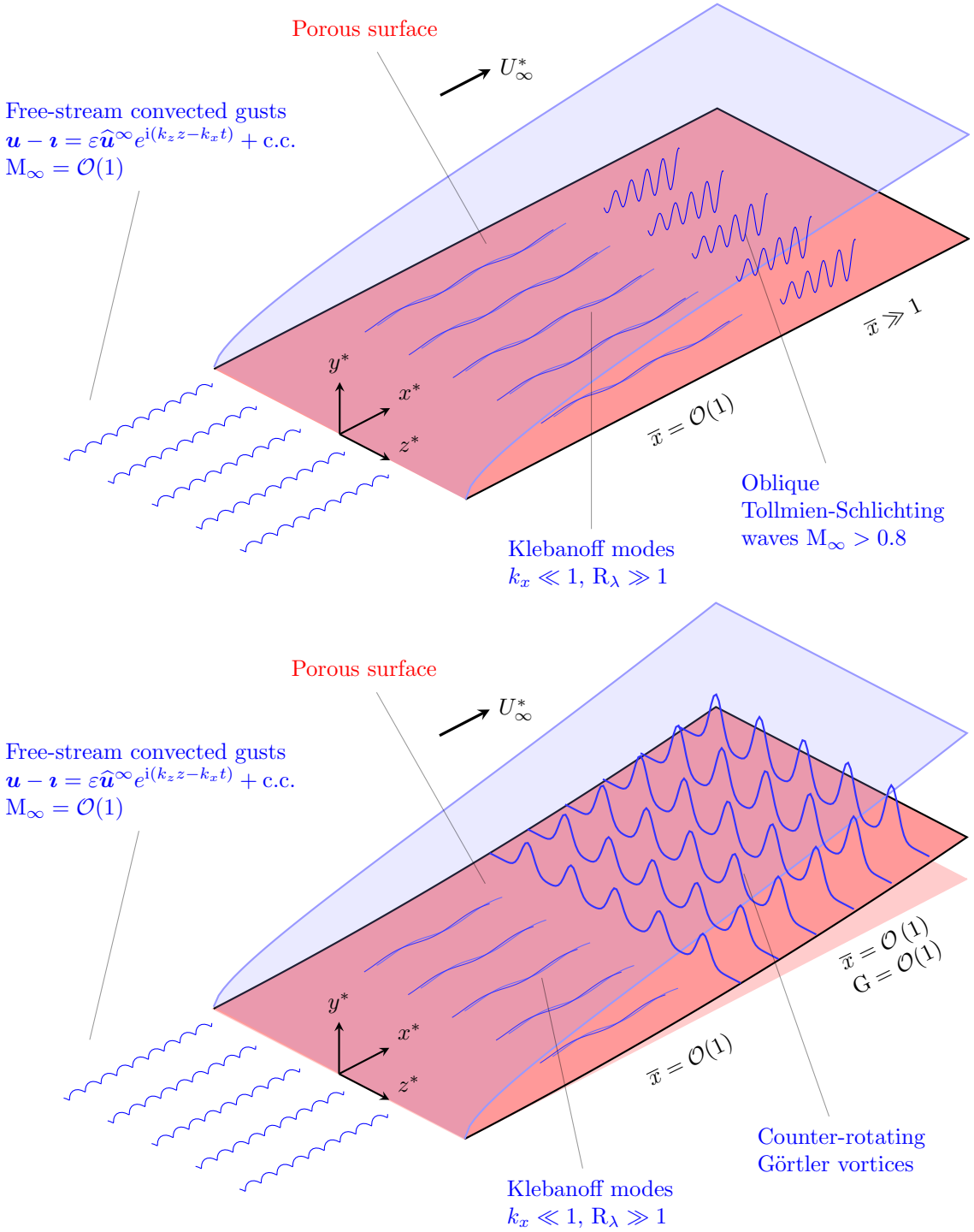

Figure 3.1: Schematics of the physical domains. Flat-plate system (top) and concave-surface system (bottom).

The base-flow solution (3.2) satisfies the coupled streamwise momentum and energy balance equations (B.19)

$$\left(\frac{\mu}{T}F''\right)' + FF'' = 0, \tag{3.4a}$$

$$\frac{1}{Pr}\left(\frac{\mu}{T}T'\right)' + FT' + (\gamma-1)Ma^2\frac{\mu}{T}\left(F''\right)^2 = 0, \tag{3.4b}$$

subject to the boundary conditions

$$\begin{array}{lll} F(0)=0, & F'(0)=0, & F'(\infty)\to 1 \\ T(0)=T_w, & T(\infty)\to 1. & \end{array} \tag{3.5}$$

The Prandtl number is $Pr = 0.7$. The dynamic viscosity has a power-law dependence on the temperature $\mu = T^{0.76}$ [Cebeci, 2002]. The numerical solutions (3.2) of the base-flow system (3.4) are compared to numerical and experimental data available in the literature, retrieved by the authors by using an image-digitizing software. The numerical profiles are plotted versus the similarity variable

$$\tilde{\eta} = \frac{y}{x}\mathrm{R}_x^{1/2} = 2^{1/2}\int_0^{\eta} T(\breve{\eta})\,\mathrm{d}\breve{\eta}, \tag{3.6}$$

where $\mathrm{R}_x = U_\infty^* x^*/\nu_\infty^*$.

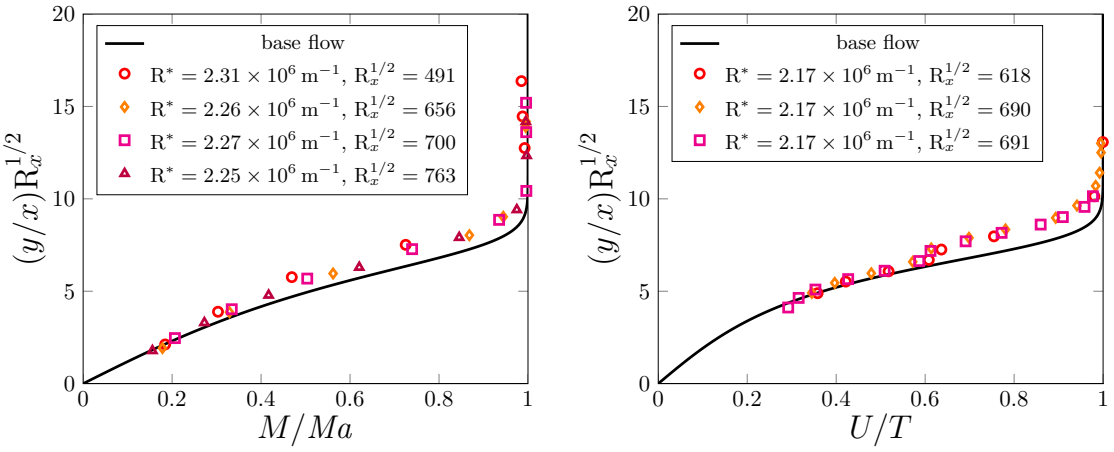

Figure 3.2: Comparison of the present base-flow numerical solution (3.2) (solid lines) with the hot-wire data by Graziosi [1999, pp. 85-110] for $Ma = 3$, $Pr = 0.72$, and $T_w/T_{ad,w} = 1.1$.

Our numerical solutions are first compared in figure 3.2 with the hot-wire data by Graziosi [1999, pp. 85-110] (refer also to Graziosi and G. L. Brown [2002]) for $Ma = 3$, $Pr = 0.72$, $T_w/T_{ad,w} = 1.1$ and at different unit Reynolds numbers $\mathrm{R}^* = U_\infty^*/\nu_\infty^*$ and streamwise locations $\mathrm{R}_x^{1/2}$. The present solutions (solid lines), plotted against

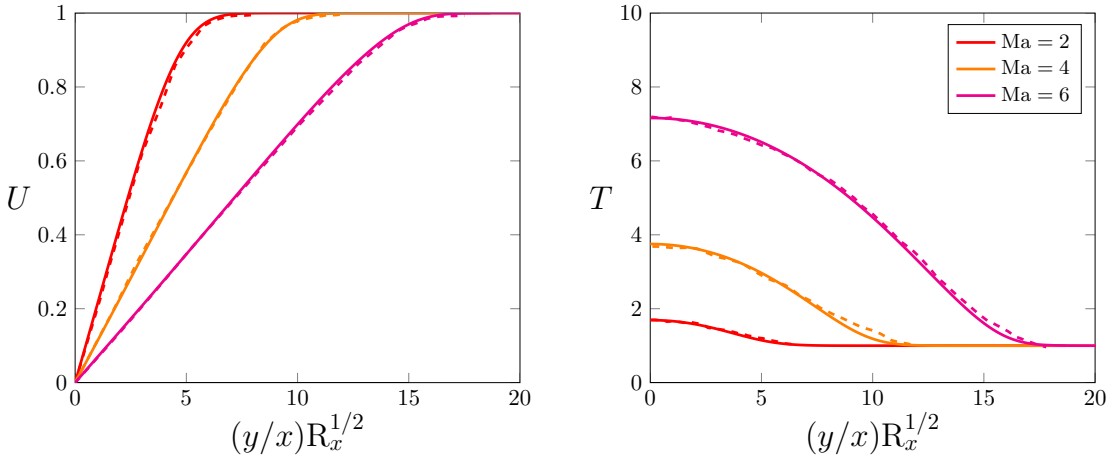

Figure 3.3: Comparison of the present base-flow numerical solutions (3.2) (solid lines) with the numerical results by van Driest [1952, pp. 40-41] (dashed lines) for a boundary layer over an adiabatic flat plate ($Pr = 0.75$).

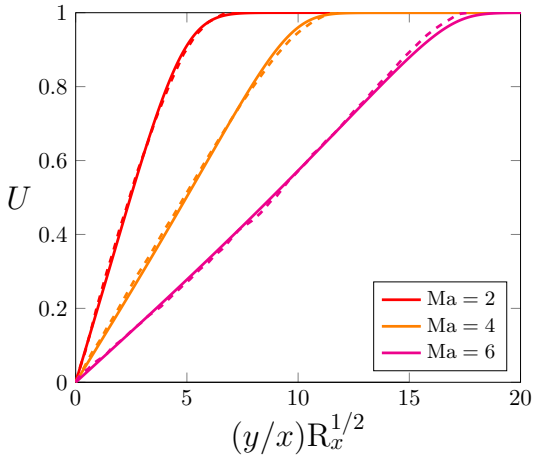

Figure 3.4: Comparison of the present base-flow numerical solutions (3.2) (solid lines) with the numerical results by Stewartson [1964, p. 40] (dashed lines) for a boundary layer over an adiabatic flat plate ($Pr = 1.0$).

$\mathrm{M}/Ma = U/T^{1/2}$ in figure 3.2a, show a satisfactory agreement with the experimental data. Other experimental data at fixed R^*, plotted against U/T and shown in figure 3.2b, show excellent agreement for $3 \leq \tilde{\eta} \leq 7$ and adequate agreement for $7 \leq \tilde{\eta} \leq 10$ ($\rho T = 1$ for a perfect gas has been used to convert ρU given by Graziosi and G. L. Brown [2002]).

Our velocity and temperature profiles (3.2) (solid lines) and those computed by van Driest [1952, pp. 40-41] (dashed lines) for a boundary layer over an adiabatic plate with $Pr = 0.75$ are shown in figure 3.3. Results were generated by modelling the dynamic viscosity with Sutherland's law $\mu = T^{3/2}(1+\chi)/(T+\chi)$, where $\chi = 0.505$, as in van Driest [1952]. A good agreement is found for both the velocity (left) and temperature (right) profiles at all the Mach numbers. Figure 3.4 shows that good agreement is also obtained between the present solutions and the velocity profiles by Stewartson [1964, p. 40] for a boundary layer with $Pr = 1$ flowing over an adiabatic plate. The dynamic viscosity was computed by using the power law $\mu = T^{0.76}$.

3.1.2 The unsteady disturbance flow

The boundary-layer flow is decomposed as the sum of the base flow and the small-amplitude perturbation flow,

$$\{u,\, v,\, w,\, \tau,\, p\} = \left\{U,\, V,\, 0,\, T,\, \frac{1}{\gamma Ma^2}\right\} + \epsilon\, \{\tilde{u}, \tilde{v}, \tilde{w}, \tilde{\tau}, \tilde{p}\}\, e^{\mathrm{i}(k_z z - k_x t)} + \text{c.c.}, \tag{3.7}$$

where

$$\{\tilde{u}, \tilde{v}, \tilde{w}, \tilde{\tau}, \tilde{p}\} = \left\{\bar{u}_0,\, \left(\frac{2\bar{x}k_x}{\mathrm{R}_\lambda}\right)^{1/2} \bar{v}_0,\, \bar{w}_0,\, \bar{\tau}_0,\, \left(\frac{k_x}{\mathrm{R}_\lambda}\right)^{1/2} \bar{p}_0\right\}(\bar{x}, \eta)\,. \tag{3.8}$$

The streamwise coordinate is scaled by the gust streamwise wavenumber $k_x^* = 2\pi/\lambda_x^*$, i.e. $\bar{x} = k_x x = 2\pi x^*/\lambda_x^* = O\,(1)$, where λ_x^* is the gust streamwise wavelength.

Following Gulyaev et al. [1989] and Choudhari [1996] and LWG99, the solution is expanded as a weighted sum of the two-dimensional $\left\{\bar{u}^{(0)},\, \bar{v}^{(0)},\, 0,\, \bar{\tau}^{(0)},\, \bar{p}^{(0)}\right\}$ and three-dimensional $\{\bar{u},\, \bar{v},\, \bar{w},\, \bar{\tau},\, \bar{p}\}$ gust signatures. The evolution of the former was considered by Ricco [2009] for the incompressible case, and is dominant in the outer part of the boundary layer. The focus is on the three-dimensional velocity components because they dominate over the two-dimensional components as they exhibit the disturbance growth in the core of the boundary layer. Expanding the solution in terms of the three-dimensional gust signatures yields

$$\{\bar{u}_0,\,\bar{v}_0,\,\bar{w}_0,\,\bar{\tau}_0,\,\bar{p}_0\} = \left(\hat{w}^\infty + \frac{\mathrm{i}k_z\hat{v}^\infty}{(k_x^2+k_z^2)^{1/2}}\right)\cdot \left\{\frac{\mathrm{i}k_z}{k_x}\bar{u},\,\mathrm{i}k_z\left(\frac{2\bar{x}}{k_x\mathrm{R}_\lambda}\right)^{1/2}\bar{v},\,\bar{w},\,\frac{\mathrm{i}k_z}{k_x}\bar{\tau},\,\mathrm{i}\kappa_z\left(\frac{k_x}{\mathrm{R}_\lambda}\right)^{1/2}\bar{p}\right\}, \quad (3.9)$$

Their evolution is governed by the compressible linearized unsteady boundary-region (CLUBR) equations [Ricco and X. Wu, 2007].

The CLUBR equations describe the evolution of the disturbances in the region III of Ricco and X. Wu [2007], which occupies locations where $\eta = O(1)$ and $\bar{x} = O(1)$ downstream of the leading edge. The CLUBR equations are the limiting form of the compressible Navier-Stokes equations where the streamwise diffusion and the streamwise pressure gradient have been neglected. The boundary-layer thickness is comparable to λ_z^* and the contribution of the spanwise diffusion to the momentum and energy balances must be taken into account. The wall-normal and spanwise diffusions are quantified by the asymptotic parameters

$$\kappa_y = \frac{k_y}{\sqrt{k_x\mathrm{R}_\lambda}} = \frac{2\pi}{\lambda_y^*}\left(\frac{\nu_\infty^*}{\omega^*}\right)^{1/2} = O(1), \quad (3.10a)$$

$$\kappa_z = \frac{k_z}{\sqrt{k_x\mathrm{R}_\lambda}} = \frac{2\pi}{\lambda_z^*}\left(\frac{\nu_\infty^*}{\omega^*}\right)^{1/2} = O(1). \quad (3.10b)$$

Free-stream gusts with equivalent wavenumbers $\kappa_y = \kappa_z$ are considered. The initial and boundary conditions are discussed in §3.1.4 and the modelling of the porous layer is presented in §3.1.3.1 and §3.1.3.2. The CLUBR equations are [Ricco and X. Wu, 2007]

$$\mathcal{C}|\ \frac{\eta_c T'}{2\bar{x}T}\bar{u} + \left.\frac{\partial\bar{u}}{\partial\bar{x}}\right|_\eta - \frac{\eta_c}{2\bar{x}}\frac{\partial\bar{u}}{\partial\eta} - \frac{T'}{T^2}\bar{v} + \frac{1}{T}\frac{\partial\bar{v}}{\partial\eta} + \bar{w} + \left(\frac{\mathrm{i}}{T} - \frac{FT'}{2\bar{x}T^2}\right)\bar{\tau} + \frac{F'}{T}\left.\frac{\partial\bar{\tau}}{\partial\bar{x}}\right|_\eta + \frac{F}{2\bar{x}T}\frac{\partial\bar{\tau}}{\partial\eta} = 0, \quad (3.11a)$$

$$\mathcal{X}|\ \left(-\mathrm{i} - \frac{\eta_c F''}{2\bar{x}} + \kappa_z^2\mu T\right)\bar{u} + F'\frac{\partial\bar{u}}{\partial\bar{x}} + \left(-\frac{F}{2\bar{x}} - \frac{\mu' T'}{2\bar{x}T} + \frac{\mu T'}{2\bar{x}T^2}\right)\frac{\partial\bar{u}}{\partial\eta} - \frac{\mu}{2\bar{x}T}\frac{\partial^2\bar{u}}{\partial\eta^2} + \frac{F''}{T}\bar{v} + \left(\frac{FF''}{2\bar{x}T} - \frac{\mu'' T' F''}{2\bar{x}T} + \frac{\mu' T' F''}{2\bar{x}T^2} - \frac{\mu' F'''}{2\bar{x}T}\right)\bar{\tau} - \frac{F''}{2\bar{x}T}\frac{\partial\bar{\tau}}{\partial\eta} = 0. \quad (3.11b)$$

$$\mathcal{Y}|\ \frac{TF + \eta_c(FT' - TF') - \eta_c^2 TF''}{4\bar{x}^2}\bar{u} + \frac{\mu' T'}{3\bar{x}}\left.\frac{\partial\bar{u}}{\partial\bar{x}}\right|_\eta + \left[\frac{\mu}{12\bar{x}^2} + \frac{\eta_c T}{12\bar{x}^2}\left(\frac{\mu}{T}\right)'\right]\frac{\partial\bar{u}}{\partial\eta} +$$

$$+\frac{\eta_c\mu}{12\bar{x}^2}\frac{\partial^2\bar{u}}{\partial\eta^2}-\frac{\mu}{6\bar{x}}\frac{\partial^2\bar{u}}{\partial\bar{x}\partial\eta}+\left(-\mathrm{i}+\frac{F'}{2\bar{x}}-\frac{T'F}{2\bar{x}T}+\frac{\eta_cF''}{2\bar{x}}+\kappa_z^2\mu T\right)\bar{v}+F'\left.\frac{\partial\bar{v}}{\partial\bar{x}}\right|_\eta+$$
$$+\left(-\frac{F}{2\bar{x}}-\frac{2\mu'T'}{3\bar{x}T}+\frac{2\mu T'}{3\bar{x}T^2}\right)\frac{\partial\bar{v}}{\partial\eta}-\frac{2\mu}{3\bar{x}T}\frac{\partial^2\bar{v}}{\partial\eta^2}+\frac{\mu'T'}{3\bar{x}}\bar{w}-\frac{\mu}{6\bar{x}}\frac{\partial\bar{w}}{\partial\eta}+\left[\frac{\eta_c\left(FF'\right)'}{4\bar{x}^2}+\right.$$
$$\left.-\frac{FF'}{4\bar{x}^2}-\frac{T'F^2}{4\bar{x}^2T}-\frac{\mu'F''}{4\bar{x}^2}-\eta_cT\left(\frac{\mu'F''}{4\bar{x}^2T}\right)'+\left(\frac{\mu'T'F}{3\bar{x}^2T}\right)'\right]\bar{\tau}-\frac{\mu'F''}{2\bar{x}}\left.\frac{\partial\bar{\tau}}{\partial\bar{x}}\right|_\eta+$$
$$+\left[-\frac{\mu'\eta_cF''}{(2\bar{x})^2}+\frac{4}{3}\frac{\mu'T'F}{(2\bar{x})^2T}\right]\frac{\partial\bar{\tau}}{\partial\eta}+\frac{1}{2\bar{x}}\frac{\partial\bar{p}}{\partial\eta}+\boxed{\frac{\widehat{G}}{\sqrt{2\bar{x}}}\left(2F'\bar{u}-\frac{\left(F'\right)^2}{T}\bar{\tau}\right)}=0, \quad (3.11c)$$

$$\mathcal{Z}|\ -\kappa_z^2\frac{\eta_c\mu'TT'}{2\bar{x}}\bar{u}+\kappa_z^2\frac{\mu T}{3}\left.\frac{\partial\bar{u}}{\partial\bar{x}}\right|_\eta-\kappa_z^2\frac{\eta_c\mu T}{6\bar{x}}\frac{\partial\bar{u}}{\partial\eta}+\kappa_z^2\mu'T'\bar{v}+\kappa_z^2\frac{\mu}{3}\frac{\partial\bar{v}}{\partial\eta}+\left(\frac{4}{3}\kappa_z^2\mu T-\mathrm{i}\right)\bar{w}+$$
$$+F'\left.\frac{\partial\bar{w}}{\partial\bar{x}}\right|_\eta-\left(\frac{F}{2\bar{x}}+\frac{\mu'T'}{2\bar{x}T}-\frac{\mu T'}{2\bar{x}T^2}\right)\frac{\partial\bar{w}}{\partial\eta}-\frac{\mu}{2\bar{x}T}\frac{\partial^2\bar{w}}{\partial\eta^2}+\kappa_z^2\frac{\mu'T'F}{3\bar{x}}\bar{\tau}-\kappa_z^2T\bar{p}=0. \quad (3.11d)$$

$$\mathcal{E}|\ -\frac{\eta_cT'}{2\bar{x}}\bar{u}+(\gamma-1)\,Ma^2\frac{\mu F''}{\bar{x}T}\frac{\partial\bar{u}}{\partial\eta}+\frac{T'}{T}\bar{v}+$$
$$+\left[-\mathrm{i}+\frac{FT'}{2\bar{x}T}-(\gamma-1)\,Ma^2\frac{\mu'\left(F''\right)^2}{2\bar{x}T}-\frac{1}{2\bar{x}Pr}\left(\frac{\mu'T'}{T}\right)'+\frac{\mu\kappa_z^2T}{Pr}\right]\bar{\tau}+$$
$$+F'\left.\frac{\partial\bar{\tau}}{\partial\bar{x}}\right|_\eta+\left(-\frac{F}{2\bar{x}}-\frac{1}{Pr}\frac{\mu'T'}{2\bar{x}T}+\frac{1}{Pr}\frac{\mu T'}{2\bar{x}T^2}\right)\frac{\partial\bar{\tau}}{\partial\eta}+\frac{1}{Pr}\frac{\mu}{2\bar{x}T}\frac{\partial^2\bar{\tau}}{\partial\eta^2}=0. \quad (3.11e)$$

Here, the global Görtler number 2.17 is rescaled accordingly [Viaro and Ricco, 2019b]

$$\widehat{G}=\frac{1}{r_c}\left(\frac{\mathrm{R}_\lambda}{k_x^3}\right)^{1/2}=\left(\frac{2\pi}{k_x\mathrm{R}_\lambda}\right)^{3/2}G, \quad (3.12)$$

where $r_c=r_c^*/\lambda_z^*$ is the scaled wall curvature radius, and $\mu'\equiv\mathrm{d}\mu/\mathrm{d}T$.

3.1.3 The flow within the pores

In the porous wall designed by Fedorov, Malmuth, et al. [2001], the pressure fluctuations at the interface between the wall and the boundary layer excite kinematic and thermal disturbances in long, thin cylindrical pores. The numerical studies of R. Zhao, T. Liu, et al. [2018] and R. Zhao, X. X. Zhang, et al. [2020] showed that the effects of acoustic scattering between adjacent pores can be neglected when the Helmholtz number $He=\omega^*h_p^*/c_w^*<4.21$, where h_p^* is the depth of the pores and

$$c_w^*=\left(\gamma\mathcal{R}^*T_w^*\right)^{1/2} \quad (3.13)$$

is the speed of sound in the pores. All the cases considered in the present work comply with that condition. Hence, the properties of the porous layer can be studied by considering the flow characteristics of an isolated pore. The propagation of small-amplitude disturbances in a single dead-end circular pore, with depth h_p^* and radius r_p^*, is derived in this section. The linearized continuity, axial momentum and energy equations are cast in cylindrical coordinates, and their solution yields an analytical radial distribution of the velocity and temperature in the form of Bessel functions [Zwikker and Kosten, 1949; Fedorov, Malmuth, et al., 2001].

In this section, we consider a single pore oriented along the wall-normal direction y and located underneath the wall [Zwikker and Kosten, 1949; Biot, 1956; Stinson, 1991; Fedorov, Malmuth, et al., 2001]. The depth of the pore h_p^* is much larger than its radius r_p^*, and the propagation of the disturbances is described in a cylindrical coordinate system. Since the pore is long and thin, and the average velocity is zero therein, one can assume the radial and azimuthal components of the velocity disturbance to be zero. The dynamic viscosity and the thermal conductivity are assumed constant, as the perturbations of the temperature field are small in amplitude. The axial coordinate is scaled with h_p^* and the radial coordinate is scaled with r_p^*. The time is scaled by the angular frequency ω^* and the pressure is scaled by $\rho_w^* \left(h_p^* \omega^*\right)^2$, where the density ρ_w^* is the density at the boundary-layer interface. The scaled quantities are denoted by the superscript $\bullet$. The pore has an open end at $y^\bullet = 0$ and is closed at $y^\bullet = -1$.

Since $r^*/h_p^* \gg 1$ one can assume the pressure disturbance to propagate as a planar wave along the pore [Kinsler et al., 2000; Stinson, 1991]. Harmonic disturbances of the type

$$p^\bullet\left(y^\bullet; t^\bullet\right) = \tilde{p}^\bullet\left(y^\bullet\right) e^{-\mathrm{i}t^\bullet} \tag{3.14a}$$

$$v^\bullet\left(r^\bullet; y^\bullet; t^\bullet\right) = \tilde{v}^\bullet\left(r^\bullet; y^\bullet\right) e^{-\mathrm{i}t^\bullet} \tag{3.14b}$$

$$\tau^\bullet\left(r^\bullet; y^\bullet; t^\bullet\right) = \tilde{\tau}^\bullet\left(r^\bullet; y^\bullet\right) e^{-\mathrm{i}t^\bullet} \tag{3.14c}$$

are introduced in the continuity equation, the axial momentum and energy equations, and the perfect gas equation, which take the linearized form

$$-\mathrm{i}\tilde{\rho}^\bullet + \frac{\partial \tilde{v}^\bullet}{\partial y^\bullet} = 0, \tag{3.15a}$$

$$-\mathrm{i}\tilde{v}^\bullet + \frac{\mathrm{d}\tilde{p}^\bullet}{\mathrm{d}y^\bullet} = \frac{1}{K_v^2}\left(\frac{\partial^2 \tilde{v}^\bullet}{\partial r^{\bullet 2}} + \frac{1}{r^\bullet}\frac{\partial \tilde{v}^\bullet}{\partial r^\bullet}\right), \tag{3.15b}$$

$$-\mathrm{i}\tilde{\tau}^\bullet = -\mathrm{i}\left(\gamma - 1\right) He^2 \tilde{p}^\bullet + \frac{1}{Pr}\frac{1}{K_v^2}\left(\frac{\partial^2 \tilde{\tau}^\bullet}{\partial r^{\bullet 2}} + \frac{1}{r^\bullet}\frac{\partial \tilde{\tau}^\bullet}{\partial r^\bullet}\right), \tag{3.15c}$$

$$\gamma He^2 \tilde{p}^\bullet = \tilde{\rho}^\bullet + \tilde{\tau}^\bullet, \tag{3.15d}$$

where $He = \mathcal{O}(1)$ and $K_v = r_p^* \left(\rho_w^* \omega^* / \mu_w^*\right)^{1/2}$ is defined in (3.24). The solutions that satisfy no-slip and isothermal boundary conditions at the wall are

$$\tilde{v}^\bullet \left(r^\bullet, y^\bullet\right) = -\mathrm{i} \frac{\mathrm{d}\tilde{p}^\bullet}{\mathrm{d}y^\bullet} \left[1 - \frac{J_0\left(\mathrm{i}^{1/2} K_v r^\bullet\right)}{J_0\left(\mathrm{i}^{1/2} K_v\right)}\right], \tag{3.16a}$$

$$\tilde{\tau}^\bullet \left(r^\bullet, y^\bullet\right) = \left(\gamma - 1\right) He^2 \tilde{p}^\bullet \left\{1 - \frac{J_0\left[\left(\mathrm{i}Pr\right)^{1/2} K_v r^\bullet\right]}{J_0\left[\left(\mathrm{i}Pr\right)^{1/2}\right]}\right\}, \tag{3.16b}$$

where J_0 is the Bessel function of the first kind and order 0.

The cross-sectional averages of the velocity and temperature solutions are

$$\left\langle \tilde{v}^\bullet \right\rangle \left(y^\bullet\right) = -\mathrm{i} \frac{\mathrm{d}\tilde{p}^\bullet}{\mathrm{d}y^\bullet} \left[1 - \widetilde{\mathcal{F}}\left(\mathrm{i}^{1/2} K_v\right)\right], \tag{3.17a}$$

$$\left\langle \tilde{\tau}^\bullet \right\rangle \left(y^\bullet\right) = \left(\gamma - 1\right) He^2 \tilde{p}^\bullet \left\{1 - \widetilde{\mathcal{F}}\left[\left(\mathrm{i}Pr\right)^{1/2} K_v\right]\right\}, \tag{3.17b}$$

and $\widetilde{\mathcal{F}}$ is a complex function of a complex variable ξ,

$$\widetilde{\mathcal{F}}\left(\xi\right) = \frac{2J_1\left(\xi\right)}{\xi J_0\left(\xi\right)} = 1 + \frac{J_2\left(\xi\right)}{J_0\left(\xi\right)}. \tag{3.18}$$

where J_1 and J_2 are the Bessel functions of the first kind and order 1 and 2, respectively. The pressure disturbance satisfies the equation [Stinson, 1991]

$$\frac{\mathrm{d}^2 \tilde{p}^\bullet}{\mathrm{d}y^{\bullet 2}} - \widetilde{\Lambda}^2 \tilde{p}^\bullet = 0, \tag{3.19}$$

where $\widetilde{\Lambda}$ is the propagation constant defined as

$$\widetilde{\Lambda}^\bullet = \mathrm{i}\left(Z_1^\bullet Y_1^\bullet\right)^{1/2}, \tag{3.20}$$

$Z_1^\bullet$ and $Y_1^\bullet$ are the non-dimensional series impedance (dynamic density) and shunt admittance (dynamic compressibility)

$$Z_1^\bullet = \left[1 - \widetilde{\mathcal{F}}\left(\mathrm{i}^{1/2} K_v\right)\right]^{-1}, \tag{3.21a}$$

$$Y_1^\bullet = He^2 \left\{1 + \left(\gamma - 1\right) \widetilde{\mathcal{F}}\left[\left(\mathrm{i}Pr\right)^{1/2} K_v\right]\right\}. \tag{3.21b}$$

The solution to (3.19) is

$$\tilde{p}^\bullet \left(y^\bullet\right) = a \left[e^{-\widetilde{\Lambda}^\bullet \left(y^\bullet + 1\right)} + e^{\widetilde{\Lambda}^\bullet \left(y^\bullet + 1\right)}\right], \tag{3.22}$$

where a is an unknown real constant. The velocity and temperature admittances at the pore inlet ($y^* = 0$) is given by the ratios of the velocity and temperature to pressure

$$A_v^\bullet(0) = \frac{\langle \tilde{v}^\bullet \rangle(0)}{\tilde{p}^\bullet(0)} = -\frac{\Lambda^\bullet}{\mathrm{i}Z_1^\bullet}\tanh(\Lambda^\bullet), \tag{3.23a}$$

$$A_\tau^\bullet(0) = \frac{\langle \tilde{\tau}^\bullet \rangle(0)}{\tilde{p}^\bullet(0)} = (\gamma-1)\,He^2\left\{1-\mathcal{F}\left[(\mathrm{i}Pr)^{1/2}K_v\right]\right\}. \tag{3.23b}$$

The velocity admittance (3.23a) is expressed by means of either the propagation constant or the characteristic impedance $Z^\bullet = (Z_1^\bullet/Y_1^\bullet)^{1/2}$. The former is preferable, since it removes the ambiguity on the choice of the branch of the complex square root (Fedorov, private communication).

3.1.3.1 Asymptotic analysis of the unsteady disturbance within the pores

The response of the pores is ruled by the frequency parameter $k_x\mathrm{R}_\lambda$ [Fedorov, Malmuth, et al., 2001; Goldstein and Ricco, 2018; Viaro and Ricco, 2019a]. The disturbances are not transmitted to the pores at very low frequencies for which $k_x\mathrm{R}_\lambda = O(1)$ or smaller. The boundary-layer disturbances are expected to interact with the porous wall as $k_x\mathrm{R}_\lambda$ increases and the magnitude of the spanwise diffusion, proportional to κ_z in (3.10), decreases. It is therefore important to investigate the behaviour of the porous layer for $k_x\mathrm{R}_\lambda \gg 1$. The terms of the momentum and energy balances in (3.15) are scaled as in the boundary layer and the parameter

$$K_v = r_p^*\left(\frac{\rho_w^*\omega^*}{\mu_w^*}\right)^{1/2} = R\left(\frac{k_x\mathrm{R}_\lambda}{\mu_w T_w}\right)^{1/2} \gg 1 \tag{3.24}$$

is introduced, where ρ_w^* and μ_w^* are the base-flow density and dynamic viscosity at the wall. The balance equations reveal a boundary-layer structure [Bender and Orszag, 1999] for the velocity and temperature fluctuations, whose values depend on the radial coordinate $r = r^*/r_p^*$, while the pressure is only a function of the axial coordinate y and is the same inside and outside the boundary layer. The outer solutions are obtained by imposing $K_v^{-1} = 0$, for which the full system (3.15) reduces to the equation for the pressure

$$\frac{\mathrm{d}^2\tilde{p}}{\mathrm{d}y^2} + He^2\tilde{p} = 0, \tag{3.25}$$

which arises from a reduction of a Helmholtz equation. The outer solutions for the velocity and pressure fluctuations are found,

$$\tilde{p} = \tilde{p}_{out}(y) = a\cos[He\,(y+1)], \tag{3.26a}$$

$$\tilde{v} = \tilde{v}_{out}(y) = -\mathrm{i}\frac{\mathrm{d}\tilde{p}}{\mathrm{d}y} = \mathrm{i}a\sin\left[He\,(y+1)\right], \tag{3.26b}$$

$$\tilde{\tau} = k_x^2\tilde{\tau}_{out}(y) = k_x^2\,(\gamma-1)\,a\frac{Ma^2L^2}{T_w}\cos\left[He\,(y+1)\right], \tag{3.26c}$$

where a is a real constant and $L = h_p^*/\lambda_z^*$. The pressure and temperature fluctuations are in phase in the outer region. In the proximity of the wall, i.e. where $r-1 \ll 1$, an inner, fast-varying variable

$$r_s = K_v\,(1-r) = O(1) \tag{3.27}$$

describes the inner solutions $\tilde{v}_{in}(r_s, y)$ and $k_x^2\tilde{\tau}_{in}(r_s, y)$. Upon introduction of the inner variable, the momentum and energy balance equations take the form

$$-\mathrm{i}\tilde{v}_{in} + \frac{\mathrm{d}\tilde{p}_{out}}{\mathrm{d}y} = \frac{\partial^2\tilde{v}_{in}}{\partial r_s^2}, \tag{3.28a}$$

$$-\mathrm{i}\tilde{\tau}_{in} + \mathrm{i}\,(\gamma-1)\,\frac{Ma^2L^2}{T_w}\tilde{p}_{out} = \frac{1}{Pr}\frac{\partial^2\tilde{\tau}_{in}}{\partial r_s^2}, \tag{3.28b}$$

subject to the boundary conditions

$$\tilde{v}_{in}(0,y) = \tilde{\tau}_{in}(0,y) = 0, \tag{3.29a}$$

$$\lim_{r_s\to\infty}\tilde{v}_{in}(r_s,y) = \tilde{v}_{out}(y), \tag{3.29b}$$

$$\lim_{r_s\to\infty}\tilde{\tau}_{in}(r_s,y) = \tilde{\tau}_{out}(y). \tag{3.29c}$$

The inner solutions are

$$\tilde{v}_{in}(r,y) = \tilde{v}_{out}(y)\left\{1-\exp\left[\mathrm{i}^{3/2}K_v\,(r-1)\right]\right\}, \tag{3.30a}$$

$$\tilde{\tau}_{in}(r,y) = \tilde{\tau}_{out}(y)\left\{1-\exp\left[\mathrm{i}^{3/2}Pr^{1/2}K_v\,(r-1)\right]\right\}. \tag{3.30b}$$

The solutions (3.30) represent azimuthal Stokes layers of velocity and temperature attached to the pore wall. The cross-sectional averages of the axial velocity (3.30a) and the temperature perturbations (3.30b) over the circular section of a pore are

$$\langle\tilde{v}_{in}\rangle(y) = \tilde{v}_{out}(y)\left[1+2\mathrm{i}\frac{\exp\left(-\mathrm{i}^{3/2}K_v\right)+\mathrm{i}^{3/2}K_v-1}{K_v^2}\right], \tag{3.31a}$$

$$\langle\tilde{\tau}_{in}\rangle(y) = \tilde{\tau}_{out}(y)\left[1+2\mathrm{i}\frac{\exp\left(-\mathrm{i}^{3/2}Pr^{1/2}K_v\right)+\mathrm{i}^{3/2}Pr^{1/2}K_v-1}{PrK_v^2}\right]. \tag{3.31b}$$

Figure 3.5 (left) shows that the agreement between the Bessel-function solutions, given in (3.16), and the asymptotic solution (3.30a) improves as K_v increases, the lines being

indistinguishable for $K_v = 33$. For $K_v \gg 1$, the cross-sectional average of the Bessel-function axial velocity (3.17a) can also be obtained by using the asymptotic expansion for large arguments of the Bessel function. The leading order terms [Abramowitz and Stegun, 1970]

$$J_m(\xi) = \left(\frac{2}{\pi\xi}\right)^{1/2} \cos\left(\xi - \frac{m\pi}{2} - \frac{\pi}{4}\right),\ m = 0, 1, 2, \ldots \tag{3.32}$$

yield

$$\langle \tilde{v}_{in} \rangle (y) = \tilde{v}_{out}(y) \left[1 - \frac{2\cos\left(\mathrm{i}^{1/2} K_v - 3\pi/4\right)}{\mathrm{i}^{1/2} K_v \cos\left(\mathrm{i}^{1/2} K_v - \pi/4\right)}\right]. \tag{3.33}$$

The asymptotic equivalence of the averaged solutions (3.31) and the expansions (3.33) for large K_v is established by recalling the identities $\mathrm{i}^{-1} = -\mathrm{i}$ and $\mathrm{i}^{1/2} = \pm 2^{-1/2}(1 + \mathrm{i})$.

$$\cos\left(\mathrm{i}^{1/2} K_v - \varphi\right) = \frac{1}{2}\exp\left[\pm\mathrm{i}\frac{\sqrt{2}}{2}K_v \mp \frac{\sqrt{2}}{2}K_v - \mathrm{i}\varphi\right] + \\ + \frac{1}{2}\exp\left[\mp\mathrm{i}\frac{\sqrt{2}}{2}K_v \pm \frac{\sqrt{2}}{2}K_v + \mathrm{i}\varphi\right], \tag{3.34a}$$

$$\exp\left(-\mathrm{i}^{3/2} K_v\right) = \exp\left(\mp\mathrm{i}\frac{\sqrt{2}}{2}K_v \pm \frac{\sqrt{2}}{2}K_v\right). \tag{3.34b}$$

The ambiguity on the argument of $\mathrm{i}^{1/2}$ is removed by imposing a bounded velocity for $K_v \gg 1$. Therefore,

$$\frac{\cos\left(\mathrm{i}^{1/2} K_v - 3\pi/4\right)}{\cos\left(\mathrm{i}^{1/2} K_v - \pi/4\right)} \sim \mathrm{i} \tag{3.35}$$

and the two expressions are the same at leading order

$$\underbrace{2\mathrm{i}\frac{\exp\left(-\mathrm{i}^{3/2} K_v\right) + \mathrm{i}^{3/2} K_v - 1}{K_v^2}}_{(3.31)} \sim -\underbrace{\frac{2\cos\left(\mathrm{i}^{1/2} K_v - 3\pi/4\right)}{\mathrm{i}^{1/2} K_v \cos\left(\mathrm{i}^{1/2} K_v - \pi/4\right)}}_{(3.33)} \sim -\frac{2\mathrm{i}}{\mathrm{i}^{1/2} K_v}. \tag{3.36}$$

The real and imaginary parts of (3.17a), (3.33), and (3.30) are normalized with respect to $\tilde{v}_{out}$ and plotted in figure 3.5 (right). The difference between the real parts becomes indiscernible for $K_v > 4$, whereas the imaginary parts match excellently for $K_v > 10$. The ratio

$$\frac{\langle \tilde{v}_{in} \rangle}{\tilde{v}_{out}} = A_v \frac{\tilde{p}}{\tilde{v}_{out}} \tag{3.37}$$

represents a normalized acoustic admittance, where the normalization factor is the large-K_v limit of A_v.

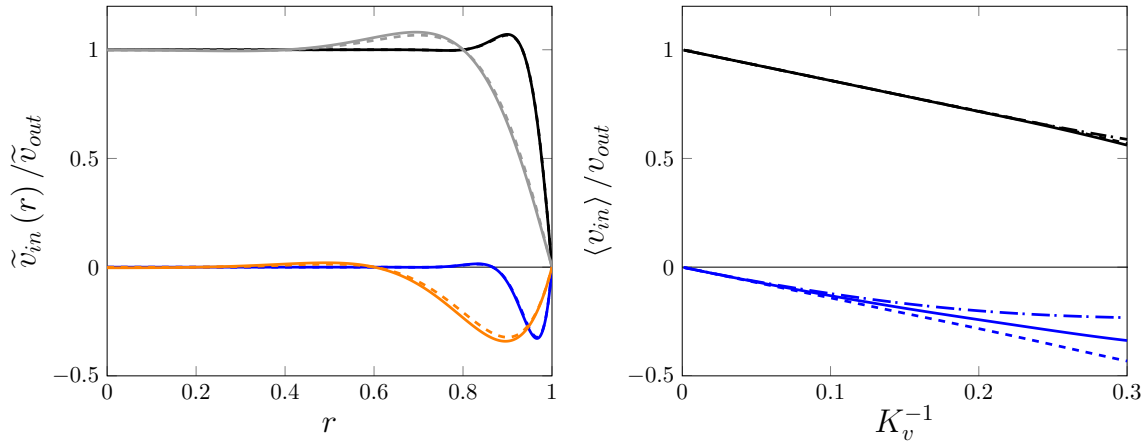

Figure 3.5: Left: radial distribution of the axial velocity within a pore at a given depth for $K_v = 11$ (gray for real part and orange for imaginary part) and $K_v = 33$ (black for real part and dark blue for imaginary part). The Bessel-function solutions (3.16a, solid lines) are compared with the asymptotic solutions (3.30a, dashed lines). Right: averaged Bessel-function solutions (3.16a, solid lines), averaged asymptotic solutions (3.30a, dashed curves), and averaged Bessel-function solutions obtained with the asymptotic form of the Bessel functions for large arguments (3.32, dash-dotted lines). The real and imaginary parts are plotted in black and blue, respectively.

3.1.3.2 Porous admittance

Following Fedorov, Malmuth, et al. [2001], the wall-normal velocity disturbance and the temperature disturbance are related to the pressure disturbance as follows,

$$\tilde{v}(\eta = 0) = A_v \tilde{p}(\eta = 0), \tag{3.38a}$$

$$\tilde{\tau}(\eta = 0) = A_\tau \tilde{p}(\eta = 0), \tag{3.38b}$$

where A_v and A_τ are the complex admittances of the porous wall evaluated at the wall-boundary layer interface ($\eta = 0$). The velocity admittance is

$$A_v = -\theta_f \frac{\mathrm{i}\widetilde{\Lambda}}{L}\left[1 - \mathcal{F}\left(\mathrm{i}^{1/2}K_v\right)\right]\tanh\widetilde{\Lambda}, \tag{3.39}$$

where

$$\widetilde{\Lambda} = \frac{\mathrm{i}k_x MaL}{T_w^{1/2}}\mathcal{H}\left(\mathrm{i}^{1/2}K_v\right), \tag{3.40}$$

$$\mathcal{H}\left(\mathrm{i}^{1/2}K_v\right) = \left\{\frac{1 + (\gamma - 1)\,\widetilde{\mathcal{F}}\left[(\mathrm{i}Pr)^{1/2}K_v\right]}{1 - \widetilde{\mathcal{F}}\left(\mathrm{i}^{1/2}K_v\right)}\right\}^{1/2}, \tag{3.41}$$

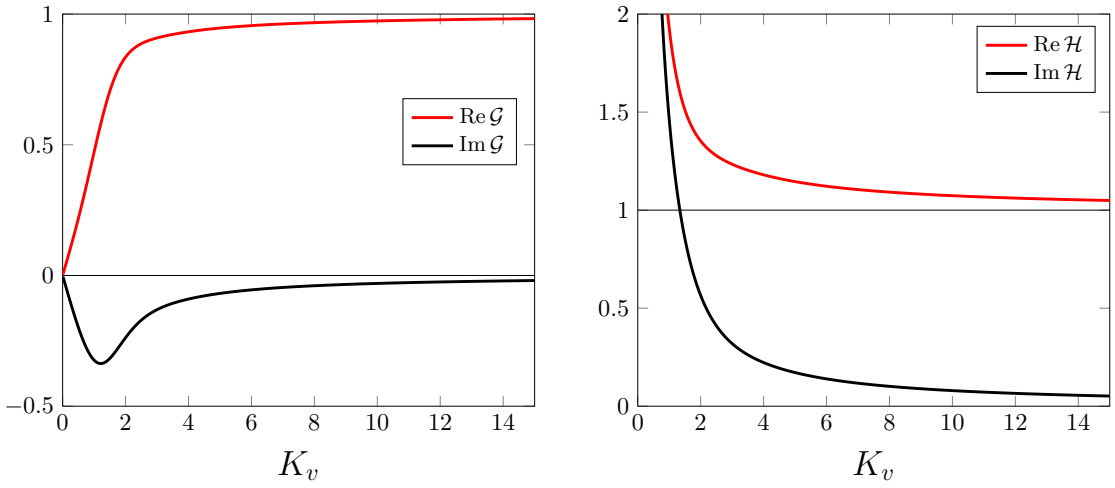

Figure 3.6: Real and imaginary parts of $\mathcal{H}$ and $\mathcal{G}$ as functions of K_v, given by the Bessel-function solutions (3.41) and (3.43), respectively.

and $\widetilde{\mathcal{F}}$ is defined in (3.18). The porosity θ_f is defined as the ratio between the surface area of the pores and the total surface area. By combining (3.39) and (3.40), the admittance of the velocity is rewritten as

$$A_v = \theta_f \frac{k_x Ma}{T_w^{1/2}} \mathcal{G}\left(\mathrm{i}^{1/2} K_v\right) \tanh \Lambda, \tag{3.42}$$

where

$$\mathcal{G}\left(\mathrm{i}^{1/2} K_v\right) = \left[1 - \widetilde{\mathcal{F}}\left(\mathrm{i}^{1/2} K_v\right)\right]^{1/2} \left\{1 + (\gamma - 1)\, \widetilde{\mathcal{F}}\left[(\mathrm{i}Pr)^{1/2} K_v\right]\right\}^{1/2}. \tag{3.43}$$

Figures 3.6a and 3.6b show the real and imaginary parts of $\mathcal{H}$ and $\mathcal{G}$, respectively. The thermal admittance (3.23b) reads

$$A_\tau = (\gamma - 1) \frac{k_x^2 Ma^2 L^2}{T_w} \left\{1 - \widetilde{\mathcal{F}}\left[(\mathrm{i}Pr)^{1/2} K_v\right]\right\}. \tag{3.44}$$

By introducing the expressions of the boundary-layer disturbances (3.9) and by using (3.10), one finds

$$\bar{v}\,(\eta = 0) = \frac{k_x \kappa_z A_v}{(2\bar{x})^{1/2} k_z} \bar{p}\,(\eta = 0) = \left(\frac{k_x}{2\bar{x}\mathrm{R}_\lambda}\right)^{1/2} A_v \bar{p}\,(\eta = 0), \tag{3.45a}$$

$$\bar{\tau}\,(\eta = 0) = \frac{k_x A_\tau}{\mathrm{R}_\lambda} \bar{p}\,(\eta = 0). \tag{3.45b}$$

The wall boundary conditions (3.45a) and (3.45b) are rewritten by using $\overline{A}_v = \left(k_x \mathrm{R}_\lambda^{-1}\right)^{1/2} A_v$ and $\overline{A}_\tau = \left(k_x \mathrm{R}_\lambda^{-1}\right) A_\tau$ in (3.46a) and (3.46b). The velocity admittance A_v defined in (3.42) is $O\left(k_x\right)$ and the thermal admittance A_τ (3.44) is $O\left(k_x^2\right)$.

The coefficients in front of the pressure in (3.45a) and (3.45b) are $O\left(k_x^{3/2}\mathrm{R}_\lambda^{-1/2}\right)$ and $O\left(k_x^3\mathrm{R}_\lambda^{-1}\right)$, respectively. The contribution of A_τ to the temperature fluctuations is thus much weaker than the contribution of A_v to the velocity fluctuations and therefore negligible. However, the porous wall affects the temperature fluctuations indirectly because of the coupling between the wall-normal momentum equation and the energy equation. For typical laminar streaks and Görtler vortices $k_x\mathrm{R}_\lambda = O(1)$, $A_v = O\left(\mathrm{R}_\lambda^{-2}\right)$, $A_\tau = O\left(\mathrm{R}_\lambda^{-4}\right)$, and wall porosity has a negligible effect on both the velocity and temperature fluctuations. As shown in §3.1.3.1 the pores begin interacting with the disturbance flow when $k_x\mathrm{R}_\lambda \gg 1$. Since the pressure and temperature fluctuations are in phase within the pores, the adiabatic boundary condition can be imposed at the wall in accordance with the homogeneous Neumann boundary condition at the dead end of the pores.

3.1.4 Initial and outer boundary conditions

The CLUBR equations are subject to wall and free-stream boundary conditions that synthesize how the boundary layer interacts with the porous wall and the external disturbance flow. Being parabolic along $\bar{x}$, the CLUBR equations also require initial conditions for $\bar{x} \ll 1$. The no-slip wall boundary condition is applied to the streamwise and spanwise disturbance velocities, i.e. $\bar{u} = \bar{w} = 0$ at $\eta = 0$. At the wall, the wall-normal velocity and the temperature are related to the pressure because of the wall porosity, as follows

$$\bar{v}(\eta = 0) = \frac{\overline{A}_v}{(2\bar{x})^{1/2}}\bar{p}(\eta = 0), \tag{3.46a}$$

$$\bar{\tau}(\eta = 0) = \frac{\overline{A}_\tau}{(2\bar{x})^{1/2}}\bar{p}(\eta = 0), \tag{3.46b}$$

where $\overline{A}_v$ and $\overline{A}_\tau$ are the scaled admittances, obtained in §3.1.3.2. The free-stream boundary conditions are the same as in Ricco and X. Wu [2007],

$$\{\bar{u},\, \bar{\tau}\} \to 0, \tag{3.47a}$$

$$\left(\frac{\partial}{\partial\eta} + |\kappa_z|(2\bar{x})^{1/2}\right)\{\bar{v},\, \bar{w},\, \bar{p}\} \to \left\{-1,\, \mathrm{i}\kappa_y(2\bar{x})^{1/2},\, 0\right\}\cdot \cdot \mathrm{e}^{\mathrm{i}\left(\bar{x}+\kappa_y(2\bar{x})^{1/2}\bar{\eta}\right)-\left(\kappa_y^2+\kappa_z^2\right)\bar{x}}, \tag{3.47b}$$

as $\eta \to \infty$, where $\bar{\eta} \equiv \eta - \beta_c$, and $\beta_c = \lim_{\eta\to\infty}(\eta - F)$. The wall-normal wavenumber κ_y only appears in (3.47) and not in the CLUBR equations because the wall-normal

length scale of the free-stream flow is λ_y^*, while, within the boundary layer, the characteristic length scale is the boundary-layer thickness.

The initial conditions are the same as those in Ricco and X. Wu [2007]. Since they are not compatible with a non-zero wall-normal velocity at $\eta = 0$, a short smoothing region is introduced along the streamwise direction, spanning between two streamwise coordinates, $\bar{x}_1$ and $\bar{x}_2$, in the vicinity of the leading edge. In this region, the velocity admittance varies proportionally to [Negi et al., 2015]

$$S(\bar{x}) = \begin{cases} 0, & \text{for } \bar{x} \leq \bar{x}_1, \\ \left[1 + \exp\left(\dfrac{1}{\tilde{x}-1} + \dfrac{1}{\tilde{x}}\right)\right]^{-1}, & \text{for } \bar{x}_1 < \bar{x} < \bar{x}_2, \\ 1, & \text{for } \bar{x} \geq \bar{x}_2, \end{cases} \tag{3.48}$$

where $\tilde{x} = (\bar{x} - \bar{x}_1)/(\bar{x}_2 - \bar{x}_1)$, and $\bar{x}_1 = 0.005$. The end point is $\bar{x}_2 = 0.01$, if exception is made for the analysis at the end of §3.2.1, where the effect of $\bar{x}_2$ is studied. The piecewise function (3.48) can be physically interpreted as a variation of the wall porosity along the smoothing region. The pores are assumed to be aligned in equally spaced rows and columns, such variation may be caused by pores of constant radius r_p^* becoming more and more packed as the distance d^* between the centres of adjacent pores decreases, or by the gradual increase of the pore radius. In both cases, the porosity in (3.42) can be written as $\theta_f = \pi R_f^{*2} S(\bar{x})/d_f^{*2}$, where the subscript f denotes quantities at the downstream end of the smoothing region. If the radius is kept constant between $\bar{x}_1$ and $\bar{x}_2$, the interpore distance is $d^*(\bar{x}) = d_f^*/\sqrt{S(\bar{x})}$. The porosity at the end of the smoothing region is thus $\theta_f = \pi R_f^{*2}/d_f^{*2}$. As only regularly-spaced circular pores are considered, the porosity may attain a maximum theoretical value of $\pi/4$ when $R_f^* = d_f^*/2$.

The base-flow solutions (3.2) are computed using a second-order accurate block-elimination algorithm [Cebeci, 2002]. The CLUBR system is solved by a second-order finite-difference scheme that is central in η and backward in $\bar{x}$. The free-stream boundary conditions (3.47) are applied by a second-order finite-difference discretization scheme. The pressure is computed on a grid staggered along the η direction with respect to that for the velocity in order to avoid the pressure decoupling phenomenon.

3.2 Results

The effectiveness of the porous wall depends on its ability to transduce a pressure disturbance into a wall-normal velocity disturbance, as described by (3.45a). In the present coatings, the phase velocity of the disturbances is equivalent to the local

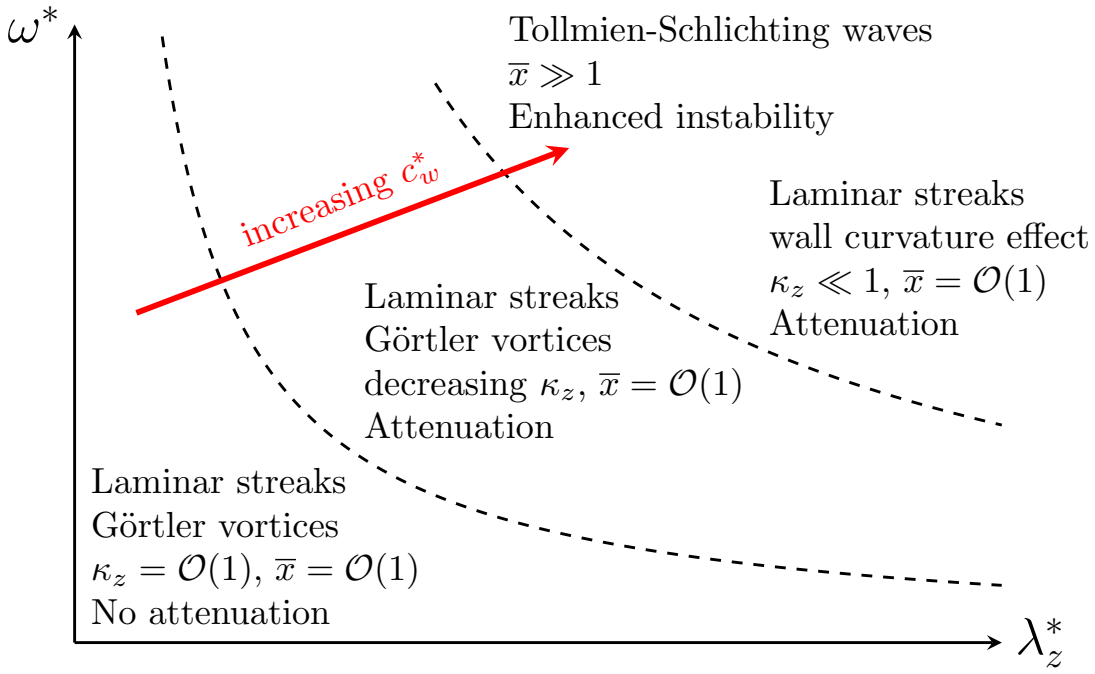

Figure 3.7: Schematic of flow regimes and the effect of wall porosity, as described by relation (3.50).

sound speed [Brès et al., 2013]. For $K_v \gg 1$, a dimensional analysis of the boundary condition (3.45a) and the velocity admittance (3.42) yields

$$\frac{\bar{v}}{\bar{p}} = O\left[\left(\frac{k_x^3}{R_\lambda}\right)^{1/2} \frac{Ma}{T_w^{1/2}}\right] = O\left(\frac{\omega^{*3/2}\lambda_z^*}{U_\infty^* c_w^*}\nu_\infty^{*1/2}\right). \tag{3.49}$$

where c_w^* is defined in (3.13). As a result, the pores interact with the boundary layer when

$$\omega^{*3/2}\lambda_z^* \text{ is comparable with } U_\infty^* c_w^* \nu_\infty^{*-1/2}. \tag{3.50}$$

A visual representation of relation (3.50) is shown in figure 3.7. The free-stream velocity, the free-stream kinematic viscosity and the speed of sound in the porous layer define the threshold above which the boundary-layer disturbances are affected by the porous layer. For given free-stream conditions, the effect of the porous layer is more intense at lower c_w^*. For a given λ_z^* and constant free-stream conditions, the minimum frequency at which a disturbance is affected scales as $T_w^{*1/3}$. The minimum wavelength for which a disturbance is attenuated at a given frequency increases as $T_w^{*1/2}$. Both hyperbolas shift away from the origin as c_w^* increases. Relation (3.50) also shows that the variation of the frequency is more influential on the performance of the porous wall than that of the spanwise wavelength.

Physical parameter	Symbol	Value	SI unit
Mach number	Ma	6	-
Total (stagnation) temperature	T_0^*	400	K
Static pressure	p_∞^*	633	Pa
Static temperature	T_∞^*	49	K
Free-stream velocity	U_∞^*	841	$\mathrm{m\,s^{-1}}$
Free-stream kinematic viscosity	ν_∞^*	$6.3 \cdot 10^{-5}$	$\mathrm{m^2/s}$
Unit Reynolds number	$\mathrm{R}^* = U_\infty^*/\nu_\infty^*$	$13.5 \cdot 10^6$	$\mathrm{m^{-1}}$
Recovery temperature	$T_{a,w}^*$	343	K
Wall temperature	$T_w^* = 0.8 T_{a,w}^*$	274	K
Pore radius	r_p^*	90	µm
Inter-pore distance	d^*	210	µm
Pore depth	h_p^*	1.5	mm
Porosity	θ_f	0.58	-
Velocity admittance	$\overline{A}_v$	$(-0.88 + 1.43\,\mathrm{i}) \cdot 10^{-3}$	-

Table 3.1: Physical parameters for wind tunnel conditions.

The physical parameters of the present study are listed in table 3.1. These values are representative of supersonic quiet tunnel conditions, such as those of the Sandia Hypersonic wind tunnel and the Boeing Mach 6 quiet tunnel [Casper et al., 2009]. The stagnation temperature of 400 K and the wall-temperature ratio of $T_w^*/T_{ad,w}^* = 0.8$ (where $T_{ad,w}^*$ is the adiabatic-wall temperature) are given by Shiplyuk et al. [2004], Casper et al. [2009], and Schneider [2008a] and Yu et al. [2018].

3.2.1 Laminar streaks

The solution of the CLUBR equations for a flat-plate boundary layer is computed for a wide range of disturbance frequencies and spanwise wavelengths. Two wall-porosity conditions are considered: a solid plate with $\theta_f = 0$ and a porous plate with $\theta_f = 0.58$.

Our computations reveal that the wall porosity does not affect the growth of the laminar streaks for very low frequencies and very short spanwise wavelengths ($k_x \mathrm{R}_\lambda = O(1)$, $\kappa_z = O(1)$). Under these conditions, the spanwise viscous diffusion plays a significant role because λ_z^* is comparable to the boundary-layer thickness δ^*, which is typically a few millimeters [Laufer and Vrebalovich, 1960; Demetriades, 1985; Graziosi, 1999; Graziosi and G. L. Brown, 2002]. The spectrum of free-stream disturbances is however wide and encompasses a wide range of spanwise wavelenghts and frequencies. Then, the response of the boundary layer to free-stream gusts with spanwise wavelengths that are larger than the boundary-layer thickness, i.e. $\lambda_z^* = 0.03\,\mathrm{m}$ and $\mathrm{R}_\lambda = \mathrm{R}^* \lambda_z^* = 418000$, is investigated. As $k_x \mathrm{R}_\lambda$ increases and κ_z

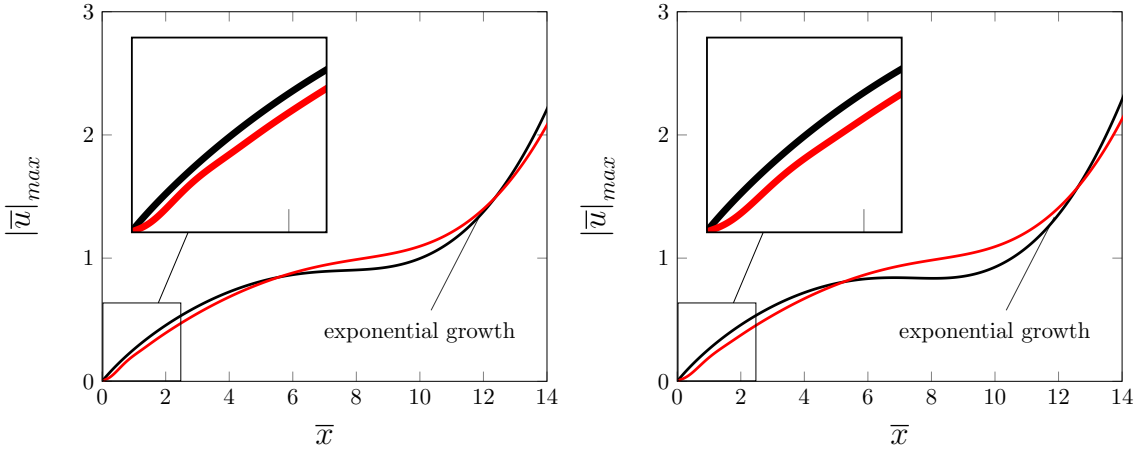

(a) $\kappa_z = 0.008$, $k_x/k_z = 0.24$.

(b) $\kappa_z = 0.0075$, $k_x/k_z = 0.27$.

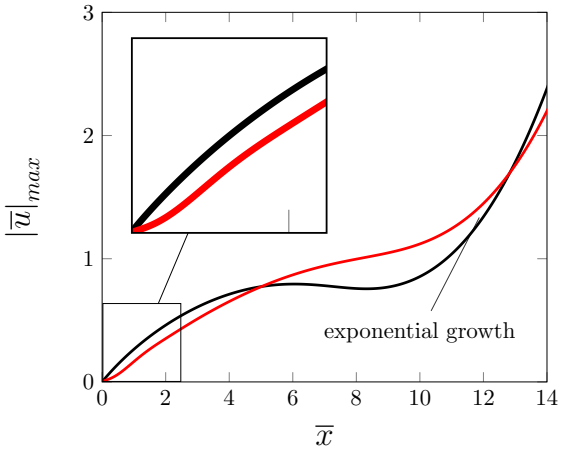

(c) $\kappa_z = 0.007$, $k_x/k_z = 0.31$.

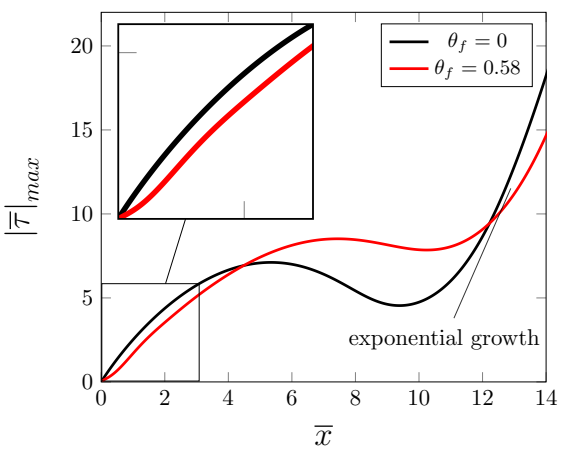

(d) $\kappa_z = 0.007$, $k_x/k_z = 0.31$.

Figure 3.8: Effect of the frequency on the attenuation streamwise velocity (figures 3.8a, 3.8b, 3.8c) and temperature 3.8d) for $\lambda_z^* = 0.03\,\mathrm{m}$ ($\mathrm{R}_\lambda = 418000$) at $\omega^*/2\pi = 6730\,\mathrm{Hz}$ (3.8a), $\omega^*/2\pi = 7570\,\mathrm{Hz}$ (3.8b) and $\omega^*/2\pi = 8600\,\mathrm{Hz}$ (3.8c-3.8d). The solid ($\theta_f = 0$) and porous ($\theta_f = 0.58$) wall cases are represented with black and red curves, respectively.

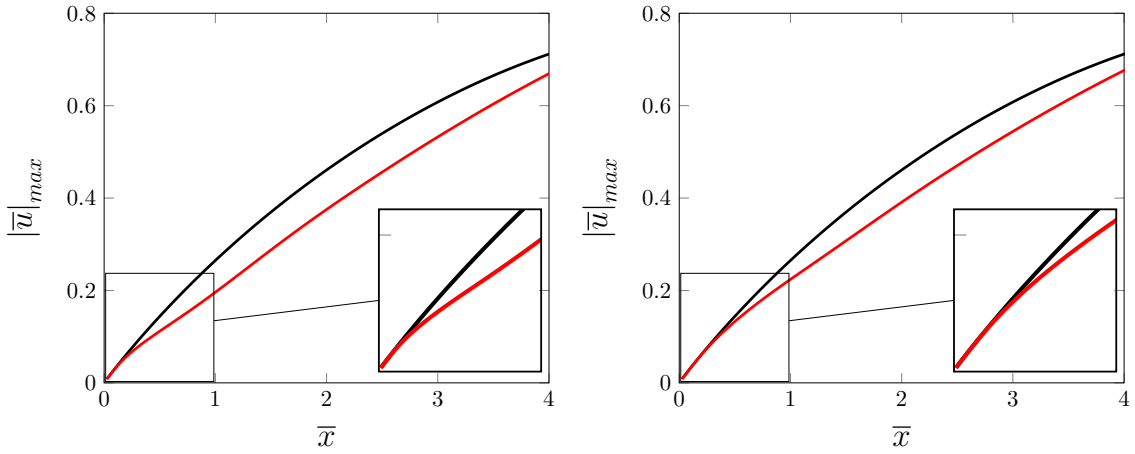

(a) $\bar{x}_2 = 0.5$ (b) $\bar{x}_2 = 1$

Figure 3.9: Effect of the length of the adjustment region in the vicinity of the leading edge on the attenuation of the laminar streaks. $\bar{x}_1 = 0.005$ is kept constant and $\bar{x}_2$ is increased to 0.5 (figure 3.9a) and 1 (figure 3.9b). The solid ($\theta_f = 0$) and porous ($\theta_f = 0.58$) wall cases are represented by the black and red curves, respectively.

decreases, the effect of the porous wall becomes relevant. Its response to increasing the disturbance frequency is reported in figures 3.8a, 3.8b, and 3.8c, which show the downstream evolution of the peak of the streamwise velocity fluctuations, $|\bar{u}|_{max}$, for $\kappa_z = 0.008, 0.0075$ and 0.007, respectively. Under these conditions, the scaled admittance $\overline{A}_v$ is $-8.82 \cdot 10^{-4} + 1.434 \cdot 10^{-3}$ i. The growth of the laminar streaks is reduced by the porous wall up to about $\bar{x} = 5$. The peak of the temperature fluctuations, shown in figure 3.8d for $\kappa_z = 0.007$, is also reduced. The attenuation becomes more significant as ω^* increases and κ_z decreases, meaning that the pores absorb and dissipate the energy of the laminar streaks when the spanwise diffusion is small. The effectiveness of the porous layer is expected to improve at frequencies higher than those considered here. However, increasing k_x beyond 0.3 might lead to a regime for which the second-order perturbation discussed in §3.1.2 becomes important. The growth of the streamwise velocity and temperature fluctuations becomes exponential further downstream, where the receptivity of highly-oblique Tollmien-Schlichting waves sets in. This regime is studied in Ricco and Fossà [2023b].

The results reported in figure 3.8 were computed by considering the leading-edge adjustment region given by equation (3.48) and extending between $\bar{x}_1 = 0.005$ and $\bar{x}_2 = 0.01$. The same case with $\kappa_z = 0.007$ and $\mathrm{R}_\lambda = 418000$ is computed for larger $\bar{x}_2$, i.e. $\bar{x}_2$=0.5 (figure 3.9a) and $\bar{x}_2$=1 (figure 3.9b). The growth of the laminar streaks is shown in figure 3.9. Extending of the length of the adjustment region results in a

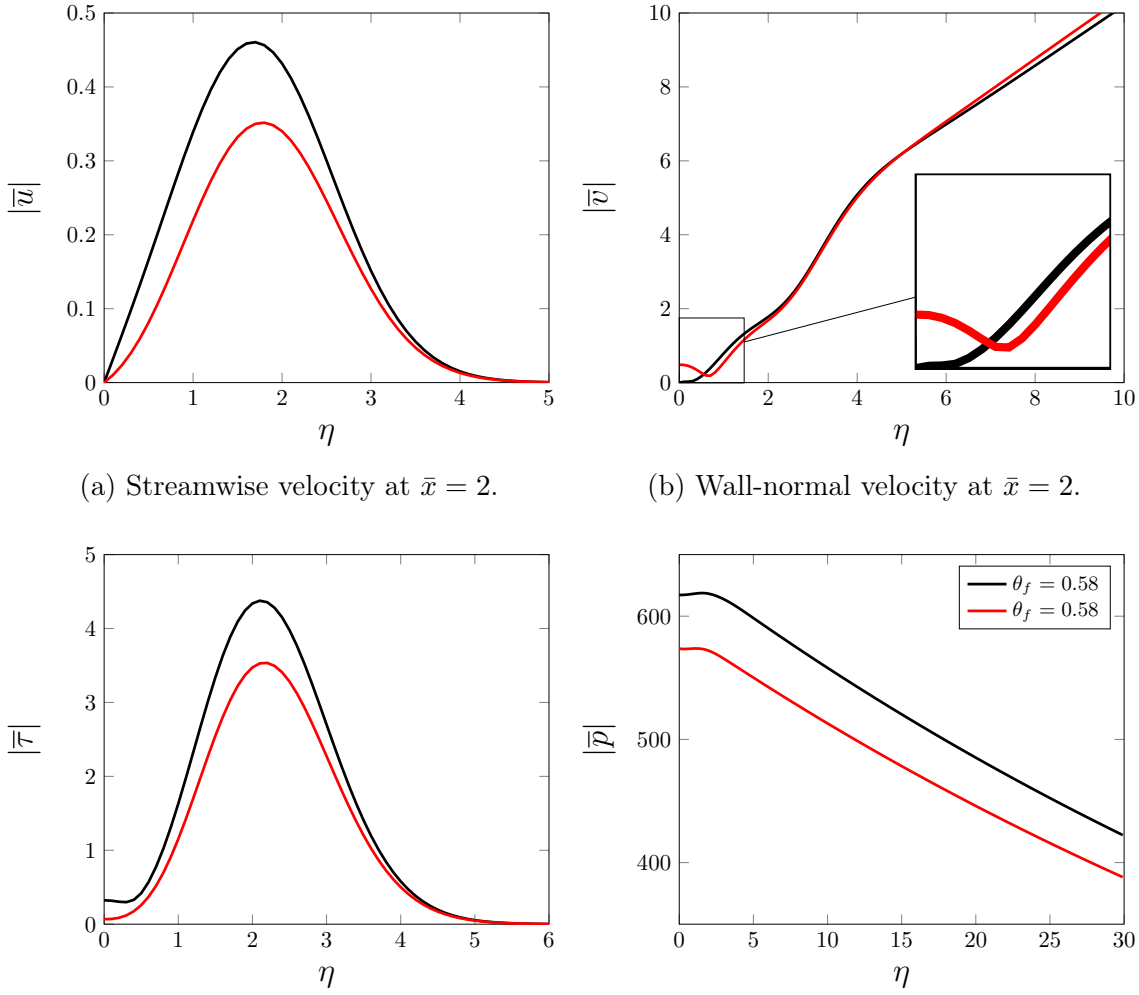

(a) Streamwise velocity at $\bar{x} = 2$.

(b) Wall-normal velocity at $\bar{x} = 2$.

(c) Temperature at $\bar{x} = 2$.

(d) Pressure at $\bar{x} = 2$.

Figure 3.10: Wall-normal profiles of the streamwise velocity (3.10a), spanwise velocity (3.10b), temperature (3.10c), and pressure (3.10d) disturbances at $\bar{x} = 2$ for $k_z/k_x = 0.3$, $\kappa_z = 0.007$, and $\mathrm{R}_\lambda = 418000$. The solid ($\theta_f = 0$) and porous ($\theta_f = 0.58$) wall cases are represented with black and red curves, respectively.

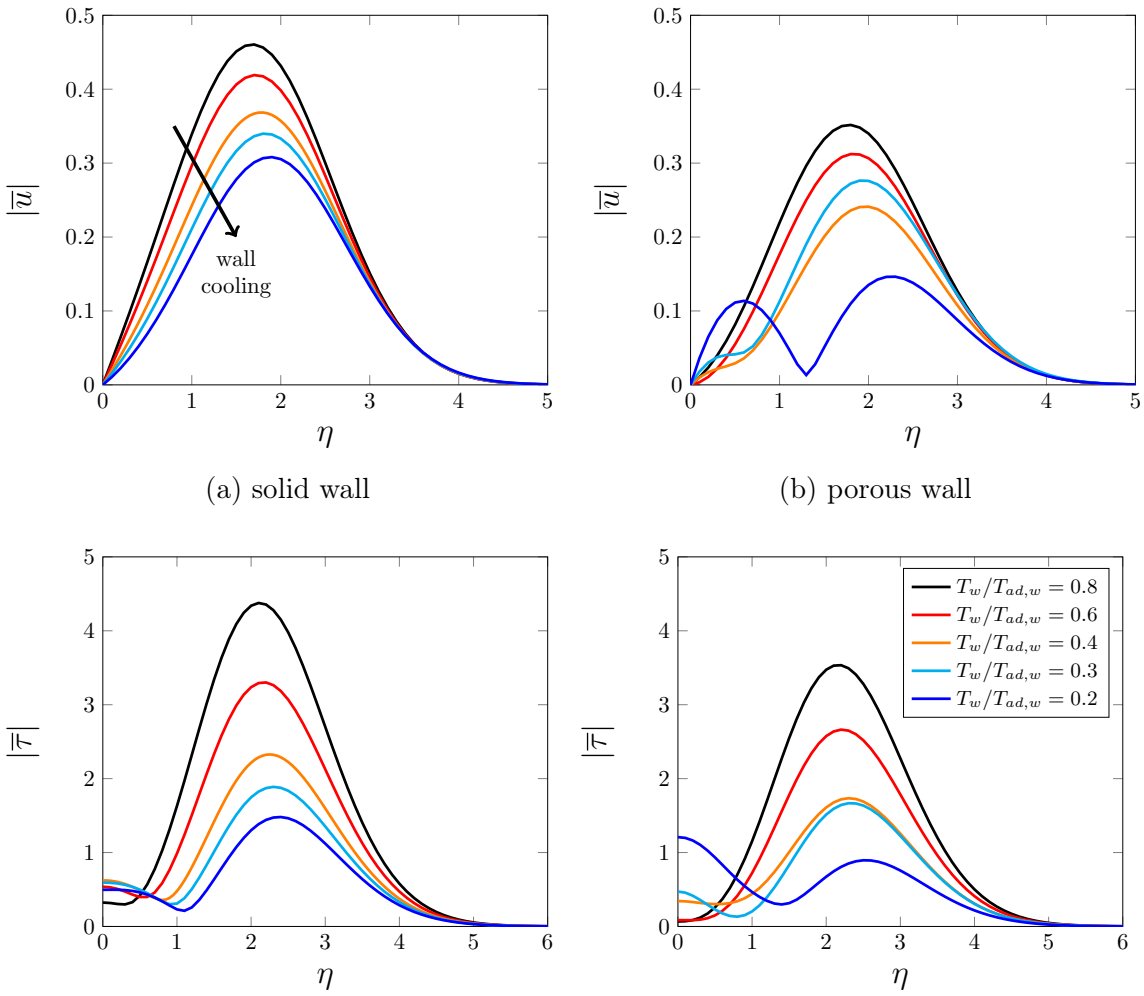

(a) solid wall

(b) porous wall

(c) solid wall

(d) porous wall

Figure 3.11: Effect of wall cooling on the streamwise velocity (top) and temperature (bottom) three-dimensional gust signatures profiles at $\bar{x} = 2$ for $k_x/k_z = 0.3$, $\kappa_z = 0.007$, and $\mathrm{R}_\lambda = 418000$.

delay of the attenuation. Albeit delayed, the damping of the laminar streaks is still appreciable in the region $\bar{x} \leq 4$.

More insights on the effect of wall porosity on the laminar streaks for $\kappa_z \ll 1$ can be inferred from the wall-normal profiles of the velocity components, the temperature and the pressure. The profiles for $|\bar{u}|$, $|\bar{v}|$, $|\bar{\tau}|$, and $|\bar{p}|$ at $\bar{x} = 2$ for the case $\kappa_z = 0.007$, $\mathrm{R}_\lambda = 418000$ are shown in figure 3.10. The streamwise velocity, the temperature, and the pressure are markedly reduced by the porous wall. The peaks of $|\bar{u}|$ and $|\bar{\tau}|$ are decreased and slightly shifted farther from the wall. The wall-normal gradient of $|\bar{u}|$ is attenuated by the porous layer. The wall-normal velocity component $|\bar{v}|$ is enhanced in the proximity of the wall (inset of figure 3.10b), but is mostly unaffected at larger wall-normal locations. The spanwise velocity component (not shown) is unchanged, which is consistent with the spanwise momentum balance being independent of $\bar{u}$, $\bar{v}$, $\bar{\tau}$ and $\bar{p}$ when $\kappa_z \ll 1$ [Ricco and X. Wu, 2007]. The pressure distribution retains its shape and is uniformly attenuated when the wall is porous.

The results of figure 3.8 are computed at a fixed wall temperature ratio $T_w/T_{ad,w} = 0.8$. As shown in the schematic of relation (3.50) of figure 3.7, the theory indicates that a lower wall temperature increases the range of ω^* and λ_z^* for which the pressure fluctuations are effectively transduced into wall-normal velocity fluctuations. The wall-normal profiles for the boundary-layer fluctuations at $Ma = 6$, $\kappa_z = 0.007$ and $\mathrm{R}_\lambda = 418000$ are computed for five different wall temperature ratios $T_w/T_{ad,w}$ and reported in figure 3.11. The graphs in the top row show the $|\bar{u}|$-profiles over solid (figure 3.11a) and porous (figure 3.11b) flat plates. Wall cooling uniformly reduces the amplitude of the velocity and temperature fluctuations in the solid and porous cases.

In the solid-wall case, wall cooling causes the peak of the wall-normal profiles to shift farther from the wall, the wall-shear stress is attenuated, and the temperature fluctuations are reduced more than the velocity fluctuations, with the exception of the near-wall region where they slightly increase. The effect of wall cooling is more intense on the temperature fluctuations than on the velocity fluctuations when the wall-temperature ratio is reduced from 0.8 to 0.4. When the wall is porous, an inflection point appears close to the wall for $T_w/T_{ad,w} = 0.4$, and a second shorter peak in the velocity distribution arises in the near-wall region between $T_w/T_{ad,w} = 0.3$ and $T_w/T_{ad,w} = 0.2$. Although the amplitude of the main velocity peak in the porous case is reduced by wall cooling, the wall-shear stress increases and the intensity of the secondary temperature peak, located at the wall, exceeds that of the main temperature peak.

3.2.2 Tollmien-Schlichting waves

For low κ_z values, the initial algebraic growth of the compressible laminar streaks is followed downstream by the exponential growth of highly-oblique Tollmien-Schlichting (TS) waves, a receptivity mechanism first discovered by Ricco and X. Wu [2007]. Numerical evidence of this receptivity mechanism is shown in figure 3.8 for $\bar{x} > 6$, where the exponential growth occurs. Although the amplitude of the laminar streaks is attenuated, the porous wall enhances the initial amplitude of the TS waves, as also schematically illustrated in figure 3.7. The present numerical result confirms the experimental findings of Shiplyuk et al. [2004] and Lukashevich et al. [2018]. The theoretical results of Michael and Stephen [2012] also reported a larger TS-wave growth rate, although the receptivity was not included in their analysis.

The onset of the oblique TS waves is caused by the receptivity mechanism described by Ricco and X. Wu [2007]. Unsteady free-stream perturbations excite quasi three-dimensional Lam-Rott boundary-layer eigensolutions [Lam and Rott, 1960], which develop downstream together with the laminar streaks. Goldstein [1983] first discovered that these low-amplitude decaying eigensolutions, believed until then to be innocuous for the flow instability, can turn into exponentially growing TS waves. For relatively high-frequency acoustic oscillations, Goldstein [1983] proved that the wavelength shortening of these eigensolutions indeed causes the generation of a streamwise pressure gradient that is responsible for the instability. Ricco and X. Wu [2007] instead showed that, in the low-frequency regime proper of the laminar streaks, a spanwise pressure gradient is induced. This pressure gradient interferes with the viscous flow by engendering a spanwise velocity component. As this component reaches the order of magnitude of the streamwise and wall-normal velocity ones, a triple-deck interacting regime sets in and a spatially-growing oblique TS wave is triggered. This receptivity mechanism is similar to the leading-edge adjustment discovered by Goldstein [1983] in that the Lam-Rott eigensolution is central for the boundary-layer dynamics. Yet, it is different because the spanwise pressure gradient is responsible for triggering the instability, while the streamwise pressure gradient is negligible. In the case of a porous wall, the wall-normal velocity near the wall is not only altered through continuity by the spanwise velocity generated by the induced spanwise pressure gradient, but also by the wall pressure via the admittance relationship (3.46a).

The triple-deck theory has the advantage of revealing the physical mechanism responsible for engendering the first-mode growth, while this result is not achieved by performing finite-Reynolds-number stability analysis or by solving the complete Navier-Stokes equations. The triple-deck analysis predicts the growth rate and the

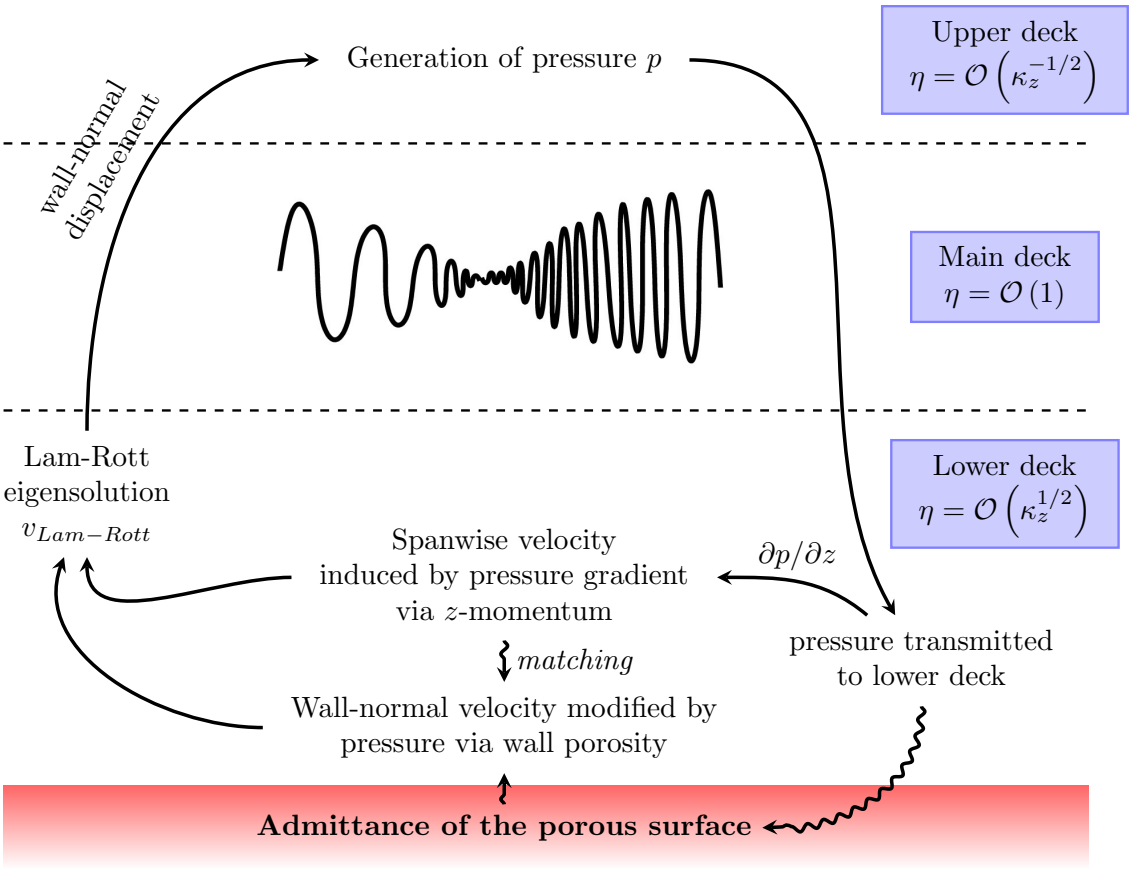

Figure 3.12: Schematic of the triple-deck interactive regime.

wavenumber of the TS instability in the solid and the porous cases, while the CLUBR solutions also give the onset of the instability.

The triple-deck analysis of Ricco and X. Wu [2007] was modified to investigate how a porous surface alters the dynamics of exponentially growing unstable waves [Ricco and Fossà, 2023b]. Analogously to Ricco and X. Wu [2007], an asymptotic eigensolution of the CLUBR equations is sought in the limits $\kappa_z \ll 1$ and $\overline{x} \gg 1$. The relevant class of eigensolutions is the one discovered by Lam and Rott [1960] (refer also to Ackerberg and Phillips [1972]). These eigensolutions are proportional to $\exp(-\hat{\psi}\overline{x}^{3/2})$, where $\hat{\psi}$ is an unknown complex eigenvalue [Ackerberg and Phillips, 1972; Goldstein, 1983]. The eigensolutions are governed by the boundary-layer equations and the pressure disturbances need not be solved [LWG99]. The boundary layer splits up into two decks: a main deck and a thin near-wall lower-deck. A triple-deck interactive regime ensues because the wall-normal displacement induced downstream by the perturbation generates an unsteady pressure (see §5.2 in Ricco and X. Wu [2007] for details). This interactive regimes occurs where

$$\overline{x} = \mathcal{O}\left(\kappa_z^{-1}\right). \tag{3.51}$$

The decaying Lam-Rott perturbation evolves into a spatially growing, highly oblique TS wave at the locations specified by (3.51) when $k_x = O(\mathrm{R}_\lambda^{-1/5})$, or $\kappa_z = O(\mathrm{R}_\lambda^{-2/5})$ for (3.10b). As the induced pressure disturbance now plays an active role, the porosity of the wall affects the flow field. The streamwise coordinate

$$x_1 = \kappa_z \overline{x} = O(1) \tag{3.52}$$

can be introduced because of (3.51) and $\kappa_z \ll 1$. An interactive triple-deck structure emerges, consisting of a lower deck $\eta = O(\kappa_z^{1/2})$, a main deck $\eta = \mathcal{O}(1)$, and an upper deck $\eta = O(\kappa_z^{-1/2})$. An exponentially-growing solution is assumed for each deck

$$\{\overline{u},\overline{v},\overline{w},\overline{p},\overline{\tau}\}_{LD} = \\ = \left\{u_1(x_1,\eta), v_1(x_1,\eta), \frac{w_1(x_1,\eta)}{\kappa_z^{1/2}}, \frac{p_1(x_1)}{\kappa_z^{5/2}}, \kappa_z^{1/2}\tau_1(x_1,\eta)\right\} E + \ldots \tag{3.53a}$$

$$\{\overline{u},\overline{v},\overline{w},\overline{p},\overline{\tau}\}_{MD} = \left\{u_1(x_1,\eta), \frac{v_1(x_1,\eta)}{\kappa_z^{1/2}}, w_1(x_1,\eta), \frac{p_1(x_1)}{\kappa_z^{5/2}}, \tau_1(x_1,\eta)\right\} E + \ldots \tag{3.53b}$$

$$\{\overline{u},\overline{v},\overline{w},\overline{p},\overline{\tau}\}_{UD} = \left\{u_1(x_1,\eta), \frac{v_1(x_1,\eta)}{\kappa_z^{1/2}}, w_1(x_1,\eta), \frac{p_1(x_1)}{\kappa_z^{5/2}}, 0\right\} E + \ldots \tag{3.53c}$$

where the growth factor

$$E = \exp\left(\frac{\mathrm{i}}{\kappa_z^{1/2}} \int_0^{\overline{x}} \alpha_1(x_1)\mathrm{d}\breve{x}\right), \tag{3.54}$$

is defined on the complex eigenvalue $\alpha_1(x)$. A dispersion relation for $\alpha_1(x_1)$ is obtained by matching the main deck solution (3.53b) to the lower (3.53a) and upper deck solutions (3.53c)

$$\Delta(x_1,\alpha_1) \equiv \int_{\eta_0}^{\infty} \mathrm{Ai}(\breve{\eta})\mathrm{d}\breve{\eta} - \left(\frac{\mu_w}{2\alpha_1 x_1 T_w}\right)^{1/3} \frac{(\mathrm{i}F''(0))^{5/3}\,\mathrm{Ai}'(\eta_0)}{\mathrm{i}\widetilde{A}_v\alpha_1 F''(0) - (2x_1)^{1/2}T_w^2} = 0, \quad (3.55)$$

where

$$\eta_0 = \frac{(2\mathrm{i}x_1 T_w)^{1/3}}{[\alpha_1 F''(0)]^{2/3}\,\mu_w^{1/3}}. \quad (3.56)$$

For the derivation of (3.55) the reader is referred to Ricco and Fossà [2023b]. The admittance $\widetilde{A}_v$ in (3.55) is absent in the dispersion relation as $x_1 \to 0$, so $\mathrm{Ai}'(\eta_0) \to 0$ as $x_1 \to 0$. Equation (3.55) reduces to the dispersion relation found by Ricco and X. Wu [2007] for a solid wall when $\widetilde{A}_v = 0$. The Airy function and its derivative are computed by an in-house code, based on the method of Gil et al. [2002]. The growth rate and the wavenumber are given by $-\mathrm{Im}(\alpha_1)/\kappa_z^{1/2}$ and $\mathrm{Re}(\alpha_1)/\kappa_z^{1/2}$, respectively, and are also found numerically from the CLUBR equations as $\mathrm{Re}(\overline{u}_{\bar{x}}/\overline{u})$ and $\mathrm{Im}(\overline{u}_{\bar{x}}/\overline{u})$ (where the subscript $\overline{x}$ indicates the derivative).

The solutions have been first computed for $\tilde{A}_v = \mathcal{O}(1)$ and Ma=2, 3, and 4 on an adiabatic wall. The free-stream disturbances are assumed to be the same in all cases and a porous wall of fixed R^*, θ_f and H^* is considered. The Mach number and Reynolds number vary together as the free-stream velocity U_∞^* increases. The wavenumber and growth rate of the CLUBR solutions and the triple-deck solutions are compared in figure 3.13 for $\kappa_z = 0.0005$ at $Ma = 2$, 3 and 4. The growth rate, which is mildly negative upstream, suddenly increases as the TS waves are triggered, while the wavenumber settles to an almost constant value. The agreement between the CLUBR solutions (solid lines) and the triple-deck solutions (dashed lines) improves as the Mach number increases. The porous wall enhances the TS-wave growth rate and shifts the onset of the instability upstream, while the wavenumber is unaffected. The impact of the porous wall, however, diminishes as the Reynolds and Mach numbers increase with the free-stream velocity. For the flow conditions studied in figure 3.13, no effect of the porous wall is found at $Ma = 6$.

The case investigated in §3.2.1 is also studied ($Ma = 6$, $\kappa_z = 0.007$, $T_w = 0.8T_{ad,w} = 5.62$, $\tilde{A}_v = -18.00 + 29.26$ i). As per definition (3.52), the onset of the TS waves shifts upstream over both the porous and the solid surfaces when κ_z increases slightly. The boundary-region and the triple-deck results, shown in figure 3.14, still show a satisfactory agreement for a relatively larger κ_z and $\bar{x} > 14$. The

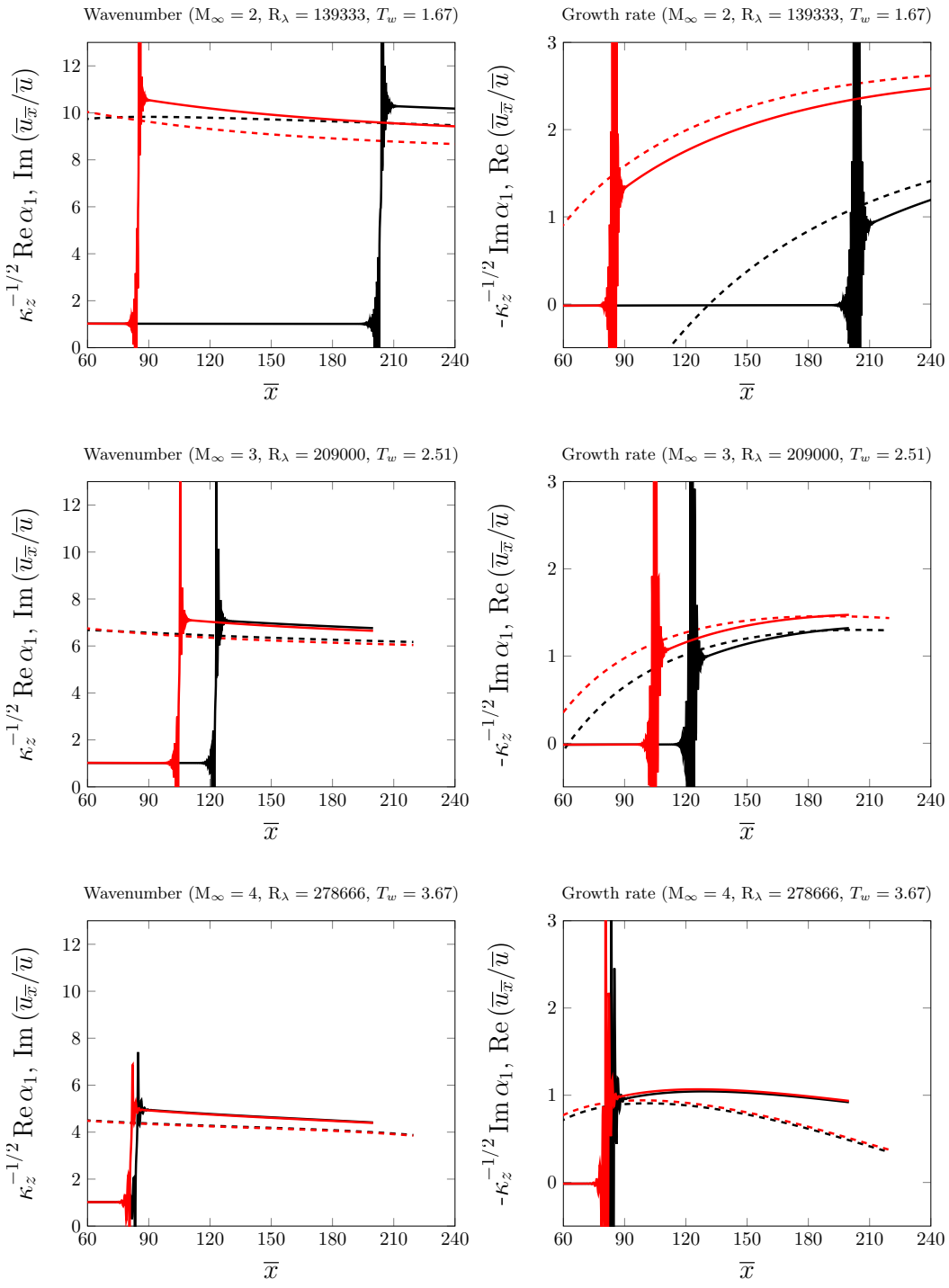

Figure 3.13: Onset of the oblique TS waves far downstream for $\kappa_z = 0.0005$ on solid (black) and porous (red) walls. The solid lines indicate the boundary-region solutions and the dashed lines denote the triple-deck solutions. The three free-stream conditions at different Mach numbers are simulated by varying the free-stream velocity U_∞^* on adiabatic wall conditions.

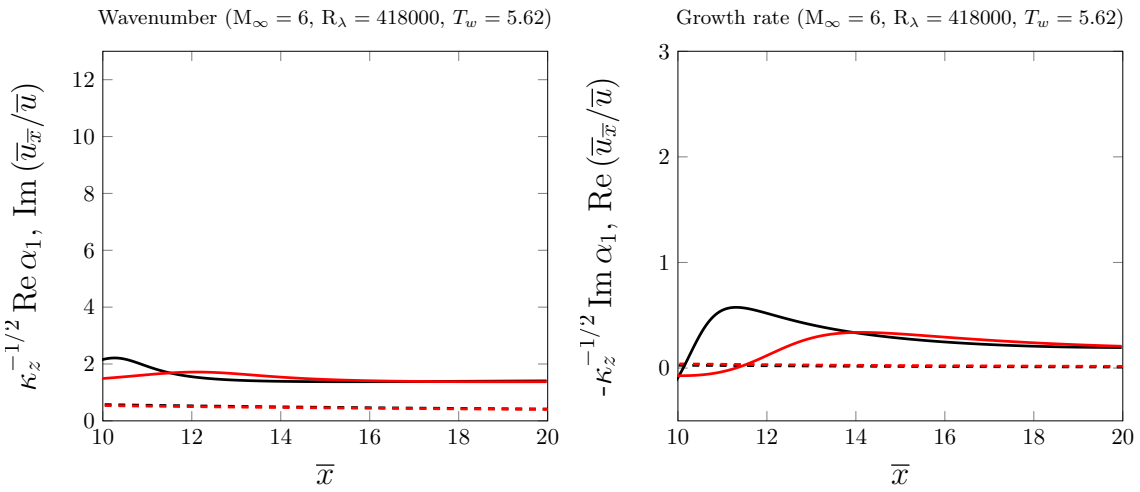

Figure 3.14: Onset of the oblique TS waves for $\kappa_z = 0.007$ on solid (black) and porous (red) walls. The solid lines indicate the boundary-region solutions and the dashed lines the triple-deck solutions. The results are computed for the flow conditions discussed in §3.2.1: $Ma = 6$, $T_w = 5.62$ and $\kappa_z = 0.007$.

porous wall has an intense effect on the growth rate before the exponential growth of the TS waves sets in. Once the TS-wave growth is established, the effect of porosity is mild.

3.2.3 Effect of wall curvature at moderate Görtler number

The combined effect of wall porosity and wall curvature is considered. As proved by Hall [1983], in the limit of large Reynolds number and large curvature radius, the curvature does not affect the base flow and the centrifugal effects are distilled in two terms in the wall-normal momentum equation (3.11c) that are proportional to $\widehat{G}$. The evolution of the boundary-layer perturbations was computed for $\kappa_z = 0.007$, $R_\lambda = 418000$, $Ma = 6$ and two different Görtler numbers, $\widehat{G} = 2.41$ and $\widehat{G} = 12$, which correspond to $r_c = 100$ and $r_c = 20$, respectively. Under these conditions, the effect of curvature enhances the growth of the velocity disturbances compared to the flat-plate case. Since both Ma and $k_x R_\lambda$ are relatively high, the onset of exponentially-growing Görtler vortices was not observed [Viaro and Ricco, 2019b]. The downstream growth of $|\bar{u}|_{max}$ is shown in figures 3.15a and 3.15b. The flat-plate ($\widehat{G} = 0$) results are plotted in light colors for comparison. The fluctuations on the concave plate are enhanced downstream of $\bar{x} = 3$ ($\widehat{G} = 2.41$) and $\bar{x} = 2$ ($\widehat{G} = 12$) with respect to those on the flat plate. The porous wall reduces the amplitude of the velocity disturbances with the centrifugal effects during their initial evolution, up to

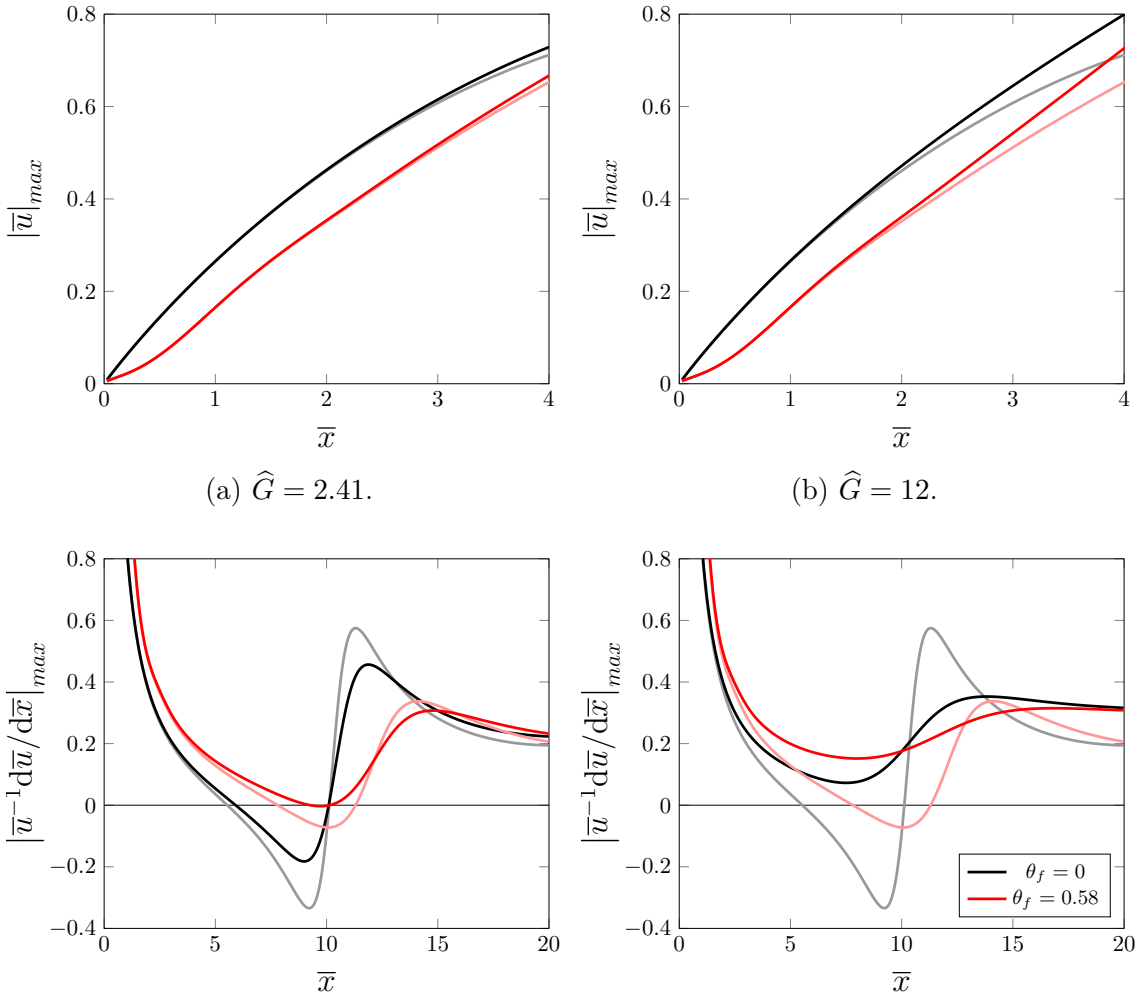

(a) $\widehat{G} = 2.41$. (b) $\widehat{G} = 12$.

(c) $\widehat{G} = 2.41$. (d) $\widehat{G} = 12$.

Figure 3.15: Effect of the porous wall on a boundary layer $\widehat{G} = O(1)$ for $\kappa_z = 0.007$, $\mathrm{R}_\lambda = 418000$ and $Ma = 6$. The black and red curves refer to the solid and porous cases, respectively. The curves for the flat-plate case $\widehat{G} = 0$ are drawn in light colors.

about $\bar{x} = 4$. Flows with higher Görtler numbers were not investigated as values of $r_c < 20$ might invalidate the hypothesis $r_c \gg \delta$.

The growth rate of $|\bar{u}|$ is shown in figures 3.15c and 3.15d. Although the amplitude of $|\bar{u}|_{max}$ is reduced up to $\bar{x} = 4$, the porous wall enhances its growth downstream of $\bar{x} = 2$ up to $\bar{x} = 10$ and attenuates it further downstream. Additional research is necessary to evince the effect of nonlinearity at these downstream locations because the magnitude of the fluctuations may be too large for the nonlinear interactions to be considered negligible.

Chapter 4

Compressible boundary layers over isotropic porous walls

This chapter examines boundary layers over highly permeable porous surfaces, where increased porosity and permeability modify the laminar base flow, allowing fluid to penetrate the substrate.

The first objective of this chapter is to extend the solutions of Tsiberkin [2018a] and Tsiberkin [2018b] to high-speed boundary layers. A self-similar solution is sought, and for the first time, the governing equations for the laminar base flow are derived using volume averaging. This formulation incorporates nonlinear drag, compressibility, and heat conduction. The second objective is to derive and solve the equations governing the evolution of compressible laminar streaks and Görtler vortices over the substrate using the volume-averaging technique [Bear and Bachmat, 1990; Whitaker, 1998].

The mathematical framework for the compressible laminar base flow, the linearized disturbance flow, and the numerical solution technique are presented in §4.1. The results of the base flow computations are discussed in §4.2, followed by an analysis of the linearized disturbance flow in §4.1.2. Einstein summation convention is assumed throughout this chapter.

4.1 Governing equations

The focus is on a two-dimensional, steady air flow over the top flat surface of an isotropic and uniform porous substrate. The substrate lies above a solid impermeable surface and is saturated with air. The governing equations for the fluid phase are derived by volume averaging the compressible Navier-Stokes equations [Whitaker, 1969; Bachmat and Bear, 1986; Bear and Bachmat, 1990; Whitaker, 1998; Sorek

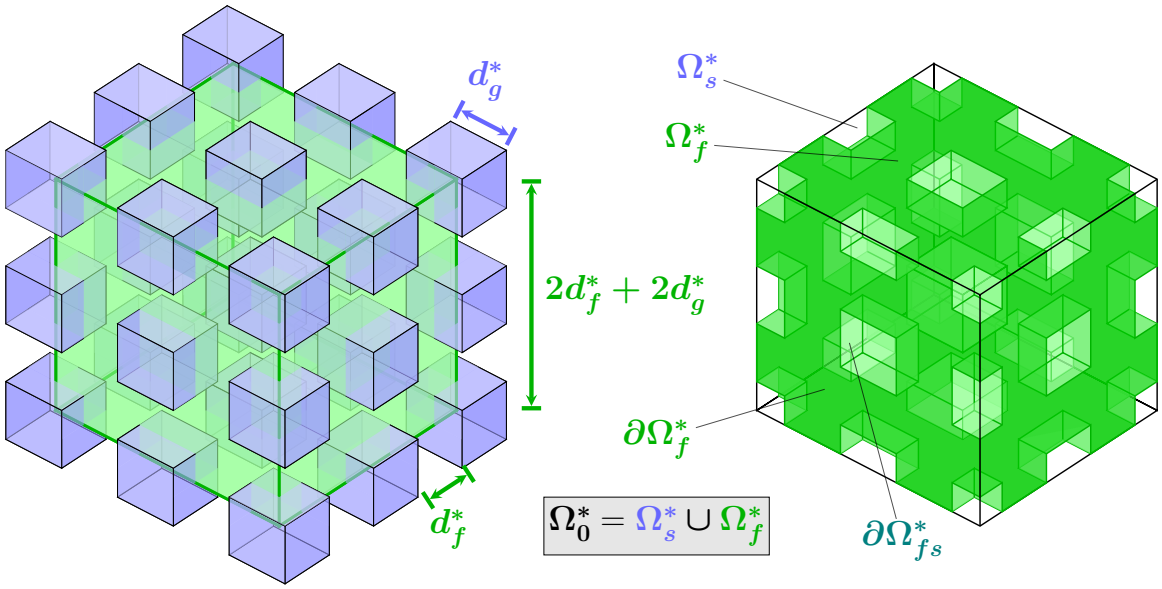

Figure 4.1: Schematic of the microscopic structure of the porous substrate. On the left side, a cubic REV (green) of volume $\Omega_0^* = 8(d_g^* + d_f^*)^3$ is placed within an array of uniformly-spaced solid grains (blue cubes) of size d_g^* and inter-grain distance d_f^*. On the right, the volume of fluid enclosed by the REV is shown (green). The fluid and solid volume fractions, Ω_f^* and Ω_s^*, are also drawn along with the fluid-solid interface surface $(\partial\Omega_{fs})^*$ and the portion of the external surface of the REV occupied by the fluid $(\partial\Omega_f)^*$.

et al., 2005]. The averaged *macroscopic* fluid quantities result from an upscaling process as the *microscopic* quantities are smoothed by applying a spatial filter $\overline{m}^*$ over a representative elementary volume (REV) that encloses portions of the fluid domain and the solid matrix. When the top-hat filter $\overline{m}^* = 1/\Omega_0^*$ [m^{-3}] [Quintard and Whitaker, 1994; Breugem and Boersma, 2005] is used (where Ω_0^* is the total volume of the REV) the intrinsic volume average of the fluid phase within the REV is $\langle\cdot\rangle_f = 1/\Omega_0^* \int_{\Omega_0^*}[\cdot]\mathrm{d}\Omega^*$. All dimensional quantities are denoted by the superscript $*$. The ratio of the fluid volume to the total volume of the REV defines the volume porosity $\theta_f = \Omega_f^*/\Omega_0^*$. The surface porosity is the ratio $\theta_{\partial ff} = (\partial\Omega_f)^*/(\partial\Omega_0)^*$, where $(\partial\Omega_f)^*$ is the portion of the external surface of the REV wetted by the fluid phase and $(\partial\Omega_0)^*$ is the total external surface of the REV. A porous substrate with the ordered microstructure shown in figure 4.1 is consider and a cellular filter, which results from the double convolution of the top-hat filter [Quintard and Whitaker, 1994; Breugem and Boersma, 2005; Breugem, Boersma, and Uittenbogaard, 2006], is employed. The averaged macroscopic quantities are defined at the centroid of the REV and vary continuously across an interface of finite thickness at the top boundary of the substrate. To simplify the notation, the normalized filter $m = \overline{m}^*\Omega_0^*$ and the

ratio $\Sigma^*_{fs} = (\partial\Omega_{fs})^*/\Omega^*_0$ [m^{-1}] are introduced, where $(\partial\Omega_{fs})^*$ is the fluid-solid interface surface within the REV [Bachmat and Bear, 1986]. The averaging operators read

$$\langle[\cdot]\rangle_f = \frac{1}{\Omega^*_0}\int_{\Omega^*_0} m\,[\cdot]\;\mathrm{d}\Omega^*, \tag{4.1a}$$

$$\langle[\cdot]\,n_j\rangle_{\partial fs}\,\Sigma^*_{fs} = \frac{1}{\Omega^*_0}\int_{(\partial\Omega_{fs})^*} m\;[\cdot]\,n_j\,\mathrm{d}\,(\partial\Omega^*)\,, \tag{4.1b}$$

and the quantities are decomposed as the sum of their volume-averaged and fluctuating parts, $[\cdot] = \langle[\cdot]\rangle_f + \widetilde{[\cdot]}$, with $\langle\widetilde{[\cdot]}\rangle_f = 0$ [Gray, 1975]. The flow is described in a Cartesian frame of reference, where x^* and y^* define the streamwise and wall-normal coordinates, respectively. The intrinsic average of the gradient (or the divergence) of a tensor G^*_{ijk} of dimension three or lower [Bear and Bachmat, 1990, eq. 2.3.29] takes the form

$$\theta_f\left\langle\frac{\partial G^*_{ijk}}{\partial x^*_\sigma}\right\rangle_f = \frac{\partial}{\partial x^*_\sigma}\left(\theta_f\left\langle G^*_{ijk}\right\rangle_f\right) + \int_{\partial\Omega_{fs}}\overline{m}^*\,G^*_{ijk}n_\sigma\mathrm{d}\,(\partial\Omega^*)\,, \tag{4.2}$$

where n_i are the versors normal to the fluid-solid interface, and $\sigma = i$ for the gradient ($\sigma = j$ for the divergence). The pressure p^*, the density ρ^*, the temperature T^*, and the velocity components u^*_i are also introduced. Provided that $\partial^2 p^*/\partial x^{*2}_j = 0$ within the REV, the average of the pressure gradient can be expanded as [Bear and Bachmat, 1990, eq. 2.3.48]

$$\theta_f\left\langle\frac{\partial p^*}{\partial x^*_i}\right\rangle_f = \theta_f\mathcal{T}_{ij}\frac{\partial\left\langle p\right\rangle^*_f}{\partial x^*_j} + \int_{\partial\Omega_{fs}}\overline{m}^*\,\widetilde{x}^*_i\frac{\partial\widetilde{p}^*}{\partial x^*_j}n_j\mathrm{d}\,(\partial\Omega^*)\,, \tag{4.3}$$

where $\mathcal{T}_{ij}$ is the non-dimensional tortuosity tensor, which is $(\theta_{\partial ff}/\theta_f)\,\delta_{ij}$ in an isotropic medium [Bachmat and Bear, 1986; Bear and Bachmat, 1990].

4.1.1 Laminar base flow

The base-flow equations are derived in cartesian coordinates in this section. Consider the steady, two-dimensional form of the equations for mass conservation and balance for the streamwise and wall-normal momentum, and the enthalpy. The solid matrix is assumed to be infinitely rigid. The divergence operator (4.2) is applied to the steady, two-dimensional mass conservation equation. By neglecting the mechanical-dispersion terms $\langle\widetilde{\rho}^*\widetilde{u}^*\rangle_f$ and assuming zero-mass transport across the impermeable fluid-solid interfaces within the REV, one finds [Bear and Bachmat, 1990]

$$\frac{\partial}{\partial x^*_j}\left(\theta_f\left\langle\rho^*\right\rangle_f\left\langle u^*_j\right\rangle_f\right) = 0, \tag{4.4}$$

where the volume porosity is, in general, a smooth function of x^* and y^*. The momentum balance takes the form

$$\theta_f \left\langle \rho^* \right\rangle_f \left\langle u_j^* \right\rangle_f \frac{\partial \left\langle u_i^* \right\rangle_f}{\partial x_j^*} + \theta_f \mathcal{T}_{ij} \frac{\partial \left\langle p^* \right\rangle_f}{\partial x_j^*} = \theta_f \left\langle \frac{\partial \tau_{ij}^*}{\partial x_j^*} \right\rangle_f - \left\langle \widetilde{x}_i^* \frac{\partial \widetilde{p}^*}{\partial x_j^*} n_j \right\rangle_{\partial fs} \Sigma_{fs}^*. \tag{4.5}$$

The solid and fluid phase velocities are zero at the solid-fluid interface and the divergence of the shear stresses τ_{ij}^* expands as [Bear and Bachmat, 1990, eq. 2.6.32]

$$\begin{aligned} \theta_f \left\langle \frac{\partial \tau_{ij}^*}{\partial x_j^*} \right\rangle_f = \frac{\partial}{\partial x_j^*} \left[\left\langle \mu^* \right\rangle_f \left(\frac{\partial \left(\theta_f \left\langle u_i^* \right\rangle_f \right)}{\partial x_j^*} + \frac{\partial \left(\theta_f \left\langle u_j^* \right\rangle_f \right)}{\partial x_i^*} \right) \right] + \\ + \frac{\partial}{\partial x_i^*} \left[\left\langle \lambda^* \right\rangle_f \frac{\partial \left(\theta_f \left\langle u_k^* \right\rangle_f \right)}{\partial x_k^*} \right] + \left\langle \mu^* \left(\frac{\partial u_i^*}{\partial x_j^*} + \frac{\partial u_j^*}{\partial x_i^*} \right) \right\rangle_{\partial fs} \Sigma_{fs}^* + \\ - \frac{\left\langle \lambda^* \right\rangle_f}{\theta_f} \frac{\partial \left(\theta_f \left\langle u_k^* \right\rangle_f \right)}{\partial x_k^*} \frac{\partial \theta_f}{\partial x_i^*}, \end{aligned} \tag{4.6}$$

where λ^* is the second coefficient of viscosity and the last term is obtained by employing the identity $\partial \theta_f / \partial x_i^* = \left\langle -n_i \right\rangle_{\partial fs} \Sigma_{fs}^*$. The surface integrals on the right-hand side of equations (4.5) and (4.6) are often modeled using a permeability tensor [Bachmat and Bear, 1986; Whitaker, 1986] and a Forchheimer tensor [Whitaker, 1996]. The latter is a nonlinear correction to Darcy's law which arises at large microscopic Reynolds numbers [Whitaker, 1996; Breugem and Boersma, 2005]. While the departure from the linear Darcian regime is very well known and has been widely reported in numerical and laboratory experiments, the mathematical modelling and the physical nature of the Forchheimer correction are a matter of current research. Nonlinear corrections with cubic, quadratic and power-law dependence on the velocity have been reported for different ranges of the microscopic Reynolds numbers on pre-transitional fluid flows inside porous media [Lasseux and Valdés-Parada, 2017; Khalifa et al., 2020]. The surface integral is modeled as the sum of a linear and a quadratic drag [Barrère et al., 1992; Whitaker, 1996; Breugem, Boersma, and Uittenbogaard, 2006]

$$\begin{aligned} \left\langle -\widetilde{x}_i^* \frac{\partial \widetilde{p}^*}{\partial x_j^*} n_j + \mu^* \left(\frac{\partial u_i^*}{\partial x_j^*} + \frac{\partial u_j^*}{\partial x_i^*} \right) n_j \right\rangle_{\partial fs} \Sigma_{fs}^* = - \left\langle \mu^* \right\rangle_f \theta_f^2 \left(K^{*-1} \right)^{ij} \left\langle u_j^* \right\rangle_f + \\ - \left\langle \rho^* \right\rangle_f \theta_f^2 \left[\left(K^{*-1} \right)^{ik} \left(c_{F,kjl}^* \left\langle u_l^* \right\rangle_f \right) \right] \left\langle u_j^* \right\rangle_f, \end{aligned} \tag{4.7}$$

where the inverse of the permeability tensor K_{ij}^* and the Forchheimer tensor $c_{F,kjl}^*$ have been introduced. The latter are often modeled using the Kozeny-Carman and

Ergun relations [Whitaker, 1996; Breugem, Boersma, and Uittenbogaard, 2006], that is $K^*_{ij} = \theta_f^3/\left(1-\theta_f\right)^2 \left(d_g^{*2}/A\right)\delta_{ij}$ and $c^*_{F,ijk} = \theta_f/(1-\theta_f)(d_g^*/B)\delta_{ijk}$, where the grain size $d_g^* = d_g^*(x^*, y^*, d_{g0}^*)$ is assumed to be a smooth function of x^*, y^* and the reference value d_{g0}^*. A and B are empirical coefficients [Whitaker, 1996]. Similar forms of the Kozeny-Carman relation of the type $K^* = C^*\theta_f^m/(1-\theta_f)^n$, where C^* is a dimensional parameter and m and n are positive real constants, have also been used [Costa, 2006]. The Forchheimer coefficient $c^*_{F,ijk}$ is sometimes modeled as an exponential function of K^* [Innocentini, Sepulveda, et al., 2006; Wedin and Cherubini, 2016]. Although the closure model (4.7) may no longer hold in the compressible regime, where the seepage velocity can be as high as $10^2\,\mathrm{m\,s^{-1}}$ for high porosity [Mironov et al., 2015], because of the lack of experimental data, the equation (4.7) is used with the incompressible values $A = 180$ and $B = 100$. Applying the operators (4.2) to the static enthalpy balance yields

$$\theta_f \left\langle \rho^* \right\rangle_f \left\langle u_j^* \right\rangle_f \frac{\partial \left\langle T^* \right\rangle_f}{\partial x_j^*} = \frac{\left\langle \mu^* \right\rangle_f}{\theta_f} \left[\frac{\partial \left(\theta_f \left\langle u_i^* \right\rangle_f \right)}{\partial x_j^*} \right]^2 + \frac{\left\langle \lambda^* \right\rangle_f}{\theta_f} \left[\frac{\partial \left(\theta_f \left\langle u_k^* \right\rangle_f \right)}{\partial x_k^*} \right]^2 + \\ + \frac{\left\langle \mu^* \right\rangle_f}{\theta_f} \frac{\partial \left(\theta_f \left\langle u_i^* \right\rangle_f \right)}{\partial x_j^*} \frac{\partial \left(\theta_f \left\langle u_j^* \right\rangle_f \right)}{\partial x_i^*} + \frac{\partial}{\partial x_j^*} \left(\theta_f \left\langle k^* \right\rangle_f \mathcal{T}_{jk} \frac{\partial \left\langle T^* \right\rangle_f}{\partial x_k^*} \right), \quad (4.8)$$

where k^* is the thermal conductivity. It is assumed that the temperature gradient at the solid-fluid interface is negligible and the fluid and solid phases are in thermal equilibrium $\left\langle T^* \right\rangle_f = \left\langle T^* \right\rangle_s$ [Bear and Bachmat, 1990, eq. 2.6.121]. Both approximations are fairly adequate for large θ_f and steady conditions [Nield and Kuznetsov, 2003]. The perfect gas equation becomes $\left\langle p^* \right\rangle_f = \left\langle \rho^* \right\rangle_f \mathcal{R}^* \left\langle T^* \right\rangle_f$, where $\mathcal{R}^* = 287.05\,\mathrm{J\,kg^{-1}\,K^{-1}}$ is the specific gas constant of air.

The fluid flow is uniform away from the substrate because the streamwise pressure gradient is null. A thin boundary layer forms above the fluid-porous interface. The velocity components, the density, the temperature, and the transport coefficients are normalized by their free-stream values, denoted by the subscript ∞. The macroscopic pressure $\left\langle p^* \right\rangle_f$ is scaled by $\rho_\infty^* U_\infty^{*2}$, where U_∞^* is the free-stream velocity. The free-stream Reynolds number is $Re = \rho_\infty^* U_\infty^* L^*/\mu_\infty^* \gg 1$, where μ_∞^* is the free-stream dynamic viscosity and L^* is a characteristic large streamwise length. The Darcy number, based on the characteristic grain size d_{g0}^*, is $Da = d_{g0}^{*2}/L^{*2} \ll 1$ and the free-stream Mach number is $Ma = U_\infty^*/c_\infty^* = O\left(1\right)$, where $c_\infty^* = \left(\gamma \mathcal{R}^* T_\infty^*\right)^{1/2}$ is the speed of sound in the free stream, and $\gamma = 1.4$ the heat capacity ratio. The dynamic viscosity is modeled by Sutherland's law. The parabolic character of the solution

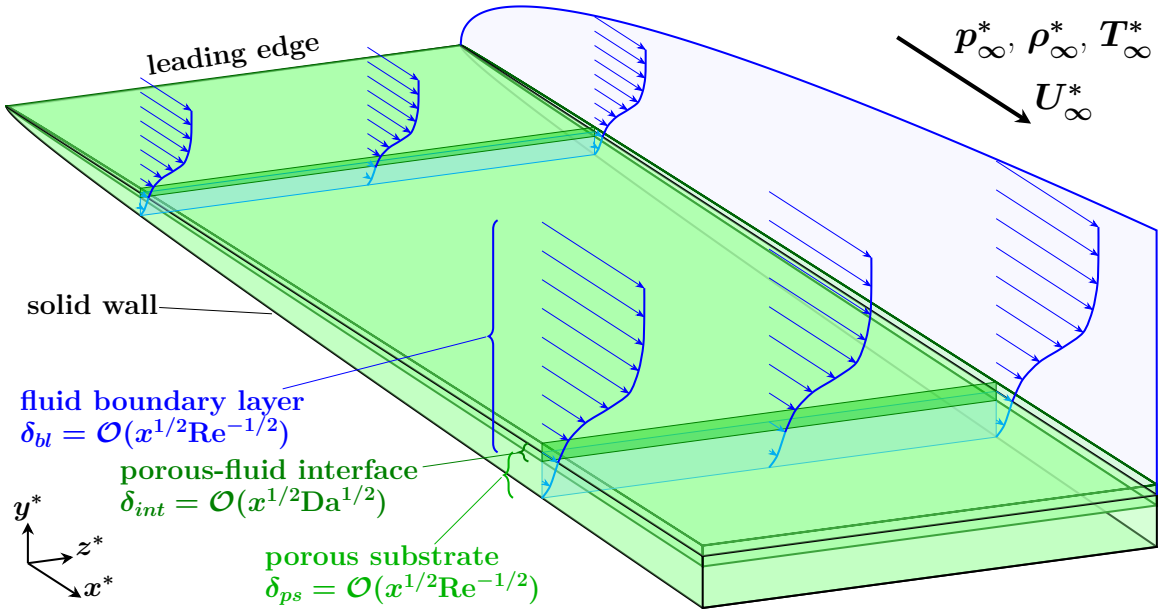

Figure 4.2: Schematic of the self-similar flow. A boundary layer (blue) of thickness δ_{bl} evolves over an isotropic porous substrate (green) of streamwise-increasing thickness δ_{ps}. The figure is not to scale.

obtained by Vafai and Kim [1990] resulted from the concurrent contribution of the Brinkman, Forchheimer, and advective terms, all of which need to be retained while performing a rigorous asymptotic analysis. The Forchheimer term cannot satisfy the boundary-layer approximation when scaled by a factor $\rho^*_\infty U^*_\infty / d^*_{g0} \gg 1$ [Tsiberkin, 2018b]. The Darcy and Forchheimer terms are a parameterization of the surface integrals in (4.7) and appropriate scaling must be applied to the integrating functions themselves. The characteristic length of the REV Σ^{*-1}_{fs} scales as d^*_g, the velocity scales as U^*_∞ [Barrère et al., 1992; Härter et al., 2023] and the microscopic pressure fluctuations $\widetilde{p}^*$ scale as $\mu^*_\infty U^*_\infty / d^*_g$ [Whitaker, 1996].

4.1.1.1 Porous-free fluid interface

A schematic of the self-similar, coupled porous substrate-boundary layer flow is shown in figure 4.2. As in classic boundary-layer theory [Stewartson, 1964; van Dyke, 1975], the flow properties are expected to vary in a region of thickness $O\left(Re^{-1/2}\right)$ near the top surface of the substrate. From this point onwards, the averaging operators $\langle\cdot\rangle_f$ are omitted for clarity, with no risk of ambiguity regarding volume averaging. The limiting form of equations (4.4), (4.5), and (4.8) for $Re \gg 1$ and $Da \ll 1$ is parabolic

in x and reads [van Dyke, 1975]

$$\frac{\partial}{\partial x}\left(\frac{\theta_f U}{T}\right)+\frac{\partial}{\partial y}\left(\frac{\theta_f V}{T}\right)=0, \tag{4.9a}$$

$$\frac{\theta_f U}{T}\frac{\partial U}{\partial x}+\frac{\theta_f V}{T}\frac{\partial U}{\partial y}=\frac{\partial}{\partial y}\left[\mu\frac{\partial\left(\theta_f U\right)}{\partial y}\right]-\frac{\theta_f^2}{\widehat{\kappa}_p^2}\left(\frac{\mu U}{K}+\frac{\theta_f\widehat{c}_F}{K^{1/2}}\frac{U^2}{T}\right), \tag{4.9b}$$

$$\frac{\theta_f U}{T}\frac{\partial T}{\partial x}+\frac{\theta_f V}{T}\frac{\partial T}{\partial y}=\frac{\mu}{\theta_f}\left[\frac{\partial\left(\theta_f U\right)}{\partial y}\right]^2+\frac{\partial}{\partial y}\left(\theta_{\partial ff}\frac{\mu}{Pr}\frac{\partial T}{\partial y}\right), \tag{4.9c}$$

where the streamwise pressure gradient is omitted and the perfect gas equation is $\rho T=1$. A similarity solution is retrieved if $\widehat{c}_F=\widehat{c}_F\left(\theta_f\right)$ is assumed to be a function of $d_g^*=d_{g0}^*$. When the low-speed, incompressible closure model (4.7) is considered, this choice is equivalent to a local-similarity assumption. Here $K=\theta_f^3/[(1-\theta_f)^2A]=O\left(1\right)$, $\widehat{c}_F=A^{1/2}ReDa/(BDa^{1/2}\theta_f^{3/2})=O\left(1\right)$, $\widehat{\kappa}_p^2=ReDa(d_g^*/d_{g0}^*)^2=O\left(1\right)$ [Tsiberkin, 2016], $A=O\left(1\right)$ and $B=O(Da^{-1/2})$. The Prandtl number of air is $Pr=c_p^*\mu_\infty^*/k_\infty^*=0.71$ and $k(T)=\mu(T)$ [Stewartson, 1964]. A no-slip, no-penetration condition is imposed at the bottom solid wall of the substrate. The boundary conditions read

$$\begin{aligned} U\left(x,0\right)&=0, & U\left(x,\infty\right)&=1,\\ T\left(x,0\right)=T_w \text{ or } \frac{\partial T}{\partial y}\left(x,0\right)&=0, & T\left(x,\infty\right)&=1, \end{aligned} \tag{4.10}$$

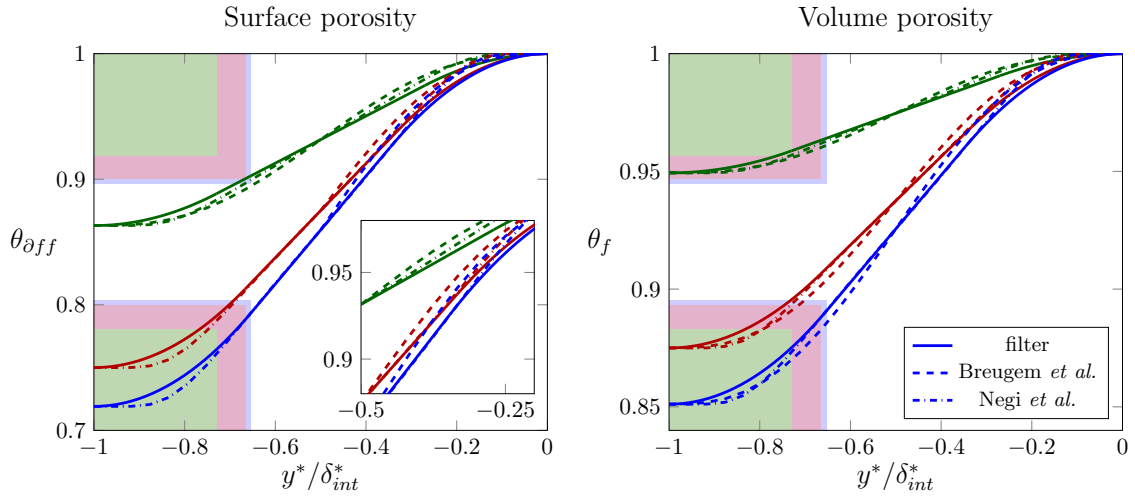

Figure 4.3: Comparison of the model equations of Breugem and Boersma [2005] (dashed curves) and Negi et al. [2015] (dash dot curves) (4.12) with the results obtained by computing the convolution integral of the cellular filter across the porous-free fluid interfacial layer of thickness δ_{int}^* (4.11) (solid curves) for $Q=0.37$ (green), $Q=0.5$ (red), and $Q=0.53$ (blue). Green, red, and blue solid grains of size $d_g^*=\delta_{int}^*Q/(1+Q)$ are drawn at the bottom side of the interface for comparison.

where the subscript w denotes the bottom solid wall. The top surface of the porous substrate is flat and located at a height y^*_{int}. The thickness of the interface is $\delta_{int} = O(Da^{1/2})$ [Goharzadeh et al., 2005] and therefore comparable to that of the boundary layer as $\delta_{int}/\delta_{bl} = O(Re^{1/2}Da^{1/2}) = O(1)$. The volume and surface porosity vary smoothly across the interface. Their uniform values below the interface are $\theta_{fp} = 1 - Q^3$ and $(\theta_{\partial ff})_p = 1 - Q^2$, respectively, where $Q = d^*_g/(d^*_f + d^*_g)$. Here, $d^*_f = d^*_f(x^*, y^*, d^*_{f0})$, where d^*_{f0} is a characteristic constant. The interfacial thickness is $\delta^*_{int} = d^*_g\,(1+Q)/Q$. The distribution of θ_f and $\theta_{\partial ff}$ is obtained analytically by sweeping the averaging operator (4.1) across the interfacial region [Breugem, 2005]. Repeating this procedure for arbitrary d^*_g and d^*_f yields the analytical piecewise-polynomial curve shown in figure 4.3 (solid curves)

$$\theta_{\partial ff}\left(\frac{y^*}{\delta^*_{int}}\right) = 1 \text{ for } \frac{y^*}{\delta^*_{int}} \geq 0, \tag{4.11a}$$

$$\theta_{\partial ff}\left(\frac{y^*}{\delta^*_{int}}\right) = 1 - \frac{Q}{\left(d^*_f + d^*_g\right)^2}\int_{-d^*_g-d^*_f}^{-d^*_g-d^*_f-y}\left(d^*_g + d^*_f + \breve{y}^*\right)\mathrm{d}\breve{y}^* = \\ = 1 - \frac{Q}{2}\left(1+Q\right)^2\left(\frac{y^*}{\delta^*_{int}}\right)^2 \text{ for } -\frac{Q}{1+Q} \leq \frac{y^*}{\delta^*_{int}} < 0, \tag{4.11b}$$

$$\theta_{\partial ff}\left(\frac{y^*}{\delta^*_{int}}\right) = 1 - \frac{Q}{\left(d^*_f + d^*_g\right)^2}\int_{-d^*_f-2d^*_g-y^*}^{-d^*_g-d^*_f-y^*}\left(d^*_g + d^*_f + \breve{y}^*\right)\mathrm{d}\breve{y}^* = \\ = 1 + Q^3\left[\frac{1}{2} + \frac{1+Q}{Q}\frac{y^*}{\delta^*_{int}}\right] \text{ for } -\frac{1}{1+Q} \leq \frac{y^*}{\delta^*_{int}} < -\frac{Q}{1+Q}, \tag{4.11c}$$

$$\theta_{\partial ff}\left(\frac{y^*}{\delta^*_{int}}\right) = 1 - \frac{Q}{\left(d^*_f + d^*_g\right)^2}\left[\int_{-d^*_g-d^*_f}^{-2d^*_g-2d^*_f-y}\left(d^*_g + d^*_f + \breve{y}^*\right)\mathrm{d}\breve{y}^* + \right. \\ \left. + \int_{0}^{-d^*_f-2d^*_g-y^*}\left(d^*_g + d^*_f + \breve{y}^*\right)\mathrm{d}\breve{y}^* + \int_{-d^*_g-d^*_f-y^*}^{0}\left(d^*_f + d^*_g - \breve{y}^*\right)\mathrm{d}\breve{y}^*\right] = \\ = 1 + Q\left[\frac{(1+Q^2)}{2} + (1+Q)^2\frac{y^*}{\delta^*_{int}} + \frac{(1+Q)^2}{2}\left(\frac{y^*}{\delta^*_{int}}\right)^2\right] \\ \text{for } -1 \leq \frac{y^*}{\delta^*_{int}} < -\frac{1}{1+Q}, \tag{4.11d}$$

$$\theta_{\partial ff}\left(\frac{y^*}{\delta^*_{int}}\right) = 1 - Q^2 \text{ for } \frac{y^*}{\delta^*_{int}} < -1, \tag{4.11e}$$

Breugem and Boersma [2005] approximated (4.11) with a fifth-order polynomial. Instead, an interpolating exponential function is used in this work [Negi et al., 2015]

$$\frac{\theta_f(\widetilde{y}) - \theta_{fp}}{1 - \theta_{fp}} = \frac{\theta_{\partial ff}(\widetilde{y}) - (\theta_{\partial ff})_p}{1 - (\theta_{\partial ff})_p} = \left[1 + \exp\left(\frac{C}{\widetilde{y}} + \frac{C}{\widetilde{y}+1}\right)\right]^{-1} \tag{4.12}$$

where $\widetilde{y} = (y^* - y^*_{int})/\delta^*_{int}$, $C = 0.75$. As shown in figure 4.3, the agreement between the analytical piecewise curve and the exponential model (4.12) is excellent at the centre of the interface.

4.1.1.2 Self-similar solution

As discussed in §1.3.3, the parabolic nature of the differential system (4.9) implies that the solution depends on the initial (upstream) flow conditions when the governing equations are non-similar. One possible assumption is that the upstream flow corresponds to a compressible Blasius boundary layer over an impermeable surface, with the wall gradually becoming porous over a finite streamwise region. However, even in this scenario, the emergence of an evolving inflection point in the velocity profile could trigger an inviscid instability, which cannot be captured if streamwise diffusion is neglected. This task is beyond the scope of the present work. Hence, a similarity solution of the differential system (4.9) is sought in this section.

First, the Dorodnitsyn-Howarth variable $\bar{y} = \int_0^y \rho(x, \breve{y})\mathrm{d}\breve{y}$ [Stewartson, 1964] is introduced. A streamfunction $\psi(x, \bar{y})$ is defined so that the continuity equation (4.9a) is satisfied $u = \theta_f^{-1}\partial\psi/\partial\bar{y}$, $v = -(T/\theta_f)\partial\psi/\partial x$. Following a standard procedure in the derivation of the self-similar boundary layer equations (see appendix B for details) a decomposition of ψ and $\bar{y}$ is sought in the form $\psi(x, \bar{y}) = (\alpha x)^a F(x, \eta)$ and $\bar{y} = (\alpha x)^b \eta$, where α, a, and b are real constants. Inspection of (4.10) shows that T cannot be a function of x in homoenthalpic flows and that no similarity solution is possible if an inhomogeneous Neumann condition for the temperature is imposed at the solid wall underneath the substrate. Since the top of the substrate is flat, the wall-normal porosity distribution (4.12) is a function of η alone when both δ_{int} and δ_{ps} are $O\left(x^b\right)$. Following [Tsiberkin, 2016; Tsiberkin, 2018a; Tsiberkin, 2018b], the grain size and the inter-grain distance are assumed to be smooth functions of x, $d^*_g = d^*_{g0}(\alpha x)^{c/2}$, and $\widehat{\kappa}_p = \kappa_p(\alpha x)^c$, where

$$\kappa_p^2 = ReDa = \frac{\rho^*_\infty U^*_\infty d^{*2}_{g0}}{\mu^*_\infty L^*} = O(1) \tag{4.13}$$

is the control parameter defined by Tsiberkin [2018a]. The parameter distills the effect of the linear Darcy drag for given free-stream conditions and grain size. A similarity

solution exists for $a = b = 1/2$, $c = 1$ and $\alpha = 2$. Equations (4.9b) and (4.9c) then reduce to a system of coupled ordinary differential equations

$$\left(\frac{\mu}{T}F''\right)' + F\left(\frac{F'}{\theta_f}\right)' - C_D\mu T\frac{(1-\theta_f)^2}{\theta_f^2}F' - C_F\frac{1-\theta_f}{\theta_f^2}\left(F'\right)^2 = 0, \tag{4.14a}$$

$$\frac{1}{Pr}\left(\theta_{\partial ff}\frac{\mu T'}{T}\right)' + FT' + \frac{(\gamma-1)}{\theta_f}\frac{\mu}{T}Ma^2\left(F''\right)^2 = 0, \tag{4.14b}$$

where the primes denote differentiation with respect to η, $C_D = A/\kappa_p^2$ and $C_F = A/(BDa^{1/2}) = O(1)$. More details on the derivation of (4.14a) are found in appendix B. For the first time, a self-similar form of the governing equations has been derived for compressible flow over a porous substrate with streamwise-increasing permeability, using a closure model with a constant Forchheimer coefficient. Equations (4.14) reduce to the compressible Blasius solution [Stewartson, 1964] above the interface, where $\theta_f, \theta_{\partial ff} = 1$. The velocity components are

$$U(\eta) = \frac{F'}{\theta_f}, \tag{4.15a}$$

$$V(\eta) = \frac{1}{\theta_f(2x)^{1/2}}\left(-TF + \eta_c TF'\right), \tag{4.15b}$$

and $\eta_c = T^{-1}\int_0^\eta T(\breve{\eta})\mathrm{d}\breve{\eta}$. The non-dimensional thickness of the fluid boundary layer, the fluid-porous interface, and the porous substrate are $O(x^{1/2}Re^{-1/2})$, $O(x^{1/2}Da^{1/2})$, and $O(x^{1/2}Re^{-1/2})$, respectively. The interfacial continuity of the surface-averaged tangential velocity $\theta_f u$ derived by Ochoa-Tapia and Whitaker [1995a] is recovered from (4.15a) for small κ_p ($\delta_{int}/d_{bl} \ll 1$).

4.1.1.3 Numerical method

The system (4.14) is solved by means of a second-order accurate block-elimination algorithm where nonlinearity is treated with the Newton-Raphson method [Cebeci, 2002]. The interfacial thickness in the η-space,

$$(\Delta\eta)_{int} = \frac{(\Delta y)_{int}}{T_{av}} = \frac{\kappa_p}{T_{av}}\frac{1+Q}{Q}, \tag{4.16}$$

depends on the average temperature of the interfacial region T_{av} and is determined iteratively. The values of $(\Delta y)_{int}$, T_{av} and $(\Delta_\eta)_{int}$ are tabulated in table 4.3. The residuals are kept below 10^{-12} for all the computations to ensure convergence.

4.1.2 Linearised disturbance flow

In this section, the method of volume averaging is applied to the Navier-Stokes equations in the curvilinear coordinate system of a concave wall, as detailed in appendix A. As in chapter 2 and 3, the flow is decomposed into a two-dimensional, steady component and a small-amplitude, three-dimensional, unsteady perturbation. The equations governing the porous-boundary-layer base flow in Cartesian coordinates are recovered, and the boundary-region equations describing the evolution of laminar streaks and Görtler vortices over an isotropic porous substrate with high porosity and permeability are derived in the high-Reynolds-number limit, assuming a large curvature radius $r_c = O(Re^2)$.

4.1.2.1 Continuity equation

Each term of the continuity equation (A.12) is multiplied by the Lamé coefficient $h_1 = 1 - y^*/r_c^*$ (A.10)

$$h_1\frac{\partial\rho^*}{\partial t^*}+u^*\frac{\partial\rho^*}{\partial x^*}+h_1v^*\frac{\partial\rho^*}{\partial y^*}+h_1w^*\frac{\partial\rho^*}{\partial z^*}=-\rho^*\left[\frac{\partial u^*}{\partial x^*}-\frac{v^*}{r_c^*}+h_1\left(\frac{\partial v^*}{\partial y^*}+\frac{\partial w^*}{\partial z^*}\right)\right], \quad (4.17)$$

or

$$h_1\left[\frac{\partial\rho^*}{\partial t^*}+\frac{\partial\left(\rho^*v^*\right)}{\partial y^*}+\frac{\partial\left(\rho^*w^*\right)}{\partial z^*}\right]+\frac{\partial\left(\rho^*u^*\right)}{\partial x^*}+\rho^*v^*\frac{\partial h_1}{\partial y^*}=0. \quad (4.18)$$

The volume averaging operators (4.2) are applied to (4.18)

$$h_1\left[\theta_f\left\langle\frac{\partial\rho^*}{\partial t^*}\right\rangle_f+\theta_f\left\langle\frac{\partial\left(\rho^*v^*\right)}{\partial y^*}\right\rangle_f+\theta_f\left\langle\frac{\partial\left(\rho^*w^*\right)}{\partial z^*}\right\rangle_f\right]+ \\ +\theta_f\left\langle\frac{\partial\left(\rho^*u^*\right)}{\partial x^*}\right\rangle_f+\theta_f\left\langle\rho^*v^*\right\rangle_f\frac{\partial h_1}{\partial y^*}=0. \quad (4.19)$$

The Lamé coefficient $h_1 \sim 1$ in the asymptotic limit $r_c = O(Re^2) \gg 1$. As in §4.1.1, the density, velocity, and the spatial lengths are normalized with respect to ρ_∞^*, U_∞^*, and Λ^*. The time is normalized with respect to Λ^*/U_∞^*. The ratio $r_c^*/\Lambda^* \gg 1$, and the last term on the left-hand side is negligible. [33] Moreover, since $y^*/\Lambda^* = O(1)$, the first Lamé coefficient h_1 and its derivative are constant in the limit of large Re

$$\left.\begin{aligned} h_1 &= 1-\frac{y}{r_c}\sim 1, && (4.20a)\\ \frac{\partial h_1}{\partial y} &= -\frac{1}{r_c}=O\left(Re^{-2}\right). && (4.20b)\end{aligned}\right\} \text{ for } Re\gg 1,$$

Neglecting the mechanical-dispersion terms $\langle\widetilde{\rho}^*\widetilde{u}^*\rangle_f$ [Bear and Bachmat, 1990] yields

$$\theta_f \frac{\partial \langle\rho\rangle_f}{\partial t} + \frac{\partial}{\partial x_i}\left(\theta_f \langle\rho\rangle_f \langle u_i\rangle_f\right) = 0. \tag{4.21}$$

The averaging operators are omitted for clarity and all the variables are assumed to be volume-averaged quantities. The decomposition (2.2) is introduced

$$\epsilon\theta_f \frac{\partial \grave{\varrho}}{\partial t} + \frac{\partial}{\partial x}\left[\theta_f \rho U + \epsilon\theta_f\left(\rho\grave{u} + \grave{\varrho}U\right)\right] + \frac{\partial}{\partial y}\left[\theta_f \rho V + \epsilon\theta_f\left(\rho\grave{v} + \grave{\varrho}V\right)\right] + \\ + \frac{\partial}{\partial z}\left(\epsilon\theta_f \rho\grave{w}\right) = 0, \tag{4.22}$$

and the leading-order balance of the laminar base flow (4.9a) is recovered. Substituting (2.14) in (4.22) yields the continuity equation for the linearised disturbance flow

$$\left(\frac{\theta_f \eta_c T'}{2\hat{x}T} - \frac{\theta_f' \eta_c}{2\hat{x}}\right)\bar{u} + \theta_f \left.\frac{\partial \bar{u}}{\partial \hat{x}}\right|_\eta - \frac{\theta_f \eta_c}{2\hat{x}}\frac{\partial \bar{u}}{\partial \eta} + \left(\frac{\theta_f'}{T} - \frac{\theta_f T'}{T^2}\right)\bar{v} + \frac{\theta_f}{T}\frac{\partial \bar{v}}{\partial \eta} + \\ + \theta_f \bar{w} + \left(\frac{\theta_f}{T}\mathrm{i}\mathcal{F} - \frac{FT'}{2\hat{x}T^2}\right)\bar{\tau} - \frac{F'}{T}\left.\frac{\partial \bar{\tau}}{\partial \hat{x}}\right|_\eta + \frac{F}{2\hat{x}T}\frac{\partial \bar{\tau}}{\partial \eta} = 0. \tag{4.23}$$

Equation (4.23) reduces to (2.9) in Viaro and Ricco [2019a] in the free-fluid region above the plate where $\theta_f \sim 1$ and $\theta_f' = 0$.

4.1.2.2 Momentum balance equation

Applying the volume-averaging operators (4.1) to (A.16) and adding (4.19) multiplied by $\langle u^*\rangle_f$ yields

$$\theta_f h_1^2 \frac{\partial}{\partial t^*}\left(\langle\rho^*\rangle_f \langle u^*\rangle_f\right) + h_1 \frac{\partial}{\partial x^*}\left(\theta_f \langle\rho^*\rangle_f \langle u^*\rangle_f \langle u^*\rangle_f\right) + h_1^2 \frac{\partial}{\partial y^*}\left(\langle\rho^*\rangle_f \langle v^*\rangle_f \langle u^*\rangle_f\right) + \\ + h_1^2 \theta_f \frac{\partial}{\partial z^*}\left(\langle\rho^*\rangle_f \langle w^*\rangle_f \langle u^*\rangle_f\right) + h_1 \theta_f \langle\rho^*\rangle_f \langle u^*\rangle_f \langle v^*\rangle_f \frac{\partial h_1}{\partial y^*} = \\ = h_1^2 \theta_f \left\langle \left[\frac{g^{jk}}{h_1}\tau_{xj,k}^* + \frac{1}{h_1}\frac{\partial p^*}{\partial x^*}\right]\right\rangle_f, \tag{4.24}$$

where all the terms have been multiplied by h_1 one more time. The right-hand side expands as

$$h_1^2 \theta_f \left\langle \left[\frac{g^{jk}}{h_1}\tau_{xj,k}^* + \frac{1}{h_1}\frac{\partial p^*}{\partial x^*}\right]\right\rangle_f = \\ = \frac{\partial}{\partial x^*}\left[\langle\mu^*\rangle_f \frac{\partial(\theta_f \langle u^*\rangle_f)}{\partial x^*}\right] + h_1 \frac{\partial}{\partial y^*}\left[h_1 \langle\mu^*\rangle_f \frac{\partial(\theta_f \langle u^*\rangle_f)}{\partial y^*}\right] +$$

$$+ h_1^2 \frac{\partial}{\partial z^*}\left[\langle\mu^*\rangle_f \frac{\partial(\theta_f \langle u^*\rangle_f)}{\partial z^*}\right] - h_1 \frac{\partial}{\partial y^*}\left(\langle\mu^*\rangle_f \langle u^*\rangle_f \frac{\partial h_1}{\partial y^*}\right) +$$
$$+ \left\langle \mu^* \frac{\partial u^*}{\partial x^*} n_x + h_1^2 \mu^* \frac{\partial u^*}{\partial y^*} n_y - h_1 \mu^* u^* \frac{\partial h_1}{\partial y^*} n_y + h_1^2 \mu^* \frac{\partial u^*}{\partial z^*} n_z \right\rangle_{\partial fs} \Sigma_{fs}^* +$$
$$+ \frac{\partial}{\partial x^*}\left[\langle\mu^*\rangle_f \frac{\partial(\theta_f \langle u^*\rangle_f)}{\partial x^*}\right] + \frac{\partial}{\partial x^*}\left(2\theta_f \langle\mu^*\rangle_f \langle v^*\rangle_f\right)\frac{\partial h_1}{\partial y^*} + \langle\mu^*\rangle_f \frac{\partial(\theta_f \langle v^*\rangle_f)}{\partial x^*}\frac{\partial h_1}{\partial y^*} +$$
$$+ \langle\mu^*\rangle_f \frac{\partial(\theta_f \langle u^*\rangle_f)}{\partial y^*}\frac{\partial h_1}{\partial y^*} - \langle\mu^*\rangle_f \frac{\langle u^*\rangle_f}{h_1}\left(\frac{\partial h_1}{\partial y^*}\right)^2 + \frac{\partial}{\partial y^*}\left[h_1 \langle\mu^*\rangle_f \frac{\partial(\theta_f \langle v^*\rangle_f)}{\partial x^*}\right] +$$
$$+ \frac{\partial}{\partial z^*}\left[h_1 \langle\mu^*\rangle_f \frac{\partial(\theta_f \langle w^*\rangle_f)}{\partial x^*}\right] + \left\langle \mu^* \frac{\partial u^*}{\partial x^*} n_x + h_1 \mu^* \frac{\partial v^*}{\partial x^*} n_y + h_1 \mu^* \frac{\partial w^*}{\partial x^*} n_z \right\rangle_{\partial fs} \Sigma_{fs}^* +$$
$$+ \frac{\partial}{\partial x^*}\left[\langle\lambda^*\rangle_f \left(\frac{1}{h_1}\frac{\partial(\theta_f \langle u^*\rangle_f)}{\partial x^*} + \frac{\partial(\theta_f \langle v^*\rangle_f)}{\partial y^*} + \frac{\theta_f \langle v^*\rangle_f}{h_1}\frac{\partial h_1}{\partial y^*} + \frac{\partial(\theta_f w^*)}{\partial z^*}\right)\right] +$$
$$- \frac{\langle\lambda^*\rangle_f}{\theta_f}\left(\frac{1}{h_1}\frac{\partial(\theta_f \langle u^*\rangle_f)}{\partial x^*} + \frac{\partial(\theta_f \langle v^*\rangle_f)}{\partial y^*} + \frac{\theta_f \langle v^*\rangle_f}{h_1}\frac{\partial h_1}{\partial y^*} + \frac{\partial(\theta_f w^*)}{\partial z^*}\right)\frac{\partial \theta_f}{\partial x^*} +$$
$$- \theta_{\partial f f} h_1 \frac{\partial \langle p^*\rangle_f}{\partial x^*} - h_1 \left\langle x^* \left(\frac{\partial p^*}{\partial x^*} n_x + \frac{\partial p^*}{\partial x_y^*} n_y + \frac{\partial p^*}{\partial z^*} n_z\right)\right\rangle_{\partial fs} \Sigma_{fs}^*. \quad (4.25)$$

The left-hand side is normalized with respect to ρ_∞^*, U_∞^* and Λ^*, the volume-averaging operators (4.1a) are omitted and only the interphase-surface average operators (4.1b) are retained for clarity

$$\frac{\rho_\infty^* U_\infty^{*2}}{\Lambda^*}\theta_f h_1^2 \left[\frac{\partial}{\partial t}(\rho u) + h_1 \frac{\partial}{\partial x}(\theta_f \rho u u) + h_1^2 \frac{\partial}{\partial y}(\rho v u) + \right.$$
$$\left. + h_1^2 \theta_f \frac{\partial}{\partial z}(\rho w u) + h_1 \theta_f \rho u v \frac{\partial h_1}{\partial y}\right] = h_1^2 \theta_f \left\langle \frac{g^{jk}}{h_1} \tau_{xj,k}^* \right\rangle_f, \quad (4.26)$$

The viscous terms on the right-hand side are normalized with respect to ρ_∞^*, U_∞^*, Λ^* and μ_∞^*:

$$h_1^2 \theta_f \left\langle \frac{g^{jk}}{h_1} \tau_{xj,k}^* \right\rangle_f = \frac{\mu_\infty^* U_\infty^*}{\Lambda^{*2}} \left\{ \frac{\partial}{\partial x}\left[\mu \frac{\partial(\theta_f u)}{\partial x}\right] + \right.$$
$$+ h_1 \frac{\partial}{\partial y}\left[h_1 \mu \frac{\partial(\theta_f u)}{\partial y}\right] + h_1^2 \frac{\partial}{\partial z}\left[\mu \frac{\partial(\theta_f u)}{\partial z}\right] - h_1 \frac{\partial}{\partial y}\left(\mu u \frac{\partial h_1}{\partial y}\right) +$$
$$+ \frac{\partial}{\partial x}\left[\mu \frac{\partial(\theta_f u)}{\partial x}\right] + \frac{\partial}{\partial x}(2\theta_f \mu v)\frac{\partial h_1}{\partial y} + \mu \frac{\partial(\theta_f v)}{\partial x}\frac{\partial h_1}{\partial y} + \mu \frac{\partial(\theta_f u)}{\partial y}\frac{\partial h_1}{\partial y} - \mu \frac{u}{h_1}\left(\frac{\partial h_1}{\partial y}\right)^2 +$$
$$+ \frac{\partial}{\partial y}\left[h_1 \mu \frac{\partial(\theta_f v)}{\partial x}\right] + \frac{\partial}{\partial z}\left[h_1 \mu \frac{\partial(\theta_f w)}{\partial x}\right] + \frac{\partial}{\partial x}\left[\frac{\lambda}{h_1}\frac{\partial(\theta_f u)}{\partial x} + \lambda \frac{\partial(\theta_f v)}{\partial y} + \lambda \frac{\theta_f v}{h_1}\frac{\partial h_1}{\partial y} + \right.$$
$$\left. + \lambda \frac{\partial(\theta_f w)}{\partial z}\right] - \frac{\lambda}{\theta_f}\left(\frac{1}{h_1}\frac{\partial(\theta_f u)}{\partial x} + \frac{\partial(\theta_f v)}{\partial y} + \frac{\theta_f v}{h_1}\frac{\partial h_1}{\partial y} + \frac{\partial(\theta_f w)}{\partial z}\right)\frac{\partial \theta_f}{\partial x}\Bigg\} +$$
$$+ \left\langle 2\mu^* \frac{\partial u^*}{\partial x^*} n_x + h_1 \mu^* \left(h_1 \frac{\partial u^*}{\partial y^*} + \frac{\partial v^*}{\partial x^*} - u^* \frac{\partial h_1}{\partial y^*}\right) n_y + \right.$$

$$+h_1\mu^*\left(h_1\frac{\partial u^*}{\partial z^*}+\frac{\partial w^*}{\partial x^*}\right)n_z\Big\rangle_{\partial fs}\Sigma^*_{fs}-\frac{\rho^*_\infty U^{*2}_\infty}{\Lambda^*}\theta_{\partial ff}h_1\frac{\partial\langle p\rangle_f}{\partial x}+$$
$$-h_1\left\langle x^*\left(\frac{\partial p^*}{\partial x^*}n_x+\frac{\partial p^*}{\partial x^*_y}n_y+\frac{\partial p^*}{\partial z^*}n_z\right)\right\rangle_{\partial fs}\Sigma^*_{fs}. \quad (4.27)$$

The Darcy-Forchheimer integral is modeled as in Breugem, Boersma, and Uittenbogaard [2006] (see also Whitaker [1996])

$$\left\langle 2\mu^*\frac{\partial u^*}{\partial x^*}n_x+h_1\mu^*\left(h_1\frac{\partial u^*}{\partial y^*}+\frac{\partial v^*}{\partial x^*}-u^*\frac{\partial h_1}{\partial y^*}\right)n_y+\right.$$
$$\left.+h_1\mu^*\left(h_1\frac{\partial u^*}{\partial z^*}+\frac{\partial w^*}{\partial x^*}\right)n_z\right\rangle\Sigma^*_{fs}+$$
$$-h_1\left\langle x^*\left(\frac{\partial p^*}{\partial x^*}n_x+\frac{\partial p^*}{\partial x^*_y}n_y+\frac{\partial p^*}{\partial z^*}n_z\right)\right\rangle_{\partial fs}\Sigma^*_{fs}=-\theta_f^2\frac{\mu^*u^*}{K^*}-\theta_f^2\frac{c_F^*}{K^*}\rho^*u^{*2} \quad (4.28)$$

As in §4.1.1, the permeability is $K^*=\theta_f^3/\left(1-\theta_f\right)^2\left(d_g^{*2}/A\right)$ and the Forchheimer coefficient is $c_F^*=\theta_f/(1-\theta_f)(d^*_{g0}/B)$, where the grain size $d_g^*=d_g^*(x^*,y^*,d^*_{g0})$ is assumed to be a smooth function of x^*, y^* and the reference value d^*_{g0}. Again, A and B are empirical coefficients [Whitaker, 1996]. Then

$$-\theta_f^2\frac{\mu^*u^*}{K^*}-\theta_f^2\frac{c_F^*}{K^*}\rho^*u^{*2}=-\frac{\mu^*_\infty U^*_\infty}{d^{*2}_{g0}}\left(\frac{d^*_{g0}}{d^*_g}\right)^2\theta_f^2\frac{A\left(1-\theta_f\right)^2}{\theta_f^3}\mu u+$$
$$-\frac{\rho^*_\infty U^{*2}_\infty}{d^{*2}_{g0}}\left(\frac{d^*_{g0}}{d^*_g}\right)^2\theta_f^2\frac{A\left(1-\theta_f\right)^2}{\theta_f^3}\frac{\theta_f}{1-\theta_f}\frac{d^*_{g0}}{B}\rho u^2. \quad (4.29)$$

The grain diameter depends on x^* as $d_g^*/d^*_{g0}=\left(2x^*/L^*\right)^{1/2}$, the porous control parameter is $\kappa_p^2=\rho^*_\infty U^*_\infty d^{*2}_{g0}/(\mu^*_\infty L^*)$. The boundary-region balance based on the expansion (2.14) yields the streamwise-momentum balance

$$\theta_f\frac{\partial}{\partial t}(\rho u)+\frac{\partial}{\partial x}(\theta_f\rho uu)+\frac{\partial}{\partial y}(\theta_f\rho vu)+\frac{\partial}{\partial z}(\theta_f\rho wu)=$$
$$=\frac{1}{Re}\frac{\partial}{\partial y}\left[\mu\frac{\partial\left(\theta_f u\right)}{\partial y}\right]+\frac{1}{Re}\frac{\partial}{\partial z}\left[\mu\frac{\partial\left(\theta_f u\right)}{\partial z}\right]+$$
$$-\frac{1}{2x}\frac{\theta_f^2}{\kappa_p^2}\left[A\frac{(1-\theta_f)^2}{\theta_f^3}\mu u+\frac{\kappa_p^2A}{BDa^{1/2}}\frac{(1-\theta_f)}{\theta_f^2}\rho u^2\right]. \quad (4.30)$$

Again, the asymptotic expansion (2.2) and the boundary-region scaling (2.14) are introduced in (4.30). The terms on the left-hand side expand as

$$\theta_f\frac{\partial}{\partial t}\left(\epsilon\rho\grave{u}+\epsilon\grave{\varrho}U\right)+\frac{\partial}{\partial x}\left[U\left(\theta_f\rho U+\epsilon\theta_f\rho\grave{u}+\epsilon\theta_f\grave{\varrho}U\right)\right]+\frac{\partial}{\partial x}\left(\epsilon\theta_f\rho U\grave{u}\right)+$$

$$+\frac{\partial}{\partial y}\left[U\left(\theta_f\rho V+\epsilon\theta_f\rho\grave{v}+\epsilon\theta_f\grave{\varrho}v\right)\right]+\frac{\partial}{\partial y}\left(\epsilon\theta_f\rho\grave{u}V\right)+$$
$$+U\frac{\partial}{\partial z}\left(\epsilon\theta_f\rho\grave{w}\right)+U\frac{\partial}{\partial z}\left(\epsilon\theta_f\rho\grave{w}\right). \quad (4.31)$$

By introducing the mass conservation equation (4.22), the left-hand side of (4.30) expands as

$$\epsilon\theta_f\rho\frac{\partial\grave{u}}{\partial t}+\theta_f\rho U\frac{\partial U}{\partial x}+\epsilon\left(\theta_f\rho\grave{u}+\theta_f\grave{\varrho}U\right)\frac{\partial U}{\partial x}+\epsilon\frac{\partial}{\partial x}\left(\theta_f\rho U\grave{u}\right)+$$
$$+\theta_f\rho V\frac{\partial U}{\partial y}+\epsilon\left(\theta_f\rho\grave{v}+\theta_f\grave{\varrho}V\right)\frac{\partial U}{\partial y}+\epsilon\frac{\partial}{\partial x}\left(\theta_f\rho V\grave{u}\right), \quad (4.32)$$

while the first term on the right-hand side of (4.30) expands as

$$\frac{1}{Re}\frac{\partial}{\partial y}\left[\mu\frac{\partial}{\partial y}\left(\theta_f u\right)\right]=\frac{1}{Re}\frac{\partial}{\partial y}\left[\left(\mu+\epsilon\frac{\partial\mu}{\partial T}\tilde{\tau}\right)\frac{\partial}{\partial y}\left(\theta_f U+\epsilon\theta_f\tilde{u}\right)\right]=$$
$$=\frac{1}{Re}\frac{\partial}{\partial y}\left[\mu\frac{\partial}{\partial y}\left(\theta_f U\right)+\epsilon\mu\frac{\partial\theta_f}{\partial y}\tilde{u}+\epsilon\mu\theta_f\frac{\partial\tilde{u}}{\partial y}+\epsilon\frac{\partial\mu}{\partial T}\tilde{\tau}\frac{\partial\theta_f}{\partial y}U+\epsilon\frac{\partial\mu}{\partial T}\tilde{\tau}\theta_f\frac{\partial U}{\partial y}\right], \quad (4.33)$$

and the second term on the right-hand side of (4.30) expands as

$$\frac{1}{Re}\frac{\partial}{\partial z}\left[\mu\frac{\partial}{\partial z}\left(\theta_f u\right)\right]=\frac{\partial}{\partial z}\left[\left(\mu+\epsilon\frac{\mathrm{d}\mu}{\mathrm{d}T}\tilde{\tau}\right)\frac{\partial}{\partial z}\left(\theta_f U+\epsilon\theta_f\tilde{u}\right)\right]=\frac{\epsilon}{Re}\theta_f\mu\frac{\partial^2\tilde{u}}{\partial z^2}. \quad (4.34)$$

The terms of the Darcy-Forchheimer integral expand as

$$\frac{1}{2x\kappa_p^2}\left[-\frac{\left(1-\theta_f\right)^2}{Re\theta_f}A\mu u-\left(1-\theta_f\right)C_F\kappa_p^2\rho u^2\right]=$$
$$=-\frac{\left(1-\theta_f\right)^2}{\theta_f}\frac{C_D}{2x}\left(\mu+\epsilon\frac{\mathrm{d}\mu}{\mathrm{d}T}\tilde{\tau}\right)\left(U+\epsilon\tilde{u}\right)-\left(1-\theta_f\right)\frac{C_F}{2x}\left(\rho+\epsilon\tilde{\varrho}\right)\left(U^2+2\epsilon U\tilde{u}\right)=$$
$$=-\frac{\left(1-\theta_f\right)^2}{\theta_f}\frac{A}{2x\kappa_p^2}\left(\mu U+\epsilon\mu\tilde{u}+\epsilon\frac{\mathrm{d}\mu}{\mathrm{d}T}\tilde{\tau}U\right)+$$
$$-\left(1-\theta_f\right)\frac{C_F}{2x}\left(\rho U^2+\epsilon 2\rho U\tilde{u}+\epsilon\tilde{\varrho}U^2\right), \quad (4.35)$$

where $C_D=A/\kappa_p^2$ and $C_F=A/(BDa^{1/2})$. Again, the leading-order streamwise momentum balance is recovered either as (4.9b) or, upon substitution of the velocity components (4.15), in the self-similar form (4.14a). Finally, expanding as in (2.2) and substituting (2.14) yields the streamwise momentum balance equation

$$\left[-\mathrm{i}\mathcal{F}\theta_f-\frac{\theta_f\eta_c}{2\hat{x}}\left(\frac{F'}{\theta_f}\right)'-\left(\frac{\theta_f'\mu}{2\hat{x}T}\right)'+\theta_f k_z^2\mu T+\frac{\left(1-\theta_f\right)^2}{\theta_f}\frac{C_D}{2\hat{x}}\mu T+\right.$$

$$+\frac{1-\theta_f}{\theta_f}\frac{C_F}{\hat{x}}F'\Bigg]\bar{u}+F'\left.\frac{\partial\bar{u}}{\partial\hat{x}}\right|_\eta-\left(\frac{F}{2\hat{x}}+\frac{\theta_f'\mu}{2\hat{x}T}\right)\frac{\partial\bar{u}}{\partial\eta}-\left(\frac{\theta_f\mu}{2\hat{x}T}\frac{\partial\bar{u}}{\partial\eta}\right)'+\frac{\theta_f}{T}\left(\frac{F'}{\theta_f}\right)'\bar{v}+$$
$$+\left[\frac{F}{2\hat{x}T}\left(\frac{F'}{\theta_f}\right)'+\frac{(1-\theta_f)^2}{\theta_f^2}\frac{C_D}{2\hat{x}}\mu'F'-\frac{1-\theta_f}{\theta_f^2}\frac{C_F}{2\hat{x}}\frac{(F')^2}{T}\right]\bar{\tau}-\left(\frac{\mu'F''}{2\hat{x}T}\bar{\tau}\right)'=0. \quad (4.36)$$

The same procedure applied to (A.20) yields the wall-normal momentum balance equation for the linearised disturbances

$$\Bigg[\frac{TF-\eta_cTF'+\eta_cT'F-\eta_c^2TF''}{4\hat{x}^2}+\frac{\theta_f'}{\theta_f}\left(\frac{TF'}{4\hat{x}^2}-\frac{\eta_cTF}{4\hat{x}^2}\right)+\frac{2GF'}{(2\hat{x})^{1/2}}+$$
$$+\left(\frac{\theta_f'\eta_c\mu}{12\hat{x}^2}\right)'\Bigg]\bar{u}+\left(\frac{\theta_f\mu'T'}{3\hat{x}}-\frac{\theta_f'}{\theta_f}\frac{\mu}{3\hat{x}}-\frac{\theta_f'\mu}{6\hat{x}}\right)\left.\frac{\partial\bar{u}}{\partial\hat{x}}\right|_\eta+\Bigg[\frac{\theta_f'\eta_c\mu}{12\hat{x}^2}+\left(\frac{\theta_f\eta_c\mu}{12\hat{x}^2}\right)'+$$
$$+\frac{\theta_f'}{\theta_f}\frac{\eta_c\mu}{6\hat{x}^2}\Bigg]\frac{\partial\bar{u}}{\partial\eta}+\frac{\theta_f\eta_c\mu}{12\hat{x}^2}\frac{\partial^2\bar{u}}{\partial\eta^2}+\Bigg[-\mathrm{i}\mathcal{F}\theta_f+\frac{F}{2\hat{x}}+\frac{\theta_f'}{\theta_f}\left(\frac{F}{2\hat{x}}-\frac{\eta_cF'}{2\hat{x}}\right)-\frac{FT'}{2\hat{x}T}+$$
$$+\frac{\eta_cF''}{2\hat{x}}-\left(\frac{2\theta_f'\mu}{3\hat{x}T}\right)'+\theta_fk_z^2\mu T+\frac{(1-\theta_f)^2}{\theta_f}\frac{C_D}{2\hat{x}}\mu T\Bigg]\bar{v}+F'\left.\frac{\partial\bar{v}}{\partial\hat{x}}\right|_\eta+$$
$$-\left[\frac{F}{2\hat{x}}+\frac{2\theta_f'\mu}{3\hat{x}T}+\frac{\theta_f'}{\theta_f}\frac{\mu}{3\hat{x}T}\right]\frac{\partial\bar{v}}{\partial\eta}-\left(\frac{2\theta_f\mu}{3\hat{x}T}\frac{\partial\bar{v}}{\partial\eta}\right)'+\left(\frac{\theta_f\mu'T'}{3\hat{x}}-\frac{\theta_f'}{\theta_f}\frac{\mu}{3\hat{x}}-\frac{\theta_f'\mu}{6\hat{x}}\right)\bar{w}+$$
$$-\frac{\theta_f\mu}{6\hat{x}}\frac{\partial\bar{w}}{\partial\eta}+\Bigg[\frac{\eta_c}{4\hat{x}^2}\left(\frac{FF'}{\theta_f}\right)'-\frac{F}{4\hat{x}^2}\left(\frac{F}{\theta_f}\right)'-\frac{1}{\theta_f}\frac{T'F^2}{4\hat{x}^2T}-\frac{G}{(2\hat{x})^{1/2}}\frac{(F')^2}{\theta_fT}+$$
$$+\left(\frac{\mu'T'F}{3\hat{x}^2T}\right)'-\left(\frac{\eta_c\mu'F''}{4\hat{x}^2}\right)'+\frac{(1-\theta_f)^2}{4\hat{x}^2\theta_f^2}C_D\left(-\mu'T^2F+\eta_c\mu'T^2F'\right)-\frac{(\theta_f')^2}{\theta_f^3}\frac{\mu'F}{6\hat{x}^2}+$$
$$+\frac{\theta_f'}{\theta_f^2}\frac{\mu'T'F}{6\hat{x}^2T}\Bigg]\bar{\tau}-\frac{\mu'F''}{2\hat{x}}\left.\frac{\partial\bar{\tau}}{\partial\hat{x}}\right|_\eta+\left(\frac{\mu'T'F}{3\hat{x}^2T}-\frac{\eta_c\mu'F''}{4\hat{x}^2}\right)\frac{\partial\bar{\tau}}{\partial\eta}+\frac{\theta_{\partial ff}}{2\hat{x}}\frac{\partial\bar{p}}{\partial\eta}=0. \quad (4.37)$$

Note that the curvature (Görtler) term is not present in the leading-order balance of the base flow, which reduces to $\partial P/\partial y=0$ since $Re^{1/2}r_c\gg1$ [Hall, 1983]. The same procedure applied to (A.24) yields the spanwise momentum balance equation for the linearised disturbances

$$-\left(k_z^2\theta_f\frac{\eta_c\mu'TT'}{2\hat{x}}+k_z^2\frac{\theta_f'\eta_c\mu T}{6\hat{x}}\right)\bar{u}+\frac{k_z^2\theta_f\mu T}{3}\left.\frac{\partial\bar{u}}{\partial\hat{x}}\right|_\eta-k_z^2\frac{\theta_f\eta_c\mu T}{6\hat{x}}\frac{\partial\bar{u}}{\partial\eta}+\Bigg(k_z^2\frac{\theta_f'\mu}{3}+$$
$$+k_z^2\theta_f\mu'T'\Bigg)\bar{v}+\frac{k_z^2\theta_f\mu}{3}\frac{\partial\bar{v}}{\partial\eta}+\Bigg[-\mathrm{i}\mathcal{F}\theta_f-\left(\frac{\theta_f'\mu}{2\hat{x}T}\right)'+\frac{4}{3}k_z^2\theta_f\mu T+\frac{(1-\theta_f)^2}{\theta_f}\frac{C_D}{2\hat{x}}\mu T\Bigg]\bar{w}+$$
$$+F'\left.\frac{\partial\bar{w}}{\partial\hat{x}}\right|_\eta-\left[\frac{F}{2\hat{x}}+\left(\frac{\theta_f\mu}{2\hat{x}T}\right)'\right]\frac{\partial\bar{w}}{\partial\eta}-\frac{\theta_f\mu}{2\hat{x}T}\frac{\partial^2\bar{w}}{\partial\eta^2}+k_z^2\frac{\mu'T'F}{3\hat{x}}\bar{\tau}-\theta_{\partial ff}k_z^2T\bar{p}=0. \quad (4.38)$$

Equations (4.36)–(4.38) reduce to (2.10)–(2.12) above the porous-free fluid interface where $\theta_f\sim\theta_{\partial ff}\sim1$ and $\theta_f'=\theta_{\partial ff}'=0$.

4.1.2.3 Static enthalpy balance

The static enthalpy balance (A.34) is multiplied by h_1 and summed to the continuity equation (A.12) multiplied by $h_1 c_p^*$. The result is multiplied by h_1 once more and the resulting terms on the left-hand side are

$$h_1^2 c_p^* \left[\frac{\partial \left(\rho^* T^*\right)}{\partial t^*} + \frac{\partial \left(\rho^* v^* T^*\right)}{\partial y^*} + \frac{\partial \left(\rho^* w^* T^*\right)}{\partial z^*} \right] + h_1 c_p^* \left[\frac{\partial \left(\rho u^* T^*\right)}{\partial x^*} \right]. \tag{4.39}$$

The volume averaging operators (4.1a) are then applied and the dispersive fluxes are neglected [Bear and Bachmat, 1990]. The transport term on the left-hand side then takes the form

$$\begin{aligned} h_1^2 c_p^* \theta_f \frac{\partial}{\partial t^*} \left(\left\langle \rho^* \right\rangle_f \left\langle T^* \right\rangle_f \right) + h_1 c_p^* \frac{\partial}{\partial x^*} \left(\theta_f \left\langle \rho^* \right\rangle_f \left\langle u^* \right\rangle_f \left\langle T^* \right\rangle_f \right) + \\ + h_1^2 c_p^* \frac{\partial}{\partial y^*} \left(\theta_f \left\langle \rho^* \right\rangle_f \left\langle v^* \right\rangle_f \left\langle T^* \right\rangle_f \right) + h_1^2 c_p^* \frac{\partial}{\partial z^*} \left(\theta_f \left\langle \rho^* \right\rangle_f \left\langle w^* \right\rangle_f \left\langle T^* \right\rangle_f \right). \end{aligned} \tag{4.40}$$

The heat conduction term expands as Bear and Bachmat [1990, eq. 2.6.121]

$$\begin{aligned} \frac{\partial}{\partial x^*} \left(\theta_{\partial ff} \left\langle k^* \right\rangle_f \frac{\partial \left\langle T^* \right\rangle_f}{\partial x^*} \right) + h_1^2 \frac{\partial}{\partial y^*} \left(\theta_{\partial ff} \left\langle k^* \right\rangle_f \frac{\partial \left\langle T^* \right\rangle_f}{\partial y^*} \right) + \\ + h_1 \frac{\partial h_1}{\partial y^*} \theta_{\partial ff} \left\langle k^* \right\rangle_f \frac{\partial \left\langle T^* \right\rangle_f}{\partial y^*} + h_1^2 \frac{\partial}{\partial z^*} \left(\theta_{\partial ff} \left\langle k^* \right\rangle_f \frac{\partial \left\langle T^* \right\rangle_f}{\partial z^*} \right), \end{aligned} \tag{4.41}$$

and the dissipation term (A.33) expands as

$$\begin{aligned} h_1 \theta_f \left\langle \Phi^* \right\rangle_f = \frac{2 \left\langle \mu^* \right\rangle_f}{\theta_f} \left[\frac{\partial (\theta_f \left\langle u^* \right\rangle_f)}{\partial x^*} \right]^2 + 2 \theta_f \left\langle \mu^* \right\rangle_f \left(\left\langle v^* \right\rangle_f \frac{\partial h_1}{\partial y^*} \right)^2 + \\ + 4 \left\langle \mu^* \right\rangle_f \left\langle v^* \right\rangle_f \frac{\partial h_1}{\partial y^*} \frac{\partial (\theta_f \left\langle u^* \right\rangle_f)}{\partial x^*} + \frac{2 h_1^2 \left\langle \mu^* \right\rangle_f}{\theta_f} \left[\frac{\partial (\theta_f \left\langle v^* \right\rangle_f)}{\partial y^*} \right]^2 + \\ + \frac{2 h_1^2 \left\langle \mu^* \right\rangle_f}{\theta_f} \left[\frac{\partial (\theta_f \left\langle w^* \right\rangle_f)}{\partial z^*} \right]^2 + \frac{\left\langle \mu^* \right\rangle_f}{\theta_f} \left[\frac{\partial (\theta_f \left\langle v^* \right\rangle_f)}{\partial x^*} \right]^2 + \frac{h_1^2 \left\langle \mu^* \right\rangle_f}{\theta_f} \left[\frac{\partial (\theta_f \left\langle u^* \right\rangle_f)}{\partial y^*} \right]^2 + \\ + \theta_f \left\langle \mu^* \right\rangle_f \left\langle u^* \right\rangle_f \left(\frac{\partial h_1}{\partial y^*} \right)^2 + h_1 \theta_f \left\langle \mu^* \right\rangle_f \frac{\partial (\theta_f \left\langle v^* \right\rangle_f)}{\partial x^*} \frac{\partial (\theta_f \left\langle u^* \right\rangle_f)}{\partial y^*} + \\ - \left\langle \mu^* \right\rangle_f \left\langle u^* \right\rangle_f \frac{\partial (\theta_f \left\langle v^* \right\rangle_f)}{\partial x^*} + \frac{\left\langle \mu^* \right\rangle_f}{\theta_f} \left[\frac{\partial (\theta_f \left\langle w^* \right\rangle_f)}{\partial x^*} \right]^2 + \frac{h_1^2 \left\langle \mu^* \right\rangle_f}{\theta_f} \left[\frac{\partial (\theta_f \left\langle u^* \right\rangle_f)}{\partial z^*} \right]^2 + \\ + 2 h_1 \frac{\left\langle \mu^* \right\rangle_f}{\theta_f} \frac{\partial (\theta_f \left\langle w^* \right\rangle_f)}{\partial x^*} \frac{\partial (\theta_f \left\langle u^* \right\rangle_f)}{\partial z^*} + \frac{h_1^2 \left\langle \mu^* \right\rangle_f}{\theta_f} \left[\frac{\partial (\theta_f \left\langle w^* \right\rangle_f)}{\partial y^*} \right]^2 + \\ + \frac{h_1^2 \left\langle \mu^* \right\rangle_f}{\theta_f} \left[\frac{\partial (\theta_f \left\langle v^* \right\rangle_f)}{\partial z^*} \right]^2 + 2 h_1 \frac{\left\langle \mu^* \right\rangle_f}{\theta_f} \frac{\partial (\theta_f \left\langle w^* \right\rangle_f)}{\partial y^*} \frac{\partial (\theta_f \left\langle v^* \right\rangle_f)}{\partial z^*}. \end{aligned} \tag{4.42}$$

All the terms are normalized with respect to the reference quantities in the free stream and $h_1 \sim 1$ for large r_c. The boundary-region balance based on the expansion (2.14) reads

$$\theta_f \frac{\partial}{\partial t}(\rho T) + \frac{\partial}{\partial x}(\rho u T) + \frac{\partial}{\partial y}(\rho v T) + \frac{\partial}{\partial z}(\rho w T) = \\ = (\gamma - 1)\frac{Ma}{Re}\left\{\frac{\mu}{\theta_f}\left[\frac{\partial(\theta_f u)}{\partial y}\right]^2 + \frac{\mu}{\theta_f}\left[\frac{\partial(\theta_f u)}{\partial z}\right]^2\right\} + \\ + \frac{1}{Pr}\frac{1}{Re}\left[\frac{\partial}{\partial y}\left(\theta_{\partial f f}\mu\frac{\partial T}{\partial y}\right) + \frac{\partial}{\partial z}\left(\theta_{\partial f f}\mu\frac{\partial T}{\partial z}\right)\right]. \quad (4.43)$$

Upon introducing the continuity equation (4.22) and the expansion (2.2), the terms on the left-hand side of (4.43) expand as

$$\theta_f \frac{\partial}{\partial t}(\rho T) + \frac{\partial}{\partial x}(\rho u T) + \frac{\partial}{\partial y}(\rho v T) + \frac{\partial}{\partial z}(\rho w T) = \\ = \frac{\partial}{\partial x}(\epsilon\theta_f \rho U\tilde{\tau}) + \frac{\partial T}{\partial x}(\epsilon\theta_f\rho\tilde{u} + \epsilon\theta_f\tilde{\varrho}U) + \\ + \frac{\partial}{\partial y}(\epsilon\theta_f\rho V\tilde{\tau}) + \frac{\partial T}{\partial y}(\epsilon\theta_f\rho\tilde{v} + \epsilon\theta_f\tilde{\varrho}V). \quad (4.44)$$

The terms of the dissipation function on the right-hand side of (4.43) expand as

$$(\gamma-1)\frac{Ma^2}{Re}\frac{\mu}{\theta_f}\left\{\left[\frac{\partial(\theta_f u)}{\partial y}\right]^2 + \left[\frac{\partial(\theta_f u)}{\partial z}\right]^2\right\} = (\gamma-1)\frac{Ma^2}{Re}\frac{\mu}{\theta_f}\left[\frac{\partial(\theta_f U)}{\partial y}\right]^2 + \\ + (\gamma-1)\frac{Ma^2}{Re}\left\{2\epsilon\frac{\mu}{\theta_f}\frac{\partial(\theta_f U)}{\partial y}\frac{\partial(\theta_f\tilde{u})}{\partial y} + \epsilon\frac{\mathrm{d}\mu}{\mathrm{d}T}\frac{1}{\theta_f}\left[\frac{\partial(\theta_f U)}{\partial y}\right]^2\tilde{\tau}\right\}, \quad (4.45)$$

and the heat conduction terms expand as

$$\frac{1}{Pr}\frac{1}{Re}\left[\frac{\partial}{\partial y}\left(\theta_{\partial f f}\mu\frac{\partial T}{\partial y}\right) + \frac{\partial}{\partial z}\left(\theta_{\partial f f}\mu\frac{\partial T}{\partial z}\right)\right] = \\ = \frac{1}{Pr}\frac{\epsilon}{Re}\frac{\partial}{\partial y}\left(\epsilon\theta_{\partial f f}\mu\frac{\partial\tilde{\tau}}{\partial y} + \epsilon\theta_{\partial f f}\frac{\mathrm{d}\mu}{\mathrm{d}T}\tilde{\tau}\frac{\partial T}{\partial y}\right) + \frac{1}{Pr}\frac{1}{Re}\frac{\partial}{\partial z}\left(\epsilon\theta_{\partial f f}\mu\frac{\partial\tilde{\tau}}{\partial z}\right). \quad (4.46)$$

Again, the static-enthalpy balance equation of the laminar base flow is recovered at leading order in the forms (4.9c) or (4.14b). Finally, substituting (2.14) yields the static enthalpy balance equation for the linearised disturbances

$$-\left[\frac{\theta_f\eta_c T'}{2\hat{x}} + (\gamma-1)\,Ma^2\frac{\theta_f'}{\theta_f}\frac{\mu F''}{\hat{x}T}\right]\bar{u} - (\gamma-1)\,Ma^2\frac{\mu F''}{\hat{x}T}\frac{\partial\bar{u}}{\partial\eta} + \theta_f\frac{T'}{T}\bar{v} + \\ + \left[-\mathrm{i}\mathcal{F}\theta_f + \frac{FT'}{2\hat{x}T} - (\gamma-1)\,Ma^2\frac{\mu'(F'')^2}{2\hat{x}T\theta_f} - \left(\frac{\theta_{\partial f f}\mu' T'}{2\hat{x}PrT}\right)' + \frac{\theta_{\partial f f}}{Pr}k_z^2\mu T\right]\bar{\tau} +$$

$$+ F' \left.\frac{\partial \bar{\tau}}{\partial \hat{x}}\right|_{\eta} - \left(\frac{F}{2\hat{x}} + \frac{\theta_{\partial ff}}{Pr}\frac{\mu' T'}{2\hat{x}T}\right)\frac{\partial \bar{\tau}}{\partial \eta} - \left(\frac{\theta_{\partial ff}\mu}{2\hat{x}PrT}\frac{\partial \bar{\tau}}{\partial \eta}\right)' = 0. \quad (4.47)$$

Equation (4.47) reduces to (2.13) in Viaro and Ricco [2019a] above the porous-free fluid interface where $\theta_f \sim \theta_{\partial ff} \sim 1$ and $\theta_f' = \theta_{\partial ff}' = 0$.

4.1.3 Upstream boundary-layer solution

The initial conditions are derived by following the procedure outlined in Leib et al. [1999] and Viaro and Ricco [2019a] (see appendix C). The velocity, temperature and pressure disturbances expand as (C.46) for $\hat{x} \ll 1$

$$\grave{\boldsymbol{q}}\left(\hat{x},\eta\right) = \sum_{n=0}^{\infty} \left(2\hat{x}\right)^{n/2} \left[2\hat{x}U_n\left(\eta\right),\, V_n\left(\eta\right),\, W_n\left(\eta\right),\, \left(2\hat{x}\right)^{-1/2} P_n\left(\eta\right),\, 2\hat{x}T_n\left(\eta\right)\right]. \quad (4.48)$$

The linearised boundary-region equations (4.23), (4.36)–(4.38) and (4.47) reduce to a series of coupled linear ordinary differential equations in η. For the first two terms of the series the continuity equation is

$$O\left(1\right)\Big| \left(2\theta_f - \theta_f'\eta_c + \frac{\theta_f \eta_c T'}{T}\right)U_0 - \theta_f \eta_c U_0' + \left(\frac{\theta_f'}{T} - \frac{\theta_f T'}{T^2}\right)V_0 + \frac{\theta_f}{T}V_0' + \\ + \theta_f W_0 - \left(\frac{FT'}{T^2} + \frac{2F'}{T}\right)T_0 + \frac{F}{T}T_0' = 0, \quad (4.49a)$$

$$O\left(\hat{x}^{1/2}\right)\Big| \left(3\theta_f - \theta_f'\eta_c + \frac{\theta_f \eta_c T'}{T}\right)U_1 - \theta_f \eta_c U_1' + \left(\frac{\theta_f'}{T} - \frac{\theta_f T'}{T^2}\right)V_1 + \frac{\theta_f}{T}V_1' + \\ + \theta_f W_1 - \left(\frac{FT'}{T^2} + \frac{3F'}{T}\right)T_1 + \frac{F}{T}T_1' = 0. \quad (4.49b)$$

The equations for the streamwise momentum balance are

$$O\left(1\right)\Big| \left[2F' - \theta_f \eta_c \left(\frac{F'}{\theta_f}\right)' - \left(\frac{\theta_f'\mu}{T}\right)' + \frac{\left(1-\theta_f\right)^2}{\theta_f}C_D \mu T + 2\frac{1-\theta_f}{\theta_f}C_F F'\right]U_0 + \\ - \left[F + \frac{\theta_f'\mu}{T} + \left(\frac{\theta_f \mu}{T}\right)'\right]U_0' - \frac{\theta_f \mu}{T}U_0'' + \frac{\theta_f}{T}\left(\frac{F'}{\theta_f}\right)'V_0 + \left[\frac{F}{T}\left(\frac{F'}{\theta_f}\right)' - \left(\frac{\mu' F''}{T}\right)' + \right. \\ \left. + \frac{\left(1-\theta_f\right)^2}{\theta_f^2}C_D \mu' F' - \frac{1-\theta_f}{\theta_f^2}C_F \frac{\left(F'\right)^2}{T}\right]T_0 - \frac{\mu' F''}{T}T_0' = 0, \quad (4.50a)$$

$$O\left(\hat{x}^{1/2}\right)\Big| \left[3F' - \theta_f \eta_c \left(\frac{F'}{\theta_f}\right)' - \left(\frac{\theta_f'\mu}{T}\right)' + \frac{\left(1-\theta_f\right)^2}{\theta_f}C_D \mu T + 2\frac{1-\theta_f}{\theta_f}C_F F'\right]U_1 +$$

$$- \left[F + \frac{\theta_f' \mu}{T} + \left(\frac{\theta_f \mu}{T}\right)'\right] U_1' - \frac{\theta_f \mu}{T} U_1'' + \frac{\theta_f}{T}\left(\frac{F'}{\theta_f}\right)' V_1 + \left[\frac{F}{T}\left(\frac{F'}{\theta_f}\right)' - \left(\frac{\mu' F''}{T}\right)' + \right.$$
$$\left. + \frac{(1-\theta_f)^2}{\theta_f^2} C_D \mu' F' - \frac{1-\theta_f}{\theta_f^2} C_F \frac{(F')^2}{T}\right] T_1 - \frac{\mu' F''}{T} T_1' = 0. \quad (4.50b)$$

The equations for the wall-normal momentum balance are

$$O(1)|P_0' = 0, \quad (4.51a)$$

$$O\left(\hat{x}^{1/2}\right)|P_1' = -\frac{1}{\theta_{\partial ff}} \left\{ \left[TF - \eta_c TF' + \eta_c T' F - \eta_c^2 TF'' - \frac{\theta_f'}{\theta_f} \eta_c TF + \frac{\theta_f'}{\theta_f} TF' + \right.\right.$$
$$\left. + \left(\frac{\theta_f' \eta_c \mu}{3}\right)' - \frac{2\theta_f' \mu}{3} + \frac{4\theta_f \mu' T'}{3} - \frac{4\theta_f'}{\theta_f}\frac{\mu}{3}\right] U_0 +$$
$$+ \left[-\frac{2\theta_f \mu}{3} + \frac{\theta_f' \eta_c \mu}{3} + \left(\frac{\theta_f \eta_c \mu}{3}\right)' + \frac{\theta_f'}{\theta_f}\frac{2\eta_c \mu}{3}\right] U_0' + \frac{\theta_f \eta_c \mu}{3} U_0'' +$$
$$+ \left[F' + \frac{\theta_f'}{\theta_f}(F - \eta_c F') - \frac{FT'}{T} + \eta_c F'' - \left(\frac{4\theta_f' \mu}{3T}\right)' + \frac{(1-\theta_f)^2}{\theta_f} C_D \mu T \right] V_0 +$$
$$- \left[F + \frac{4\theta_f' \mu}{3T} + \left(\frac{4\theta_f \mu}{3T}\right)' + \frac{\theta_f'}{\theta_f}\frac{2\mu}{3T}\right] V_0' - \frac{4\theta_f \mu}{3T} V_0'' + \left(\frac{2\theta_f \mu' T'}{3} - \frac{\theta_f' \mu}{3} - \frac{\theta_f'}{\theta_f}\frac{2\mu}{3}\right) W_0 +$$
$$- \frac{\theta_f \mu}{3} W_0' + \left[\eta_c \left(\frac{FF'}{\theta_f}\right)' - F\left(\frac{F}{\theta_f}\right)' - \frac{1}{\theta_f}\frac{T'F^2}{T} + \left(\frac{4\mu' T' F}{3T}\right)' - (\eta_c \mu' F'')' + \right.$$
$$+ \frac{(1-\theta_f)^2}{\theta_f^2} C_D \left(-\mu' T^2 F + \eta_c \mu' T^2 F'\right) - \frac{(\theta_f')^2}{\theta_f^3}\frac{2\mu' F}{3} + \frac{\theta_f'}{\theta_f^2}\frac{2\mu' T' F}{3T}\Bigg] T_0 - 2\mu' F'' T_0' +$$
$$\left. + \left(\frac{4\mu' T' F}{3T} - \eta_c \mu' F''\right) T_0' \right\}. \quad (4.51b)$$

The equations for the spanwise momentum balance are

$$O(1)| - \left[\left(\frac{\theta_f' \mu}{T}\right)' - \frac{(1-\theta_f)^2}{\theta_f} C_D \mu T\right] W_0 +$$
$$- \left[F + \frac{\theta_f' \mu}{T} + \left(\frac{\theta_f \mu}{T}\right)'\right] W_0' - \frac{\theta_f \mu}{T} W_0'' = 0, \quad (4.52a)$$

$$O\left(\hat{x}^{1/2}\right)| - \left[\left(\frac{\theta_f' \mu}{T}\right)' - \frac{(1-\theta_f)^2}{\theta_f} C_D \mu T - F'\right] W_1 +$$
$$- \left[F + \frac{\theta_f' \mu}{T} + \left(\frac{\theta_f \mu}{T}\right)'\right] W_1' - \frac{\theta_f \mu}{T} W_1'' = \theta_{\partial ff} k_z^2 T P_0. \quad (4.52b)$$

The equations for the static enthalpy balance are

$$O\left(1\right)\Big|\left[-\theta_f\eta_c T' - \left(\gamma-1\right)Ma^2\frac{\theta_f'}{\theta_f}\frac{2\mu F''}{T}\right]U_0 - \left(\gamma-1\right)Ma^2\frac{2\mu F''}{T}U_0' + \theta_f\frac{T'}{T}V_0 + \\ + \left[\frac{FT'}{T} - \left(\gamma-1\right)Ma^2\frac{\mu'\left(F''\right)^2}{\theta_f T} - \left(\frac{\theta_{\partial ff}\mu' T'}{PrT}\right)' + 2F'\right]T_0 + \\ - \left[F + \frac{\theta_{\partial ff}\mu' T'}{T} + \left(\frac{\theta_{\partial ff}\mu}{PrT}\right)'\right]T_0' - \frac{\theta_{\partial ff}\mu}{PrT}T_0'' = 0, \quad (4.53a)$$

$$O\left(\hat{x}^{1/2}\right)\Big|\left[-\theta_f\eta_c T' - \left(\gamma-1\right)Ma^2\frac{\theta_f'}{\theta_f}\frac{2\mu F''}{T}\right]U_1 - \left(\gamma-1\right)Ma^2\frac{2\mu F''}{T}U_1' + \theta_f\frac{T'}{T}V_1 + \\ + \left[\frac{FT'}{T} - \left(\gamma-1\right)Ma^2\frac{\mu'\left(F''\right)^2}{\theta_f T} - \left(\frac{\theta_{\partial ff}\mu' T'}{PrT}\right)' + 3F'\right]T_1 + \\ - \left[F + \frac{\theta_{\partial ff}\mu' T'}{T} + \left(\frac{\theta_{\partial ff}\mu}{PrT}\right)'\right]T_1' - \frac{\theta_{\partial ff}\mu}{PrT}T_1'' = 0. \quad (4.53b)$$

The wall-normal momentum balance is absent at leading order, and the $O(1)$-equations are effectively the unsteady, compressible boundary-layer equations of Ricco and X. Wu [2007] above the interface. The two systems are solved subject to the wall and outer boundary conditions outlined in §C.3 using a standard block elimination algorithm.

4.2 Results

The results presented in this section were obtained using physical parameters representative of real supersonic and hypersonic wind-tunnel conditions, as listed in tables 4.1 and 4.2. The corresponding numerical parameters, such as the factor Q, the interfacial thicknesses $(\Delta y)_{int}$ and $(\Delta\eta)_{int}$, and the surface temperature T_{av}, are provided in table 4.3 for reference. The results for the laminar base flow are discussed in §4.2.1, while a brief discussion on the upstream initial conditions of the linearised disturbance flow is provided in §4.2.2.

4.2.1 Laminar base flow

The flow is studied for different values of the free-stream Mach number, the static pressure and temperature, the reference grain size d_{g0}^*, and the volume porosity below the interface θ_{fp}. The combination of these physical parameters determines κ_p, C_D, C_F and $(\theta_{\partial ff})_p$. The values relevant to the investigated cases are listed in table 4.2.

Table 4.1: Wind tunnel measurements of compressible boundary layers over impermeable flat plates. Data retrieved from Graziosi and G. L. Brown [2002, GB02], Maslov, Shiplyuk, et al. [2001, M01], Running et al. [2023, R23].

Ref.	Ma	p_o^* [kPa]	T_o^* [K]	p_∞^* [kPa]	T_∞^* [K]	$T_w^*/T_{ad,w}^*$	δ_{99}^* [mm][1]
GB02	2.98	31	290	0.87	104	1.1	$[1.8, 3.3]$
M01	5.92	1080	390	0.74	49	1	$[1.8, 2.2]$
R23	6.1	$[490, 3044]$	473	56.03	$[54.25, 57.81]$	n.a.	n.a.

[1]Measured between $x = 89\,\text{mm}$ and $x = 305\,\text{mm}$ (GB02) and at $x = 96\,\text{mm}$ (M01).

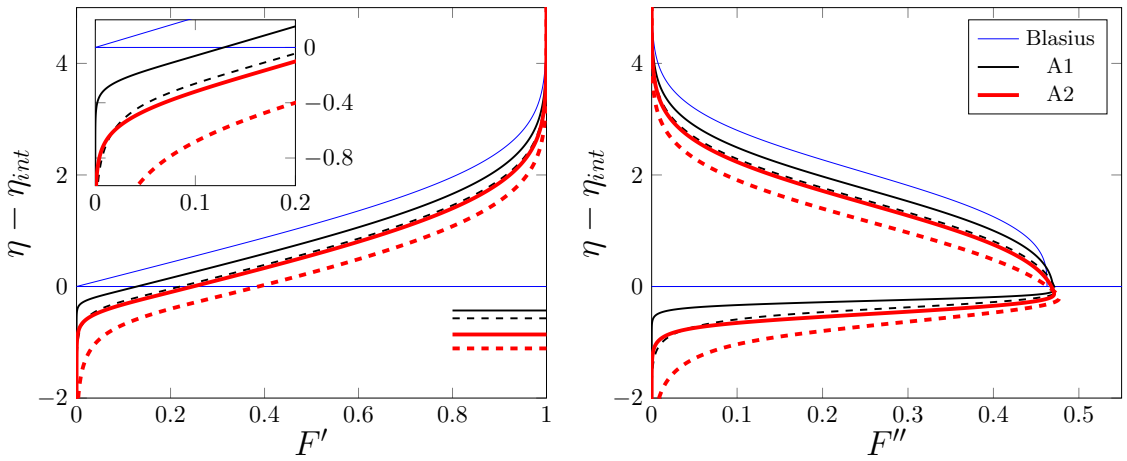

Figure 4.4: First (left plot) and second (right plot) derivative of F as a function of η for an incompressible flow ($Ma = 0.01$). The black and red curves show cases A1 and A2, respectively, for $\theta_{fp} = 0.85$ (solid) and $\theta_{fp} = 0.95$ (dashed). The Blasius solution over a non-permeable wall is plotted in blue for comparison. The top boundary of the interfacial region is located at η_{int} (blue line), while the bottom one is marked by the horizontal lines for each case.

Table 4.2: Physical parameters. The volume and surface porosity in the region below the interface are denoted with θ_{fp} and $(\theta_{\partial ff})_p$, respectively.

Ma -	p^*_∞ kPa	$p^*_\circ$ kPa	T^*_∞ K	$T^*_\circ$ K	U^*_∞ $\mathrm{m\,s^{-1}}$	δ^*_{99} mm	d^*_{g0} µm	κ_p^2 -	case -
0.01	100	100	293	293	3.43	3.3	100	0.02	A1
							200	0.09	A2
3	0.82	30.12	104	291	611	1.8	100	0.24	B1
							200	0.96	B2
6	0.76	1200	60	492	927	1.6	100	1.10	C1
							200	4.35	C2

Q	$1-Q$	$(\theta_{\partial ff})_p = 1-Q^2$	$\theta_{fp} = 1-Q^3$	$\delta^*_{int}/d^*_g = (1+Q)/Q$
0.22	0.78	0.95	0.99	5.55
0.37	0.63	0.86	0.95	3.70
0.5	0.5	0.75	0.875	3
0.53	0.47	0.72	0.85	2.89

Table 4.3: Numerical parameters used in the computations.

Ma	d^*_{g0} [µm]	κ_p^2	C_D	C_F	θ_{fp}	Q	$(\Delta y)_{int}$	T_{av}	$(\Delta\eta)_{int}$	case
0.01	100	0.02	9000	1800	0.85	0.53	0.43	1	0.43	A1
					0.95	0.37	0.57	1	0.57	
	200	0.09	2000	900	0.85	0.53	0.86	1	0.86	A2
					0.95	0.37	1.11	1	1.11	
3	100	0.24	750	1800	0.85	0.53	1.42	2.43	0.58	B1
					0.95	0.37	1.83	2.31	0.79	
	200	0.96	187.5	900	0.85	0.53	2.83	2.32	1.22	B2
					0.95	0.37	3.63	2.23	1.63	
6	100	1.10	163.6	1800	0.85	0.53	3.01	6.74	0.45	C1
					0.95	0.37	3.88	6.28	0.62	
	200	4.35	41.3	900	0.85	0.53	6.02	6.39	0.94	C2
					0.95	0.37	7.76	5.64	1.38	

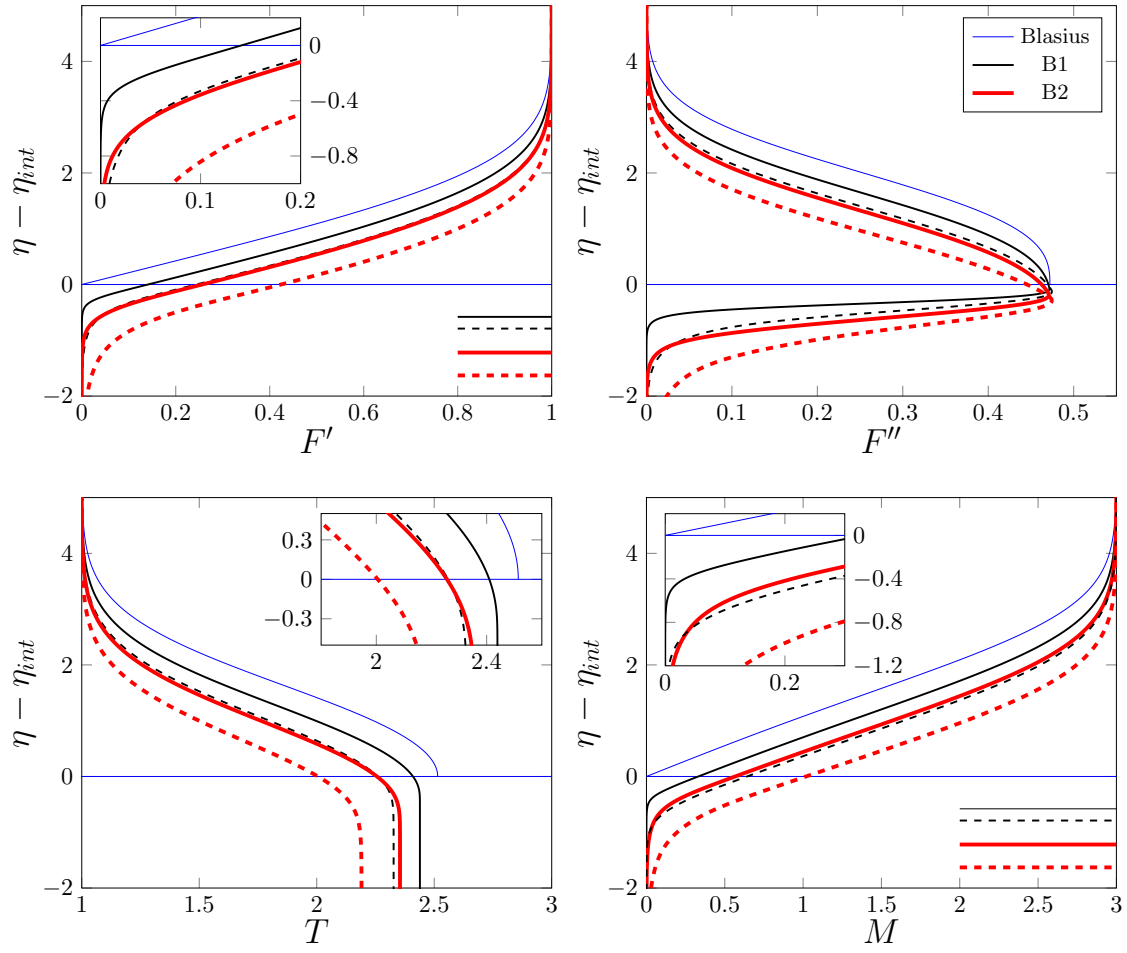

Figure 4.5: First (top left) and second derivative (top right) of F as a function of η for a supersonic flow at $Ma = 3$. The static temperature T and the local Mach number M are shown in the bottom-left and bottom-right plots, respectively. The black and red curves show cases B1 and B2, respectively, for $\theta_{fp} = 0.85$ (solid) and $\theta_{fp} = 0.95$ (dashed). The Blasius solution over a non-permeable wall is plotted in blue for comparison. The top boundary of the interfacial region is located at η_{int} (blue line), while the bottom one is marked by the horizontal lines for each case.

For every case, the letter (A, B or C) defines a set of free-stream conditions, while the number (1 or 2) defines d^*_{g0}. The dimensional thickness of the Blasius boundary layer at $x^* = L^*$ is $\delta^*_{99} = \widehat{\delta}_{99}\,(\nu^*_\infty L^*/U^*_\infty)^{1/2}$. Here $\widehat{\delta}_{99} = 2^{1/2}\int_0^{\eta_{99}} T(\breve{\eta})\mathrm{d}\breve{\eta}$ increases with Ma and is a function of γ, Pr, and the temperature boundary condition at the bottom solid wall. The values of δ^*_{99}, estimated in table 4.2, are in good agreement with wind tunnel measurements (refer to table 4.1). The stagnation pressure is $p^*_\circ$, the stagnation temperature is $T^*_\circ$, the dimensional wall temperature is T^*_w and the adiabatic recovery temperature of the Blasius solution is $T^*_{ad,w}$.

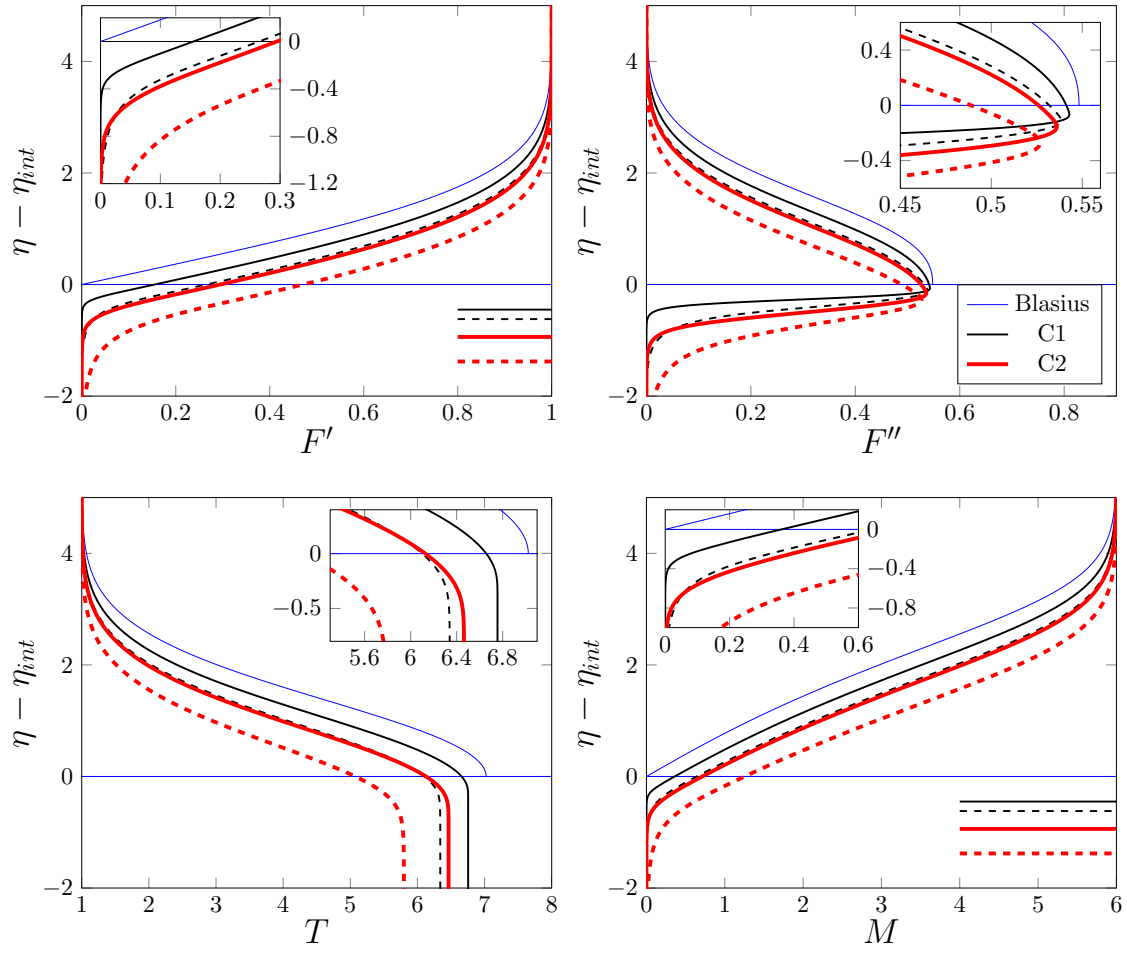

Figure 4.6: First (top left) and second derivative (top right) of F as a function of η for a supersonic flow at $Ma = 6$. The static temperature T and the local Mach number M are shown in the bottom-left and bottom-right plots, respectively. The black and red curves show cases C1 and C2, respectively, for $\theta_{fp} = 0.85$ (solid) and $\theta_{fp} = 0.95$ (dashed). The Blasius solution over a non-permeable wall is plotted in blue for comparison. The top boundary of the interfacial region is located at η_{int} (blue line), while the bottom one is marked by the horizontal lines for each case.

Results for an incompressible, isothermal ($T_{av} = 1$) boundary layer at $Ma = 0.01$ (cases A1 and A2) are shown in figure 4.4. The first and second derivative of the streamfunction F are plotted as functions of η for two different values of the volume porosity θ_{fp} and characteristic grain size d^*_{g0} (κ_p). The top of the free fluid-porous interfacial region described in figure 4.3 is located at $\eta = \eta_{int}$ (thin horizontal blue line in figure 4.4), and its lower boundary is denoted by a thin horizontal black or red line for each case. The Blasius solution for a flat-plate boundary layer is also drawn for comparison (blue curve), its solid wall being located at the top of the

interfacial region [Breugem and Boersma, 2005], where $\theta_f = 1$ and the Darcy and Forchheimer terms become zero. The slip velocity, obtained by evaluating (4.15a) at the interface, increases with θ_{fp} and d^*_{g0}, in qualitative agreement with the results of Tsiberkin [2018a] and Tsiberkin [2018b], which showed increasing interfacial velocity for increasing values of the control parameter κ_p^2 without the Forchheimer correction. The incompressible intrinsic shear stresses $\tau = (F'' - F'\theta_f'/\theta_f)/\theta_f$ [Breugem, Boersma, and Uittenbogaard, 2005, equations 116-117] are mostly influenced by F'' and grow to a peak located at the interface in all cases. Both F' and F'' undergo a rapid decay across the interface and within the porous region.

The results of the supersonic cases are shown in figure 4.5 and 4.6. Adiabatic boundary conditions were imposed at the solid wall below the substrate. The profiles for F' and F'' are shown along with the temperature T (bottom left) and the local Mach number $M = u^*/(\gamma \mathcal{R}^* T^*)^{1/2} = Ma\, F'/(\theta_f T^{1/2})$ (bottom right). The slip velocity increases and F'' decreases with increasing d^*_{g0} and θ_{fp} for constant free-stream conditions. Moreover, the temperature T does not recover the adiabatic value of the compressible Blasius solution and it reduces sharply at the interface when a porous substrate is introduced. The reduction becomes more marked with increasing κ_p and θ_{fp}. The peak of F'' is not sensitive to the geometry of the substrate. The influence of the porous substrate on the velocity profiles extends far from the interface, where F'' is reduced. As the F' profile shifts towards the interface and the magnitude of T decreases, the local Mach number M increases across the boundary layer (refer to the bottom right plots of figures 4.5 and 4.6). The insets in the bottom-right plot of figures 4.5 and 4.6 show that M is always well below unity near the bottom boundary of the interfacial region where the top solid cubes are located. This finding rules out the presence of shock waves and choking.

Figure 4.7 shows that the Darcy term and Forchheimer term in the momentum equation (4.14a) reach a comparable magnitude for all values of Ma, κ_p and θ_{fp}. The Forchheimer correction is considerably lower than the Darcy drag for low κ_p (low d^*_{g0}) and θ_{fp}, but increases and becomes slightly larger as either κ_p or θ_{fp} increase. This behavior is reported for all Mach numbers as shown in the right plot of figure 4.7, in which the free-stream conditions are fixed and the grain size and the porosity are gradually increased. Because the coefficient C_F is assumed to be a function of d^*_{g0} instead of d^*_g, this result suggests that the local similarity assumption holds better at moderate θ_{fp} and κ_p [Tsiberkin, 2018b] for all Mach numbers.

The dimensional profiles of the streamwise velocity u^* and the static temperature T^* are computed at a distance $x^* = L^*$ from the leading edge and are plotted in

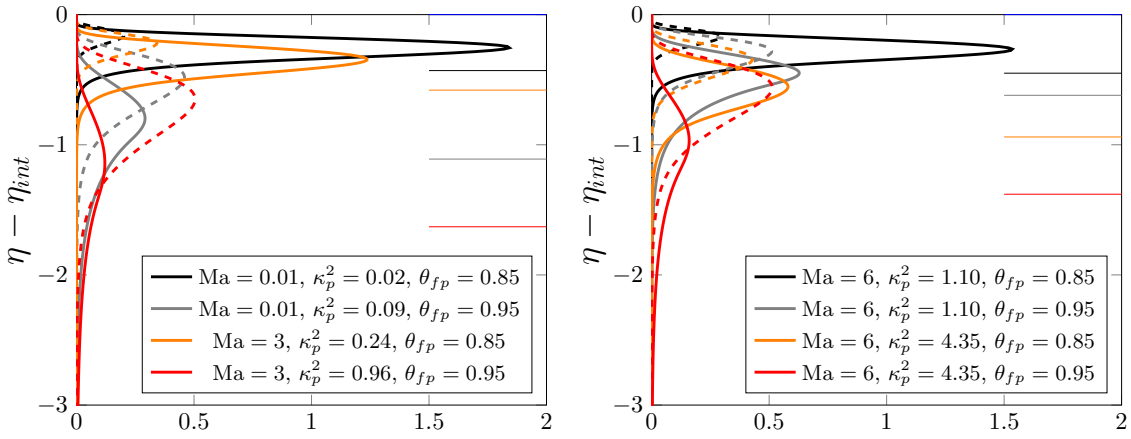

Figure 4.7: Wall-normal profiles of the Darcy term (solid curves) and Forchheimer term (dashed curves) within the interfacial region for the cases A1, A2, B1 and B2 (left plot) and C1 and C2 (right plot).

figure 4.8 for the Mach-3 cases B1 and B2 and the Mach-6 cases C1 and C2. The physical coordinate y^* is computed by $y^* = x^*(2/Re_x)^{1/2} \int_0^\eta T\,(\breve{\eta})\,\mathrm{d}\breve{\eta}$, where Re_x is the Reynolds number based on x^* [Stewartson, 1964]. The boundary-layer thickness of the Blasius solution (blue curve) compares well to the measurements of Graziosi and G. L. Brown [2002] and Maslov, Shiplyuk, et al. [2001] (refer to table 4.1). Both F' and F'' are small at the bottom solid wall ($\cong 10^{-4}$), which makes the choice of η_{int} arbitrary. Because the depth of the porous substrate is kept constant at $\eta_{int} = 10$ in the η-space and varies slightly in the y-space, the physical plots in figure 4.8 are offset and centered at the interface. Again, the velocity profiles shift towards the interface and the boundary-layer thickness is reduced as both d_{g0}^* and θ_{fp} increase, while the temperature at the interface decreases. To better compare the porous-plate and the solid-plate results, the center of the interfacial region and the wall of the non-porous solution are placed at the same height in figure 4.8. The upper and lower boundaries of the interface are here denoted by the horizontal black and red lines. The departure of the velocity profile from the compressible Blasius solution is very small in the case C1, $\theta_{fp} = 0.85$. Only for larger porosities and grain sizes the seepage becomes significant. This finding agrees qualitatively with the recent experiments of Running et al. [2023], who studied the development of a boundary layer over a porous substrate. Their measurements agreed well with the numerical results obtained from the computation of a no-slip, flat-plate, boundary-layer flow. They used a silicon-carbide foam porous insert with $\theta_{fp} = 0.862$ and 3.9 pores per linear millimeter, which corresponds to

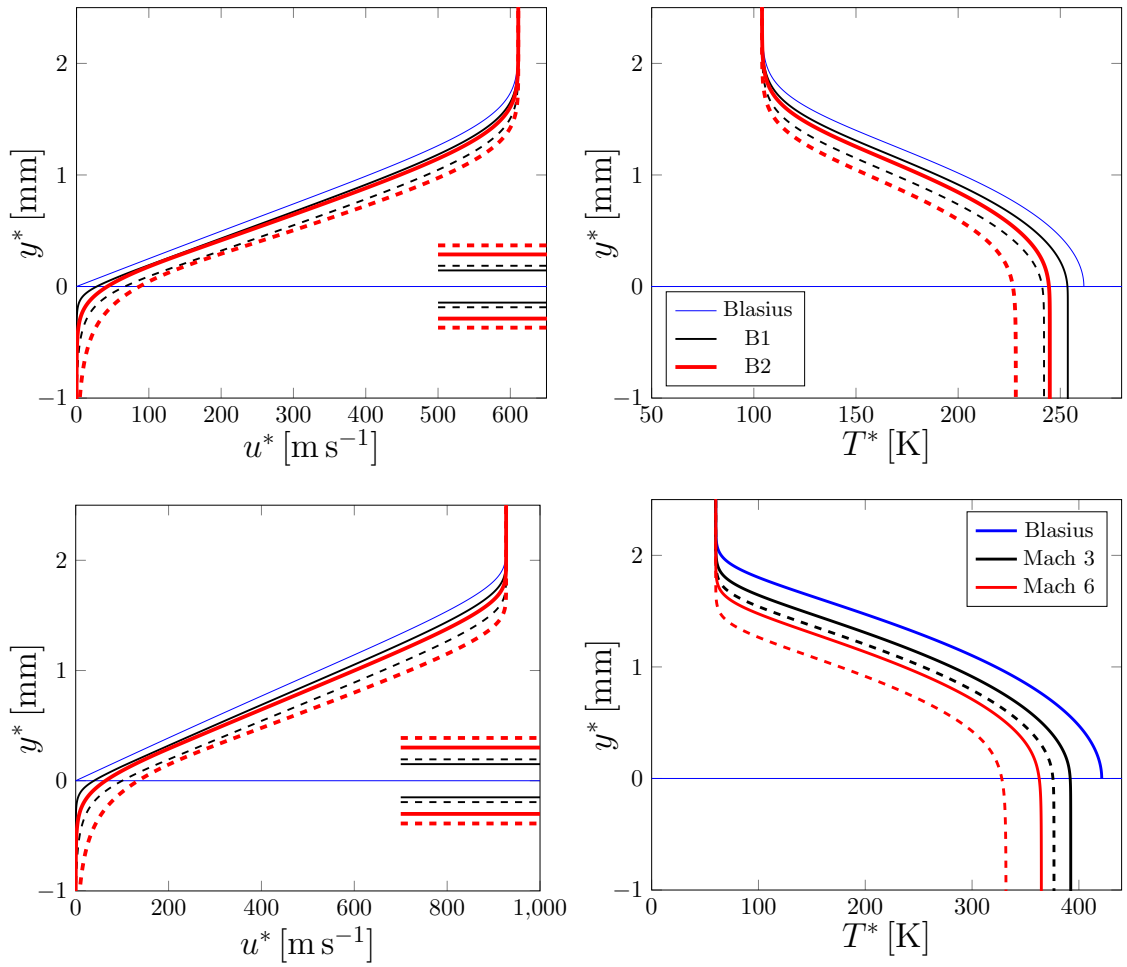

Figure 4.8: Dimensional velocity and temperature profiles at a free-stream Mach number 3 (cases C1 and C2, top) and 6 (cases C1 and C2, bottom). The interfacial thickness is $\delta^*_{int} = 408\,\mu$m (B1 and C1, $\theta_{fp} = 0.85$), 525 µm (B1 and C1, $\theta_{fp} = 0.95$), 815 µm (B2 and C2, $\theta_{fp} = 0.85$), 1051 µm (B2 and C2, $\theta_{fp} = 0.95$). The effect of varying θ_{fp} and d^*_{g0} is shown. The Mach-3 and Mach-6 adiabatic Blasius solution is plotted in blue.

$d^*_{g0} = 130\,\mu$m in the present model. The present results suggest that porous media with higher θ_{fp} and d^*_{g0} should be used to affect the base flow significantly.

The effect of varying the temperature of the bottom solid wall is shown in figure 4.9 for the case C2, $\theta_{fp} = 0.85$. Because natural convection within the medium is not captured by the present model, wall-cooling conditions for which the bottom-wall temperature T_w is lower than the adiabatic recovery temperature of the substrate are considered. The temperature curves (figure 4.9, left plot) approach the adiabatic case as the ratio $T_w/T_{ad,w}$ increases. The temperature at the interface decreases from $T_w/T_{ad,w} = 1$ to $T_w/T_{ad,w} = 0.85$ with respect to the Blasius solution. However, as the

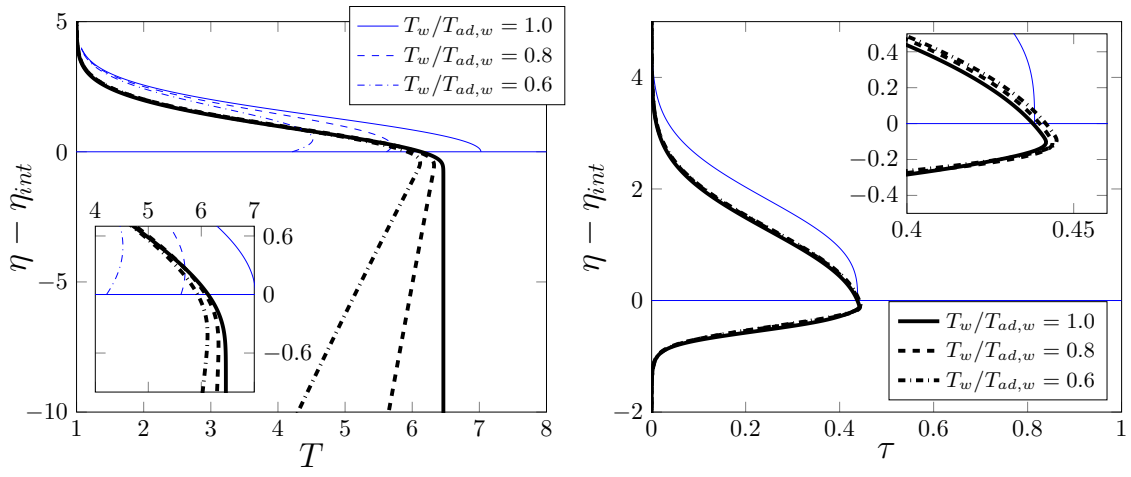

Figure 4.9: Effect of the temperature boundary conditions at the wall at $Ma = 6$. The curves are computed for different values of $T_w/T_{ad,w}$, where $T_{ad,w} = 7.02$ is the adiabatic wall temperature of the Blasius solution. The blue curves represent the Blasius solution, and the black ones the porous substrate solution (C2, $\theta_{fp} = 0.85$). The adiabatic recovery temperature at the solid wall is 6.46.

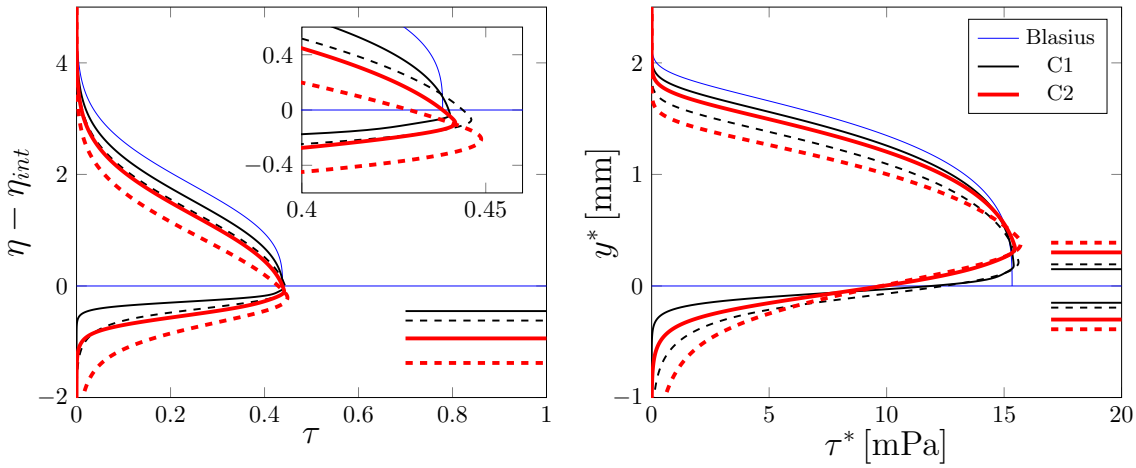

Figure 4.10: Distribution of the intrinsic shear stresses for variable geometry (κ_p and θ_{fp}) in transformed (left) and real, dimensional coordinates at $x^* = L^*$ (right).

ratio decreases further, the temperature at the interface remains higher and decreases linearly where the flow is stagnant. Equations (4.9c) and (4.14b) then reduce to the steady homogeneous heat conduction equation as in the model of Nield and Kuznetsov [2003]. The value of F'' at the wall of a Blasius boundary layer is quite sensitive to the temperature boundary condition, a behavior not observed at the top surface of a porous wall. The F' and F'' profiles are unaffected by the ratio $T_w/T_{ad,w}$ (refer to the right plot of figure 4.9). The distribution of the compressible intrinsic shear stresses

$\tau = \mu(F'' - F'\theta_f'/\theta_f)/(\theta_f T)$, shown in the plots in figure 4.10, is mostly affected by the geometry of the substrate, whereas the effect of $T_w/T_{ad,w}$ is again negligible. The peaks increase slightly and appear to be always located near the top boundary of the interface. A sharp reduction in the intrinsic shear stresses occurs in the free-fluid region above the interface when a substrate of high porosity is introduced.

4.2.2 Upstream perturbation profiles

The velocity and thermal streaks computed in the vicinity of the leading-edge $\hat{x} \ll 1$ are shown in figure 4.11 for an adiabatic, Mach-3 boundary layer. The results for an impermeable flat plate (blue curves) are compared to those computed by solving the base flow (4.14) and the initial perturbation profiles at order zero (4.49a), (4.50a), (4.51a), (4.52a), (4.53a) for $d_{g0}^* = 200\mu$m and a volume porosity of $\theta_{fp} = 0.85$ (solid) and $\theta_{fp} = 0.95$ (dashed) and compared to the solutions of a compressible Blasius boundary layer over a solid wall.

The profiles are computed for different values of the self-similar streamfunction at the solid wall underneath the porous layer $F_w = F(\eta = 0)$. Non-zero values of F_w correspond to non-zero values of the wall-normal velocity (4.15b) and self-similar suction at the bottom solid boundary. A strong attenuation is obtained when suction is applied at a moderate volume porosity $\theta_{fp} = 0.85$. A negative vertical velocity is imposed at the solid wall underneath the porous wall by specifying a positive value of the stream function, which is $F_w = 1.5$ in the cases shown in figure 4.11. While the presence of a passive porous wall without suction increases the intensity of the velocity streaks and decreases the intensity of the thermal streaks, the application of suction at moderate porosities strongly attenuates the velocity streaks when $\theta_{fp} = 0.85$.

Attempts to solve the porous-CLUBR equations (4.23), (4.36), (4.37), (4.38), and (4.47) using a block-elimination algorithm have been unsuccessful. While the submatrices of the tridiagonal system are well-conditioned and the computed solutions appear to satisfy the boundary conditions, they exhibit pronounced non-physical oscillations near the interface. The underlying cause of this behavior remains unclear and requires further investigation.

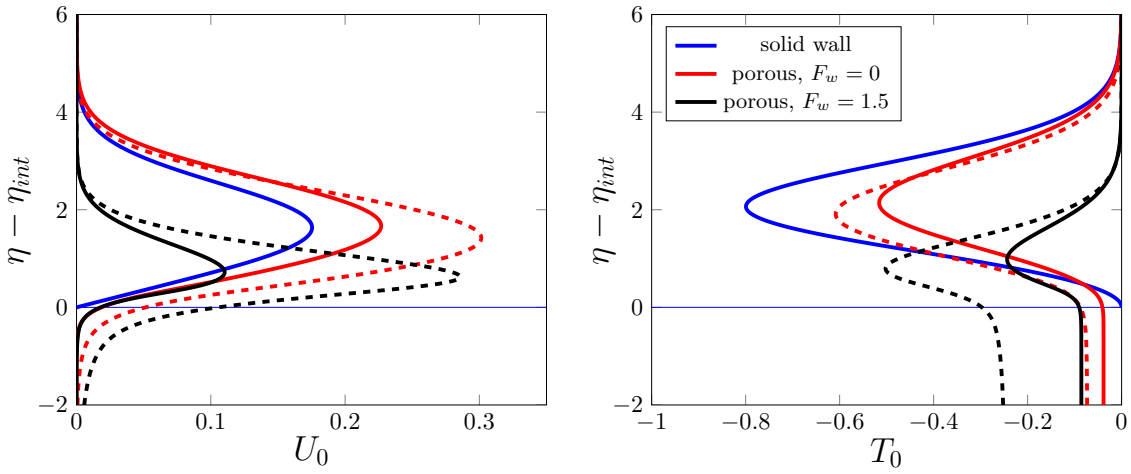

Figure 4.11: Velocity streaks (left) and thermal streaks (right) in the vicinity of the leading edge at Mach 3. The blue curves represent the solution over an impermeable plate. The solution over a porous plate with (black, $F_w = 1.5$) and without (red $F_w = 0$) self-similar suction is plotted for comparison. The solid curves represent the case $\theta_{fp} = 0.85$, and the dashed curves the case $\theta_{fp} = 0.95$.

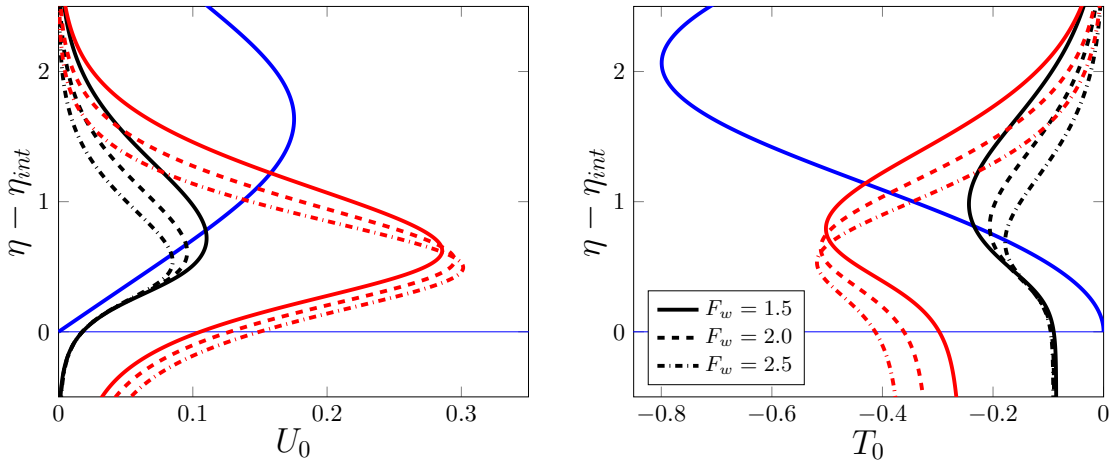

Figure 4.12: Velocity (left) and thermal streaks (right) in the vicinity of the leading edge at Mach 3. The blue curves represent the solution over an impermeable plate. The solution over a porous plate with self-similar suction is plotted for different values of the streamfunction at the bottom solid wall F_w.

Chapter 5

Conclusions

In this thesis, the effect of uniform wall suction and passive porous coatings on the receptivity of compressible boundary layers to free-stream vortical disturbances has been explored using asymptotic and numerical methods. Control mechanisms hinder disturbance growth by modifying either the structure of the unperturbed laminar base flow (i.e., the compressible Blasius solution) or the disturbances within the boundary layer. For the first time, this work has explored how uniform wall suction reshapes the laminar base flow and how passive porous coatings influence both the base flow and the evolution of laminar streaks and Görtler vortices. The excitation mechanisms of these disturbances have been analysed in detail, revealing their sensitivity to different control strategies and providing new insights into their suppression in the early stage of transition.

Chapter 2 has focused on uniform wall suction. A laminar boundary layer developing over a suction actuator undergoes a complex transition from the impermeable leading-edge region to its asymptotic-suction state. Since receptivity is crucial near the leading edge, neither the self-similar nor the asymptotic-suction model accurately captures the base-flow evolution or the effect of suction on disturbance growth. To address this, the boundary-region framework of Leib et al. [1999], Ricco and X. Wu [2007], X. Wu, D. Zhao, et al. [2011], and Viaro and Ricco [2019a] has been extended to non-similar compressible flows and solved numerically for the first time. The non-similarity of the viscous layer alters the asymptotic matching between the external flow and the boundary layer, affecting the free-stream boundary conditions. The computed base flow with suction has been validated against incompressible wind-tunnel data and direct numerical simulations of hypersonic boundary layers. The disturbance analysis shows that wall suction significantly reduces the amplitude of compressible Görtler vortices. Neutral stability curves quantify the stabilizing effect, revealing that higher suction rates enlarge stability regions. These findings suggest that suction is

effective in delaying transition on streamwise-concave surfaces for subsonic and moderately supersonic Mach numbers. However, its effectiveness diminishes at hypersonic speeds due to increased wall temperature. Nonetheless, wall suction remains valuable for delaying transition in supersonic wind tunnel nozzles and as a control strategy for high-speed vehicles.

The effect of regular-microstructure porous coatings on the receptivity of supersonic pre-transitional boundary layers to free-stream vortical disturbances has been studied in chapter 3. The focus has been on the downstream evolution of laminar streaks over flat and concave surfaces and Tollmien-Schlichting waves generated by the external perturbations. The downstream development of the laminar streaks is largely unaffected by the wall porosity when the spanwise wavelength of the oncoming perturbation is of the same order of magnitude of the boundary-layer thickness. As either the frequency or the spanwise wavelength of the disturbances increases, the wall-normal velocity and the pressure interact at the wall and the boundary-layer streamwise velocity and temperature fluctuations are attenuated. This beneficial effect is enhanced further by wall cooling. The growth rate of Tollmien-Schlichting waves, triggered by a leading-edge adjustment mechanism, is enhanced by the wall porosity, and the location of instability moves upstream. These waves are the first modes of compressible instability, so this finding confirms previous experimental results. A triple-deck asymptotic analysis quantitatively confirms the numerical results and reveals how the physical mechanism of instability is altered in the presence of wall porosity. The porous layer also reduces the amplitude of the streaks over concave surfaces during their initial development and the growth rate of the streamwise velocity fluctuations further downstream.

In chapter 4, a self-similar solution has been derived for a compressible laminar boundary layer flowing over an isotropic porous substrate of streamwise-increasing permeability. The solution includes a linear Darcy term and a quadratic Forchheimer correction. The volume averaged momentum and enthalpy balance equations become parabolic in the limit of high Reynolds and small Darcy numbers. The effect of the porous substrate is distilled in the distributions of the volume and surface porosity, the control parameter κ_p and the Forchheimer coefficient C_F. The thicknesses of the interface and the boundary layer are comparable, and the volume and surface porosity vary smoothly therein. The wall-normal profiles of the streamwise velocity F', its wall-normal derivative F'' and the temperature T have been computed for different values of the Mach number, the control parameter, and the volume porosity below the interface. The profiles bear a strong resemblance to the Blasius solution

for low values of κ_p and $\theta_{fp} \leq 0.85$. The slip velocity at the porous-free fluid interface increases, and the intrinsic shear stresses decrease sharply, as the volume porosity approaches unity. Wall cooling at the bottom solid boundary affects neither the velocity profiles nor the shear stresses when the porous substrate is sufficiently thick. A sharp reduction in the intrinsic shear stresses and the static temperature is observed above the interface. This result shows that the introduction of a porous substrate of high porosity and permeability can substantially alter the properties of a supersonic laminar boundary layer, which is significant to flow control applications [Maslov, Mironov, et al., 2019; Running et al., 2023]. The amplitude of the streamwise velocity fluctuations is enhanced by the wall-porosity near the leading edge.

5.1 Future developments

Future work should focus on extending the non-similar boundary-region formulation to take into account nonlinearity and the secondary instability of the compressible Görtler vortices as next steps to evince the influence of wall suction on transition delay. Suction non-uniformity at the pore scale and the coexistence of acoustic and vortical disturbances should also be studied.

Further work is required to solve the boundary-region equations for isotropic porous surfaces. Future research should focus on testing alternative numerical schemes and extending the current framework to non-similar boundary-layer flows over porous media with uniform permeability. An important next step involves investigating the effects of porous coatings with regular microstructure on nonlinear compressible flows, as studied by Marensi, Ricco, and X. Wu [2017], and incorporating the higher-frequency second-Mack mode instability into the analysis [Goldstein and Ricco, 2018]. Additionally, it is important to explore how wall porosity affects secondary instability and the final stages of transition, with the goal of precisely determining the influence of the porous wall on the transition location.

The present thesis has focused on the linear response of boundary layers over porous walls to a monochromatic vortical disturbance. The full spectrum of free-stream disturbances, including acoustic and temperature fluctuations, and the nonlinear interaction of different modes should be considered in a more realistic context. Some of these aspects have been investigated by Y. Zhang et al. [2011], Xu, Y. Zhang, et al. [2017] and Xu, J. Liu, et al. [2020].

The theoretical and numerical results presented in this thesis require further numerical and experimental validation. The lack of experimental data of suction through

concave porous walls in the compressible regime represents a critical issue to be addressed. Direct numerical simulations and wind tunnel or in-flight measurements of supersonic boundary-layer receptivity to free-stream vortical disturbances remain ambitious yet critical objectives. Hopefully, this study will encourage further research into boundary-layer control through the use of porous surfaces.

Appendix A

Governing equations in curvilinear coordinates

The Navier-Stokes equations in curvilinear coordinates are derived using the vector identities reported by Sutter [1962] (see also Sokolnikoff [1951, pp. 319–325] and Mattioli [1992, pp. 182–207]). Additionally, the derivation of the dissipation term in the static enthalpy equation, which is not readily available in the literature, is presented. Dimensional quantities are denoted by a superscript $*$.

The vector identities are introduced in §A.1, while the curvilinear coordinate system for a concave plate and the corresponding Lamé coefficients are introduced in §A.2. The continuity and momentum balance equations are derived in §A.2.1, while the static enthalpy balance equation is presented in §A.2.2. Einstein summation convention is assumed throughout this chapter.

A.1 Vector identities

Let g_{ii} be the metric tensor and g its determinant. The velocity vector is $\boldsymbol{u} = u_i$, where $i = 1, 2, 3$ and $u_1^* = u^*$, $u_2^* = v^*$ and $u_3^* = w^*$. The divergence of the vector field in the mass conservation equation is

$$\nabla^* \cdot (\rho^* \boldsymbol{u}^*) = \frac{1}{\sqrt{g}} \frac{\partial}{\partial x^j} \left(\frac{\sqrt{g}}{\sqrt{g_{jj}}} \rho^* u_j^* \right). \tag{A.1}$$

The nonlinear advection term

$$\left[\frac{\mathrm{D}\boldsymbol{u}^*}{\mathrm{D}t^*} \right]_i = \frac{\partial u_i^*}{\partial t^*} + \frac{1}{\sqrt{g_{ii}}} \left\{ u_j^* \frac{\partial u_j^*}{\partial x^{i*}} + \frac{u_j^*}{\sqrt{g_{jj}}} \left[\frac{\partial}{\partial x^{j*}} \left(\sqrt{g_{ii}} u_i^* \right) - \frac{\partial}{\partial x^{i*}} \left(\sqrt{g_{jj}} u_j^* \right) \right] \right\}, \tag{A.2}$$

is rewritten in the compact form

$$\left[\frac{\mathrm{D}\boldsymbol{u}^*}{\mathrm{D}t^*} \right]_i = \frac{\partial u_i^*}{\partial t^*} + \frac{u_j^*}{\sqrt{g_{jj}}} \frac{\partial u_i^*}{\partial x^{j*}} + \frac{u_j^*}{\sqrt{g_{ii} g_{jj}}} \left(u_i^* \frac{\partial \sqrt{g_{ii}}}{\partial x^{j*}} - u_j^* \frac{\partial \sqrt{g_{jj}}}{\partial x^{i*}} \right) \tag{A.3}$$

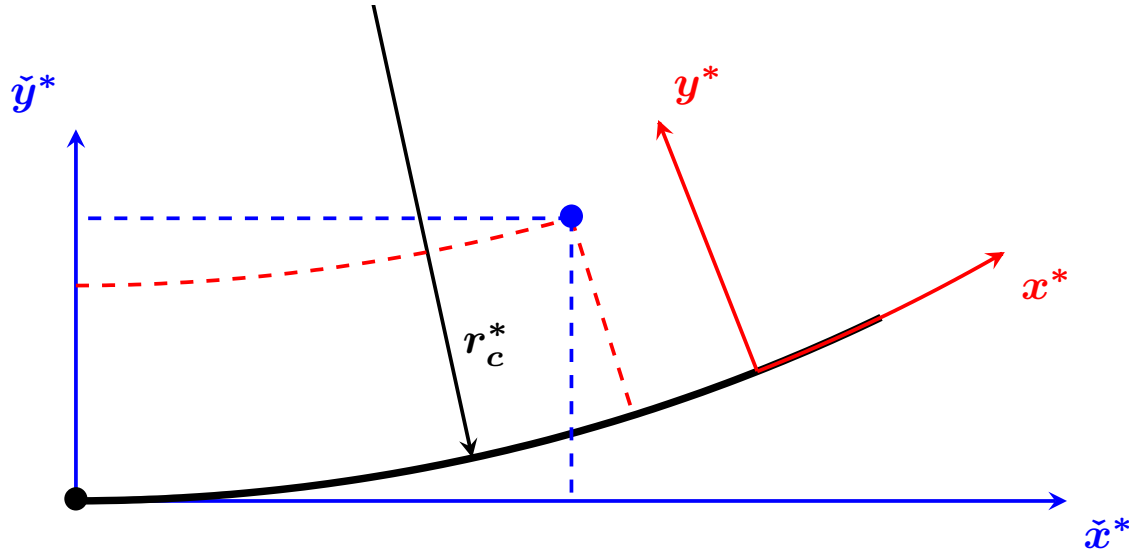

Figure A.1: Schematic of the coordinate system of a concave wall. The streamwise coordinate x^* follows the curvature of the plate and y^* is normal to the plate. The radius of curvature is r_c^*. The coordinates of the blue dot in the cartesian frame of reference (blue, $\check{x}^*$, $\check{y}^*$) are related to those in the curvilinear frame of reference (red, x^*,y^*) through the transformation (A.7).

The *virtual* viscous stress tensor is

$$\pi^{ij*} = \mu^* \left[g^{im} \frac{\partial}{\partial x^{m*}} \left(\frac{u_j^*}{\sqrt{g_{jj}}} \right) + g^{jm} \frac{\partial}{\partial x^{m*}} \left(\frac{u_i^*}{\sqrt{g_{ii}}} \right) + \right.$$
$$\left. + \frac{1}{2} \frac{\partial g_{m\beta}}{\partial x^{\alpha*}} \left(g^{im} g^{j\beta} + g^{jm} g^{i\beta} \right) \frac{u_\alpha^*}{\sqrt{g_{\alpha\alpha}}} \right] +$$
$$+ \left(\mu_b^* - \frac{2}{3} \mu^* \right) \frac{g^{ij}}{\sqrt{g}} \frac{\partial}{\partial x^{m*}} \left(\frac{\sqrt{g}}{\sqrt{g_{mm}}} u_m^* \right), \quad \text{(A.4)}$$

the *physical* viscous stress tensor is

$$\widetilde{\pi}^{ij*} = \sqrt{g_{ii} g_{jj}} \pi^{ij*}, \quad \text{(A.5)}$$

and

$$\frac{g^{jk}}{\sqrt{g_{ii}}} \tau_{ij,k}^* = \frac{1}{\sqrt{g_{ii}}} \left[-p_{,i}^* + \frac{1}{\sqrt{g}} \frac{\partial}{\partial x^{k*}} \left(\frac{g_{ij} \sqrt{g}}{\sqrt{g_{jj} g_{kk}}} \widetilde{\pi}^{jk*} \right) - \frac{1}{2\sqrt{g_{jj} g_{kk}}} \frac{\partial g_{jk}}{\partial x^{i*}} \widetilde{\pi}^{jk*} \right]. \quad \text{(A.6)}$$

A.2 Curvilinear coordinate system of a concave wall

The coordinate system of a concave wall is drawn in the schematic in figure A.1. The streamwise (x^*) direction follows the (uniform) curvature of the plate. The

cartesian system of coordinates (blue, $\check{x}^*$, $\check{y}^*$, $\check{z}^*$) is related to the concave-wall system of coordinates (red, x^*, y^*, z^*) through the transformation

$$\begin{cases} \check{x}^* = r_c^* \sin\left(\dfrac{x^*}{r_c^*}\right) - y^* \sin\left(\dfrac{x^*}{r_c^*}\right), & \text{(A.7a)} \\ \check{y}^* = r_c^* \sin\left(\dfrac{x^*}{r_c^*}\right) \tan\left(\dfrac{1}{2}\dfrac{x^*}{r_c^*}\right) + y^* \cos\left(\dfrac{x^*}{r_c^*}\right), & \text{(A.7b)} \\ \check{z}^* = z^*, & \text{(A.7c)} \end{cases}$$

The transformation (A.7) is obtained by trigonometric arguments. The components of the metric tensor g_{ii} and the Lamé coefficients h_i are

$$\begin{cases} g_{xx} = h_1^2 = \left(\dfrac{\partial \check{x}^*}{\partial x^*}\right)^2 + \left(\dfrac{\partial \check{y}^*}{\partial x^*}\right)^2 + \left(\dfrac{\partial \check{z}^*}{\partial x^*}\right)^2, & \text{(A.8a)} \\ g_{yy} = h_2^2 = \left(\dfrac{\partial \check{x}^*}{\partial y^*}\right)^2 + \left(\dfrac{\partial \check{y}^*}{\partial y^*}\right)^2 + \left(\dfrac{\partial \check{z}^*}{\partial y^*}\right)^2, & \text{(A.8b)} \\ g_{zz} = h_3^2 = \left(\dfrac{\partial \check{x}^*}{\partial z^*}\right)^2 + \left(\dfrac{\partial \check{y}^*}{\partial z^*}\right)^2 + \left(\dfrac{\partial \check{z}^*}{\partial z^*}\right)^2. & \text{(A.8c)} \end{cases}$$

The derivatives in (A.8) are

$$\frac{\partial \check{x}^*}{\partial x^*} = \cos\left(\frac{x^*}{r_c^*}\right)\left(1 - \frac{y^*}{r_c^*}\right), \tag{A.9a}$$

$$\begin{aligned} \frac{\partial \check{y}^*}{\partial x^*} &= \cos\left(\frac{x^*}{r_c^*}\right)\tan\left(\frac{x^*}{2r_c^*}\right) + \frac{\sin\left(x^*/r_c^*\right)}{2\cos^2\left[x^*/(2r_c^*)\right]} - \frac{y^*}{r_c^*}\sin\left(\frac{x^*}{r_c^*}\right) = \\ &= \left[\cos^2\left(\frac{x^*}{2r_c^*}\right) - \sin^2\left(\frac{x^*}{2r_c^*}\right)\right]\tan\left(\frac{x^*}{2r_c^*}\right) + \tan\left(\frac{x^*}{2r_c^*}\right) - \frac{y^*}{r_c^*}\sin\left(\frac{x^*}{r_c^*}\right) = \\ &= 2\sin\left(\frac{x^*}{2r_c^*}\right)\cos\left(\frac{x^*}{2r_c^*}\right) - \frac{y^*}{r_c^*}\sin\left(\frac{x^*}{r_c^*}\right) = \sin\left(\frac{x^*}{r_c^*}\right)\left(1 - \frac{y^*}{r_c^*}\right), \end{aligned} \tag{A.9b}$$

$$\frac{\partial \check{z}^*}{\partial x^*} = \frac{\partial \check{z}^*}{\partial y^*} = \frac{\partial \check{x}^*}{\partial z^*} = \frac{\partial \check{y}^*}{\partial z^*} = 0, \tag{A.9c}$$

$$\frac{\partial \check{x}^*}{\partial y^*} = -\sin\left(\frac{x^*}{r_c^*}\right), \tag{A.9d}$$

$$\frac{\partial \check{y}^*}{\partial y^*} = \cos\left(\frac{x^*}{r_c^*}\right), \tag{A.9e}$$

$$\frac{\partial \check{z}^*}{\partial z^*} = 1. \tag{A.9f}$$

Thus, $h_2 = h_3 = 1$ and the determinant of the metric tensor is

$$g = h_1^2 = \left(1 - \frac{y^*}{r_c^*}\right)^2. \tag{A.10}$$

A.2.1 Continuity and momentum balances

The terms in the mass conservation (continuity) equation

$$\frac{\mathrm{D}\rho^*}{\mathrm{D}t^*} + \rho^* \nabla \cdot \boldsymbol{u}^* = 0 \tag{A.11}$$

are derived by introducing (A.1). Because $h_2 = h_3 = 1$ the continuity equation reduces to

$$\frac{\partial \rho^*}{\partial t^*} + \frac{u^*}{h_1}\frac{\partial \rho^*}{\partial x^*} + v^*\frac{\partial \rho^*}{\partial y^*} + w^*\frac{\partial \rho^*}{\partial z^*} + \\ + \rho^*\left(\frac{1}{h_1}\frac{\partial u^*}{\partial x^*} + \frac{v^*}{h_1}\frac{\partial h_1}{\partial y^*} + \frac{\partial v^*}{\partial y^*} + \frac{\partial w^*}{\partial z^*}\right) = 0. \tag{A.12}$$

The streamwise (x^*, $i = 1$), wall-normal (y^*, $i = 2$) and spanwise (z^*, $i = 3$) momentum balances are now derived. For $i = 1$, the material derivative (A.3) becomes

$$\rho^*\frac{\mathrm{D}u^*}{\mathrm{D}t^*} = \rho^*\left(\frac{\partial u^*}{\partial t^*} + \frac{u^*}{h_1}\frac{\partial u^*}{\partial x^*} + v^*\frac{\partial u^*}{\partial y^*} + w^*\frac{\partial u^*}{\partial z^*} + \frac{u^* v^*}{h_1}\frac{\partial h_1}{\partial y^*}\right), \tag{A.13}$$

the components of the virtual stress tensor (A.4) are

$$\widetilde{\pi}^{xx*} = 2\mu^*\left(\frac{1}{h_1}\frac{\partial u^*}{\partial x^*} + \frac{v^*}{h_1}\frac{\partial h_1}{\partial y^*}\right) - \frac{2}{3}\mu^*\nabla^* \cdot \boldsymbol{u}^*, \tag{A.14a}$$

$$\widetilde{\pi}^{xy*} = \mu^*\left[\frac{1}{h_1}\frac{\partial v^*}{\partial x^*} + h_1\frac{\partial}{\partial y^*}\left(\frac{u^*}{h_1}\right)\right], \tag{A.14b}$$

$$\widetilde{\pi}^{xz*} = \mu^*\left(\frac{1}{h_1}\frac{\partial w^*}{\partial z^*} + \frac{\partial u^*}{\partial z^*}\right), \tag{A.14c}$$

the physical stresses are (A.5)

$$\frac{g^{jk}}{h_1}\tau^*_{xj,k} = -\frac{1}{h_1}\frac{\partial p^*}{\partial x^*} + \frac{1}{h_1}\frac{\partial}{\partial x^*}\left[2\mu^*\left(\frac{1}{h_1}\frac{\partial u^*}{\partial x^*} + \frac{v^*}{h_1}\frac{\partial h_1}{\partial y^*}\right) - \frac{2}{3}\mu^*\nabla^* \cdot \boldsymbol{u}^*\right] + \\ + \frac{\mu^*}{h_1^2}\left[\frac{\partial v^*}{\partial x^*} + h_1\frac{\partial}{\partial y^*}\left(\frac{u^*}{h_1}\right)\right]\frac{\partial h_1}{\partial y^*} + \frac{1}{h_1}\frac{\partial}{\partial y^*}\left\{\mu^*\left[\frac{\partial v^*}{\partial x^*} + h_1^2\frac{\partial}{\partial y^*}\left(\frac{u^*}{h_1}\right)\right]\right\} + \\ + \frac{\partial}{\partial z^*}\left[\mu^*\left(\frac{1}{h_1}\frac{\partial w^*}{\partial x^*} + \frac{\partial u^*}{\partial z^*}\right)\right], \tag{A.15}$$

and the streamwise momentum equation is

$$\begin{aligned}\rho^*\left(\frac{\partial u^*}{\partial t^*}+\frac{u^*}{h_1}\frac{\partial u^*}{\partial x^*}+v^*\frac{\partial u^*}{\partial y^*}+w^*\frac{\partial u^*}{\partial z^*}+\frac{u^*v^*}{h_1}\frac{\partial h_1}{\partial y^*}\right)=\\ =-\frac{1}{h_1}\frac{\partial p^*}{\partial x^*}+\frac{1}{h_1}\frac{\partial}{\partial x^*}\left[2\mu^*\left(\frac{1}{h_1}\frac{\partial u^*}{\partial x^*}+\frac{v^*}{h_1}\frac{\partial h_1}{\partial y^*}\right)-\frac{2}{3}\mu^*\nabla^*\cdot\boldsymbol{u}^*\right]+\\ +\frac{\mu^*}{h_1^2}\left[\frac{\partial v^*}{\partial x^*}+h_1\frac{\partial}{\partial y^*}\left(\frac{u^*}{h_1}\right)\right]\frac{\partial h_1}{\partial y^*}+\\ +\frac{1}{h_1}\frac{\partial}{\partial y^*}\left\{\mu^*\left[\frac{\partial v^*}{\partial x^*}+h_1^2\frac{\partial}{\partial y^*}\left(\frac{u^*}{h_1}\right)\right]\right\}+\\ +\frac{\partial}{\partial z^*}\left[\mu^*\left(\frac{1}{h_1}\frac{\partial w^*}{\partial x^*}+\frac{\partial u^*}{\partial z^*}\right)\right].\end{aligned}\tag{A.16}$$

For $i=2$, the material derivative (A.3) is

$$\rho^*\frac{\mathrm{D}v^*}{\mathrm{D}t^*}=\rho^*\left(\frac{\partial v^*}{\partial t^*}+\frac{u^*}{h_1}\frac{\partial v^*}{\partial x^*}+v^*\frac{\partial v^*}{\partial y^*}+w^*\frac{\partial v^*}{\partial z^*}-\frac{u^{*2}}{h_1}\frac{\partial h_1}{\partial y^*}\right),\tag{A.17}$$

the components of the virtual stress tensor (A.4) are

$$\widetilde{\pi}^{yx*}=\mu^*\left[\frac{1}{h_1}\frac{\partial v^*}{\partial x^*}+h_1\frac{\partial}{\partial y^*}\left(\frac{u^*}{h_1}\right)\right],\tag{A.18a}$$

$$\widetilde{\pi}^{yy*}=2\mu^*\frac{\partial v^*}{\partial y^*}+\lambda^*\nabla^*\cdot\boldsymbol{u}^*,\tag{A.18b}$$

$$\widetilde{\pi}^{yz*}=\mu^*\left(\frac{\partial w^*}{\partial y^*}+\frac{\partial v^*}{\partial z^*}\right),\tag{A.18c}$$

the physical stresses (A.5) are

$$\begin{aligned}\frac{g^{jk}}{1}\tau^*_{yj,k}=-\frac{\partial p^*}{\partial y^*}+\frac{1}{h_1}\frac{\partial}{\partial x^*}\left[\mu^*\left(\frac{1}{h_1}\frac{\partial v^*}{\partial x^*}+h_1\frac{\partial}{\partial y^*}\left(\frac{u^*}{h_1}\right)\right)\right]+\\ +\frac{1}{h_1}\frac{\partial}{\partial y^*}\left(2\mu^*h_1\frac{\partial v^*}{\partial y^*}+h_1\lambda^*\nabla^*\cdot\boldsymbol{u}^*\right)+\frac{1}{h_1}\frac{\partial}{\partial z^*}\left[h_1\mu^*\left(\frac{\partial w^*}{\partial y^*}+\frac{\partial v^*}{\partial z^*}\right)\right]+\\ -\frac{1}{h_1}\left[2\mu^*\left(\frac{1}{h_1}\frac{\partial u^*}{\partial x^*}+\frac{v^*}{h_1}\frac{\partial h_1}{\partial y^*}\right)+\lambda^*\nabla^*\cdot\boldsymbol{u}^*\right],\end{aligned}\tag{A.19}$$

and the wall-normal momentum balance is

$$\rho^*\left(\frac{\partial v^*}{\partial t^*}+\frac{u^*}{h_1}\frac{\partial v^*}{\partial x^*}+v^*\frac{\partial v^*}{\partial y^*}+w^*\frac{\partial v^*}{\partial z^*}\right)\boxed{-\frac{\rho^* u^{*2}}{h_1}\frac{\partial h_1}{\partial y^*}}=$$
$$=-\frac{\partial p^*}{\partial y^*}+\frac{1}{h_1}\frac{\partial}{\partial x^*}\left\{\mu^*\left[\frac{1}{h_1}\frac{\partial v^*}{\partial x^*}+h_1\frac{\partial}{\partial y^*}\left(\frac{u^*}{h_1}\right)\right]\right\}+$$
$$+\frac{1}{h_1}\frac{\partial}{\partial y^*}\left(2\mu^* h_1\frac{\partial v^*}{\partial y^*}+h_1\lambda^*\nabla^*\cdot\boldsymbol{u}^*\right)+$$
$$+\frac{1}{h_1}\frac{\partial}{\partial z^*}\left[h_1\mu^*\left(\frac{\partial w^*}{\partial y^*}+\frac{\partial v^*}{\partial z^*}\right)\right]+$$
$$-\frac{1}{h_1}\left[2\mu^*\left(\frac{1}{h_1}\frac{\partial u^*}{\partial x^*}+\frac{v^*}{h_1}\frac{\partial h_1}{\partial y^*}\right)+\lambda^*\nabla^*\cdot\boldsymbol{u}^*\right]\frac{\partial h_1}{\partial y^*}. \tag{A.20}$$

Here, the boxed term on the left-hand side is the Görtler term. In the limit of large radii $r_c^*\Lambda^{*-1}=O\left(Re^2\right)\ll 1$, $h_1\sim 1$, $\mathrm{d}h_1/\mathrm{d}y=-r_c^{-1}$ and the curvature terms in the wall normal momentum balance (2.16c) are retrieved.

For $i=3$, the material derivative (A.3) is

$$\rho^*\frac{\mathrm{D}w^*}{\mathrm{D}t^*}=\rho^*\left(\frac{\partial w^*}{\partial t^*}+\frac{u^*}{h_1}\frac{\partial w^*}{\partial x^*}+v^*\frac{\partial w^*}{\partial y^*}+w^*\frac{\partial w^*}{\partial z^*}\right), \tag{A.21}$$

the components of the virtual stress tensor (A.4) are

$$\widetilde{\pi}^{xz*}=\mu^*\left(\frac{1}{h_1}\frac{\partial w^*}{\partial z^*}+\frac{\partial u^*}{\partial z^*}\right), \tag{A.22a}$$
$$\widetilde{\pi}^{zy*}=\mu^*\left(\frac{\partial w^*}{\partial y^*}+\frac{\partial v^*}{\partial z^*}\right), \tag{A.22b}$$
$$\widetilde{\pi}^{zz*}=2\mu^*\frac{\partial w^*}{\partial z^*}+\lambda^*\nabla^*\cdot\boldsymbol{u}^*, \tag{A.22c}$$

the physical stresses are (A.5)

$$\frac{g^{jk}}{1}\tau^*_{3j,k}=-\frac{\partial p^*}{\partial z^*}+\frac{1}{h_1}\frac{\partial}{\partial x^*}\left[\mu^*\left(\frac{1}{h_1}\frac{\partial w^*}{\partial x^*}+\frac{\partial u^*}{\partial z^*}\right)\right]+$$
$$+\frac{1}{h_1}\frac{\partial}{\partial y^*}\left[h_1\mu^*\left(\frac{\partial w^*}{\partial y^*}+\frac{\partial v^*}{\partial z^*}\right)\right]+\frac{1}{h_1}\frac{\partial}{\partial z^*}\left(2\mu^* h_1\frac{\partial w^*}{\partial z^*}+h_1\lambda^*\nabla^*\cdot\boldsymbol{u}^*\right), \tag{A.23}$$

and the spanwise momentum balance equation is

$$\rho^*\left(\frac{\partial w^*}{\partial t^*}+\frac{u^*}{h_1}\frac{\partial w^*}{\partial x^*}+v^*\frac{\partial w^*}{\partial y^*}+w^*\frac{\partial w^*}{\partial z^*}\right)=$$
$$=-\frac{\partial p^*}{\partial z^*}+\frac{1}{h_1}\frac{\partial}{\partial x^*}\left[\mu^*\left(\frac{1}{h_1}\frac{\partial w^*}{\partial x^*}+\frac{\partial u^*}{\partial z^*}\right)\right]+$$
$$+\frac{1}{h_1}\frac{\partial}{\partial y^*}\left[h_1\mu^*\left(\frac{\partial w^*}{\partial y^*}+\frac{\partial v^*}{\partial z^*}\right)\right]+$$
$$+\frac{1}{h_1}\frac{\partial}{\partial z^*}\left(2\mu^* h_1\frac{\partial w^*}{\partial z^*}+h_1\lambda^*\nabla^*\cdot\boldsymbol{u}^*\right). \tag{A.24}$$

A.2.2 Static enthalpy balance and the dissipation term

The terms in the static enthalpy balance are

$$\rho^* c_p^* \frac{\mathrm{D}T^*}{\mathrm{D}t^*} = \frac{\mathrm{D}p^*}{\mathrm{D}t^*} + \Phi^* + \nabla^* \cdot (k^* \nabla^* T^*)\,, \tag{A.25}$$

where

$$\rho^* c_p^* \frac{\mathrm{D}T^*}{\mathrm{D}t^*} = \rho^* c_p^* \left(\frac{\partial T^*}{\partial t^*} + \frac{u^*}{h_1}\frac{\partial T^*}{\partial x^*} + v^* \frac{\partial T^*}{\partial y^*} + w^* \frac{\partial T^*}{\partial z^*} \right), \tag{A.26}$$

$$\frac{\mathrm{D}p^*}{\mathrm{D}t^*} = \frac{\partial p^*}{\partial t^*} + \frac{u^*}{h_1}\frac{\partial p^*}{\partial x^*} + v^* \frac{\partial p^*}{\partial y^*} + w^* \frac{\partial p^*}{\partial z^*}, \tag{A.27}$$

$$\nabla^* \cdot (k^* \nabla^* T^*) = \frac{1}{h_1}\left[\frac{\partial}{\partial x^*}\left(\frac{k^*}{h_1}\frac{\partial T^*}{\partial x^*} \right) + \frac{\partial}{\partial y^*}\left(h_1 k^* \frac{\partial T^*}{\partial y^*} \right) + \right.$$
$$\left. + \frac{\partial}{\partial z^*}\left(h_1 k^* \frac{\partial T^*}{\partial z^*} \right) \right]. \tag{A.28}$$

here, $c_p^* = \gamma\,(\gamma - 1)^{-1}\,\mathcal{R}^*$. The dissipation term Φ^* is the double-dot product of the viscous stress tensor and the velocity gradient

$$\Phi^* = \boldsymbol{\tau}^* : \nabla^* \boldsymbol{u}^* = \nabla^* \cdot (\boldsymbol{\tau}^* \cdot \boldsymbol{u}^*) - \boldsymbol{u}^* \cdot (\nabla^* \cdot \boldsymbol{\tau}^*)\,, \tag{A.29}$$

and is not discussed in Sutter [1962], who considered the balance of the total enthalpy and reported the expression of the term $\nabla^* \cdot (\boldsymbol{\tau}^* \cdot \boldsymbol{u}^*)$

$$\nabla^* \cdot (\boldsymbol{\tau}^* \cdot \boldsymbol{u}^*) = \frac{1}{\sqrt{g}}\frac{\partial}{\partial x_j^*}\left(\frac{\sqrt{g}}{\sqrt{g_{jj}}} u_i^* \widetilde{\pi}^{ij*} \right) = \frac{1}{h_1}\left[\frac{\partial}{\partial x^*}\left(u^* \widetilde{\pi}^{xx*} + v^* \widetilde{\pi}^{yx*} + w^* \widetilde{\pi}^{zx*} \right) + \right.$$
$$+ \frac{\partial}{\partial y^*}\left(h_1 u^* \widetilde{\pi}^{xy*} + h_1 v^* \widetilde{\pi}^{yy*} + h_1 w^* \widetilde{\pi}^{zy*} \right) +$$
$$\left. + \frac{\partial}{\partial z^*}\left(h_1 u^* \widetilde{\pi}^{xz*} + h_1 v^* \widetilde{\pi}^{yz*} + h_1 w^* \widetilde{\pi}^{zz*} \right) \right] \equiv A + B + C. \tag{A.30}$$

Here, the terms A, B and C are obtained by introducing (A.14), (A.18) and (A.22) in (A.30)

$$A = \frac{1}{h_1}\frac{\partial}{\partial x^*}\left[u^* 2\mu^* \left(\frac{1}{h_1}\frac{\partial u^*}{\partial x^*} + \frac{1}{h_1}\frac{\partial h_1}{\partial y^*} v^* \right) - \frac{2}{3} u^* \mu^* \nabla^* \cdot \boldsymbol{u}^* \right] +$$
$$+ \frac{1}{h_1}\frac{\partial}{\partial x^*}\left\{ v^* \mu^* \left[\frac{1}{h_1}\frac{\partial v^*}{\partial x^*} + h_1 \frac{\partial}{\partial y^*}\left(\frac{u^*}{h_1} \right) \right] \right\} +$$
$$+ \frac{1}{h_1}\frac{\partial}{\partial x^*}\left[w^* \mu^* \left(\frac{1}{h_1}\frac{\partial w^*}{\partial x^*} + \frac{\partial u^*}{\partial z^*} \right) \right], \tag{A.31a}$$

$$B = \frac{1}{h_1}\frac{\partial}{\partial y^*}\left\{h_1 u^* \mu^* \left[\frac{1}{h_1}\frac{\partial v^*}{\partial x^*} + h_1 \frac{\partial}{\partial y^*}\left(\frac{u^*}{h_1}\right)\right]\right\} + \\ + \frac{1}{h_1}\frac{\partial}{\partial y^*}\left[h_1 v^* \left(2\mu^* \frac{\partial v^*}{\partial y^*} - \frac{2}{3}\mu^* \nabla^* \cdot \boldsymbol{u}^*\right)\right] + \\ + \frac{1}{h_1}\frac{\partial}{\partial y^*}\left[h_1 w^* \mu^* \left(\frac{\partial w^*}{\partial y^*} + \frac{\partial v^*}{\partial z^*}\right)\right], \quad \text{(A.31b)}$$

$$C = \frac{1}{h_1}\frac{\partial}{\partial z^*}\left[h_1 u^* \mu^* \left(\frac{1}{h_1}\frac{\partial w^*}{\partial x^*} + \frac{\partial u^*}{\partial z^*}\right)\right] + \\ + \frac{1}{h_1}\frac{\partial}{\partial z^*}\left[h_1 v^* \mu^* \left(\frac{\partial w^*}{\partial y^*} + \frac{\partial v^*}{\partial z^*}\right)\right] + \\ + \frac{1}{h_1}\frac{\partial}{\partial z^*}\left[h_1 w^* \left(2\mu^* \frac{\partial w^*}{\partial z^*} - \frac{2}{3}\mu^* \nabla^* \cdot \boldsymbol{u}^*\right)\right]. \quad \text{(A.31c)}$$

The work of the viscous shear stresses is the scalar product

$$\boldsymbol{u}^* \cdot (\nabla^* \cdot \boldsymbol{\tau}^*) = \frac{u^*}{h_1}\frac{\partial}{\partial x^*}\left[2\mu^*\left(\frac{1}{h_1}\frac{\partial u^*}{\partial x^*} + \frac{v^*}{h_1}\frac{\partial h_1}{\partial y^*}\right) - \frac{2}{3}\mu^* \nabla^* \cdot \boldsymbol{u}^*\right] + \\ + \frac{u^*}{h_1}\frac{\partial}{\partial y^*}\left[\mu^* \frac{\partial v^*}{\partial x^*} + \mu^* h_1^2 \frac{\partial}{\partial y^*}\left(\frac{u^*}{h_1}\right)\right] + \frac{u^*}{h_1}\frac{\partial}{\partial z^*}\left(\mu^* h_1 \frac{\partial u^*}{\partial z^*} + \mu^* \frac{\partial w^*}{\partial x^*}\right) + \\ + u^* \mu^* \left[\frac{1}{h_1^2}\frac{\partial v^*}{\partial x^*} + \frac{\partial}{\partial y^*}\left(\frac{u^*}{h_1}\right)\right]\frac{\partial h_1}{\partial y^*} + \frac{v^*}{h_1}\frac{\partial}{\partial x^*}\left\{\mu^*\left[\frac{1}{h_1}\frac{\partial v^*}{\partial x^*} + h_1 \frac{\partial}{\partial y^*}\left(\frac{u^*}{h_1}\right)\right]\right\} + \\ + \frac{v^*}{h_1}\frac{\partial}{\partial y^*}\left(2\mu^* h_1 \frac{\partial v^*}{\partial y^*} - \frac{2}{3}h_1 \mu^* \nabla^* \cdot \boldsymbol{u}^*\right) + \frac{v^*}{h_1}\frac{\partial}{\partial z^*}\left[h_1 \mu^*\left(\frac{\partial w^*}{\partial x^*} + \frac{\partial v^*}{\partial z^*}\right)\right] + \\ - \frac{v^*}{h_1}\frac{\partial h_1}{\partial y^*}\left[2\mu^*\left(\frac{1}{h_1}\frac{\partial u^*}{\partial x^*} + \frac{v^*}{h_1}\frac{\partial h_1}{\partial y^*}\right) - \frac{2}{3}\mu^* \nabla^* \cdot \boldsymbol{u}^*\right] + \frac{w^*}{h_1}\frac{\partial}{\partial x^*}\left[h_1 \mu^*\left(\frac{\partial u^*}{\partial z^*} + \frac{\partial w^*}{\partial x^*}\right)\right] + \\ + \frac{w^*}{h_1}\frac{\partial}{\partial y^*}\left[h_1 \mu^*\left(\frac{\partial w^*}{\partial x^*} + \frac{\partial u^*}{\partial z^*}\right)\right] + \frac{w^*}{h_1}\frac{\partial}{\partial z^*}\left[2\mu^* h_1 \frac{\partial w^*}{\partial z^*} - \frac{2}{3}\mu^* h_1 \nabla^* \cdot \boldsymbol{u}^*\right], \quad \text{(A.32)}$$

and the dissipation term is obtained by introducing (A.30) and (A.32) in (A.29)

$$\Phi^* = 2\mu^*\left[\left(\frac{1}{h_1}\frac{\partial u^*}{\partial x^*} + \frac{v^*}{h_1}\frac{\partial h_1}{\partial y^*}\right)^2 + \left(\frac{\partial v^*}{\partial y^*}\right)^2 + \left(\frac{\partial w^*}{\partial z^*}\right)^2\right] - \frac{2}{3}\mu^*\left(\nabla^* \cdot \boldsymbol{u}^*\right)^2 + \\ + \mu^*\left\{\left[\frac{1}{h_1}\frac{\partial v^*}{\partial x^*} + h_1 \frac{\partial}{\partial y^*}\left(\frac{u^*}{h_1}\right)\right]^2 + \left[\frac{1}{h_1}\frac{\partial w^*}{\partial x^*} + \frac{\partial u^*}{\partial z^*}\right]^2 + \left[\frac{\partial w^*}{\partial y^*} + \frac{\partial v^*}{\partial z^*}\right]^2\right\}. \quad \text{(A.33)}$$

Finally, the static enthalpy balance is recovered

$$\rho^* c_p^* \left(\frac{\partial T^*}{\partial t^*} + \frac{u^*}{h_1}\frac{\partial T^*}{\partial x^*} + v^*\frac{\partial T^*}{\partial y^*} + w^*\frac{\partial T^*}{\partial z^*} \right) = \frac{\partial p^*}{\partial t^*} + \frac{u^*}{h_1}\frac{\partial p^*}{\partial x^*} + v^*\frac{\partial p^*}{\partial y^*} + \\ + w^*\frac{\partial p^*}{\partial z^*} + \frac{1}{h_1}\left[\frac{\partial}{\partial x^*}\left(\frac{k^*}{h_1}\frac{\partial T^*}{\partial x^*} \right) + \frac{\partial}{\partial y^*}\left(h_1 k^* \frac{\partial T^*}{\partial y^*} \right) + \right. \\ \left. + \frac{\partial}{\partial z^*}\left(h_1 k^* \frac{\partial T^*}{\partial z^*} \right) \right] + 2\mu^* \left[\left(\frac{1}{h_1}\frac{\partial u^*}{\partial x^*} + \frac{v^*}{h_1}\frac{\partial h_1}{\partial y^*} \right)^2 + \left(\frac{\partial v^*}{\partial y^*} \right)^2 + \right. \\ \left. + \left(\frac{\partial w^*}{\partial z^*} \right)^2 \right] - \frac{2}{3}\mu^* \left(\nabla^* \cdot \boldsymbol{u}^* \right)^2 + \mu^* \left\{ \left[\frac{1}{h_1}\frac{\partial v^*}{\partial x^*} + h_1 \frac{\partial}{\partial y^*}\left(\frac{u^*}{h_1} \right) \right]^2 + \right. \\ \left. + \left[\frac{1}{h_1}\frac{\partial w^*}{\partial x^*} + \frac{\partial u^*}{\partial z^*} \right]^2 + \left[\frac{\partial w^*}{\partial y^*} + \frac{\partial v^*}{\partial z^*} \right]^2 \right\} \tag{A.34}$$

Appendix B

The laminar base flow

The equations that govern the evolution of a two-dimensional, compressible, steady laminar boundary layer are derived in this appendix. The general assumptions and asymptotic scaling are discussed in §B.1. The similar and non-similar solutions of a compressible laminar boundary layer are treated in section §B.2. The streamwise momentum balance equation for a steady boundary layer over an isotropic porous substrate with streamwise-increasing permeability is derived in detail in §B.3.

B.1 The boundary-layer equations

The base flow is governed by the two-dimensional, steady, compressible Navier-Stokes equations with variable dynamic viscosity μ^* and thermal conductivity k^*. The Stokes' hypothesis is assumed, and μ^* and k^* are modeled by interpolating tabulated values at a pressure of 100 kPa [Haynes, 2014]. All the properties are scaled with respect to their values at 300 K and plotted in figure B.1. The tabulated values of μ^* and k^* are interpolated by a function of the type [Sutherland, 1893]

$$\mu = T^{3/2}\frac{\chi_\mu + 1}{\chi_\mu + T}, \quad k = T^{3/2}\frac{\chi_k + 1}{\chi_k + T}, \tag{B.1}$$

with $\chi_\mu = 0.43$, $\chi_k = 0.66$. The reference values are $\mu^*_{ref} = 18.5\,\mu\text{Pa}\,\text{s}$ at $T^*_{ref} = 300\,\text{K}$. The standard deviation is 4.4% for the ratio μ/k, 2.1% for the Prandtl number, 2.1% for the specific gas constant of air $c^*_p - c^*_v$, and 1.9% for the heat capacity ratio γ. Hence, the Prandtl number and heat capacity ratio are assumed to be constant while the viscosity and the conductivity are assumed to be governed by the first of (B.1).

Under these premises, the governing equations are

$$\mathcal{C}|\ \frac{\partial}{\partial x}(\rho U) + \frac{\partial}{\partial y}(\rho V) = 0, \tag{B.2a}$$

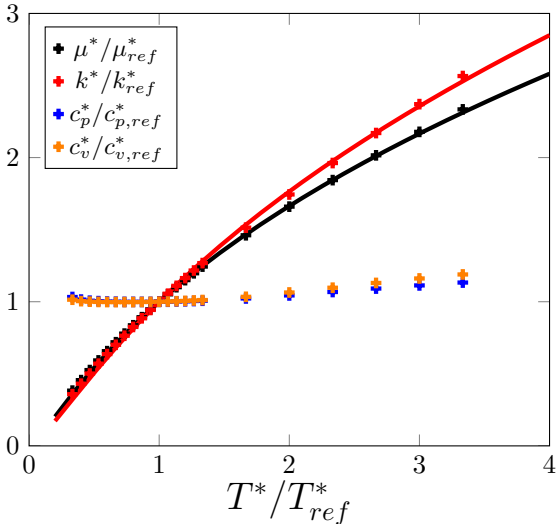

Figure B.1: Thermophysical properties of air taken from Haynes [2014] in the range 100-1000 K and normalized with respect to the reference values at $T^*_{ref} = 300\,\mathrm{K}$: $\mu^*_{ref} = 18.54 \cdot 10^{-6}\,\mathrm{Pa\,s}$, $k^*_{ref} = 26.38 \cdot 10^{-3}\,\mathrm{W\,m^{-1}\,K^{-1}}$, $c^*_{p,ref} = 1007\,\mathrm{J\,kg^{-1}\,K^{-1}}$, $c^*_{v,ref} = 718.1\,\mathrm{J\,kg^{-1}\,K^{-1}}$.

$$\mathcal{X}|\ \rho U\frac{\partial U}{\partial x}+\rho V\frac{\partial U}{\partial y}=\frac{1}{Re}\left[\frac{\partial}{\partial x}\left(\mu\frac{\partial U}{\partial x}\right)+\frac{\partial}{\partial y}\left(\mu\frac{\partial U}{\partial y}\right)\right]+ \\ -\frac{2}{3Re}\frac{\partial}{\partial x}\left[\mu\left(\frac{\partial U}{\partial x}+\frac{\partial V}{\partial y}\right)\right], \quad \text{(B.2b)}$$

$$\mathcal{Y}|\ \rho U\frac{\partial V}{\partial x}+\rho V\frac{\partial V}{\partial y}+\frac{\partial P}{\partial y}=\frac{1}{Re}\left[\frac{\partial}{\partial x}\left(\mu\frac{\partial V}{\partial x}\right)+\frac{\partial}{\partial y}\left(\mu\frac{\partial V}{\partial y}\right)\right]+ \\ -\frac{2}{3Re}\frac{\partial}{\partial y}\left[\mu\left(\frac{\partial U}{\partial x}+\frac{\partial V}{\partial y}\right)\right], \quad \text{(B.2c)}$$

$$\mathcal{E}|\ \rho U\frac{\partial T}{\partial x}+\rho V\frac{\partial T}{\partial y}=(\gamma-1)\,\frac{Ma^2}{Re}\left[2\mu\left(\frac{\partial U}{\partial x}\right)^2-\frac{2}{3}\mu\left(\frac{\partial U}{\partial x}+\frac{\partial V}{\partial y}\right)\frac{\partial U}{\partial x}+\right. \\ \left.+\mu\left(\frac{\partial U}{\partial y}+\frac{\partial V}{\partial x}\right)\frac{\partial U}{\partial y}+\mu\left(\frac{\partial V}{\partial x}+\frac{\partial U}{\partial y}\right)\frac{\partial V}{\partial x}+2\mu\left(\frac{\partial V}{\partial y}\right)^2-\frac{2}{3}\mu\left(\frac{\partial U}{\partial x}+\frac{\partial V}{\partial y}\right)\frac{\partial V}{\partial y}\right]+ \\ +\frac{1}{RePr}\left[\frac{\partial}{\partial x}\left(\mu\frac{\partial T}{\partial x}\right)+\frac{\partial}{\partial y}\left(\mu\frac{\partial T}{\partial y}\right)\right]+(\gamma-1)\,Ma^2V\frac{\partial p}{\partial y}. \quad \text{(B.2d)}$$

The streamwise pressure gradient is absent, the Reynolds number $Re = \rho^*_\infty U^*_\infty L^*/\mu^*_\infty \gg 1$ and the Mach number $Ma = U^*_\infty/\left(\gamma\mathcal{R}^*T^*_\infty\right)^{1/2} = O\left(1\right)$. The Prandtl number is $Pr = \gamma\left(\gamma-1\right)^{-1}\mu^*_\infty\mathcal{R}^*/k^*_\infty = 0.71$. The fast-varying variables $Y = yRe^{1/2}$ and $\widetilde{V} = VRe^{1/2}$ [van Dyke, 1975; Bender and Orszag, 1999] are introduced, and the balances (B.2) reduce to [Stewartson, 1964]

$$\mathcal{C}|\ \frac{\partial}{\partial x}\left(\rho U\right)+\frac{\partial}{\partial Y}\left(\rho\widetilde{V}\right)=0, \tag{B.3a}$$

$$\mathcal{X}|\ \rho U\frac{\partial U}{\partial x}+\rho\widetilde{V}\frac{\partial U}{\partial Y}=\frac{\partial}{\partial Y}\left(\mu\frac{\partial U}{\partial Y}\right), \tag{B.3b}$$

$$\mathcal{E}|\ \rho U\frac{\partial T}{\partial x}+\rho\widetilde{V}\frac{\partial T}{\partial Y}=\left(\gamma-1\right)Ma^{2}\mu\left(\frac{\partial U}{\partial Y}\right)^{2}+\frac{1}{Pr}\frac{\partial}{\partial Y}\left(\mu\frac{\partial T}{\partial Y}\right). \tag{B.3c}$$

Equations (B.3) are subject to the boundary conditions

$$U\left(x,0\right)=\widetilde{V}\left(x,0\right)=0\text{ and either }T\text{ or }\frac{\partial T}{\partial Y}\text{ specified at }Y=0\ \forall x>0, \tag{B.4a}$$

$$U\left(x,\infty\right)=1\text{ and }T\left(x,\infty\right)=1\text{ for }Y\gg1\text{ and }y=O\left(1\right). \tag{B.4b}$$

Because the pressure is constant across the boundary layer, the perfect gas equation reduces to

$$\rho T=1. \tag{B.5}$$

A stream function $\psi\left(x,Y\right)$ that satisfies the two-dimensional continuity equation (B.2a) is defined for the symmetry of second derivatives

$$\rho U=\frac{\partial\psi}{\partial Y},\quad\rho\widetilde{V}=-\frac{\partial\psi}{\partial x}. \tag{B.6}$$

Introducing the Dorodnitsyn-Howarth transformation (2.3) [Dorodnitsyn, 1942]

$$\bar{y}(x,Y)=\int_{0}^{Y}\frac{\mathrm{d}\breve{Y}}{T(x,\breve{Y})}, \tag{B.7}$$

and expanding the derivatives in (B.3) with the chain rule [e.g. Howarth and Taylor, 1948]

$$\frac{\partial\psi\left(x,Y\right)}{\partial x}=\left.\frac{\partial\psi\left(x,\bar{y}\right)}{\partial x}\right|_{\bar{y}}+\left.\frac{\partial\psi\left(x,\bar{y}\right)}{\partial\bar{y}}\right|_{x}\left.\frac{\partial\bar{y}}{\partial x}\right|_{Y}, \tag{B.8a}$$

$$\frac{\partial\psi\left(x,Y\right)}{\partial Y}=\left.\frac{\partial\psi\left(x,\bar{y}\right)}{\partial\bar{y}}\right|_{x}\frac{1}{T\left(x,\bar{y}\right)}, \tag{B.8b}$$

yields the boundary-layer equations for the streamfunction ψ

$$\frac{\partial\psi}{\partial\bar{y}}\frac{\partial}{\partial x}\left(\frac{\partial\psi}{\partial\bar{y}}\right)-\frac{\partial\psi}{\partial x}\frac{\partial^{2}\psi}{\partial\bar{y}^{2}}=\frac{\partial}{\partial\bar{y}}\left(\frac{\mu}{T}\frac{\partial^{2}\psi}{\partial\bar{y}^{2}}\right), \tag{B.9a}$$

$$\frac{\partial\psi}{\partial\bar{y}}\frac{\partial T}{\partial x}-\frac{\partial\psi}{\partial x}\frac{\partial T}{\partial\bar{y}}=\left(\gamma-1\right)Ma^{2}\frac{\mu}{T}\left(\frac{\partial^{2}\psi}{\partial\bar{y}^{2}}\right)^{2}+\frac{1}{Pr}\frac{\partial}{\partial\bar{y}}\left(\frac{\mu}{T}\frac{\partial T}{\partial\bar{y}}\right). \tag{B.9b}$$

The velocity components are obtained by expanding the derivatives in (B.6)

$$U = \frac{\partial \psi}{\partial \bar{y}}, \tag{B.10a}$$

$$V = -\frac{T}{Re^{1/2}} \left[\left. \frac{\partial \psi}{\partial x} \right|_{\bar{y}} + \left. \frac{\partial \bar{y}}{\partial x} \right|_{Y} \frac{\partial \psi}{\partial \bar{y}} \right], \tag{B.10b}$$

while the boundary conditions (B.4) are cast in terms of ψ

$$\psi(x,0) = \frac{\partial \psi}{\partial \bar{y}}(x,0) = 0 \text{ and either } T_w \text{ or } \left. \frac{\partial T}{\partial \bar{y}} \right|_{w} \text{ at } \bar{y} = 0 \ \forall x > 0, \tag{B.11a}$$

$$u(x,\infty) = 1 \text{ and } T(x,\infty) = 1 \text{ for } \bar{y} \gg 1. \tag{B.11b}$$

B.2 Similar and non-similar laminar base flows

The system (B.9) is parabolic in x. If a self-similar solution exists, (B.9) can be reduced to a system of ODEs through an appropriate change of variable [e.g. Sobey, 2000]. In some cases, such a change of variable is convenient even when a self-similar solution does not exist for all x [Cebeci, 2002]. The decompositions $\bar{y} = \eta (\alpha x)^a$, $\psi = F(x,\eta)(\alpha x)^b$ and $T = \widetilde{T}(x,\eta)(\alpha x)^c$ are introduced in the governing equations (B.9) and the boundary conditions (B.11). Here, a, b, c and α are real constants, and $c = 0$ for flows that are homoenthalpic in the free-stream. Neither the power-law or the Sutherland models for μ and k allow for self-similar solutions for nonzero c [Stewartson, 1964, chapter 3]. The terms of the momentum equation expand as

$$\frac{\partial \psi}{\partial \bar{y}} \frac{\partial}{\partial x} \left(\frac{\partial \psi}{\partial \bar{y}} \right) = (\alpha x)^{b-a} \frac{\partial F}{\partial \eta} \frac{\partial}{\partial x} \left(\frac{\partial \psi}{\partial \bar{y}} \right), \tag{B.12a}$$

$$-\frac{\partial \psi}{\partial x} \frac{\partial^2 \psi}{\partial \bar{y}^2} = -\frac{\partial \psi}{\partial x} (\alpha x)^{b-2a} \frac{\partial^2 F}{\partial \eta^2}, \tag{B.12b}$$

$$\frac{\partial}{\partial \bar{y}} \left(\frac{\mu}{T} \frac{\partial^2 \psi}{\partial \bar{y}} \right) = (\alpha x)^{b-3a} \frac{\partial}{\partial \eta} \left(\frac{\mu}{T} \frac{\partial^2 F}{\partial \eta^2} \right), \tag{B.12c}$$

and those of the enthalpy balance equation expand as

$$\frac{\partial \psi}{\partial \bar{y}} \frac{\partial T}{\partial x} = (\alpha x)^{b-a} \frac{\partial F}{\partial \eta} \frac{\partial T}{\partial x}, \tag{B.13a}$$

$$-\frac{\partial \psi}{\partial x} \frac{\partial T}{\partial \bar{y}} = -\frac{\partial \psi}{\partial x} (\alpha x)^{-a} \frac{\partial T}{\partial \eta}, \tag{B.13b}$$

$$(\gamma - 1) Ma^2 \frac{\mu}{T} \left(\frac{\partial^2 \psi}{\partial \bar{y}^2} \right)^2 = (\gamma - 1) Ma^2 \frac{\mu}{T} (\alpha x)^{2b-4a} \left(\frac{\partial^2 F}{\partial \eta^2} \right)^2 \tag{B.13c}$$

$$\frac{1}{Pr} \frac{\partial}{\partial \bar{y}} \left(\frac{\mu}{T} \frac{\partial T}{\partial \bar{y}} \right) = \frac{(\alpha x)^{-2a}}{Pr} \frac{\partial}{\partial \eta} \left(\frac{\mu}{T} \frac{\partial T}{\partial \eta} \right). \tag{B.13d}$$

The terms in the streamwise derivatives expand as in (B.8), where

$$\left.\frac{\partial \bar{y}}{\partial x}\right|_Y = \left.\frac{\partial \bar{y}}{\partial \eta}\right|_Y \left.\frac{\partial \eta}{\partial x}\right|_Y = \alpha a \left(\alpha x\right)^{a-1} \left.\frac{\partial \eta}{\partial x}\right|_Y, \tag{B.14}$$

and

$$\frac{\partial \psi}{\partial x} = \left(\alpha x\right)^b \left.\frac{\partial F}{\partial x}\right|_\eta + \alpha b \left(\alpha x\right)^{b-1} F + a\alpha \left(\alpha x\right)^{b-1} \left.\frac{\partial \eta}{\partial x}\right|_Y \frac{\partial F}{\partial \eta}, \tag{B.15a}$$

$$\frac{\partial}{\partial x}\left(\frac{\partial \psi}{\partial \bar{y}}\right) = \alpha \left(b-a\right) \left(\alpha x\right)^{b-a-1} \frac{\partial F}{\partial \eta} + \left(\alpha x\right)^{b-a} \frac{\partial}{\partial x}\left(\frac{\partial F}{\partial \eta}\right)_\eta + \\ + a\alpha \left(\alpha x\right)^{b-a-1} \left.\frac{\partial \eta}{\partial x}\right|_Y \frac{\partial^2 F}{\partial \eta^2}, \tag{B.15b}$$

$$\frac{\partial T}{\partial x} = \left.\frac{\partial T}{\partial x}\right|_\eta + \alpha a \left(\alpha x\right)^{a-1} \left.\frac{\partial \eta}{\partial x}\right|_Y \frac{\partial T}{\partial \eta}. \tag{B.15c}$$

The momentum equation becomes

$$\left(\alpha x\right)^{a+b-1} \alpha \left(b-a\right) \left(\frac{\partial F}{\partial \eta}\right)^2 + \left(\alpha x\right)^{a+b} \frac{\partial F}{\partial \eta} \frac{\partial}{\partial x}\left(\frac{\partial F}{\partial \eta}\right)_\eta - \left(\alpha x\right)^{a+b} \left.\frac{\partial F}{\partial x}\right|_\eta \frac{\partial^2 F}{\partial \eta^2} + \\ - \left(\alpha x\right)^{a+b-1} \alpha b F \frac{\partial^2 F}{\partial \eta^2} = \frac{\partial}{\partial \eta}\left(\frac{\mu}{T}\frac{\partial^2 F}{\partial \eta^2}\right), \tag{B.16}$$

and the enthalpy balance equation becomes

$$\left(\alpha x\right)^{a+b} \frac{\partial F}{\partial \eta} \left.\frac{\partial T}{\partial x}\right|_\eta - \left(\alpha x\right)^{a+b} \frac{\partial T}{\partial \eta} \left.\frac{\partial F}{\partial x}\right|_\eta - \alpha b \left(\alpha x\right)^{a+b-1} F \frac{\partial T}{\partial \eta} = \\ = \left(\alpha x\right)^{2b-2a} \left(\gamma - 1\right) Ma^2 \frac{\mu}{T}\left(\frac{\partial^2 F}{\partial \eta^2}\right)^2 + \frac{1}{Pr}\frac{\partial}{\partial \eta}\left(\frac{\mu}{T}\frac{\partial T}{\partial \eta}\right). \tag{B.17}$$

The functions F and T are independent on x when the streamwise derivatives in (B.16) and (B.17) are zero and the coefficients of all the other terms do not depend on x. The system

$$\begin{cases} a + b - 1 = 0, \\ 2b - 2a = 0, \end{cases} \tag{B.18}$$

yields $a = b = 1/2$. The choice of α is arbitrary, here $\alpha = 1/b = 2$. The boundary layer equations then reduce to a system of nonlinear ODEs in $\eta = \bar{y}\left(2x\right)^{-1/2}$ and $F = \psi\left(2x\right)^{-1/2}$

$$\left(\frac{\mu}{T}F''\right)' + FF'' = 0, \tag{B.19a}$$

$$FT' + \left(\gamma - 1\right) Ma^2 \frac{\mu}{T}\left(F''\right)^2 + Pr^{-1}\left(\frac{\mu}{T}T'\right)' = 0, \tag{B.19b}$$

where the prime denotes differentiation in η, subject to the boundary conditions (B.11)

$$F = F' = 0 \text{ and either } T = T_w \text{ or } \frac{\partial T}{\partial \eta} = 0 \text{ at } \eta = 0, \tag{B.20a}$$

$$F = 1 \text{ and } T = 1 \text{ for } \eta \gg 1 \text{ and } y \ll 1. \tag{B.20b}$$

Only Dirichlet or homogeneous Neumann conditions for the temperature at the wall allow for a self-similar solution. An inhomogeneous boundary condition of the type

$$\frac{\partial T}{\partial \eta} = q_w \left(2x\right)^{1/2} \text{ at } \eta = 0, \tag{B.21}$$

yields a similarity solution only in the vicinity of the leading edge $x \ll 1$. The non-similar governing equations are written using the similarity variables nevertheless

$$\left(\frac{\mu}{T} F''\right)' + F F'' = 2x \left[F' \left.\frac{\partial F'}{\partial x}\right|_\eta - F'' \left.\frac{\partial F}{\partial x}\right|_\eta \right], \tag{B.22a}$$

$$F T' + (\gamma - 1)\, Ma^2 \frac{\mu}{T} \left(F''\right)^2 + \left(\frac{\mu T'}{PrT}\right)' = 2x \left[F' \left.\frac{\partial T}{\partial x}\right|_\eta - T' \left.\frac{\partial F}{\partial x}\right|_\eta \right]. \tag{B.22b}$$

The system (B.22) is parabolic in x and it is computed by streamwise marching with the solution to (B.19) as initial condition [Cebeci, 2002]. The equations for the laminar base flow are expressed as a function of the scaled variable $\hat{x} = xRe^{-1}$. The velocity components (B.10) are not self-similar. Introducing (B.14) yields

$$U\left(x, \eta\right) = F', \tag{B.23a}$$

$$V\left(x, \eta\right) = -\frac{T}{Re^{1/2}} \left[\frac{F}{\left(2x\right)^{1/2}} + \left(2x\right)^{1/2} \left.\frac{\partial F}{\partial x}\right|_\eta + \left(2x\right)^{1/2} \left.\frac{\partial \eta}{\partial x}\right|_Y \frac{\partial F}{\partial \eta} \right], \tag{B.23b}$$

as the wall-normal component is x-dependent even when the boundary-layer flow is self-similar

$$U\left(x, \eta\right) = F', \tag{B.24a}$$

$$V\left(x, \eta\right) = -\frac{T}{Re^{1/2}} \left[\frac{F}{\left(2x\right)^{1/2}} + \left(2x\right)^{1/2} \left.\frac{\partial \eta}{\partial x}\right|_Y \frac{\partial F}{\partial \eta} \right]. \tag{B.24b}$$

The derivative $\partial\eta/\partial x|_Y$ is derived in chapter 2 by inverting (B.7) and considering the chain rule

$$\frac{\partial Y}{\partial x} = \left.\frac{\partial Y}{\partial x}\right|_\eta + \left.\frac{\partial \eta}{\partial x}\right|_Y \frac{\partial Y}{\partial \eta}, \text{ and } \left.\frac{\partial \eta}{\partial x}\right|_Y \equiv -\frac{\eta_c}{2x}, \tag{B.25}$$

where the compressible similarity variable (2.10)

$$\eta_c(x,\eta) = \frac{1}{T(x,\eta)} \int_0^\eta \left[T(x,\breve{\eta}) + 2x \left.\frac{\partial T}{\partial x}\right|_{\breve{\eta}} \right] \mathrm{d}\breve{\eta}, \tag{B.26}$$

extends the definition $\eta_c = T^{-1}\int_0^\eta T \mathrm{d}\breve{\eta}$ of Ricco and X. Wu [2007] to the non-similar case. The derivative of (2.10) with respect to η is

$$\frac{\partial \eta_c}{\partial \eta} = 1 - \frac{\eta_c T'}{T} + \frac{2x}{T} \left.\frac{\partial T}{\partial x}\right|_\eta . \tag{B.27}$$

B.2.1 Identities

The following identities, which are expressed with the scaled coordinate $\hat{x} = xRe^{-1}$, are used in the derivation of the boundary-region equations in chapters 2 and 3. The streamwise derivative at constant y subject to the change of variable $(\hat{x}, y) \to (\hat{x}, \eta)$ expands as in (B.8),

$$\frac{\partial}{\partial \hat{x}} = \left.\frac{\partial}{\partial \hat{x}}\right|_\eta - \frac{\eta_c}{2\hat{x}} \frac{\partial}{\partial \eta}, \tag{B.28}$$

where (2.9) was introduced. The wall-normal derivative of the base-flow wall-normal velocity is, for (B.27),

$$Re \frac{\partial V}{\partial y} = -\frac{FT'}{2\hat{x}T} - \frac{T'}{T} \left.\frac{\partial F}{\partial \hat{x}}\right|_\eta - \left.\frac{\partial F'}{\partial \hat{x}}\right|_\eta + \frac{F'}{T} \left.\frac{\partial T}{\partial \hat{x}}\right|_\eta + \frac{\eta_c F''}{2\hat{x}}. \tag{B.29}$$

The streamwise derivative of the base-flow wall-normal velocity is, for (B.28) and (B.27),

$$\begin{aligned} \frac{Re}{(2\hat{x})^{1/2}} \frac{\partial V}{\partial \hat{x}} = {} & \frac{TF - \eta_c TF' + \eta_c T'F - \eta_c^2 TF''}{4\hat{x}^2} + \frac{\eta_c T' - T}{2\hat{x}} \left.\frac{\partial F}{\partial \hat{x}}\right|_\eta + \frac{\eta_c T'}{\hat{x}} \left.\frac{\partial F'}{\partial \hat{x}}\right|_\eta + \\ & - \frac{F}{2\hat{x}} \left.\frac{\partial T}{\partial \hat{x}}\right|_\eta + \frac{TF'}{2\hat{x}} \left.\frac{\partial \eta_c}{\partial \hat{x}}\right|_\eta - \left.\frac{\partial T}{\partial \hat{x}}\right|_\eta \left.\frac{\partial F}{\partial \hat{x}}\right|_\eta - T \left.\frac{\partial^2 F}{\partial \hat{x}^2}\right|_\eta . \end{aligned} \tag{B.30}$$

The second wall-normal derivative of the wall-normal velocity is, for (B.27),

$$\begin{aligned} \frac{ReT}{(2\hat{x})^{1/2}} \frac{\partial^2 V}{\partial y^2} = {} & -\frac{FT''}{4\hat{x}^2 T} - \frac{F'T'}{4\hat{x}^2 T} + \frac{F(T')^2}{4\hat{x}^2 T^2} - \frac{1}{2\hat{x}} \left(\frac{T'}{T}\right)' \left.\frac{\partial F}{\partial \hat{x}}\right|_\eta - \frac{T'}{2\hat{x}T} \left.\frac{\partial F'}{\partial \hat{x}}\right|_\eta + \\ & - \frac{1}{2\hat{x}} \left.\frac{\partial F''}{\partial \hat{x}}\right|_\eta + \frac{1}{2\hat{x}} \left(\frac{F'}{T}\right)' \left.\frac{\partial T}{\partial \hat{x}}\right|_\eta + \frac{F'}{2\hat{x}T} \left.\frac{\partial T'}{\partial \hat{x}}\right|_\eta + \\ & + \frac{F''}{4\hat{x}^2} - \frac{\eta_c T'F''}{4\hat{x}^2 T} + \frac{F''}{2\hat{x}T} \left.\frac{\partial T}{\partial \eta}\right|_\eta + \frac{\eta_c F'''}{4\hat{x}^2}. \end{aligned} \tag{B.31}$$

The mixed second derivative of the streamwise velocity is, for (B.28) and (B.27),

$$\frac{1}{(2\hat{x})^{1/2}} \frac{\partial^2 U}{\partial \hat{x} \partial y} = \frac{1}{2\hat{x}T} \left.\frac{\partial F''}{\partial \hat{x}}\right|_\eta - \frac{F''}{4\hat{x}^2 T} + \frac{\eta_c T'F''}{4\hat{x}^2 T^2} - \frac{F''}{2\hat{x}T^2} \left.\frac{\partial T}{\partial \hat{x}}\right|_\eta - \frac{\eta_c F'''}{4\hat{x}^2 T}. \tag{B.32}$$

B.3 The Darcy-Forchheimer integral in the momentum equation

Starting from the dimensional streamwise momentum balance equation (4.5), where only the leading-order terms are retained and the volume-averaging operators are omitted

$$\theta_f \rho^* U^* \frac{\partial U^*}{\partial x^*} + \theta_f \rho^* V^* \frac{\partial U^*}{\partial y^*} = \frac{\partial}{\partial y^*}\left[\mu^* \frac{\partial \left(\theta_f U^*\right)}{\partial y^*}\right] + \\ - \theta_f^2 \frac{\mu^* U^*}{K^*} - \theta_f^2 \frac{c_F^*}{K^*} \rho^* U^{*2} + O\left(Re^{-1}\right), \quad \text{(B.33)}$$

The form of $K^*\left(d_g^*\right)$ and $c_F^*\left(d_{g0}^*\right)$ which allows for a self-similar solution is

$$K^* = \frac{\theta_f^3}{\left(1-\theta_f\right)^2} \frac{d_g^{*2}}{A}, \quad \text{(B.34a)}$$

$$c_F^* = \frac{\theta_f}{1-\theta_f} \frac{d_{g0}^*}{B}. \quad \text{(B.34b)}$$

The terms in B.33 are normalized on the reference quantities

$$\frac{\rho_\infty^* U_\infty^*}{L^*}\left(\theta_f \rho U \frac{\partial U}{\partial x} + \theta_f \rho V \frac{\partial U}{\partial y}\right) = \frac{\mu_\infty^* U_\infty^*}{L^{*2}} \frac{\partial}{\partial y}\left[\mu \frac{\partial \left(\theta_f U\right)}{\partial y}\right] + \\ - \frac{\mu_\infty^* U_\infty^*}{d_{g0}^{*2}} \left(\frac{d_{g0}^*}{d_g^*}\right)^2 \theta_f^2 \frac{A\left(1-\theta_f\right)^2}{\theta_f^3} \mu U + \\ - \frac{\rho_\infty^* U_\infty^{*2}}{d_{g0}^{*2}} \left(\frac{d_{g0}^*}{d_g^*}\right)^2 \theta_f^2 \frac{A\left(1-\theta_f\right)^2}{\theta_f^3} \frac{\theta_f}{1-\theta_f} \frac{d_{g0}^*}{B} \rho U^2, \quad \text{(B.35)}$$

and rearranging yields the leading-order balance for $A = O\left(1\right)$ and $B = O(Da^{-1/2})$

$$\theta_f \rho U \frac{\partial U}{\partial x} + \theta_f \rho V \frac{\partial U}{\partial y} = \frac{\partial}{\partial y}\left[\mu \frac{\partial \left(\theta_f u\right)}{\partial y}\right] + \\ - \frac{\theta_f^2}{ReDa} \left(\frac{d_{g0}^*}{d_g^*}\right)^2 \left[A \frac{(1-\theta_f)^2}{\theta_f^3} \mu U + ARe Da \frac{1-\theta_f}{\theta_f^2} \frac{\rho U^2}{BDa^{1/2}}\right]. \quad \text{(B.36)}$$

By introducing the identities $\rho T = 1$, $C_D = A/\kappa_p^2 = A(ReDa)^{-1}$ and $C_F = A/(BDa^{1/2})$, and the velocity components (4.15), the momentum balance becomes

$$(\alpha x)^{a+b-1} \alpha \frac{(b-a)}{\theta_f} \left(\frac{\partial F}{\partial \eta}\right)^2 + (\alpha x)^{a+b} \frac{\partial F}{\partial \eta} \frac{\partial}{\partial x}\left(\frac{1}{\theta_f} \frac{\partial F}{\partial \eta}\right)_\eta + \\ - (\alpha x)^{a+b} \left.\frac{\partial F}{\partial x}\right|_\eta \frac{\partial}{\partial \eta}\left(\frac{1}{\theta_f} \frac{\partial F}{\partial \eta}\right) - (\alpha x)^{a+b-1} \alpha b F \frac{\partial}{\partial \eta}\left(\frac{1}{\theta_f} \frac{\partial F}{\partial \eta}\right) = \frac{\partial}{\partial \eta}\left(\frac{\mu}{T} \frac{\partial^2 F}{\partial \eta^2}\right) +$$

$$- (\alpha x)^{3b-a} \left(\frac{d^*_{g0}}{d^*_g}\right)^2 \left[C_D \frac{(1-\theta_f)^2}{\theta_f^2} \mu T \frac{\partial F}{\partial \eta} + C_F \frac{1-\theta_f}{\theta_f^2} \left(\frac{\partial F}{\partial \eta}\right)^2\right]. \quad \text{(B.37)}$$

The self-similar solution (4.14a) is recovered if $a = b = 1/2$, $\alpha = 2$ and $d^*_g/d^*_{g0} = (2x)^{1/2}$ [Tsiberkin, 2018a].

B.3.1 Identities

The following identities, which are expressed with the scaled coordinate $\hat{x} = xRe^{-1}$, are used in the derivation of the boundary-region equations in chapter 4. The streamwise derivative at constant y subject to the change of variable $(\hat{x}, y) \to (\hat{x}, \eta)$ expands as

$$\frac{\partial}{\partial \hat{x}} = \frac{\partial}{\partial \hat{x}}\bigg|_\eta - \frac{\eta_c}{2\hat{x}} \frac{\partial}{\partial \eta}. \quad \text{(B.38)}$$

The wall-normal derivative of the base-flow wall-normal velocity is, for (B.27),

$$Re \frac{\partial V}{\partial y} = \frac{1}{(2\hat{x})^{1/2}} \frac{1}{T} \frac{\partial}{\partial \eta} \left[\frac{1}{(2\hat{x})^{1/2}} \frac{1}{\theta_f} \left(-TF + \eta_c TF'\right)\right] =$$
$$= \frac{\theta_f'}{\theta_f^2} \frac{F}{2\hat{x}} - \frac{\theta_f'}{\theta_f^2} \frac{\eta_c F'}{2\hat{x}} - \frac{1}{\theta_f} \frac{T'F}{2\hat{x}T} + \frac{1}{\theta_f} \frac{\eta_c F''}{2\hat{x}} \quad \text{(B.39)}$$

The streamwise derivative of the base-flow wall-normal velocity is, for (B.28) and (B.27),

$$\frac{Re}{(2\hat{x})^{1/2}} \frac{\partial V}{\partial \hat{x}} = \frac{1}{(2\hat{x})^{1/2}} \frac{\partial}{\partial \hat{x}} \left[\frac{1}{\theta_f} \frac{1}{(2\hat{x})^{1/2}} \left(-TF + \eta_c TF'\right)\right]_\eta +$$
$$- \frac{\eta_c}{2\hat{x}} \frac{\partial}{\partial \eta} \left[\frac{1}{\theta_f} \frac{1}{(2\hat{x})^{1/2}} \left(-TF + \eta_c TF'\right)\right] =$$
$$= -\frac{1}{2\hat{x}} \left[-\frac{TF}{2\hat{x}\theta_f} + \frac{\eta_c TF'}{2\hat{x}\theta_f} + \frac{\eta_c}{2\hat{x}} \left(\frac{\theta_f'}{\theta_f^2} TF - \frac{\theta_f'}{\theta_f^2} \eta_c TF' - \frac{T'F}{\theta_f} + \frac{\eta_c TF''}{\theta_f}\right)\right] =$$
$$= -\frac{1}{2\hat{x}} \left(-\frac{TF}{2\hat{x}\theta_f} + \frac{\eta_c TF'}{2\hat{x}\theta_f} + \frac{\theta_f'}{\theta_f^2} \frac{\eta_c TF}{2\hat{x}} - \frac{\theta_f'}{\theta_f^2} \frac{\eta_c^2 TF'}{2\hat{x}} - \frac{\eta_c T'F}{2\hat{x}\theta_f} + \frac{\eta_c^2 TF''}{2\hat{x}\theta_f}\right) =$$
$$= \frac{TF}{4\hat{x}^2\theta_f} - \frac{\eta_c TF'}{4\hat{x}^2\theta_f} - \frac{\theta_f'}{\theta_f^2} \frac{\eta_c TF}{4\hat{x}^2} + \frac{\theta_f'}{\theta_f^2} \frac{\eta_c^2 TF'}{4\hat{x}^2} + \frac{\eta_c T'F}{4\hat{x}^2\theta_f} - \frac{\eta_c^2 TF''}{4\hat{x}^2\theta_f}. \quad \text{(B.40)}$$

The second wall-normal derivative of the wall-normal velocity is, for (B.27),

$$\frac{ReT}{(2\hat{x})^{1/2}} \frac{\partial^2 (\theta_f V)}{\partial y^2} = \frac{1}{Re} \frac{T}{4\hat{x}^2} \frac{\partial}{\partial \eta} \left(-\frac{T'F}{T} + \eta_c F''\right) =$$
$$= \frac{1}{4\hat{x}^2} \left(-\frac{T''F}{T} - \frac{T'F'}{T} + \frac{F(T')^2}{T^2} + F'' - \frac{\eta_c T'F''}{T} + \eta_c F'''\right). \quad \text{(B.41)}$$

Appendix C

Receptivity and disturbance growth: linearized framework

This appendix provides additional details on the receptivity framework of LWG99, focusing on the inviscid flow in region I and the derivation of both the outer and initial boundary conditions used in the computation of the boundary-region equations in region III (refer to schematics 2.2 and 2.3).

The asymptotic framework developed by LWG99 is based on the rapid distortion theory of Goldstein [1978], which describes the deformation of compressible potential flows around arbitrary obstacles. Their analysis assumes constant far-field properties, i.e., properties that remain unchanged away from the obstacle. The nature of free-stream disturbances had been previously examined by Kovasznay [1953], who identified three distinct disturbance modes: vortical, acoustic, and entropic. As long as their amplitude remains small and their spatial scale sufficiently large, these modes do not interact. Among them, the solenoidal component of the disturbances represents the isentropic, rotational vortical mode.

The focus of this thesis is on purely convected (i.e. frozen within the flow) vortical gusts of amplitude $\hat{\boldsymbol{u}}^{\infty *}$. The upstream velocity field at an infinite distance from the obstacle ($x^* \to -\infty$)

$$\begin{aligned} \boldsymbol{u}^*\left(x^*, y^*, z^*, t^*\right) &= U_\infty^* \boldsymbol{i} + \hat{\boldsymbol{u}}^{\infty *}\left(x^* - U_\infty^* t^*, y^*, z^*, t\right), \\ \nabla^* \cdot \hat{\boldsymbol{u}}^{\infty *} &= 0, \end{aligned} \tag{C.1}$$

satisfies the three-dimensional Euler equations. The presence of a solid obstacle is modeled using the concept of hydrodynamic drift, which accounts for the relative displacement of a group of fluid particles on the same material surface. This surface is distorted by a hole in the fluid domain. The concept of drift was first introduced for the elementary case of a two-dimensional cylinder [Darwin, 1953], and later extended to three-dimensional bodies of arbitrary shape [Lighthill, 1956].

C.1 Inviscid outer flow in region I

Consider a uniform flow past a plate which is infinitely thin at the leading edge. Shock waves, if present, are assumed to be weak enough so that the effect of the acoustic and entropy modes is negligible [McKenzie and Westphal, 1968]. The static pressure is taken to be zero far upstream, and the dynamic pressure is isentropically converted in its static form at the leading edge. Because the pressure, density and entropy fluctuations are absent, the free-stream vorticity is virtually incompressible and the disturbance flow near the leading edge is described by the homogeneous Poisson equation [Goldstein, 1978; Ricco, 2006]

$$\begin{cases} \nabla^2\phi = 0, & \text{(C.2a)} \\ \dfrac{\partial\phi}{\partial y} + v^\infty = 0 \text{ at } y = 0,\ x > 0, & \text{(C.2b)} \\ \phi \to 0 \text{ as } x \to -\infty, & \text{(C.2c)} \\ \phi \to 0 \text{ as } y \to +\infty, & \text{(C.2d)} \\ \phi = 0 \text{ at } y = 0,\ x < 0, & \text{(C.2e)} \end{cases}$$

where ϕ is the perturbation potential. The solution to the problem (C.2) is obtained using the Wiener-Hopf technique (Choudhari [1996]) and consists in a regular and a singular part. The latter has a singularity at $x = 0$ but decays exponentially as $\sim \exp(-k_z x)$ for large $x \gg 1$ (but $\hat{x} \ll 1$). The regular part is obtained by separation of variables and variation of parameters. It is reasonable to assume a harmonic solution for the perturbation potential [Goldstein, 1978; Choudhari, 1996]

$$\phi(x, y, z, t) = \hat{\phi}(x, y)\mathrm{e}^{i(k_x x + k_y y + k_z z - k_x t)}, \tag{C.3}$$

where the dimensional time frequency is normalized as

$$\omega^* = k_x^* U_\infty^* = k_x^* \Lambda^* \frac{U_\infty^*}{\Lambda^*} = k_x \frac{U_\infty^*}{\Lambda^*}, \tag{C.4}$$

and the non-dimensional time scale is defined as $t = t^* U_\infty^*/\Lambda^*$, so that $\omega^* t^* = k_x t = \mathcal{F}\hat{t}$. The solution

$$\phi\,(x, y, z, t) = \frac{\hat{v}^\infty}{\sqrt{k_x^2 + k_z^2}} \mathrm{e}^{\mathrm{i}k_x(x-t) + \mathrm{i}k_z z - \sqrt{k_x^2 + k_z^2}\, y}, \tag{C.5}$$

does not satisfy the boundary condition for $y = 0$, $x \to -\infty$. The perturbation velocity is [Goldstein, 1978]

$$\boldsymbol{u} = \hat{\boldsymbol{u}}^{\infty} + \nabla\phi = \begin{cases} \left(\hat{u}^{\infty} \mathrm{e}^{ik_y y} + \dfrac{ik_x \hat{v}^{\infty}}{\sqrt{k_x^2 + k_z^2}} \mathrm{e}^{-y\sqrt{k_x^2+k_z^2}} \right) \mathrm{e}^{i(k_x x + k_z z - k_x t)}, & \text{(C.6a)} \\ \left(\hat{v}^{\infty} \mathrm{e}^{ik_y y} - \hat{v}^{\infty} \mathrm{e}^{-y\sqrt{k_x^2+k_z^2}} \right) \mathrm{e}^{i(k_x x + k_z z - k_x t)}, & \text{(C.6b)} \\ \left(\hat{w}^{\infty} \mathrm{e}^{ik_y y} + \dfrac{ik_z \hat{v}^{\infty}}{\sqrt{k_x^2 + k_z^2}} \mathrm{e}^{-y\sqrt{k_x^2+k_z^2}} \right) \mathrm{e}^{i(k_x x + k_z z - k_x t)}. & \text{(C.6c)} \end{cases}$$

Only the wall normal component of the perturbation field (C.6b) tends to zero as $y \to 0$ to satisfy the non-penetration condition (C.2b). The reflected disturbances decay exponentially for $y \gg 1$ and (2.1) is retrieved. The-non dimensional pressure is [Goldstein, 1978]

$$p = -\frac{\partial\phi}{\partial t} - \frac{\partial\phi}{\partial x} = -\frac{\mathrm{D}\phi}{\mathrm{D}t} = 0. \tag{C.7}$$

C.2 Outer boundary conditions for region III

The CLUBR equations (2.16a)–(2.16e) and (4.23)–(4.47) are solved subject to the outer boundary conditions of the mixed type (2.20) and (3.47). These boundary conditions are derived by considering the far-field limit of the CLUBR equations. For $\eta \to \infty$, the functions $F \sim \eta - \beta_c(x)$, $F' \sim 1$, $F'' = 0$, $T \sim 1$, $T' = T'' = 0$, $\mu \sim 1$, $\mu' = \mu'' = 0$, and $\theta_f \sim \theta_{\partial ff} \sim 1$ and $\theta_f' = \theta_f'' = \theta_{\partial ff}' = 0$, and $\eta_c \sim \eta - \gamma_c(\hat{x})$.

The far-field form of the CLUBR equations (2.16a)–(2.16e) is

$$\mathcal{C}| \; \frac{\partial\bar{v}}{\partial\eta} + \bar{w} = 0, \tag{C.8a}$$

$$\mathcal{Y}| \left(\frac{1}{2\hat{x}} - \mathrm{i}\mathcal{F} + k_z^2 \right) \bar{v} + \left.\frac{\partial\bar{v}}{\partial\hat{x}}\right|_{\eta} - \left(\frac{\eta - \beta_c(\hat{x})}{2\hat{x}} - \frac{\mathrm{d}\beta_c}{\mathrm{d}\hat{x}} \right) \frac{\partial\bar{v}}{\partial\eta} + \\ - \frac{2}{3\hat{x}} \frac{\partial^2\bar{v}}{\partial\eta^2} - \frac{1}{6\hat{x}} \frac{\partial\bar{w}}{\partial\eta} + \frac{1}{2\hat{x}} \frac{\partial\bar{p}}{\partial\eta} = 0, \tag{C.8b}$$

$$\mathcal{Z}| \; \frac{k_z^3}{3} \frac{\partial\bar{v}}{\partial\eta} + \left(\frac{4}{3} k_z^2 - \mathrm{i}\mathcal{F} \right) \bar{w} + \left.\frac{\partial\bar{w}}{\partial\hat{x}}\right|_{\eta} + \\ - \left(\frac{\eta - \beta_c(\hat{x})}{2\hat{x}} - \frac{\mathrm{d}\beta_c}{\mathrm{d}\hat{x}} \right) \frac{\partial\bar{w}}{\partial\eta} - \frac{1}{2\hat{x}} \frac{\partial^2\bar{w}}{\partial\eta^2} - k_z^2 \bar{p} = 0. \tag{C.8c}$$

where the identity

$$\left.\frac{\partial F}{\partial \hat{x}}\right|_{\eta} = -\frac{\mathrm{d}\beta_c}{\mathrm{d}\hat{x}} \tag{C.9}$$

was used. Applying the transformation $(\hat{x}, \eta) \rightarrow (\hat{x}, y^{(0)})$, where y_0 is defined in (2.29)

$$y^{(0)} \equiv (2\hat{x}\mathcal{F})^{1/2} \left[\eta - \beta_c\left(\hat{x}\right)\right] - \mathcal{F}^{1/2} \int^{\hat{x}} \frac{\gamma_c\left(\hat{x}\right)}{\left(2\hat{x}\right)^{1/2}} \mathrm{d}\breve{x}, \tag{C.10}$$

to the large-η form of the CLUBR equations, yields the far-field balances

$$\mathcal{C}| \left(2\hat{x}\mathcal{F}\right)^{1/2} \frac{\partial \bar{v}}{\partial y^{(0)}} + \bar{w} = 0, \tag{C.11a}$$

$$\mathcal{Y}| \left(\frac{1}{2\hat{x}} + k_z^2 - \mathrm{i}\mathcal{F}\right) \bar{v} + \left.\frac{\partial \bar{v}}{\partial \hat{x}}\right|_{\eta} - \frac{\mathcal{F}^{1/2}\gamma_c(\hat{x})}{\left(2\hat{x}\right)^{1/2}} \frac{\partial \bar{v}}{\partial y^{(0)}} - \mathcal{F}\frac{\partial^2 \bar{v}}{\partial y^{(0)2}} + \frac{\mathcal{F}^{1/2}}{\left(2\hat{x}\right)^{1/2}} \frac{\partial \bar{p}}{\partial y^{(0)}} = 0, \tag{C.11b}$$

$$\mathcal{Z}| \left(k_z^2 - \mathrm{i}\mathcal{F}\right) \bar{w} + \left.\frac{\partial \bar{w}}{\partial \hat{x}}\right|_{y^{(0)}} - \frac{\mathcal{F}^{1/2}\gamma_c(\hat{x})}{\left(2\hat{x}\right)^{1/2}} \frac{\partial \bar{w}}{\partial y^{(0)}} - \mathcal{F}\frac{\partial^2 \bar{w}}{\partial y^{(0)2}} - k_z^2 \bar{p} = 0. \tag{C.11c}$$

Equations (C.11) are first manipulated to find a solution for the pressure $\bar{p}$. The wall-normal and spanwise momentum balances are combined

$$\left(2\hat{x}\mathcal{F}\right)^{1/2} \frac{\partial}{\partial y^{(0)}} \left[\mathcal{Y}\right] + \left[\mathcal{Z}\right], \tag{C.12}$$

recalling that

$$\left(2\hat{x}\mathcal{F}\right)^{1/2} \frac{\partial}{\partial y^{(0)}} \left(\left.\frac{\partial \bar{v}}{\partial \hat{x}}\right|_{y^{(0)}} \right) = \frac{\partial}{\partial \hat{x}} \left[\left(2\hat{x}\mathcal{F}\right)^{1/2} \frac{\partial \bar{v}}{\partial y^{(0)}} \right]_{y^{(0)}} - \frac{\mathcal{F}^{1/2}}{\left(2\hat{x}\right)^{1/2}} \frac{\partial \bar{v}}{\partial y^{(0)}}, \tag{C.13}$$

and yield the Poisson equation for the pressure

$$\mathcal{F}\frac{\partial^2 \bar{p}}{\partial y^{(0)2}} - k_z^2 \bar{p} = 0. \tag{C.14}$$

The solution that vanishes in the free stream is

$$\bar{p}\left(\hat{x}, y^{(0)}\right) = g\left(\hat{x}\right) \mathrm{e}^{-|\kappa_z| y^{(0)}} \tag{C.15}$$

where $\kappa_z = k_z \mathcal{F}^{-1/2}$ and $g\left(\hat{x}\right)$ is not known at this stage. The solution is the same as in LWG99. Eliminating $\bar{v}$ from (C.11c) with (C.11a) yields a inhomogeneous, convective heat equation for $\bar{w}$

$$\left.\frac{\partial \bar{w}}{\partial \hat{x}}\right|_{y^{(0)}} = \mathcal{F}\frac{\partial^2 \bar{w}}{\partial y^{(0)2}} + \frac{\mathcal{F}^{1/2}\gamma_c(\hat{x})}{\left(2\hat{x}\right)^{1/2}} \frac{\partial \bar{w}}{\partial y^{(0)}} + \left(\mathrm{i}\mathcal{F} - k_z^2\right) \bar{w} + k_z^2 \bar{p}. \tag{C.16}$$

Equation (C.16) can be reduced to the inhomogeneous heat equation by applying the transformations [Polyanin and Nazaikinskii, 2015, §3.8.7.4, p. 385]

$$\bar{w}\left(\hat{x}, y^{(0)}\right) = \breve{w}\left(\hat{x}, \grave{y}^{(0)}\right) \exp\left[\int^{\hat{x}} \left(\mathrm{i}\mathcal{F} - k_z^2\right) \mathrm{d}\breve{x}\right] = \breve{w}\left(\hat{x}, \grave{y}^{(0)}\right) \mathrm{e}^{(\mathrm{i}\mathcal{F} - k_z^2)\hat{x}}, \tag{C.17a}$$

$$\grave{y}^{(0)} = y^{(0)} + \int^{\hat{x}} \frac{\mathcal{F}^{1/2}\gamma_c(\breve{x})}{(2\breve{x})^{1/2}} \mathrm{d}\breve{x} = (2\hat{x}\mathcal{F})^{1/2}\left[\eta - \beta_c(\hat{x})\right], \tag{C.17b}$$

hence

$$\left.\frac{\partial}{\partial \hat{x}}\right|_{y^{(0)}} = \mathcal{F}\left.\frac{\partial}{\partial \bar{x}}\right|_{\grave{y}^{(0)}} + \frac{\mathcal{F}^{1/2}\gamma_c(\hat{x})}{(2\hat{x})^{1/2}} \frac{\partial}{\partial \grave{y}^{(0)}} \text{ and } \frac{\partial}{\partial y^{(0)}} = \frac{\partial}{\partial \grave{y}^{(0)}}, \tag{C.18}$$

which yield

$$\frac{\partial \breve{w}}{\partial \hat{x}} - \mathcal{F}\frac{\partial^2 \breve{w}}{\partial \grave{y}^{(0)2}} = k_z^2 \bar{p} \mathrm{e}^{(k_z^2 - \mathrm{i}\mathcal{F})\hat{x}}. \tag{C.19}$$

An analytical solution for the spanwise velocity $\bar{w}$ is obtained by solving (C.19) subject to the upstream (initial) and outer boundary conditions (refer to schematics 2.2 and 2.3). These conditions are obtained by matching with region I and region IV

$$\lim_{\hat{x}\to 0} \bar{w}^{(III)} = \lim_{\hat{x}\to 0} \breve{w}^{(III)} = \lim_{x\to\infty} \bar{w}^{(I)}, \tag{C.20a}$$

$$\lim_{\grave{y}^{(0)}\to\infty} \breve{w}^{(III)} = \lim_{\hat{y}\to 0} \bar{w}^{(IV)} \mathrm{e}^{(k_z^2 - \mathrm{i}\mathcal{F})\hat{x}}. \tag{C.20b}$$

By matching the velocity in region III and IV (2.27) the following asymptotic identity is derived

$$\mathrm{i}k_z Re\left(\hat{w}^\infty + \frac{\mathrm{i}k_z \hat{v}^\infty}{(k_x^2 + k_z^2)^{1/2}}\right) \frac{\bar{w}}{\mathrm{i}k_z Re} = \hat{w}^\infty \mathrm{e}^{\mathrm{i}\kappa_y \grave{y}^{(0)} - k_y^2 \hat{x}}. \tag{C.21}$$

Here, equations (2.14) and (2.15) were used along with the continuity equation for the vortical gusts in the free-stream $\boldsymbol{k}\cdot\hat{\boldsymbol{u}}^\infty \sim k_y\hat{v}^\infty + k_z\hat{w}^\infty = 0$ ($k_x \ll 1$) yields the outer boundary condition for $\grave{y}^{(0)} \gg 1$ and $\hat{x} = O(1)$

$$\bar{w} \to \frac{k_y}{k_y - \mathrm{i}\,|k_z|} \mathrm{e}^{\mathrm{i}\mathcal{F}\hat{x} + \mathrm{i}\kappa_y \grave{y}^{(0)} - \left(k_y^2 + k_z^2\right)\hat{x}}. \tag{C.22}$$

The far-field solution matches with region I (2.1) upstream

$$\lim_{\hat{x}\to 0} \bar{w}^{(III)} = \lim_{x\to\infty} \bar{w}^{(I)}. \tag{C.23}$$

By introducing (C.6b) for $\hat{x} \ll 1$

$$\left(\mathrm{i}\hat{v}^\infty - \frac{k_y}{|k_z|}\hat{v}^\infty\right) \bar{w} \mathrm{e}^{\mathrm{i}k_z z - i\mathcal{F}\hat{t}} = \left(-\frac{k_y}{|k_z|}\hat{v}^\infty \mathrm{e}^{\mathrm{i}k_y y} + \mathrm{i}\hat{v}^\infty \mathrm{e}^{-y|k_z|}\right) \mathrm{e}^{\mathrm{i}k_z z - i\mathcal{F}\hat{t}}, \tag{C.24}$$

the initial condition for $\hat{x} \ll 1$ and $y^{(0)} = O(1)$ is obtained

$$\bar{w} \sim \breve{w} \to \frac{k_y}{k_y - \mathrm{i}\,|k_z|} \mathrm{e}^{\mathrm{i}k_y y} - \frac{ik_z}{k_y - \mathrm{i}\,|k_z|} \mathrm{e}^{-y|k_z|}. \tag{C.25}$$

The Cauchy problem problem for (C.19) reads

$$\begin{cases} \left.\dfrac{\partial \breve{w}}{\partial \hat{x}}\right|_{y^{(0)}} - \mathcal{F} \dfrac{\partial^2 \breve{w}}{\partial \grave{y}^{(0)2}} = k_z^2 \bar{p}\, \mathrm{e}^{\left(k_z^2 - \mathrm{i}\mathcal{F}\right)\hat{x}}, & \text{(C.26a)} \\ \breve{w} \to \dfrac{k_y}{k_y - \mathrm{i}\,|k_z|} \mathrm{e}^{\mathrm{i}\kappa_y \grave{y}^{(0)} - k_y^2 \hat{x}} \text{ as } \grave{y}^{(0)} \to \infty, & \text{(C.26b)} \\ \breve{w} \to \dfrac{k_y}{k_y - \mathrm{i}\,|k_z|} \mathrm{e}^{\mathrm{i}k_y y} - \dfrac{i\,|k_z|}{k_y - \mathrm{i}\,|k_z|} \mathrm{e}^{-y|k_z|} \text{ as } \hat{x} \to 0. & \text{(C.26c)} \end{cases}$$

Here, the identity $\Psi \sim y \sim \grave{y}^{(0)} \mathcal{F}^{-1/2}$ (for $\hat{x} \ll 1$) was used to enforce the initial conditions. The linear problem (C.26) is split into two homogeneous problems and an inhomogeneous problem. The homogeneous problems are solved by separation of variables

$$\breve{w} = A\left(\hat{x}\right) B(\grave{y}^{(0)}) \tag{C.27}$$

where

$$A(\hat{x}) = A_0 \mathrm{e}^{C\hat{x}}, \tag{C.28a}$$

$$B(\grave{y}^{(0)}) = B_0 \mathrm{e}^{-C^{1/2}\mathcal{F}^{-1/2}\grave{y}^{(0)}} + B_1 \mathrm{e}^{C^{1/2}\mathcal{F}^{-1/2}\grave{y}^{(0)}}, \tag{C.28b}$$

the solution to the two homogeneous problems of (C.26) is

$$\breve{w}_H\left(\hat{x}, \grave{y}^{(0)}\right) = \frac{1}{k_y - \mathrm{i}\,|k_z|} \left(k_y \mathrm{e}^{-k_y^2 \hat{x} + \mathrm{i}\kappa_y \grave{y}^{(0)}} - \mathrm{i}\,|k_z|\, \mathrm{e}^{-|k_z|\grave{y}^{(0)} + k_z^2 \hat{x}} \right), \tag{C.29}$$

or

$$\bar{w}_H\left(\hat{x}, \grave{y}^{(0)}\right) = \frac{\mathrm{e}^{\mathrm{i}\mathcal{F}\hat{x}}}{k_y - \mathrm{i}\,|k_z|} \left(k_y \mathrm{e}^{\mathrm{i}\kappa_y \grave{y}^{(0)} - \left(k_y^2 + k_z^2\right)\hat{x}} - \mathrm{i}\,|k_z|\, \mathrm{e}^{-|k_z|\grave{y}^{(0)}} \right), \tag{C.30}$$

Note that the initial and outer boundary condition were imposed to find the solution to the homogeneous problem. The inhomogeneous problem is solved subject to the initial condition $\breve{w}_I \to 0$ for $\hat{x} \ll 1$. Its solution is [Polyanin and Nazaikinskii, 2015, §3.1.2, p. 270]

$$\breve{w}_I\left(\hat{x}, \grave{y}^{(0)}\right) = \int_0^{\hat{x}} \int_{-\infty}^{\infty} \frac{k_z^2 \bar{p}\left(\hat{x}, \grave{y}^{(0)}\right) \mathrm{e}^{\left(k_z^2 - \mathrm{i}\mathcal{F}\right)\hat{x}}}{2\left[\pi \mathcal{F}\left(\hat{x} - \breve{x}\right)\right]^{1/2}} \exp\left[-\frac{\left(\grave{y}^{(0)} - \breve{y}\right)^2}{4\mathcal{F}\left(\hat{x} - \breve{x}\right)} \right] \mathrm{d}\breve{y}\mathrm{d}\breve{x}. \tag{C.31}$$

that is, for (C.15)

$$\breve{w}_I\left(\hat{x}, \grave{y}^{(0)}\right) =$$

$$= \int_0^{\hat{x}} \frac{k_z^2 g\left(\breve{x}\right) \mathrm{e}^{\left(k_z^2 - \mathrm{i}\mathcal{F}\right)\breve{x}}}{2\left[\pi\mathcal{F}\left(\hat{x}-\breve{x}\right)\right]^{1/2}} \left\{ \int_{-\infty}^{+\infty} \exp\left[-\frac{\left(\grave{y}^{(0)} - \breve{y}\right)^2}{4\mathcal{F}\left(\hat{x}-\breve{x}\right)} - \left|\kappa_z\right| \breve{y} \right] \mathrm{d}\breve{y} \right\} \mathrm{d}\breve{x}. \quad \text{(C.32)}$$

The innermost integral is written as [Polyanin and Manzhirov, 2008, suppl. 4.2.16]

$$\int_{-\infty}^{+\infty} \exp\left[-\frac{\left(\grave{y}^{(0)} - \breve{y}\right)^2}{4\mathcal{F}\left(\hat{x}-\breve{x}\right)} - \left|\kappa_z\right| \breve{y} \right] \mathrm{d}\breve{y} = \exp\left[-\frac{\hat{y}^{(0)2}}{4\mathcal{F}\left(\hat{x}-\breve{x}\right)} \right] \int_{-\infty}^{\infty} \mathrm{e}^{b\breve{y} - a^2\breve{y}^2} \mathrm{d}\breve{y}, \quad \text{(C.33)}$$

where $a^2 = \left[4\mathcal{F}\left(\breve{x}-\hat{x}\right)\right]^{-1}$ and $b = 2\grave{y}^{(0)}\left[4\mathcal{F}\left(\breve{x}-\hat{x}\right)\right]^{-1} - \left|\kappa_z\right|$. Its solution is

$$\int_{-\infty}^{\infty} \mathrm{e}^{-a^2\breve{y}^2 - b\breve{y}} \mathrm{d}\breve{y} = \frac{\pi^{1/2}}{|a|} \mathrm{e}^{b^2/(2a)^2}, \quad \text{(C.34)}$$

and

$$\exp\left[\frac{\grave{y}^{(0)2}}{4\mathcal{F}\left(\hat{x}-\breve{x}\right)} \right] \int_{-\infty}^{\infty} \mathrm{e}^{-a^2\breve{y}^2 - b\breve{y}} \mathrm{d}\breve{y} = 2\left[\pi\mathcal{F}\left(\hat{x}-\breve{x}\right)\right]^{1/2} \mathrm{e}^{-\left|\kappa_z\right|\grave{y}^{(0)} + k_z^2\left(\hat{x}-\breve{x}\right)}. \quad \text{(C.35)}$$

The inhomogeneous solution to (C.26) is

$$\breve{w}_I\left(\hat{x}, \grave{y}^{(0)}\right) = \int_0^{\hat{x}} k_z^2 g\left(\breve{x}\right) \mathrm{e}^{\left(k_z^2 - \mathrm{i}\mathcal{F}\right)\breve{x}} \mathrm{e}^{-\left|\kappa_z\right|\grave{y}^{(0)} + k_z^2\left(\hat{x}-\breve{x}\right)} \mathrm{d}\breve{x} =$$

$$= k_z^2 \mathrm{e}^{-\left|\kappa_z\right|\grave{y}^{(0)} + k_z^2\hat{x}} \int_0^{\hat{x}} g\left(\breve{x}\right) \mathrm{e}^{-\mathrm{i}\mathcal{F}\breve{x}} \mathrm{d}\breve{x}, \quad \text{(C.36)}$$

which, by introducing the transformation (C.17a), becomes

$$\bar{w}_I = k_z^2 \mathrm{e}^{\mathrm{i}\mathcal{F}\hat{x} - \left|\kappa_z\right|\grave{y}^{(0)}} \int_0^{\hat{x}} g\left(\breve{x}\right) \mathrm{e}^{-\mathrm{i}\mathcal{F}\breve{x}} \mathrm{d}\breve{x}. \quad \text{(C.37)}$$

The complete solution for the spanwise velocity

$$\bar{w}\left(\hat{x}, \grave{y}^{(0)}\right) = \bar{w}_H + \bar{w}_I = \frac{\mathrm{e}^{\mathrm{i}\mathcal{F}\hat{x}}}{k_y - \mathrm{i}\left|k_z\right|} \left(k_y \mathrm{e}^{\mathrm{i}\kappa_y \grave{y}^{(0)} - \left(k_y^2 + k_z^2\right)\hat{x}} - \mathrm{i}\left|k_z\right| \mathrm{e}^{-\left|\kappa_z\right|\grave{y}^{(0)}} \right) +$$

$$+ k_z^2 \mathrm{e}^{\mathrm{i}\mathcal{F}\hat{x} - \left|\kappa_z\right|\grave{y}^{(0)}} \int_0^{\hat{x}} g\left(\breve{x}\right) \mathrm{e}^{-\mathrm{i}\mathcal{F}\breve{x}} \mathrm{d}\breve{x} \quad \text{(C.38)}$$

is rewritten as a function of η by substituting (C.17b)

$$\bar{w}\left(\hat{x}, \eta\right) = \frac{\mathrm{e}^{\mathrm{i}\mathcal{F}\hat{x}}}{k_y - \mathrm{i}\left|k_z\right|} \Big[k_y \mathrm{e}^{\mathrm{i}k_y(2\hat{x})^{1/2}\left[\eta - \beta_c(\hat{x})\right] - \left(k_y^2 + k_z^2\right)\hat{x}} +$$

$$- \mathrm{i}\left|k_z\right| \mathrm{e}^{-\left|k_z\right|(2\hat{x})^{1/2}\left[\eta - \beta_c(\hat{x})\right]} \Big] + k_z^2 \mathrm{e}^{\mathrm{i}\mathcal{F}\hat{x} - \left|k_z\right|(2\hat{x})^{1/2}\left[\eta - \beta_c(\hat{x})\right]} \int_0^{\hat{x}} g\left(\breve{x}\right) \mathrm{e}^{-\mathrm{i}\mathcal{F}\breve{x}} \mathrm{d}\breve{x}. \quad \text{(C.39)}$$

The wall-normal velocity is found by integrating the mass conservation equation in the far field (C.38)

$$\bar{v}\left(\hat{x}, \grave{y}^{(0)}\right) = -\frac{1}{\left(2\hat{x}\mathcal{F}\right)^{1/2}} \int \bar{w}\left(\hat{x}, \grave{y}^{(0)}\right) \mathrm{d}\grave{y}^{(0)} + C_v\left(\hat{x}\right), \quad \text{(C.40)}$$

where $\bar{w}$ is given by (C.39). The integral is

$$\bar{v}\left(\hat{x},\grave{y}^{(0)}\right)=\frac{1}{\left(2\hat{x}\right)^{1/2}}\frac{\mathrm{i}\mathrm{e}^{\mathrm{i}\mathcal{F}\hat{x}}}{k_y-\mathrm{i}\left|k_z\right|}\left(\mathrm{e}^{\mathrm{i}\kappa_y\grave{y}^{(0)}-\left(k_y^2+k_z^2\right)\hat{x}}-\mathrm{e}^{-\left|\kappa_z\right|\grave{y}^{(0)}}\right)+$$
$$+\frac{\left|k_z\right|}{\left(2\hat{x}\right)^{1/2}}\mathrm{e}^{\mathrm{i}\mathcal{F}\hat{x}-\left|\kappa_z\right|\grave{y}^{(0)}}\int_0^{\hat{x}}g\left(\breve{x}\right)\mathrm{e}^{-\mathrm{i}\mathcal{F}\breve{x}}\mathrm{d}\breve{x}+C_v\left(\hat{x}\right). \quad \text{(C.41)}$$

Here the function $C_v(\hat{x})$ is found by matching with the outer solution

$$\lim_{\grave{y}^{(0)}\to\infty}\bar{v}^{(III)}=\lim_{\hat{y}\to 0}\bar{v}^{(IV)}, \quad \text{(C.42)}$$

where (2.27) is introduced

$$\mathrm{i}k_z Re\frac{\left(2\hat{x}\right)^{1/2}}{Re}\left[\hat{w}^{\infty}+\frac{\mathrm{i}k_z\hat{v}^{\infty}}{\left(k_x^2+k_z^2\right)^{1/2}}\right]\left[\frac{1}{\left(2\hat{x}\right)^{1/2}}\frac{\mathrm{i}\mathrm{e}^{\mathrm{i}\mathcal{F}\hat{x}}}{k_y-\mathrm{i}\left|k_z\right|}\mathrm{e}^{\mathrm{i}\kappa_y\grave{y}^{(0)}-\left(k_y^2+k_z^2\right)\hat{x}}+C_v\left(\hat{x}\right)\right]=$$
$$=\hat{v}^{\infty}\mathrm{e}^{\mathrm{i}\left(\mathcal{F}\hat{x}+\kappa_y\grave{y}^{(0)}\right)-\left(k_y^2+k_z^2\right)\hat{x}}. \quad \text{(C.43)}$$

Matching yields $C_v\left(\hat{x}\right)=0$, and the wall-normal velocity is

$$\bar{v}\left(\hat{x},y^{(0)}\right)=\frac{1}{\left(2\hat{x}\right)^{1/2}}\frac{\mathrm{i}\mathrm{e}^{\mathrm{i}\mathcal{F}\hat{x}}}{k_y-\mathrm{i}\left|k_z\right|}\left(\mathrm{e}^{\mathrm{i}\kappa_y y^{(0)}-\left(k_y^2+k_z^2\right)\hat{x}}-\mathrm{e}^{-\left|\kappa_z\right|y^{(0)}}\right)+$$
$$+\frac{\left|k_z\right|}{\left(2\hat{x}\right)^{1/2}}\mathrm{e}^{\mathrm{i}\mathcal{F}\hat{x}-\left|\kappa_z\right|y^{(0)}}\int_0^{\hat{x}}g\left(\breve{x}\right)\mathrm{e}^{-\mathrm{i}\mathcal{F}\breve{x}}\mathrm{d}\breve{x}, \quad \text{(C.44)}$$

or, by introducing (C.17b),

$$\bar{v}\left(\hat{x},\eta\right)=\frac{1}{\left(2\hat{x}\right)^{1/2}}\frac{\mathrm{i}\mathrm{e}^{\mathrm{i}\mathcal{F}\hat{x}}}{k_y-\mathrm{i}\left|k_z\right|}\left(\mathrm{e}^{\mathrm{i}k_y\left(2\hat{x}\right)^{1/2}\left[\eta-\beta_c(\hat{x})\right]-\left(k_y^2+k_z^2\right)\hat{x}}+\right.$$
$$\left.-\mathrm{e}^{-\left|k_z\right|\left(2\hat{x}\right)^{1/2}\left[\eta-\beta_c(\hat{x})\right]}\right)+$$
$$+\frac{\left|k_z\right|}{\left(2\hat{x}\right)^{1/2}}\mathrm{e}^{\mathrm{i}\mathcal{F}\hat{x}-\left|k_z\right|\left(2\hat{x}\right)^{1/2}\left[\eta-\beta_c(\hat{x})\right]}\int_0^{\hat{x}}g\left(\breve{x}\right)\mathrm{e}^{-\mathrm{i}\mathcal{F}\breve{x}}\mathrm{d}\breve{x}. \quad \text{(C.45)}$$

The far-field solutions (C.15), (C.39) and (C.45) contain the unknown function $g(\hat{x})$ and cannot be imposed as Dirichlet conditions for solving the CLUBR equations. The conditions of the mixed type (2.20) are obtained by combining (C.15), (C.39) and (C.45) with their derivatives in η to eliminate $g(\hat{x})$.

C.3 Initial conditions for region III

The initial perturbation profiles are found by asymptotically matching the upstream ($\hat{x}\ll 1$) limit of the CLUBR equations to the upstream limit of the far-field solutions

(C.39) and (C.45) (i.e. the initial outer condition IOC in the schematic 2.3). The velocity components, the temperature and the pressure expand in the power series [Ricco and X. Wu, 2007]

$$\grave{\boldsymbol{q}}\left(\hat{x},\eta\right)=\sum_{n=0}^{\infty}\left(2\hat{x}\right)^{n/2}\left[2\hat{x}U_n\left(\eta\right),V_n\left(\eta\right),W_n\left(\eta\right),\left(2\hat{x}\right)^{-1/2}P_n\left(\eta\right),2\hat{x}T_n\left(\eta\right)\right]. \quad \text{(C.46)}$$

By introducing (C.46) in the CLUBR equations and retaining the $O\left(1\right)$ and $O\left(\hat{x}^{1/2}\right)$ balances, two systems of coupled linear ordinary differential equations in η are derived [Viaro and Ricco, 2019a]. At leading order, the continuity, momentum and enthalpy balances read

$$\mathcal{C}_0|\ \left(\frac{\eta_c T'}{T}+2\right)U_0-\eta_c U_0'-\frac{T'}{T^2}V_0+\frac{1}{T}V_0'+W_0+ \\ -\left(\frac{FT'}{T^2}+2\frac{F'}{T}\right)T_0+\frac{F}{T}T_0'=0, \quad \text{(C.47a)}$$

$$\mathcal{X}_0|\ \left(2F'-\eta_c F''\right)U_0-\left[F+\left(\frac{\mu}{T}\right)'\right]U_0'-\frac{\mu}{T}U_0''+\frac{F''}{T}V_0+ \\ +\left[\frac{FF''}{T}-\left(\frac{\mu' F''}{T}\right)'\right]T_0-\frac{\mu' F''}{T}T_0'=0, \quad \text{(C.47b)}$$

$$\mathcal{Y}_0|\ P_0'=0, \quad \text{(C.47c)}$$

$$\mathcal{Z}_0|\ \left[F+\left(\frac{\mu}{T}\right)'\right]W_0'+\frac{\mu}{T}W_0''=0, \quad \text{(C.47d)}$$

$$\mathcal{E}_0|\ -\eta_c T'U_0-\left(\gamma-1\right)Ma^2\frac{2\mu F''}{T}U_0'+\frac{T'}{T}V_0+ \\ +\left[\frac{FT'}{T}-\left(\gamma-1\right)Ma^2\frac{\mu'(F'')^2}{T}-\frac{1}{Pr}\left(\frac{\mu' T'}{T}\right)'+2F'\right]T_0+ \\ -\left[F+\frac{1}{Pr}\left(\frac{\mu}{T}\right)'+\frac{1}{Pr}\frac{\mu' T'}{T}\right]T_0'+\frac{1}{Pr}\frac{\mu}{T}T_0''=0, \quad \text{(C.47e)}$$

where the prime denotes differentiation in η. The balances $O\left(\hat{x}^{1/2}\right)$ are

$$\mathcal{C}_1|\ \left(\frac{\eta_c T'}{T}+3\right)U_1-\eta_c U_1'-\frac{T'}{T^2}V_1+\frac{1}{T}V_1'+W_1+ \\ -\left(\frac{FT'}{T^2}+3\frac{F'}{T}\right)T_1+\frac{F}{T}T_1'=0, \quad \text{(C.48a)}$$

$$\mathcal{X}_1|\ \left(3F' - \eta_c F''\right) U_1 - \left[F + \left(\frac{\mu}{T}\right)'\right] U_1' - \frac{\mu}{T} U_1'' + \frac{F''}{T} V_1 + \left[\frac{FF''}{T} + \right.$$
$$\left. - \left(\frac{\mu' F''}{T}\right)'\right] T_1 - \frac{\mu' F''}{T} T_1' = 0, \quad \text{(C.48b)}$$

$$\mathcal{Y}_1|\ \left[\left(TF - \eta_c TF' + \eta_c T' F - \eta_c^2 TF''\right) + \frac{4\mu' T'}{3}\right] U_0 + \frac{2}{3}\left[\left(\eta_c \mu\right)' - \mu\right] U_0' +$$
$$+ \frac{\eta_c \mu}{3} U_0'' + \left(F' - \frac{T'F}{T} + \eta_c F''\right) V_0 - \left[F + \frac{4}{3}\left(\frac{\mu}{T}\right)'\right] V_0' - \frac{4}{3}\frac{\mu}{T} V_0'' + \frac{2\mu' T'}{3} W_0 +$$
$$- \frac{\mu}{3} W_0' + \left[\frac{4}{3}\left(\frac{\mu' T' F}{T}\right)' + \eta_c \left(FF'\right)' - \eta_c T \left(\frac{\mu' F''}{T}\right)' - 3\mu' F'' - FF' - \frac{F^2 T'}{T}\right] T_0 +$$
$$+ \left(\frac{4\mu' T' F}{3T} - \eta_c \mu' F''\right) T_0' + P_1' = 0, \quad \text{(C.48c)}$$

$$\mathcal{Z}_1|\ F' W_1 - \left[F - \left(\frac{\mu}{T}\right)'\right] W_1' - \frac{\mu}{T} W_1'' - k_z^2 T P_0 = 0, \quad \text{(C.48d)}$$

$$\mathcal{E}_1|\ -\eta_c T' U_1 - \left(\gamma - 1\right) Ma^2 \frac{2\mu F''}{T} U_1' + \frac{T'}{T} V_1 +$$
$$+ \left[\frac{FT'}{T} - \left(\gamma - 1\right) Ma^2 \frac{\mu' (F'')^2}{T} - \frac{1}{Pr}\left(\frac{\mu' T'}{T}\right)' + 3F'\right] T_1 +$$
$$- \left[F + \frac{1}{Pr}\left(\frac{\mu}{T}\right)' + \frac{1}{Pr}\frac{\mu' T'}{T}\right] T_1' - \frac{1}{Pr}\frac{\mu}{T} T_1'' = 0. \quad \text{(C.48e)}$$

Equations (C.47a)–(C.47e) and (C.48a)–(C.48e) are solved by means of a block-elimination algorithm for U_0, U_0', V_0, W_0, W_0', T_0, T_0', and U_1, U_1', V_1, W_1, W_1', T_1, T_1'. Seven boundary conditions need to be imposed on the systems (C.47a)–(C.47e) and (C.48a)–(C.48e). Three no-slip conditions $U_0 = V_0 = W_0 = U_1 = V_1 = W_1 = 0$ and a null temperature gradient $T_0' = T_1' = 0$ are imposed at the bottom boundary. Two of these far-field conditions must be $U_0 = U_1 = 0$ and $T_0 = T_1 = 0$. The question is as to whether one needs to impose the remaining far-field condition on the wall-normal or the spanwise component. The answer is found by examining the small-$\hat{x}$ expansion of (C.39) and (C.45) (i.e. the initial outer condition in the schematic 2.3). This limit is obtained by expanding the exponential function for small arguments [e.g. Bender and Orszag, 1999]

$$\mathrm{e}^{C\hat{x}} = \sum_{n=0}^{\infty} \frac{(C\hat{x})^n}{n!} \text{ for } \hat{x} \ll 1. \quad \text{(C.49)}$$

Upstream, the unknown function $g(\hat{x})$ expands as the pressure (C.15)

$$g(\hat{x}) \sim \frac{g_0}{(2\hat{x})^{1/2}} + g_1 + \ldots \text{ for } \hat{x} \ll 1 \quad \text{(C.50)}$$

where g_0 and g_1 are real constants $O(1)$, and

$$\int_0^{\hat{x}} g(\breve{x})\, \mathrm{e}^{-\mathrm{i}\breve{x}} \mathrm{d}\breve{x} \sim g_0 (2\hat{x})^{1/2} + g_1 \hat{x} + \dots \text{ for } \hat{x} \ll 1,\ \eta = O(1). \tag{C.51}$$

and $\bar{\eta} = \eta - \beta_c$. The upstream expansion of the large-η solution of the wall-normal velocity (C.45) is

$$\bar{v} \sim -\bar{\eta} + |k_z|\, g_0 + \left[-\mathrm{i}\,(k_y + \mathrm{i}\,|k_z|)\, \frac{\bar{\eta}^2 + 1}{2} + |k_z|\, \frac{g_1}{2} - g_0 k_z^2 \bar{\eta} \right] (2\hat{x})^{1/2} + \dots \tag{C.52}$$

The large-η solution of the spanwise velocity is also expanded for small $\hat{x}$

$$\bar{w} \sim 1 + \left[\mathrm{i}\,(k_y + \mathrm{i}\,|k_z|)\, \bar{\eta} + k_z^2 g_0 \right] (2\hat{x})^{1/2} + \dots \tag{C.53}$$

The expansion in (C.53) provides the last boundary condition for the spanwise velocity

$$W_0 = 1, \tag{C.54a}$$

$$W_1 = \mathrm{i}\,(k_y + \mathrm{i}\,|k_z|)\, \bar{\eta} + k_z^2 g_0. \tag{C.54b}$$

The constant g_0 is determined by observing that the first term of the upstream expansion (C.46) is $O(\bar{\eta})$ in the far field. No boundary condition is imposed on the wall-normal velocity components V_0 and V_1. The leading order terms in (C.52) then read

$$\lim_{\bar{\eta}\to\infty} (V_0 + \bar{\eta}) = |k_z|\, g_0 \equiv V_C, \tag{C.55}$$

and

$$g_0 = -\frac{V_C}{|k_z|}. \tag{C.56}$$

In the incompressible limit, $\beta_c \to \beta = 1.21678$ [van Dyke, 1975] and $V_C/\beta \to 3/4$ [LWG99]. In summary, the far-field boundary conditions are

$$U_0 \to 0,\ W_0 \to 1,\ T_0 \to 0 \text{ at } O(1), \tag{C.57a}$$

$$U_1 \to 0,\ W_1 \to \mathrm{i}\,(k_y + \mathrm{i}\,|k_z|)\, \bar{\eta} - |k_z|\, V_C,\ T_1 \to 0 \text{ at } O\left(\hat{x}^{1/2}\right) \tag{C.57b}$$

C.3.1 Upstream solution for the pressure

The constant g_1 appears in the large-η, small-$\hat{x}$ asymptotic limit of $\bar{v}$ (C.52). Its value is determined by considering the large-η limit of the continuity equation at $O\left(\hat{x}^{1/2}\right)$ (C.48a)

$$\lim_{\eta\to\infty} (V_1' + W_1) = 0. \tag{C.58}$$

Matching with the $O\left(\hat{x}^{1/2}\right)$-term in the spanwise velocity expansion (C.53) yields

$$V_1' \to -\mathrm{i}\left(k_y + \mathrm{i}\left|k_z\right|\right)\bar{\eta} + \left|k_z\right| V_C, \tag{C.59}$$

and

$$V_1 = -\mathrm{i}\left(k_y + \mathrm{i}\left|k_z\right|\right)\left(\frac{\eta^2}{2} - \beta_c\eta\right) + V_C\left|k_z\right|\eta + c_1. \tag{C.60}$$

The complex constant c_1 is obtained by computing $\lim_{\eta\to\infty} V_1$. Matching the latter expression with the large-η, small-$\hat{x}$ limit of $\bar{v}$ (C.52) at $O\left(\hat{x}^{1/2}\right)$ yields

$$g_1 \to \frac{\mathrm{i}}{\left|k_z\right|}\left(k_y + \mathrm{i}\left|k_z\right|\right)\frac{\beta_c^2 + 1}{2} + V_C\beta_c + \frac{2c_1}{\left|k_z\right|}. \tag{C.61}$$

Both g_1 and c_1 are obtained as outputs of (C.48a)–(C.48e) because no far-field condition is imposed on the wall-normal velocity component. The constants g_1 and c_1 are used to construct the initial profiles of $g(\hat{x})$

$$g\left(\hat{x}\right)\mathrm{e}^{-(2\hat{x})^{1/2}\bar{\eta}|k_z|} \sim \frac{g_0}{\left(2\hat{x}\right)^{1/2}} - g_0\left|k_z\right|\bar{\eta} + g_1 + \ldots \text{ as } \hat{x} \ll 1, \tag{C.62}$$

and the pressure

$$P_0 = -\frac{V_C}{\left|k_z\right|}, \quad P_1 = g_1 + V_C\bar{\eta}. \tag{C.63}$$

C.3.2 Composite initial profiles

The upstream solution to the LUBR equations which is uniformly valid for small $\hat{x}$ and $\eta = O\left(1\right)$ is obtained by matching the asymptotic expansions [Bender and Orszag, 1999]

$$\bar{v}_{init} = \bar{v}_{BL} + \bar{v}_{FF} - \bar{v}_c, \tag{C.64a}$$

$$\bar{w}_{init} = \bar{w}_{BL} + \bar{w}_{FF} - \bar{w}_c, \tag{C.64b}$$

$$\bar{p}_{init} = \bar{p}_{BL} + \bar{p}_{FF} - \bar{p}_c, \tag{C.64c}$$

where the subscript BL denotes the steady boundary-layer velocity (C.46). The far-field velocity FF is given by (C.45) and (C.39) and $\bar{v}_c$, $\bar{w}_c$ and $\bar{p}_c$ are the common parts is the common part. The common part is inferred by comparing the far-field limits of V_0, V_1, W_0, W_1 and $\bar{v}_{FF}$, $\bar{w}_{FF}$ and $\bar{p}_{FF}$. The common parts are [Viaro and Ricco, 2019a]

$$\bar{v}_c = -\bar{\eta} - V_C + \left(2\hat{x}\right)^{1/2}\left[-\frac{\mathrm{i}}{2}\left(k_y + \mathrm{i}\left|k_z\right|\right)\left(\bar{\eta}^2 + 1\right) + V_c\left|k_z\right|\bar{\eta} + \frac{\left|k_z\right| g_1}{2}\right], \tag{C.65a}$$

$$\bar{w}_c = 1 + \left(2\hat{x}\right)^{1/2}\left[\mathrm{i}\left(k_y + \mathrm{i}\left|k_z\right|\right)\bar{\eta} - V_C\left|k_z\right|\right], \tag{C.65b}$$

$$\bar{p}_c = \frac{P_0}{\left(2\hat{x}\right)^{1/2}} + g_1 + V_C\bar{\eta}. \tag{C.65c}$$

Bibliography

Abramowitz, M. and I. A. Stegun [1970]. *Handbook of mathematical functions with formulas, graphs, and mathematical tables*. Appl. Math. Series v. 55, no. 1972. U.S. Gov. Print. Office.

Ackerberg, R. C. and J. H. Phillips [1972]. "The unsteady laminar boundary layer on a semi-infinite flat plate due to small fluctuations in the magnitude of the free-stream velocity". In: *J. Fluid Mech.* 51, pp. 137–157.

Anderson, J. D. [2016]. *Fundamentals of aerodynamics*. McGraw-Hill Education.

— [2019]. *Hypersonic and high-temperature gas dynamics*. AIAA. ISBN: 9781624105142.

— [2020]. *Modern compressible flow: with historical perspective*. McGraw-Hill Education. ISBN: 9781260471441.

Andersson, P., M. Berggren, and D. S. Henningson [Jan. 1999]. "Optimal disturbances and bypass transition in boundary layers". In: *Phys. Fluids* 11.1, pp. 134–150. ISSN: 1070-6631. DOI: 10.1063/1.869908.

Angot, P., B. Goyeau, and J. A. Ochoa-Tapia [June 2017]. "Asymptotic modeling of transport phenomena at the interface between a fluid and a porous layer: Jump conditions". In: *Phys. Rev. E* 95 [6], p. 063302. DOI: 10.1103/PhysRevE.95.063302.

Antoniadis, P. D. and M. V. Papalexandris [2015]. "Dynamics of shear layers at the interface of a highly porous medium and a pure fluid". In: *Phys. Fluids* 27.1, p. 014104. DOI: 10.1063/1.4905558.

— [2016]. "Numerical study of unsteady, thermally-stratified shear flows in superposed porous and pure-fluid domains". In: *Int. J. Heat Mass Transf.* 96, pp. 643–659. ISSN: 0017-9310. DOI: 10.1016/j.ijheatmasstransfer.2016.01.056.

Aref, H. and S. Balachandar [2018]. *A first course in computational fluid dynamics*. Camb. Univ. Press. ISBN: 9781107178519.

Attenborough, K. [1982]. "Acoustical characteristics of porous materials". In: *Phys. Rep.* 82.3, pp. 179–227. ISSN: 0370-1573. DOI: 10.1016/0370-1573(82)90131-4.

Bachmat, Y. and J. Bear [1986]. "Macroscopic modelling of transport phenomena in porous media. 1: The continuum approach". In: *Transp. Porous Media* 1.3, pp. 213–240. ISSN: 1573-1634. DOI: 10.1007/BF00238181.

Barrère, J., O. Gipouloux, and S. Whitaker [Mar. 1992]. "On the Closure Problem for Darcy's Law". In: *Transp. Porous Media* 7.3, pp. 209–222. ISSN: 1573-1634. DOI: 10.1007/BF01063960.

Bear, J. [2018]. *Modeling phenomena of flow and transport in porous media*. Vol. 31. Springer.

Bear, J. and Y. Bachmat [Jan. 1967]. "A Generalized Theory on Hydrodynamic Dispersion in Porous Media". In: *Int. Union Geod. Geophys. Publ.* 72.

— [Sept. 1986]. "Macroscopic modelling of transport phenomena in porous media. 2: Applications to mass, momentum and energy transport". In: *Transp. Porous Media* 1.3, pp. 241–269. ISSN: 1573-1634. DOI: 10.1007/BF00238182.

— [1990]. *Introduction to modeling of transport phenomena in porous media*. Dordrecht: Kluwer Acad. Publ. ISBN: 9789400919266.

Beavers, G. S. and D. D. Joseph [1967]. "Boundary conditions at a naturally permeable wall". In: *J. Fluid Mech.* 30.1, pp. 197–207. DOI: 10.1017/S0022112067001375.

Beavers, G. S. and E. M. Sparrow [Dec. 1969]. "Non-Darcy flow through fibrous porous media". In: *J. Appl. Mech.* 36.4, pp. 711–714. ISSN: 0021-8936. DOI: 10.1115/1.3564760.

— [1971]. "Compressible gas flow through a porous material". In: *Int. J. Heat Mass Transf.* 14.11, pp. 1855–1859. ISSN: 0017-9310. DOI: 10.1016/0017-9310(71)90053-6.

Beavers, G. S., E. M. Sparrow, and R. A. Magnuson [Dec. 1970]. "Experiments on coupled parallel flows in a channel and a bounding porous medium". In: *J. Basic Eng.* 92.4, pp. 843–848. ISSN: 0021-9223. DOI: 10.1115/1.3425155.

Beavers, G. S., E. M. Sparrow, and D. E. Rodenz [Sept. 1973]. "Influence of bed size on the flow characteristics and porosity of randomly packed beds of spheres". In: *J. Appl. Mech.* 40.3, pp. 655–660. ISSN: 0021-8936. DOI: 10.1115/1.3423067.

Beckwith, I. E. and M. H. Bertram [1972]. *A survey of NASA Langley studies on high-speed transition and the quiet tunnel*. Tech. rep. NASA-TM-X-2566. NASA Tech. Memo. NASA Langley Res. Center.

Beckwith, I. E., W. D. Harvey, J. E. Harris, and B. B. Holley [1973]. *Control of supersonic wind-tunnel noise by laminarization of nozzle-wall boundary layer*. Tech. rep. NASA-TM-X-2879. NASA Tech. Memo. NASA Langley Res. Center.

Bender, C. M. and S. A. Orszag [1999]. *Advanced mathematical methods for scientists and engineers*. Springer.

Biot, M. A. [1956]. "Theory of Propagation of Elastic Waves in a Fluid-Saturated Porous Solid. Part II. Higher Frequency Range". In: *J. Acous. Soc. Am.* 28.2, pp. 179–191. DOI: 10.1121/1.1908241.

Borg, M. P., R. L. Kimmel, J. W. Hofferth, and Bowersox R. D. W. [Jan. 2015]. "Freestream Effects on Boundary Layer Disturbances for HIFiRE-5". In: *53rd AIAA Aerosp. Sci. & Meet., Kissimmee, FL*. AIAA Paper 2015-0278. AIAA. DOI: 10.2514/6.2015-0278.

Borodulin, V. I., A. V. Ivanov, Y. S. Kachanov, and D. A. Mischenko [2018]. "Systematic study of distributed excitation of unsteady Görtler modes by freestream vortices". In: *Eur. J. Mechanics - B/Fluids* 68, pp. 167–183. ISSN: 0997-7546. DOI: 10.1016/j.euromechflu.2017.11.008.

Bottaro, A. [2019]. "Flow over natural or engineered surfaces: an adjoint homogenization perspective". In: *J. Fluid Mech.* 877, P1. DOI: 10.1017/jfm.2019.607.

Bountin, D. A., Y. V. Gromyko, A. A. Maslov, P. A. Polivanov, and A. A. Sidorenko [Sept. 2016]. "Effect of the surface roughness of blunt cone forebody on the position of laminar-turbulent transition". In: *Thermophys. Aeromech.* 23.5, pp. 629–638. ISSN: 1531-8699. DOI: 10.1134/S0869864316050012.

Bradshaw, P. [1965]. "The effect of wind-tunnel screens on nominally two-dimensional boundary layers". In: *J. Fluid Mech.* 22.4, pp. 679–687. DOI: 10.1017/S0022112065001064.

Brès, G. A., M. Inkman, T. Colonius, and A. V. Fedorov [2013]. "Second-mode attenuation and cancellation by porous coatings in a high-speed boundary layer". In: *J. Fluid Mech.* 726, pp. 312–337. DOI: 10.1017/jfm.2013.206.

Breugem, W. P. [2005]. "The influence of wall permeability on laminar and turbulent flows: theory and simulations". PhD thesis. TU Delft.

Breugem, W. P. and B. J. Boersma [2005]. "Direct numerical simulations of turbulent flow over a permeable wall using a direct and a continuum approach". In: *Phys. Fluids* 17.2, p. 025103. DOI: 10.1063/1.1835771.

Breugem, W. P., B. J. Boersma, and R. E. Uittenbogaard [June 2005]. "The laminar boundary layer over a permeable wall". In: *Transp. Porous Media* 59.3, pp. 267–300. ISSN: 1573-1634. DOI: 10.1007/s11242-004-2557-1.

— [2006]. "The influence of wall permeability on turbulent channel flow". In: *J. Fluid Mech.* 562, pp. 35–72. DOI: 10.1017/S0022112006000887.

Brinkerhoff, J. R. and M. I. Yaras [2015]. "Numerical investigation of transition in a boundary layer subjected to favourable and adverse streamwise pressure gradients and elevated free stream turbulence". In: *J. Fluid Mech.* 781, pp. 52–86. DOI: 10.1017/jfm.2015.457.

Brinkman, H. C. [Dec. 1949]. "A calculation of the viscous force exerted by a flowing fluid on a dense swarm of particles". In: *Flow Turb. Comb.* 1.1, p. 27. ISSN: 1573-1987. DOI: 10.1007/BF02120313.

Butler, Kathryn M. and Brian F. Farrell [Aug. 1992]. "Three-dimensional optimal perturbations in viscous shear flow". In: *Phys. Fluids A: Fluid Dyn.* 4.8, pp. 1637–1650. ISSN: 0899-8213. DOI: 10.1063/1.858386.

Casper, K., S. Beresh, J. Henfling, R. Spillers, B. Pruett, and S. P. Schneider [June 2009]. "Hypersonic wind-tunnel measurements of boundary-layer pressure fluctuations". In: *39th AIAA Fluid Dyn. Conf.* AIAA Paper 2009-4054. AIAA. DOI: 10.2514/6.2009-4054.

Cebeci, T. [2002]. *Convective Heat Transfer*. Horizons Pub.

Chandesris, M. and D. Jamet [2006]. "Boundary conditions at a planar fluid–porous interface for a Poiseuille flow". In: *Int. J. Heat Mass Transf.* 49.13, pp. 2137–2150. ISSN: 0017-9310. DOI: 10.1016/j.ijheatmasstransfer.2005.12.010.

Chapman, S. and T.G. Cowling [1990]. *The mathematical theory of non-uniform gases*. Cambridge: Camb. Univ. Press.

Charru, F. and P. de Forcrand-Millard [2011]. *Hydrodynamic Instabilities*. Cambr. Texts Appl. Math. Camb. Univ. Press. ISBN: 9781139500548.

Chen, F.-J., M. R. Malik, and I. E. Beckwith [1989]. "Boundary-layer transition on a cone and flat plate at Mach 3.5". In: *AIAA J.* 27.6, pp. 687–693. DOI: 10.2514/3.10166.

Chen, F.-J., M. R. Malik, and I. E. Beckwith [1992]. "Görtler instability and supersonic quiet nozzle design". In: *AIAA J.* 30.8, pp. 2093–2094. DOI: 10.2514/3.11184.

Chen, L., W. Fang, Q. Kang, J. De'Haven Hyman, H. S. Viswanathan, and W.-Q. Tao [Mar. 2015]. "Generalized lattice Boltzmann model for flow through tight porous media with Klinkenberg's effect". In: *Phys. Rev. E* 91 [3], p. 033004. DOI: 10.1103/PhysRevE.91.033004.

Choudhari, M. [Jan. 1996]. "Boundary-layer receptivity to three-dimensional unsteady vortical disturbances in free stream". In: *34th Aerosp. Sci. Meet. & Exhib., Reno, NV*. AIAA Paper 96-0181. AIAA. DOI: 10.2514/6.1996-181.

Ciolkosz L. D., Spina E. F. [July 2006]. "An Experimental Study of Görtler Vortices in Compressible Flow". In: *42nd AIAA/ASME/SAE/ASEE Jt. Propuls. Conf. & Exhib.* AIAA Paper 2006-4512. AIAA. DOI: 10.2514/6.2006-4512.

Costa, Antonio [2006]. "Permeability-porosity relationship: A reexamination of the Kozeny-Carman equation based on a fractal pore-space geometry assumption". In: *Geophys. Res. Lett.* 33.2. DOI: 10.1029/2005GL025134.

Criminale, W. O., T. L. Jackson, and R. D. Joslin [2003]. *Theory and Computation of Hydrodynamic Stability*. Camb. Univ. Press. DOI: 10.1017/CBO9780511550317.

Crow, S. C. [1966]. "The spanwise perturbation of two-dimensional boundary layers". In: *J. Fluid Mech.* 24.1, pp. 153–164. DOI: 10.1017/S0022112066000557.

Darcy, H. [1856]. *Les fontaines publiques de la ville de Dijon*. Victor Dalmont.

Darwin, C. [1953]. "Note on hydrodynamics". In: *Math. Proc. Camb. Philos. Soc.* 49.2, pp. 342–354. DOI: 10.1017/S0305004100028449.

Demetriades, A. [1960]. "An experiment on the stability of hypersonic laminar boundary layers". In: *J. Fluid Mech.* 7.3, pp. 385–396. DOI: 10.1017/S0022112060000153.

— [Nov. 1985]. *Boundary layer stability measurements over a flat plate at Mach 3*. Tech. Rep. AFOSR-TR-86-0056. Bozeman, MT 59717, USA: Mont. State Univ.

Dimond, B., M. Costantini, and C. Klein [2022]. "Experimental Analysis of the Effect of Suction and Step Height on Boundary-Layer Transition". In: *IUTAM Laminar-Turbul. Transit.* Ed. by S. Sherwin, P. Schmid, and X. Wu. Cham: Springer Int. Publ., pp. 171–180. ISBN: 978-3-030-67902-6.

Dimond, B., M. Costantini, S. Risius, C. Klein, and M. Rein [2020]. "Experimental investigation of the delay of gap- and step-induced transition by means of suction". In: *New Results Numer. Exp. Fluid Mech. XII*. Cham: Springer Int. Publ., pp. 165–174. ISBN: 978-3-030-25253-3.

Dorodnitsyn, A. A. [1942]. "Boundary layer in compressible gas". (*Пограничный слой в сжимаемом газе*). In: *J. Applied Math. Mech.* (*Прикладная математика и механика*) 6.6, pp. 449–486.

van Driest, E. R. [Jan. 1952]. *Investigation of Laminar Boundary Layer in Compressible Fluids Using the Crocco Method*. Tech. Note NACA-TN-2597. Washington, DC, USA: N. Am. Aviat., Inc.

Dryden, H. L. [Jan. 1937]. *Air Flow in the Boundary Layer Near a Plate*. Tech. Rep. NACA-TR-562. NACA.

Duan, L., M. M. Choudhari, A. Chou, F. Munoz, R. Radespiel, T. Schilden, W. Schröder, E. C. Marineau, K. M. Casper, R. S. Chaudhry, G. V. Candler, K. A. Gray, and S. P. Schneider [2019]. "Characterization of freestream disturbances in conventional hypersonic wind tunnels". In: *J. Spacecr. Rockets* 56.2, pp. 357–368. DOI: 10.2514/1.A34290.

van Dyke, M. [1975]. *Perturbation methods in fluid mechanics*. Stanford: Parabolic Press.

Egorov, I. V., A. V. Fedorov, and V. G. Soudakov [2008]. "Receptivity of a hypersonic boundary layer over a flat plate with a porous coating". In: *J. Fluid Mech.* 601, pp. 165–187. DOI: 10.1017/S0022112008000669.

Ellingsen, T. and E. Palm [1975]. "Stability of linear flow". In: *Phys. Fluids* 18.4, pp. 487–488. DOI: 10.1063/1.861156.

Emanuel, G. and J. P. Jones [1968]. "Compressible flow through a porous plate". In: *Int. J. Heat Mass Transf.* 11.5, pp. 827–836. ISSN: 0017-9310. DOI: 10.1016/0017-9310(68)90127-0.

Fedorov, A. V. [2011]. "Transition and stability of high-speed boundary layers". In: *Ann. Rev. Fluid Mech.* 43.1, pp. 79–95. DOI: 10.1146/annurev-fluid-122109-160750.

Fedorov, A. V., V. E. Kozlov, A. N. Shiplyuk, A. A. Maslov, and N. D. Malmuth [2006]. "Stability of hypersonic boundary layer on porous wall with regular microstructure". In: *AIAA J.* 44.8, pp. 1866–1871. DOI: 10.2514/1.21013.

Fedorov, A. V., N. D. Malmuth, A. Rasheed, and H. G. Hornung [2001]. "Stabilization of hypersonic boundary layers by porous coatings". In: *AIAA J.* 39.4, pp. 605–610. DOI: 10.2514/2.1382.

Finnis, M. V. and A. Brown [1997]. "The linear growth of Görtler vortices". In: *Int. J. Heat Fluid Flow* 18.4, pp. 389–399. ISSN: 0142-727X. DOI: 10.1016/S0142-727X(97)00022-2.

Flechner, S. G., P. F. Jacobs, and R. T. Whitcomb [July 1976]. *A high subsonic speed wind tunnel investigation of winglets on a representative second-generation jet transport wing*. NASA Technical Note (TN) NASA-TN-D-8264. Hampton, VA, United States: NASA Langley Res. Center.

Floryan, J. M. and W. S. Saric [1983]. "Effects of suction on the Görtler instability of boundary layers". In: *AIAA J.* 21.12, pp. 1635–1639. DOI: 10.2514/3.8304.

Fomin, V. M., A. V. Fedorov, A. N. Shiplyuk, A. A. Maslov, E. V. Burov, and N. D. Malmuth [May 2002]. "Stabilization of a hypersonic boundary layer by ultrasound-absorbing coatings". In: *Doklady Phys.* 47.5, pp. 401–404. DOI: 10.1134/1.1484415.

Forchheimer, P. [1901]. "Wasserbewegung durch boden". In: *Z. Ver. Deutsch, Ing.* 45, pp. 1782–1788.

Fransson, J. H. M. and P. H. Alfredsson [2003]. "On the disturbance growth in an asymptotic suction boundary layer". In: *J. Fluid Mech.* 482, pp. 51–90. DOI: 10.1017/S0022112003003926.

Ghosh, S., J.-C. Loiseau, W.-P. Breugem, and L. Brandt [2019]. "Modal and non-modal linear stability of Poiseuille flow through a channel with a porous substrate".

In: *Eur. J. Mech. - B/Fluids* 75, pp. 29–43. ISSN: 0997-7546. DOI: 10.1016/j.euromechflu.2018.11.013.

Gil, A., J. Segura, and N. M. Temme [May 2002]. "Computing Complex Airy Functions by Numerical Quadrature". In: *Numer. Algorithms* 30.1, pp. 11–23. ISSN: 1572-9265. DOI: 10.1023/A:1015636825525.

Goharzadeh, A., A. Khalili, and B. B. Jørgensen [Apr. 2005]. "Transition layer thickness at a fluid-porous interface". In: *Phys. Fluids* 17.5, p. 057102. ISSN: 1070-6631. DOI: 10.1063/1.1894796.

Goldstein, M. E. [1978]. "Unsteady vortical and entropic distortions of potential flows round arbitrary obstacles". In: *J. Fluid Mech.* 89.3, pp. 433–468.

— [1983]. "The evolution of Tollmien–Sclichting waves near a leading edge". In: *J. Fluid Mech.* 127, pp. 59–81. DOI: 10.1017/S002211208300261X.

— [1985]. "Scattering of acoustic waves into Tollmien-Schlichting waves by small streamwise variations in surface geometry". In: *J. Fluid Mech.* 154, pp. 509–529. DOI: 10.1017/S0022112085001641.

— [2014]. "Effect of free-stream turbulence on boundary layer transition". In: *Philos. Trans. R. Soc. A: Math., Phys. Eng. Sci.* 372.2020, p. 20130354. DOI: 10.1098/rsta.2013.0354.

Goldstein, M. E. and L. S. Hultgren [1989]. "Boundary-Layer Receptivity to Long-Wave Free-Stream Disturbances". In: *Ann. Rev. Fluid Mech.* 21.1, pp. 137–166. DOI: 10.1146/annurev.fl.21.010189.001033.

Goldstein, M. E. and S. J. Leib [1993]. "A note on the distortion of a flat-plate boundary layer by free-stream vorticity normal to the plate". In: *J. Fluid Mech.* 248, pp. 531–541. DOI: 10.1017/S0022112093000023.

Goldstein, M. E., S. J. Leib, and S. J. Cowley [1992]. "Distortion of a flat-plate boundary layer by free-stream vorticity normal to the plate". In: *J. Fluid Mech.* 237, pp. 231–260. DOI: 10.1017/S0022112092003409.

Goldstein, M. E. and P. Ricco [2018]. "Non-localized boundary layer instabilities resulting from leading edge receptivity at moderate supersonic Mach numbers". In: *J. Fluid Mech.* 838, pp. 435–477. DOI: 10.1017/jfm.2017.889.

Goldstein, M. E. and D. W. Wundrow [1998]. "On the environmental realizability of algebraically growing disturbances and their relation to Klebanoff modes". In: *Theor. Comp. Fluid Dyn.* 10, pp. 171–186. DOI: 10.1007/s001620050057.

Görtler, H. [1957]. "On the calculation of steady laminar boundary layer flows with continuous suction". In: *J. Math. Mech.* 6.3, pp. 323–340. DOI: 10.1512/iumj.1957.6.56015.

Goyeau, B., D. Lhuillier, D. Gobin, and M. G. Velarde [2003]. "Momentum transport at a fluid–porous interface". In: *Int. J. Heat Mass Transf.* 46.21, pp. 4071–4081. ISSN: 0017-9310. DOI: 10.1016/S0017-9310(03)00241-2.

Gray, W. G. [1975]. "A derivation of the equations for multi-phase transport". In: *Chem. Eng. Sci.* 30.2, pp. 229–233. ISSN: 0009-2509. DOI: 10.1016/0009-2509(75)80010-8.

Graziosi, P. [1999]. "An experimental investigation on stability and transition at Mach 3". PhD thesis. Princet. Univ.

Graziosi, P. and G. L. Brown [2002]. "Experiments on stability and transition at Mach 3". In: *J. Fluid Mech.* 472, pp. 83–124. DOI: 10.1017/S0022112002002094.

Griffith, A. A. and F. W. Meredith [Mar. 1936]. *The possible improvement in aircraft performance due to the use of boundary-layer suction.* Tech. rep. 2315 RAE E 3501. Aeronaut. Res. Counc.

Gui, Y., W. Wang, R. Zhao, J. Zhao, and J. Wu [2022]. "Hypersonic boundary-Layer instability characteristics on sharp cone with porous coating". In: *AIAA J.* 60.7, pp. 4453–4461. DOI: 10.2514/1.J060930.

Gui, Y., C. Zhang, X. Li, D. Xu, and J. Wu [Sept. 2023]. "Hypersonic boundary-layer instability characterization and transition downstream of distributed roughness". In: *Exp. Fluids* 64.10, p. 159. ISSN: 1432-1114. DOI: 10.1007/s00348-023-03703-x.

Gulyaev, A. N., V. E. Kozlov, V. R. Kuznetsov, B. I. Mineev, and A. N. Sekundov [1989]. "Interaction of a laminar boundary layer with external turbulence". In: *Fluid Dyn.* 24.5, pp. 700–710. DOI: 10.1007/BF01051722.

Hader, C. and H. F. Fasel [Jan. 2021]. "Flow control using steady blowing and suction strips in a Mach 6 boundary layer on a flared cone". In: *AIAA Scitech 2021 Forum.* AIAA Paper 2021-1206. DOI: 10.2514/6.2021-1206.

El-Hady, N. M. and A. K. Verma [June 1981]. "Growth of Görtler vortices in compressible boundary layers along curves surfaces". In: *14th Fluid Plasma Dyn. Conf.* AIAA Paper 1981-1278. AIAA. DOI: 10.2514/6.1981-1278.

— [1984]. "Instability of compressible boundary layers along curved walls with suction or cooling". In: *AIAA J.* 22.2, pp. 206–213. DOI: 10.2514/3.8369.

Hall, P. [1983]. "The linear development of Görtler vortices in growing boundary layers". In: *J. Fluid Mech.* 130, pp. 41–58. DOI: 10.1017/S0022112083000968.

Härter, J., D. S. Martínez, R. Poser, B. Weigand, and G. Lamanna [Feb. 2023]. "Coupling between a turbulent outer flow and an adjacent porous medium: High resolved Particle Image Velocimetry measurements". In: *Phys. Fluids* 35.2. ISSN: 1070-6631. DOI: 10.1063/5.0132193.

Hassanizadeh, M. and W. G. Gray [1979]. "General conservation equations for multi-phase systems: 1. Averaging procedure". In: *Adv. Water Resour.* 2, pp. 131–144. ISSN: 0309-1708. DOI: 10.1016/0309-1708(79)90025-3.

Haynes, W. M. [2014]. *CRC Handbook of Chemistry and Physics.* 95th ed. Boca Raton: CRC Press. DOI: 10.1201/b17118.

Hoare, C. A. R. [Jan. 1962]. "Quicksort". In: *Comput. J.* 5.1, pp. 10–16. ISSN: 0010-4620. DOI: 10.1093/comjnl/5.1.10.

Hofferth, J. W., R. A. Humble, D. C. Floryan, and W. S. Saric [Jan. 2013]. "High-Bandwidth Optical Measurements of the Second-Mode Instability in a Mach 6 Quiet Tunnel". In: *51st AIAA Aerosp. Sci. & Meet., Grapevine, TX.* AIAA Paper 2013-0378. AIAA. DOI: 10.2514/6.2013-378.

Hollender, C., A. Dwivedi, and G. V. Candler [June 2019]. "Response of a Mach 6 cone-flare Geometry to steady vortical disturbances: effect of steady suction". In: *AIAA Aviat. 2019 Forum.* AIAA Paper 2019-3219. DOI: 10.2514/6.2019-3219.

Howarth, L. and G. I. Taylor [1948]. "Concerning the effect of compressibility on laminar boundary layers and their separation". In: *Proc. Royal Soc. London A* 194.1036, pp. 16–42. DOI: 10.1098/rspa.1948.0064.

Howes, F. A. and S. Whitaker [1985]. "The spatial averaging theorem revisited". In: *Chem. Eng. Sci.* 40.8, pp. 1387–1392. ISSN: 0009-2509. DOI: 10.1016/0009-2509(85)80078-6.

Innocentini, M. D. M. and V. C. Pandolfelli [2001]. "Permeability of Porous Ceramics Considering the Klinkenberg and Inertial Effects". In: *J. Am. Ceram. Soc.* 84.5, pp. 941–944. DOI: 10.1111/j.1151-2916.2001.tb00772.x.

Innocentini, M. D. M., P. Sepulveda, and F. S. Ortega [2006]. "Permeability". In: *Cellular ceramics: structure, manufacturing, properties and applications*. Ed. by M. Scheffler and P. Colombo. Wiley-VCH. Chap. 4.2. ISBN: 9783527313204.

Jacobs, R. G. and P. A. Durbin [2001]. "Simulations of bypass transition". In: *J. Fluid Mech.* 428, pp. 185–212. DOI: 10.1017/S0022112000002469.

Joseph, D. D., D. A. Nield, and G. Papanicolaou [1982]. "Nonlinear equation governing flow in a saturated porous medium". In: *Water Resour. Res.* 18.4, pp. 1049–1052. DOI: 10.1029/WR018i004p01049.

Kang, J. and M. Wang [2024]. "Flow behavior prediction at free-fibrous interface". In: *Int. J. Heat Mass Transf.* 228, p. 125621. ISSN: 0017-9310. DOI: 10.1016/j.ijheatmasstransfer.2024.125621.

von Kármán, T. [July 1934]. "Some aspects of the turbulence problem". In: *Proc. 4th Int. Congr. Appl. Mech.* Camb. Univ. Press, pp. 54–91.

Kaviany, M. [May 1987]. "Boundary-layer treatment of forced convection heat transfer from a semi-infinite flat plate embedded in porous media". In: *J. Heat Transf.* 109.2, pp. 345–349. ISSN: 0022-1481. DOI: 10.1115/1.3248086.

Kay, J. M. [1953]. *Boundary-layer flow along a flat plate with uniform suction*. ARC Tech. Rep. 2628. Camb. Univ. Eng. Lab.

Keller, H. B. and T. Cebeci [Sept. 1970]. "Accurate numerical methods for boundary layer flows I. Two dimensional laminar flows". In: *Proc. 2nd Int. Conf. Numer. Methods Fluid Dyn.* Ed. by M. Holt. Springer Berlin Heidelberg, pp. 92–100. DOI: 10.1007/3-540-05407-3_15.

— [1972]. "Accurate Numerical Methods for Boundary-Layer Flows. II: Two Dimensional Turbulent Flows". In: *AIAA J.* 10.9, pp. 1193–1199. DOI: 10.2514/3.50349.

Kendall, J. M. [1975]. "Wind tunnel experiments relating to supersonic and hypersonic boundary-layer transition". In: *AIAA J.* 13.3, pp. 290–299. DOI: 10.2514/3.49694.

— [July 1985]. "Experimental study of disturbances produced in a pre-transitional laminar boundary layer by weak freestream turbulence". In: *18th Fluid Dyn. Plasmadyn. Lasers Conf.* AIAA Paper 85–1695. AIAA. DOI: 10.2514/6.1985-1695.

— [June 1990]. "Boundary layer receptivity to freestream turbulence". In: *21st Fluid Dyn. Plasma Dyn. Lasers Conf.* AIAA Paper 90–1504. AIAA. DOI: 10.2514/6.1990-1504.

— [Jan. 1998]. "Experiments on boundary-layer receptivity to freestream turbulence". In: *36th AIAA Aerosp. Sci. Meet. & Exhib.* AIAA Paper 1998-530. DOI: 10.2514/6.1998-530.

Khalifa, Z., L. Pocher, and N. Tilton [2020]. "Regimes of flow through cylinder arrays subject to steady pressure gradients". In: *Int. J. Heat Mass Transf.* 159, p. 120072. ISSN: 0017-9310. DOI: 10.1016/j.ijheatmasstransfer.2020.120072.

Kinsler, L. E., A. R. Frey, A. B. Coppens, and J. V. Sanders [2000]. *Fundamentals of Acoustics*. Wiley.

Klebanoff, P. S. [1971]. "Effect of free-stream turbulence on a laminar boundary layer". In: *Bull. Am. Phys. Soc.* Vol. 16. 11, p. 1323.

Klebanoff, P. S. and K. D. Tidstrom [Sept. 1959]. *Evolution of amplified waves leading to transition in a boundary layer with zero pressure gradient*. Tech. Note TN-D-195. NASA.

Klebanoff, P. S., K. D. Tidstrom, and L. M. Sargent [1962]. "The three-dimensional nature of boundary-layer instability". In: *J. Fluid Mech.* 12.1, pp. 1–34. DOI: 10.1017/S0022112062000014.

Kobayashi, R. [1972]. "Note on the stability of a boundary layer on a concave wall with suction". In: *J. Fluid Mech.* 52.2, pp. 269–272. DOI: 10.1017/S0022112072001405.

— [1974]. "Taylor-Görtler instability of a boundary layer with suction or blowing". In: *AIAA J.* 12.3, pp. 394–395. DOI: 10.2514/3.49247.

Kovasznay, L. S. G. [1953]. "Turbulence in supersonic flow". In: *J. Aeronaut. Sci.* 20.10, pp. 657–674. DOI: 10.2514/8.2793.

Krishnan, K. S. G., O. Bertram, and O. Seibel [2017]. "Review of hybrid laminar flow control systems". In: *Prog. Aerosp. Sci.* 93, pp. 24–52. ISSN: 0376-0421. DOI: 10.1016/j.paerosci.2017.05.005.

Kurian, T. and J. H. M. Fransson [2011]. "Transient growth in the asymptotic suction boundary layer". In: *Exp. Fluids* 51.3, pp. 771–784. ISSN: 1432-1114. DOI: 10.1007/s00348-011-1095-1.

Lam, S. H. and N. Rott [1960]. *Theory of linearized time-dependent boundary layers*. Tech. Note AFOSR-TN-60-1100. Ithaca, NY 14853: Cornell Univ.

Landahl, M. T. [1980]. "A note on an algebraic instability of inviscid parallel shear flows". In: *J. Fluid Mech.* 98.2, pp. 243–251. DOI: 10.1017/S0022112080000122.

Lasseux, D. and F. J. Valdés-Parada [2017]. "On the developments of Darcy's law to include inertial and slip effects". In: *C. R. Méc.* 345.9, pp. 660–669. ISSN: 1631-0721. DOI: 10.1016/j.crme.2017.06.005.

Laufer, J. and T. Vrebalovich [1960]. "Stability and transition of a supersonic laminar boundary layer on an insulated flat plate". In: *J. Fluid Mech.* 9.2, pp. 257–299. DOI: 10.1017/S0022112060001092.

Leib, S. J., D. W. Wundrow, and M. E. Goldstein [1999]. "Effect of free-stream turbulence and other vortical disturbances on a laminar boundary layer". In: *J. Fluid Mech.* 380, pp. 169–203. DOI: 10.1017/S0022112098003504.

Leontiev, A. I. and A. M. Pavlyuchenko [Aug. 2008]. "Investigation of laminar-turbulent transition in supersonic boundary layers in an axisymmetric aerophysical flight complex and in a model in a wind tunnel in the presence of heat transfer and suction of air". In: *High Temp.* 46.4, pp. 542–565. ISSN: 1608-3156. DOI: 10.1134/S0018151X08040159.

Lew, H. G. and J. B. Fanucci [1955]. "On the laminar compressible boundary layer over a flat plate with suction or injection". In: *J. Aeronaut. Sci.* 22.9, pp. 589–597. DOI: 10.2514/8.3408.

Li, F., M. M. Choudhari, P. Paredes, S. P. Schneider, and P. Portoni [June 2018]. "Görtler instability and its control via surface suction over an axisymmetric cone at Mach 6". In: *2018 Fluid Dyn. Conf.* AIAA Paper 2018-3069. AIAA. DOI: 10.2514/6.2018-3069.

Lighthill, M. J. [1956]. "Drift". In: *J. Fluid Mech.* 1.1, pp. 31–53. DOI: 10.1017/S0022112056000032.

de Luca, L., G. Cardone, D. Aymer de la Chevalerie, and A. Fonteneau [Nov. 1993]. "Goertler instability of a hypersonic boundary layer". In: *Exp. Fluids* 16.1, pp. 10–16. ISSN: 1432-1114. DOI: 10.1007/BF00188500.

Luchini, P. [2000]. "Reynolds-number-independent instability of the boundary layer over a flat surface: optimal perturbations". In: *J. Fluid Mech.* 404, pp. 289–309. DOI: 10.1017/S0022112099007259.

Lukashevich, S. V., S. O. Morozov, and A. N. Shiplyuk [July 2018]. "Passive porous coating effect on a hypersonic boundary layer on a sharp cone at small angle of attack". In: *Exp. Fluids* 59.8, p. 130. DOI: 10.1007/s00348-018-2585-1.

Mack, L. M. [1984]. *Boundary Layer Stability Theory.* AGARD rep. 709, part 3. 91109 Pasadena, CA, USA: Jet Prop. Lab., Calif. Inst. Tech.

Al-Malki, M., Z. Hussain, S. Garrett, and S. Calabretto [Nov. 2021]. "Effects of parietal suction and injection on the stability of the Blasius boundary-layer flow over a permeable, heated plate". In: *Phys. Rev. Fluids* 6 [11], p. 113902. DOI: 10.1103/PhysRevFluids.6.113902.

Malmuth, N. D., A. V. Fedorov, V. Shalaev, J. Cole, M. Hites, D. Williams, and A. Khokhlov [June 1998]. "Problems in high speed flow prediction relevant to control". In: *2nd AIAA Theor. Fluid Mech. Meet., Albuquerque, NM.* AIAA Paper 98-2695. AIAA. DOI: 10.2514/6.1998-2695.

Mangalam, S., J. Dagenhart, and V. Kalburgi [Jan. 1987]. "Influence of suction and curvature on the growth of Görtler vortices on an airfoil". In: *25th AIAA Aerosp. Sci. Meet.* AIAA Paper 1987-0481. AIAA. DOI: 10.2514/6.1987-481.

Marensi, E. and P. Ricco [Nov. 2017]. "Growth and wall-transpiration control of nonlinear unsteady Görtler vortices forced by free-stream vortical disturbances". In: *Phys. Fluids* 29.11, p. 114106. ISSN: 1070-6631. DOI: 10.1063/1.4999993.

Marensi, E., P. Ricco, and X. Wu [2017]. "Nonlinear unsteady streaks engendered by the interaction of free-stream vorticity with a compressible boundary layer". In: *J. Fluid Mech.* 817, pp. 80–121. DOI: 10.1017/jfm.2017.88.

Martin, A., L. C. Scalabrin, and I. D. Boyd [2012]. "High performance modeling of atmospheric re-entry vehicles". In: *High Perform. Comput. Symp. 2011.* J. Phys.: Conf. Series 341-1. IOP Publ., p. 012002. DOI: 10.1088/1742-6596/341/1/012002.

Maslov, A. A. [May 2003]. *Experimental and theoretical studies of hypersonic laminar flow control using ultrasonically absorptive coatings (UAC).* Final Project Rep. 2172-2001. Instit. Theor. Applied Mech.

Maslov, A. A., S. G. Mironov, T. V. Poplavskaya, and S. V. Kirilovskiy [2019]. "Supersonic flow around a cylinder with a permeable high-porosity insert: experiment and numerical simulation". In: *J. Fluid Mech.* 867, pp. 611–632. DOI: 10.1017/jfm.2019.165.

Maslov, A. A., A. N. Shiplyuk, A. A. Sidorenko, and D. Arnal [2001]. "Leading-edge receptivity of a hypersonic boundary layer on a flat plate". In: *J. Fluid Mech.* 426, pp. 73–94. DOI: 10.1017/S0022112000002147.

Matsubara, M. and P. H. Alfredsson [2001]. "Disturbance growth in boundary layers subjected to free-stream turbulence". In: *J. Fluid Mech.* 430, pp. 149–168. DOI: 10.1017/S0022112000002810.

Mattioli, E. [1992]. *Aerodinamica*. Levrotto & Bella. ISBN: 9788882180294.

McKenzie, J. F. and K. O. Westphal [1968]. "Interaction of linear waves with oblique shock waves". In: *Phys. Fluids* 11.11, pp. 2350–2362. DOI: 10.1063/1.1691825.

Messing, R. and M. J. Kloker [2010]. "Investigation of suction for laminar flow control of three-dimensional boundary layers". In: *J. Fluid Mech.* 658, pp. 117–147. DOI: 10.1017/S0022112010001576.

Methel, J., M. Forte, O. Vermeersch, and G. Casalis [2021]. "Experimental investigation on the effect of forward-facing steps and gaps combined with wall suction on boundary layer transition". In: *Exp. Fluids* 63.1, p. 21. ISSN: 1432-1114. DOI: 10.1007/s00348-021-03361-x.

Michael, V. and S. O. Stephen [2012]. "Nonlinear stability of hypersonic flow over a cone with passive porous walls". In: *J. Fluid Mech.* 713, pp. 528–563. DOI: 10.1017/jfm.2012.472.

Mironov, S. G., A. A. Maslov, T. V. Poplavskaya, and S. V. Kirilovskiy [July 2015]. "Modeling of a supersonic flow around a cylinder with a gas-permeable porous insert". In: *J. Appl. Mech. Tech. Phys.* 56.4, pp. 549–557. ISSN: 1573-8620. DOI: 10.1134/S0021894415040021.

Morad, M.R. and A. Khalili [Sept. 2008]. "Transition layer thickness in a fluid-porous medium of multi-sized spherical beads". In: *Exp. Fluids* 46.2, p. 323. ISSN: 1432-1114. DOI: 10.1007/s00348-008-0562-9.

Morduchow, M. [1963]. "General asymptotic solution of the laminar compressible boundary layer with heat transfer". In: *AIAA J.* 1.8, pp. 1949–1951. DOI: 10.2514/3.1974.

Morkovin, M. V. [June 1959]. "On supersonic wind tunnels with low free-stream disturbances". In: *J. Appl. Mech.* 26.3, pp. 319–324. ISSN: 0021-8936. DOI: 10.1115/1.4012040.

— [Mar. 1969]. *Critical evaluation of transition from laminar to turbulent shear layers with emphasis on hypersonically traveling bodies*. Tech. rep. AFFDL-TR-08-149. USAF Flight Dyn. Lab.

— [1985]. *Bypass Transition to Turbulence and Research Desiderata*. Commun. Progr. NASA-CP-2386. NASA.

Muñoz, F., D. Heitmann, and R. Radespiel [2014]. "Instability Modes in Boundary Layers of an Inclined Cone at Mach 6". In: *J. Spacecr. Rockets* 51.2, pp. 442–454. DOI: 10.2514/1.A32564.

Myose, R. Y. and R. F. Blackwelder [1995]. "Control of streamwise vortices using selective suction". In: *AIAA J.* 33.6, pp. 1076–1080. DOI: 10.2514/3.12667.

Nagarajan, S., S. K. Lele, and J. H. Ferziger [2007]. "Leading-edge effects in bypass transition". In: *J. Fluid Mech.* 572, pp. 471–504. DOI: 10.1017/S0022112006001893.

Nakayama, A., T. Kokudai, and H. Koyama [Feb. 1990]. "Non-Darcian boundary layer flow and forced convective heat transfer over a flat plate in a fluid-saturated porous medium". In: *J. Heat Transf.* 112.1, pp. 157–162. ISSN: 0022-1481. DOI: 10.1115/1.2910338.

Naqvi, S. B. and A. Bottaro [2021]. "Interfacial conditions between a free-fluid region and a porous medium". In: *Int. J. Multiph. Flow* 141, p. 103585. ISSN: 0301-9322. DOI: 10.1016/j.ijmultiphaseflow.2021.103585.

Neale, G. and W. Nader [1974]. "Practical significance of Brinkman's extension of Darcy's law: Coupled parallel flows within a channel and a bounding porous medium". In: *Can. J. Chem. Eng.* 52.4, pp. 475–478. DOI: 10.1002/cjce.5450520407.

Negi, P. S., M. Mishra, and M. Skote [June 2015]. "DNS of a single low-speed streak subject to spanwise wall oscillations". In: *Flow Turbul. Combust.* 94.4, pp. 795–816. DOI: 10.1007/s10494-015-9599-z.

Nield, D. A. [1991]. "The limitations of the Brinkman-Forchheimer equation in modeling flow in a saturated porous medium and at an interface". In: *Int. J. Heat Fluid Flow* 12.3, pp. 269–272. ISSN: 0142-727X. DOI: 10.1016/0142-727X(91)90062-Z.

— [Jan. 1994]. "Modelling high speed flow of a compressible fluid in a saturated porous medium". In: *Transp. Porous Media* 14.1, pp. 85–88. ISSN: 1573-1634. DOI: 10.1007/BF00617029.

— [Dec. 2000]. "Resolution of a paradox involving viscous dissipation and nonlinear drag in a porous medium". In: *Transp. Porous Media* 41.3, pp. 349–357. ISSN: 1573-1634. DOI: 10.1023/A:1006636605498.

Nield, D. A. and A. Bejan [1999]. *Convection in porous media*. Springer. ISBN: 9780387984438.

— [2017]. *Convection in Porous Media*. New York: Springer Int. Publ. ISBN: 9783319495620.

Nield, D. A. and A. V. Kuznetsov [Dec. 2003]. "Boundary-layer analysis of forced convection with a plate and porous substrate". In: *Acta Mech.* 166.1, pp. 141–148. ISSN: 1619-6937. DOI: 10.1007/s00707-003-0050-5.

Ochoa-Tapia, J. A. and S. Whitaker [1995a]. "Momentum transfer at the boundary between a porous medium and a homogeneous fluid—I. Theoretical development". In: *Int. J. Heat Mass Transf.* 38.14, pp. 2635–2646. ISSN: 0017-9310. DOI: 10.1016/0017-9310(94)00346-W.

— [1995b]. "Momentum transfer at the boundary between a porous medium and a homogeneous fluid—II. Comparison with experiment". In: *Int. J. Heat Mass Transf.* 38.14, pp. 2647–2655. ISSN: 0017-9310. DOI: 10.1016/0017-9310(94)00347-X.

Ochoa-Tapia, J. A. and S. Whitaker [1997]. "Heat transfer at the boundary between a porous medium and a homogeneous fluid". In: *Int. J. Heat Mass Transf.* 40.11, pp. 2691–2707. ISSN: 0017-9310. DOI: 10.1016/S0017-9310(96)00250-5.

— [1998]. "Momentum jump condition at the boundary between a porous medium and a homogeneous fluid: inertial effects". In: *J. Porous Media* 1.3, pp. 201–217.

Ohno, D., B. Selent, M. J. Kloker, and U. Rist [2023]. "Direct numerical simulation of bypass transition under free-stream turbulence for compressible flows". In: *High Perform. Comput. Sci. Eng. '21*. Springer Int. Publ., pp. 223–238. ISBN: 978-3-031-17937-2. DOI: 10.1007/978-3-031-17937-2_13.

Ovchinnikov, V., M. M. Choudhari, and U. Piomelli [2008]. "Numerical simulations of boundary-layer bypass transition due to high-amplitude free-stream turbulence". In: *J. Fluid Mech.* 613, pp. 135–169. DOI: 10.1017/S0022112008003017.

Oz, F. and K. Kara [July 2024]. "Controlling hypersonic boundary layer transition with localized cooling and metasurface treatments". In: *Sci. Rep.* 14.1, p. 15928. ISSN: 2045-2322. DOI: 10.1038/s41598-024-66867-4.

Papalexandris, M. V. [May 2023]. "Boundary-layer Flow in a Porous Domain Above a Flat Plate". In: *J. Eng. Math.* 140.1, p. 4. ISSN: 1573-2703. DOI: 10.1007/s10665-023-10269-4.

Polyanin, A. D. and A. V. Manzhirov [2008]. *Handbook of integral equations*. eng. 2nd ed. Handbooks of mathematical equations. Boca Raton, Fla. ; London: Chapman & Hall/CRC. ISBN: 9781584885078.

Polyanin, A. D. and V. E. Nazaikinskii [2015]. *Handbook of Linear Partial Differential Equations for Engineers and Scientists*. 2nd. CRC Press.

Quintard, M. and S. Whitaker [Feb. 1994]. "Transport in ordered and disordered porous media II: Generalized volume averaging". In: *Transp. Porous Media* 14.2, pp. 179–206. DOI: 10.1007/BF00615200.

Rai, M. M. and P. Moin [1993]. "Direct Numerical Simulation of Transition and Turbulence in a Spatially Evolving Boundary Layer". In: *J. Comput. Phys.* 109.2, pp. 169–192. ISSN: 0021-9991. DOI: 10.1006/jcph.1993.1210.

Rasheed, A., H. G. Hornung, A. V. Fedorov, and N. D. Malmuth [2002]. "Experiments on passive hypervelocity boundary-layer control using an ultrasonically absorptive surface". In: *AIAA J.* 40.3, pp. 481–489. DOI: 10.2514/2.1671.

Reed, H. L., W. S. Saric, and D. Arnal [1996]. "Linear stability theory applied to boundary layers". In: *Ann. Rev. Fluid Mech.* 28, pp. 389–428. ISSN: 1545-4479. DOI: 10.1146/annurev.fl.28.010196.002133.

Reshotko, E. [2001]. "Transient growth: A factor in bypass transition". In: *Phys. Fluids* 13.5, pp. 1067–1075. DOI: 10.1063/1.1358308.

Ricco, P. [2006]. "Response of a compressible laminar boundary layer to free-stream turbulent disturbances". PhD thesis. Imp. Coll. - Univ. Lond.

— [2009]. "The pre-transitional Klebanoff modes and other boundary layer disturbances induced by small-wavelength free-stream vorticity". In: *J. Fluid Mech.* 638, pp. 267–303. DOI: 10.1017/S0022112009990838.

Ricco, P. and F. Dilib [Apr. 2010]. "The influence of wall suction and blowing on boundary-layer laminar streaks generated by free-stream vortical disturbances". In: *Phys. Fluids* 22.4, p. 044101. ISSN: 1070-6631. DOI: 10.1063/1.3407651.

Ricco, P. and L. Fossà [July 2023b]. "Receptivity of compressible boundary layers over porous surfaces". In: *Phys. Rev. Fluids* 8 [7], p. 073903. DOI: 10.1103/PhysRevFluids.8.073903.

Ricco, P., J. Luo, and X. Wu [2011]. "Evolution and instability of unsteady nonlinear streaks generated by free-stream vortical disturbances". In: *J. Fluid Mech.* 677, pp. 1–38. DOI: 10.1017/jfm.2011.41.

Ricco, P., D. Shah, and P. D. Hicks [May 2013]. "Compressible laminar streaks with wall suction". In: *Phys. Fluids* 25.5, p. 054110. ISSN: 1070-6631. DOI: 10.1063/1.4807066.

Ricco, P., E. J. Walsh, F. Brighenti, and D. M. McEligot [2016]. "Growth of boundary-layer streaks due to free-stream turbulence". In: *Int. J. Heat Fluid Flow* 61, pp. 272–283. DOI: 10.1016/j.ijheatfluidflow.2016.05.003.

Ricco, P. and X. Wu [2007]. "Response of a compressible laminar boundary layer to free-stream vortical disturbances". In: *J. Fluid Mech.* 587, pp. 97–138. DOI: 10.1017/S0022112007007070.

Richardson, S. [1971]. "A model for the boundary condition of a porous material. Part 2". In: *J. Fluid Mech.* 49.2, pp. 327–336. DOI: 10.1017/S002211207100209X.

Running, C. L., B. L. Bemis, J. L. Hill, M. P. Borg, J. J. Redmond, K. Jantze, and C. Scalo [Mar. 2023]. "Attenuation of hypersonic second-mode boundary-layer instability with an ultrasonically absorptive silicon-carbide foam". In: *Exp. Fluids* 64.4, p. 79. ISSN: 1432-1114. DOI: 10.1007/s00348-023-03615-w.

Ruth, D. and H. Ma [Mar. 1992]. "On the derivation of the Forchheimer equation by means of the averaging theorem". In: *Transp. Porous Media* 7.3, pp. 255–264. ISSN: 1573-1634. DOI: 10.1007/BF01063962.

Saffman, P. G. [1971]. "On the boundary condition at the surface of a porous medium". In: *Stud. Appl. Math.* 50.2, pp. 93–101. DOI: 10.1002/sapm197150293.

Es-Sahli, O., A. Sescu, M. Z. A. Koshuriyan, Y. Hattori, and M. Hirota [2023]. "Lagrange multiplier-based optimal control technique for streak attenuation in high-speed boundary layers". In: *AIAA J.* 61.1, pp. 63–75. DOI: 10.2514/1.J062255.

Sahraoui, M. and M. Kaviany [1992]. "Slip and no-slip velocity boundary conditions at interface of porous, plain media". In: *Int. J. Heat Mass Transf.* 35.4, pp. 927–943. ISSN: 0017-9310. DOI: 10.1016/0017-9310(92)90258-T.

Saric, W. S. [1985]. "Laminar flow control with suction: theory and experiment". In: *AGARD Rep.* 723.

— [1994]. "Görtler Vortices". In: *Ann. Rev. Fluid Mech.* 26.1, pp. 379–409. ISSN: 1545-4479. DOI: 10.1146/annurev.fl.26.010194.002115.

Schmidt, B. E. [2014]. *Compressible flow through porous media with application to injection.* IR-FM 2014.001. Calif. Inst. Tech.

Schmidt, B. E., N. P. Bitter, H. G. Hornung, and J. E. Shepherd [2016]. "Injection into Supersonic Boundary Layers". In: *AIAA J.* 54.1, pp. 161–173. DOI: 10.2514/1.J054123.

Schmisseur, J. D. [2015]. "Hypersonics into the 21st century: a perspective on AFOSR-sponsored research in aerothermodynamics". In: *Prog. Aerosp. Sci.* 72, pp. 3–16. DOI: 10.1016/j.paerosci.2014.09.009.

Schneider, S. P. [2001]. "Effects of high-speed tunnel noise on laminar-turbulent transition". In: *J. Spacecr. Rockets* 38.3, pp. 323–333. DOI: 10.2514/2.3705.
— [2008a]. "Development of hypersonic quiet tunnels". In: *J. Spacecr. Rockets* 45.4, pp. 641–664.
— [2008b]. "Effects of roughness on hypersonic boundary-layer transition". In: *J. Spacecr. Rockets* 45.2, pp. 193–209.
Schubauer, G. B. and H. K. Skramstad [1947]. "Laminar boundary-layer oscillations and stability of laminar flow". In: *J. Aeronaut. Sci.* 14.2, pp. 69–78. DOI: 10.2514/8.1267.
Sescu, A., R. Alaziz, and M. Afsar [Jan. 2018]. "Control of Görtler vortices in high-speed boundary layers". In: *2018 AIAA Aerosp. Sci. Meet.* AIAA Paper 2018-1078. DOI: 10.2514/6.2018-1078.
— [2019]. "Effect of wall transpiration and heat transfer on Görtler vortices in high-speed flows". In: *AIAA J.* 57.3, pp. 1159–1171. DOI: 10.2514/1.J057330.
Shepherd, J. E. and D. R. Begeal [Jan. 1988]. *Transient compressible flow in porous materials*. Tech. rep. SAND 83-1788 UC-45. 87185 Albuquerque, NM, USA: Sandia Natl. Lab.
Shiplyuk, A. N., E. V. Burov, A. A. Maslov, and V. M. Fomin [2004]. "Effect of porous coatings on stability of hypersonic boundary layers". In: *J. Appl. Mech. Tech. Phys.* 45.2, pp. 286–291. DOI: 10.1023/B:JAMT.0000017593.33499.c4.
Shreeve, R. P. [1968]. "Supersonic flow from a porous metal plate." In: *AIAA J.* 6.4, pp. 752–753. DOI: 10.2514/3.4589.
Sims, J. L. [1964]. *Tables for supersonic flow around right circular cones at zero angle of attack*. Tech. rep. NASA-SP-3004. NASA Special Publ. NASA Marshall Space Flight Center.
Sobey, I. J. [2000]. *Introduction to interactive boundary layer theory*. Oxford: Oxf. Univ. Press. ISBN: 9780198506751.
Sokolnikoff, I. S. [1951]. *Tensor analysis: theory and applications*. Vol. 31. New York: Chapman & Hall.
Sorek, S., D. Levi-Hevroni, A. Levy, and G. Ben-Dor [Nov. 2005]. "Extensions to the macroscopic Navier–Stokes equation". In: *Transp. Porous Media* 61.2, pp. 215–233. ISSN: 1573-1634. DOI: 10.1007/s11242-004-7906-6.
Sousa, V. C. B., D. Patel, J.-B. Chapelier, V. Wartemann, A. Wagner, and C. Scalo [2019]. "Numerical investigation of second-mode attenuation over carbon/carbon porous surfaces". In: *J. Spacecr. Rockets* 56.2, pp. 319–332. DOI: 10.2514/1.A34294.
Sparrow, E. M., G. S. Beavers, T. S. Chen, and J. R. Lloyd [June 1973]. "Breakdown of the Laminar Flow Regime in Permeable-Walled Ducts". In: *J. Appl. Mech.* 40.2, pp. 337–342. ISSN: 0021-8936. DOI: 10.1115/1.3422984.
Sparrow, E. M., H. Quack, and C. J. Boerner [1970]. "Local nonsimilarity boundary-layer solutions". In: *AIAA J.* 8.11, pp. 1936–1942. DOI: 10.2514/3.6029.
Stewartson, K. [1964]. *The theory of laminar boundary layers in compressible fluids*. Oxf. Math. Monogr. Clarendon Press.

Stinson, M. R. [1991]. "The propagation of plane sound waves in narrow and wide circular tubes, and generalization to uniform tubes of arbitrary cross-sectional shape". In: *J. Acoust. Soc. Am.* 89.2, pp. 550–558. DOI: 10.1121/1.400379.

Sutherland, W. [1893]. "The viscosity of gases and molecular force". In: *Philos. Mag. Ser. 5* 36.223, pp. 507–531. DOI: 10.1080/14786449308620508.

Sutter, B. [Aug. 1962]. "The equations of fluid mechanics expressed in curvilinear coordinates". MA thesis. Air Force Inst. Tech.

Swearingen, J. D. and R. F. Blackwelder [1987]. "The growth and breakdown of streamwise vortices in the presence of a wall". In: *J. Fluid Mech.* 182, pp. 255–290. DOI: 10.1017/S0022112087002337.

Tandiono, T., S. H. Winoto, and D. A. Shah [Sept. 2008]. "On the linear and nonlinear development of Görtler vortices". In: *Phys. Fluids* 20.9, p. 094103. ISSN: 1070-6631. DOI: 10.1063/1.2980349.

Tani, I. [1962]. "Production of longitudinal vortices in the boundary layer along a concave wall". In: *J. Geophys. Res.* 67.8, pp. 3075–3080. DOI: 10.1029/JZ067i008p03075.

— [1969]. "Boundary-Layer Transition". In: *Ann. Rev. Fluid Mech.* 1.1, pp. 169–196. DOI: 10.1146/annurev.fl.01.010169.001125.

Taylor, G. I. [1971]. "A model for the boundary condition of a porous material. Part 1". In: *J. Fluid Mech.* 49.2, pp. 319–326. DOI: 10.1017/S0022112071002088.

Thasu, P. S. and S. Duvvuri [Mar. 2024]. "Measurement of freestream noise in a hypersonic wind tunnel". In: *Exp. Fluids* 65.4, p. 45. ISSN: 1432-1114. DOI: 10.1007/s00348-024-03783-3.

Tilton, N. and L. Cortelezzi [2006]. "The destabilizing effects of wall permeability in channel flows: A linear stability analysis". In: *Phys. Fluids* 18.5, p. 051702. DOI: 10.1063/1.2202649.

— [2008]. "Linear stability analysis of pressure-driven flows in channels with porous walls". In: *J. Fluid Mech.* 604, pp. 411–445. DOI: 10.1017/S0022112008001341.

— [2015]. "Stability of boundary layers over porous walls with suction". In: *AIAA J.* 53.10, pp. 2856–2868. DOI: 10.2514/1.J053716.

Traub, H., J. Kube, S. Jose, A. Prasannakumar, and C. Hühne [Apr. 2024]. "Structural and aerodynamic characteristics of micro-perforated porous sheets for laminar flow control". In: *ASME 2024 Aerosp. Struct. Struct. Dyn. Mater. Conf.* Aerosp. Struc. Struct. Dyn. Mater. Conf. V001T03A020. DOI: 10.1115/SSDM2024-121620.

Trefethen, L. N., A. E. Trefethen, S. C. Reddy, and T. A. Driscoll [1993]. "Hydrodynamic Stability Without Eigenvalues". In: *Sci.* 261.5121, pp. 578–584. DOI: 10.1126/science.261.5121.578.

Tsiberkin, K. B. [Aug. 2016]. "On the structure of the steady-state flow velocity field near the interface between a homogeneous liquid and a Brinkman porous medium". In: *Tech. Phys.* 61.8, pp. 1181–1186. ISSN: 1090-6525. DOI: 10.1134/S1063784216080272.

— [2018a]. "Effect of inertial terms on fluid–porous medium flow coupling". In: *Transp. Porous Media* 121.1, pp. 109–120. ISSN: 1573-1634. DOI: 10.1007/s11242-017-0951-8.

Tsiberkin, K. B. [2018b]. "Inertial and Darcy's terms ratio in boundary layer at fluid–porous medium interface". In: *Transp. Porous Media* 125.2, pp. 259–269. ISSN: 1573-1634. DOI: 10.1007/s11242-018-1117-z.

Vafai, K. and S.-J. Kim [Aug. 1990]. "Analysis of surface enhancement by a porous substrate". In: *J. Heat Transf.* 112.3, pp. 700–706. ISSN: 0022-1481. DOI: 10.1115/1.2910443.

Viaro, S. and P. Ricco [2019a]. "Compressible unsteady Görtler vortices subject to free-stream vortical disturbances". In: *J. Fluid Mech.* 867, pp. 250–299. DOI: 10.1017/jfm.2019.83.

— [2019b]. "Neutral stability curves of compressible Görtler flow generated by low-frequency free-stream vortical disturbances". In: *J. Fluid Mech.* 876, pp. 1146–1157. DOI: 10.1017/jfm.2019.590.

Wang, Q., Z. Wang, and Y. Zhao [2018]. "Visualization of Görtler vortices in supersonic concave boundary layer". In: *J. Vis.* 21.1, pp. 57–62. ISSN: 1875-8975. DOI: 10.1007/s12650-017-0443-5.

Wartemann, V., H. Lüdeke, and N. D. Sandham [2012]. "Numerical Investigation of Hypersonic Boundary-Layer Stabilization by Porous Surfaces". In: *AIAA J.* 50.6, pp. 1281–1290. DOI: 10.2514/1.J051355.

Wartemann, V., A. Wagner, T. Giese, T. Eggers, and K. Hannemann [Mar. 2014]. "Boundary-layer stabilization by an ultrasonically absorptive material on a cone in hypersonic flow: numerical investigations". In: *CEAS Space J.* 6.1, pp. 13–22. DOI: 10.1007/s12567-013-0053-6.

Wedin, H. and S. Cherubini [Nov. 2016]. "Permeability models affecting nonlinear stability in the asymptotic suction boundary layer: the Forchheimer versus the Darcy model". In: *Fluid Dyn. Res.* 48.6, p. 061411. DOI: 10.1088/0169-5983/48/6/061411.

Wedin, H., S. Cherubini, and A. Bottaro [July 2015]. "Effect of plate permeability on nonlinear stability of the asymptotic suction boundary layer". In: *Phys. Rev. E* 92 [1], p. 013022. DOI: 10.1103/PhysRevE.92.013022.

Westin, K. J. A., A. V. Boiko, B. G. B. Klingmann, V. V. Kozlov, and P. H. Alfredsson [1994]. "Experiments in a boundary layer subjected to free stream turbulence. Part 1. Boundary layer structure and receptivity". In: *J. Fluid Mech.* 281, pp. 193–218. DOI: 10.1017/S0022112094003083.

Whang, C. and X. Zhong [Jan. 2003]. "Leading Edge Receptivity of Görtler Vortices in a Mach 15 Flow over a Blunt Wedge". In: *41st Aerosp. Sci. Meet. & Exhib.* AIAA Paper 2003-0790. AIAA. DOI: 10.2514/6.2003-790.

Whitaker, S. [1966]. "The equations of motion in porous media". In: *Chem. Eng. Sci.* 21.3, pp. 291–300. ISSN: 0009-2509. DOI: 10.1016/0009-2509(66)85020-0.

— [1967]. "Diffusion and dispersion in porous media". In: *AIChE J.* 13.3, pp. 420–427. DOI: 10.1002/aic.690130308.

— [1969]. "Advances in Theory of Fluid Motion in Porous Media". In: *Ind. Eng. Chem.* 61.12, pp. 14–28. DOI: 10.1021/ie50720a004.

— [Mar. 1986]. "Flow in porous media I: A theoretical derivation of Darcy's law". In: *Transp. Porous Media* 1.1, pp. 3–25. ISSN: 1573-1634. DOI: 10.1007/BF01036523.

Whitaker, S. [Oct. 1996]. "The Forchheimer equation: a theoretical development". In: *Transp. Porous Media* 25.1, pp. 27–61. ISSN: 1573-1634. DOI: 10.1007/BF00141261.

— [1998]. *The method of volume averaging*. Dordrecht: Kluwer Acad. Publ. ISBN: 9780792354864.

Wood, B. D., X. He, and S. V. Apte [2020]. "Modeling Turbulent Flows in Porous Media". In: *Ann. Rev. Fluid Mech.* 52.1, pp. 171–203. DOI: 10.1146/annurev-fluid-010719-060317.

Wu, X. [1999]. "Generation of Tollmien–Schlichting waves by convecting gusts interacting with sound". In: *J. Fluid Mech.* 397, pp. 285–316. DOI: 10.1017/S0022112099006114.

Wu, X. and M. Dong [2016]. "Entrainment of short-wavelength free-stream vortical disturbances in compressible and incompressible boundary layers". In: *J. Fluid Mech.* 797, pp. 683–728. DOI: 10.1017/jfm.2016.318.

Wu, X., D. Zhao, and J. Luo [2011]. "Excitation of steady and unsteady Görtler vortices by free-stream vortical disturbances". In: *J. Fluid Mech.* 682, pp. 66–100. DOI: 10.1017/jfm.2011.224.

Wu, Z. and P. Mirbod [2018]. "Experimental analysis of the flow near the boundary of random porous media". In: *Phys. Fluids* 30.4, p. 047103. DOI: 10.1063/1.5021903.

Wundrow, D. W. and M. E. Goldstein [2001]. "Effect on a laminar boundary layer of small-amplitude streamwise vorticity in the upstream flow". In: *J. Fluid Mech.* 426, pp. 229–262. DOI: 10.1017/S0022112000002354.

Xu, D., J. Liu, and X. Wu [2020]. "Görtler vortices and streaks in boundary layer subject to pressure gradient: excitation by free stream vortical disturbances, nonlinear evolution and secondary instability". In: *J. Fluid Mech.* 900, A15. DOI: 10.1017/jfm.2020.438.

Xu, D., P. Ricco, and L. Duan [2024]. "Görtler Instability and Transition in Compressible Flows". In: *AIAA J.* 62.2, pp. 489–517. DOI: 10.2514/1.J062866.

Xu, D., Y. Zhang, and X. Wu [2017]. "Nonlinear evolution and secondary instability of steady and unsteady Görtler vortices induced by free-stream vortical disturbances". In: *J. Fluid Mech.* 829, pp. 681–730. DOI: 10.1017/jfm.2017.572.

Yang, G. and B. Weigand [Apr. 2018]. "Investigation of the Klinkenberg effect in a micro/nanoporous medium by direct simulation Monte Carlo method". In: *Phys. Rev. Fluids* 3 [4], p. 044201. DOI: 10.1103/PhysRevFluids.3.044201.

Yoshioka, S., J. H. M. Fransson, and P. H. Alfredsson [Oct. 2004]. "Free stream turbulence induced disturbances in boundary layers with wall suction". In: *Phys. Fluids* 16.10, pp. 3530–3539. ISSN: 1070-6631. DOI: 10.1063/1.1775222.

Young, A. D. [Jan. 1948]. "Note on the velocity and temperature distributions attained with suction on a flat plate of infinite extent in compressible flow". In: *Quart. J. Mech. Appl. Math.* 1.1, pp. 70–75. ISSN: 0033-5614. DOI: 10.1093/qjmam/1.1.70.

Yu, K., J. Xu, S. Liu, and X. Zhang [2018]. "Starting characteristics and phenomenon of a supersonic wind tunnel coupled with inlet model". In: *Aerosp. Sci. Tech.* 77, pp. 626–637. DOI: 10.1016/j.ast.2018.03.050.

Zhang, Y., T. Zaki, S. Sherwin, and X. Wu [June 2011]. "Nonlinear Response of a Laminar Boundary Layer to Isotropic and Spanwise Localized Free-stream Tur-

bulence". In: *6th AIAA Theor. Fluid Mech. Conf.* AIAA Paper 2011-3292. AIAA. DOI: 10.2514/6.2011-3292.

Zhao, R., T. Liu, C. Y. Wen, J. Zhu, and L. Cheng [2018]. "Theoretical modeling and optimization of porous coating for hypersonic laminar flow control". In: *AIAA J.* 56.8, pp. 2942–2946. DOI: 10.2514/1.J057272.

Zhao, R., X. X. Zhang, and C. Y. Wen [2020]. "Theoretical modeling of porous coatings with simple microstructures for hypersonic boundary-layer stabilization". In: *AIAA J.* 58.2, pp. 981–986. DOI: 10.2514/1.J058403.

Zhong, X. and C. Whang [Jan. 2002]. "Receptivity of Görtler vortices in hypersonic boundary layers". In: *40th AIAA Aerosp. Sci. Meet. & Exhib.* AIAA Paper 2002-0151. AIAA. DOI: 10.2514/6.2002-151.

Zolotukhin, A. B. and A. T. Gayubov [Aug. 2022]. "Analysis of nonlinear effects in fluid flows through porous media". In: *J. Petroleum Explor. Prod. Tech.* 12.8, pp. 2237–2255. ISSN: 2190-0566. DOI: 10.1007/s13202-021-01444-3.

Zwikker, C. and C. W. Kosten [1949]. *Sound Absorbing Materials*. Elsevier Publ. Co.